

Synchronous reluctance machine optimization based on reduced set of geometric parameters with improved convergence and robust geometric feasibility verification

Ban, Branko

Doctoral thesis / Disertacija

2022

Degree Grantor / Ustanova koja je dodijelila akademski / stručni stupanj: **University of Zagreb, Faculty of Electrical Engineering and Computing / Sveučilište u Zagrebu, Fakultet elektrotehnike i računarstva**

Permanent link / Trajna poveznica: <https://um.nsk.hr/um:nbn:hr:168:932677>

Rights / Prava: [In copyright](#) / [Zaštićeno autorskim pravom.](#)

Download date / Datum preuzimanja: **2025-02-18**



Repository / Repozitorij:

[FER Repository - University of Zagreb Faculty of Electrical Engineering and Computing repozitory](#)





University of Zagreb

FACULTY OF ELECTRICAL ENGINEERING AND COMPUTING

Branko Ban

**SYNCHRONOUS RELUCTANCE MACHINE
OPTIMIZATION BASED ON REDUCED SET OF
GEOMETRIC PARAMETERS WITH IMPROVED
CONVERGENCE AND ROBUST GEOMETRIC
FEASIBILITY VERIFICATION**

DOCTORAL THESIS

Zagreb, 2022.



Sveučilište u Zagrebu
FAKULTET ELEKTROTEHNIKE I RAČUNARSTVA

Branko Ban

**SYNCHRONOUS RELUCTANCE MACHINE
OPTIMIZATION BASED ON REDUCED SET OF
GEOMETRIC PARAMETERS WITH IMPROVED
CONVERGENCE AND ROBUST GEOMETRIC
FEASIBILITY VERIFICATION**

DOCTORAL THESIS

Supervisor: Associate Professor Stjepan Stipetić, PhD

Zagreb, 2022.



Sveučilište u Zagrebu
FAKULTET ELEKTROTEHNIKE I RAČUNARSTVA

Branko Ban

**OPTIMIZACIJA SINKRONIH RELUKTANTNIH
STROJEVA TEMELJENA NA REDUCIRANOM
SKUPU GEOMETRIJSKIH PARAMETARA S
POBOLJŠANOM KONVERGENCIJOM I
ROBUSNOM PROVJEROM GEOMETRIJSKE
IZVEDIVOSTI**

DOKTORSKI RAD

Mentor: izv. prof. dr. sc. Stjepan Stipetić

Zagreb, 2022.

The doctoral thesis was completed at the University of Zagreb Faculty of Electrical Engineering and Computing, Department of Electric Machines and Automation, Zagreb, Croatia

Supervisor: Associate Professor Stjepan Stipetić, PhD

The thesis has:165pages.

Thesis number: _____

About the Supervisor

Stjepan Stipetić is an associate professor at University of Zagreb, Faculty of Electrical Engineering and Computing, Department of Electric Machines, Drives and Automation. He graduated from the same Department in 2008 under the supervision of prof. Ivan Gašparac and received PhD degree in 2014 under the supervision of prof. Damir Žarko. In the period from 2008 to 2014, he worked as a junior researcher and postdoc, then in 2015 and 2016 he worked in France as a Marie Curie Fellow on the EU FP7 project ADEPT. In 2017, he returned to FER as an assistant professor, and since 2019 he has worked as an associate professor.

Scientific interest of associate professor Stjepan Stipetić includes design, modelling, testing and optimizing electrical machines and electrical drives. Stjepan Stipetić is the principal researcher on the scientific project Synchronous reluctance generators for micro hydropower plants, financed by the Croatian Science Foundation. During his tenure, Stjepan Stipetić was involved as a researcher in several national and international scientific projects and was a principal researcher or researcher in numerous industrial projects with domestic and foreign companies. He is the author of many papers published in international journals and on international conferences, of which over 15 papers in category A journals and over 30 papers in the proceedings of international conferences. He reviewed over 150 papers in high ranked scientific journals and on scientific conferences. He supervised more than twenty undergraduate and graduate students. He is a member of the HRO CIGRÉ, IEEE and EDZ professional associations.

O mentoru

Stjepan Stipetić izvanredni je profesor na Sveučilištu u Zagrebu, Fakultetu elektrotehnike i računarstva, na Zavodu za elektrostrojarnstvo i automatizaciju. Na istom Zavodu diplomirao je 2008. godine pod mentorstvom prof. dr. sc. Ivana Gašparca, a doktorirao 2014. godine pod mentorstvom prof. dr. sc. Damira Žarka. U razdoblju od 2008. do 2014. radio je kao znanstveni novak i poslijedoktorand, zatim se u 2015. i 2016. usavršavao u Francuskoj kao stipendist na EU FP7 projektu ADEPT iz zaklade Marie Curie. 2017. godine se vraća na FER u zvanje docenta, a od 2019. godine je u zvanju izvanrednog profesora.

Znanstveni interes izv. prof. dr. sc. Stjepana Stipetića obuhvaća projektiranje, modeliranje, ispitivanje i optimiranje električnih strojeva i elektromotornih pogona. Stjepan Stipetić je voditelj znanstvenog projekta Sinkroni reluktantni generatori za mikro hidroelektrane, financiranog od Hrvatske zaklade za znanost. Tijekom svojeg radnog staža Stjepan Stipetić je bio uključen kao istraživač u više nacionalnih i međunarodnih znanstvenih projekata te je bio voditelj ili suradnik na brojnim stručnim projektima s domaćim i inozemnim poduzećima. Autor je većeg broja radova objavljenih u međunarodnim časopisima i međunarodnim konferencijama, od toga preko 15 radova u časopisima A kategorije i preko 30 radova u zbornicima međunarodnih skupova. Recenzirao je preko 150 radova u visokorangiranim znanstvenim časopisima i na znanstvenim skupovima. Mentorirao je više od dvadeset studenata na preddiplomskom i diplomskom studiju. Član je udruge HRO CIGRÉ, IEEE i EDZ.

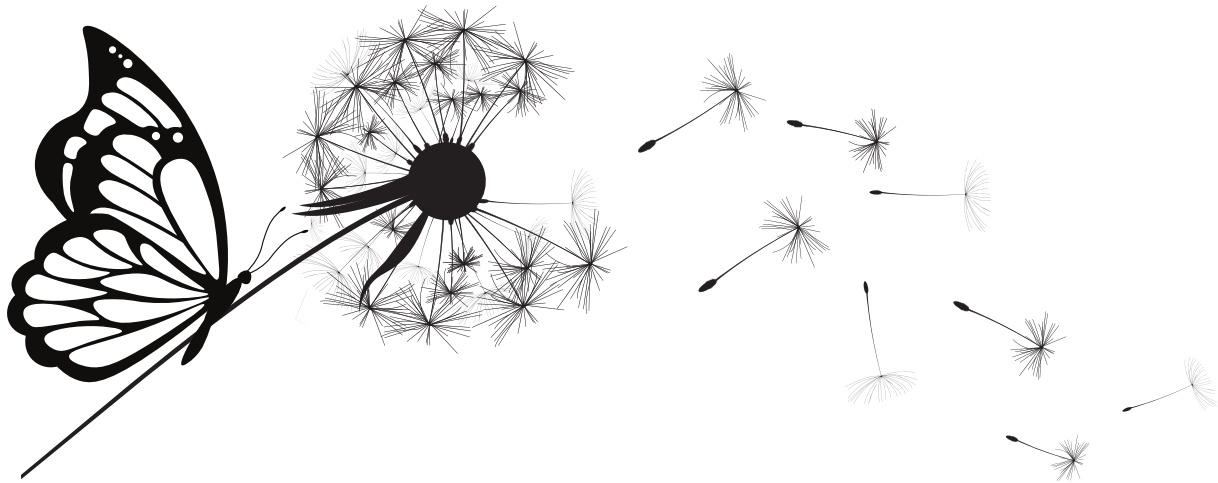
Preface and credits

This thesis is based on the results of the research conducted from March 2017. to August 2022. The inspiration for the proposed scientific contribution was mostly derived from my day-to-day work as a response to related industrial challenges. The research has been supported in various formats by Alten Sweden, Volvo AB, China Euro Vehicle Technology (CEVT), Torquery Consulting, Motor Design Limited, and project "HYDREL - Synchronous reluctance generators for micro hydropower plants" funded by the Croatian science foundation under grant number IP-2018-01-5822, supervised by professor Associate Professor Stjepan Stipetić, PhD.

The thesis was completed thanks to the incredible support of my family and friends. I am deeply grateful to Tino Jerčić, PhD for the numerous meetings and patient answers to all my questions. He was the key in the decision to commence the PhD studies. I wish to thank my supervisor Prof. Stipetić for endless support which often lead to late evening WhatsApp messaging. In my opinion, his level of mentorship is unprecedented, and it is the main reason I chose the PhD studies at University of Zagreb over some top-ranked European universities.

Furthermore, I wish to thank my mother for teaching me that hard work is the key to success. My father, who taught me to always plan and think in advance. My brother, who showed me the importance of being calm in the moments of crisis. To my grandparents, who always offered simply formulated, but universal advice. An example is a piece of classic advice from my grandfather, Branko Lalić: "Ako je klopa dobra, sve je dobro. Ako klopa ne valja, ništa nije dobro". In English: "If the food is good, everything is good. If the food is lousy, you are good for nothing".

And finally, I wish to give my inexpressible thanks to my girlfriend Pavla Aleksić (maybe a wife one day, when we become tired and really really old), for understanding. I am sorry for all those activities we missed because I was exhausted from work. Things will get better from now, I promise ☺. I dedicate the following poem to Pavla.



Djevojka iz moga kraja

Provela je noć na putu
kojim kreću od davnina
naši snovi prema svijetu
s Perkovića preko Knina

U očima njenim more
svjetluca joj sol u kosi
ona ne da da je slome
otima se i prkosi

Djevojka iz moga kraja
na usnama njenim kušam
okus prvih poljubaca
okus prvih oskоруša

Ona pamti davne riječi
slatke boje zavičaja
ima želju da me liječi
djevojka iz moga kraja

Provela je noć na putu
na kojem se nade gase
ostala je svu noć budna
u vagonu druge klase

U očima njenim more
svjetluca joj sol u kosi
ona ne da da je slome
otima se i prkosi

A girl from the homeland

She spent the night on the road
over which from long ago
our dreams set off to the world
from Perković through Knin

The sea is in her eyes
salt shimmers in her hair
she won't allow to be broken
she fights and defies

A girl from the homeland
on her lips I feel
the taste of first kisses
the taste of first rowan berries

She remembers the old words
sweet colours of motherland
she feels the wish to cure me
a girl from the homeland

She spent the night on the road
on which hopes disappear
she stayed awake the whole night
in the second class wagon

The sea is in her eyes
salt shimmers in her hair
she won't allow to be broken
she fights and defies

Arsen Dedić

Short abstract

Currently, electric automobiles are predominantly powered by interior permanent magnet electric machines which possess high efficiency and torque density in comparison to alternative machine types. Although the performance benefits are undisputed, the use of rare earth permanent magnet materials has historically been a commercial risk. To mitigate the potential issues, the automotive industry is considering alternative electric machine designs, which will either use none or a minimal amount of rare earth material. In parallel, synchronous reluctance machines are "magnet-free" electric machine type currently the focus of process industry. Electric power take-off was selected as the application niche for the introduction of synchronous reluctance machine to the automotive sector. The goals of the thesis are to improve the synchronous reluctance machine optimization process by reducing rotor radial cross-section parametric complexity, and to create a software framework for the rotor geometry feasibility validation. The research concentrates on a novel approach of defining rotor geometry on a shape object level, instead of the classical approach which uses geometrical primitives like points, lines, and arcs. This methodology allows simple and robust feasibility validation and robust calculation of at least one point inside every object, which is extremely important for assigning the material to different regions in the finite element analysis tool. The presented solution can be applied on any electric machine type. Furthermore, the thesis defines a set of absolutely feasible synchronous reluctance machine rotor geometries using a minimal set of parameters in order to reduce design complexity. Consequently causing a reduction of overall optimization time due to the smaller number of parameters that define the optimization problem. After selecting the geometry and commencing optimization, the optimization system (software code) must be able to detect if generated geometry is unfeasible (e.g., rotor barriers are overlapping). One of the proposed solutions is a novel concept of forced feasibility, where every unfeasible design is forced to change parameters until reaching feasibility. Otherwise, the infeasible candidate is rejected, which can affect the optimization convergence. Both approaches were compared concluding that forced feasibility causes faster optimization convergence.

Scientific contribution of the thesis is reflected in:

1. Robust feasibility and region detection algorithm based on the shape object approach in the definition of electrical machine geometry.
2. Improvement of optimization convergence through the reduction of feasible geometry search-time for synchronous reluctance machines using novel forced feasibility approach
3. Method for synchronous reluctance machine rotor geometry parametrization with the reduced parameter set.

Keywords: synchronous reluctance machine, optimization, robust feasibility, forced feasibility, minimal complexity

Extended abstract (Prošireni sažetak)

U svrhu smanjenja emisije ispušnih plinova, otpada i buke, direktive Europske Unije trenutno obvezuju proizvođače automobila na drastično prosječno smanjenje emisije ispušnih plinova ukupne flote vozila. Tehnologija motora na unutarnje izgaranje je u pogledu korisnosti dosegla vrhunac, što znači da je jedini način za ispunjavanje navedene direktive postupno povećanje proizvodnje automobila s električnim i hibridnim pogonom. To je uzrokovalo tektonske promjene u automobilskoj industriji, poglavito u primjeni novih znanja i tehnologija u tradicionalnim proizvodnim lancima. Zbog visoke cijene i ograničenog prostora, nove komponente kao što su baterija, pretvarači i električni strojevi postaju najvažniji faktori pri projektiranju vozila. Baterija je najčešće modularna komponenta, a pretvarač ima relativno mali volumen što pojednostavljuje integraciju u vozilo. S druge strane, električni stroj je najčešće integriran s nekom vrstom prijenosnika koji zauzima razmjerno velik prostor. Kako bi se smanjio volumen vučnog sustava, električni stroj treba imati minimalne dimenzije pri čemu korisnost i gustoća snage moraju zadovoljiti tražene karakteristike.

U automobilskoj vuči trenutno prevladavaju strojevi s permanentnim magnetima postavljenima unutar rotora koje u usporedbi s alternativnim tipovima strojeva karakterizira visoka korisnost i gustoća momenta. Premda imaju najbolje tehničke karakteristike, korištenje permanentnih magneta s elementima rijetkih zemalja (eng. *rare-earth*) kao što su neodimij i disprozij predstavlja značajan problem. Narodna Republika Kina kao najveći proizvođač je 2011. i 2012. zaprijetila prestankom opskrbe te uzrokovala dramatični kratkoročni skok cijene (cijena disprozija je privremeno narasla 3000%).

Naziv "elementi rijetkih zemalja" može navesti čitatelja na zaključak, da im je pojava u prirodi analogna primjerice zlatu ili srebru. Zapravo, elementi rijetkih zemalja se dosta često pojavljuju u prirodi, a visoka tržišna cijena je proporcionalna količini ulaganja u rudarenje. Stoga je razumljivo zašto Narodna Republika Kina trenutno vlada tržištem, prvenstveno zbog jeftine radne snage, te zbog iznimno razvijenog rudarskog sektora. Teoretski postoje i jeftinije alternative, kao što su primjerice feritni magneti. Međutim, praksa je pokazala da feritni materijali ne mogu zadovoljiti zahtjeve auto-industrije za visokom gustoćom momenta i snage pri maksimalnom opterećenju. Nadalje, automobilska industrija ne može dozvoliti značajno kolebanje cijene strateških sirovina, što je usmjerilo inženjere na razvoj električnih strojeva bez ili s minimalnom količinom permanentnih magneta s elementima rijetkih zemalja.

Rješenje koje bi obuhvatilo nižu cijenu asinkronog stoja uz bolju korisnost i performanse motora s permanentnim magnetima je sinkroni reluktantni stroj s pripadajućim podvrstama. Glavna karakteristika sinkronog reluktantnog stroja je dominantna reluktantna komponenta momenta što znači da stroj teoretski ne treba permanentne magnete ili kavez unutar rotora. Sinkroni reluktantni strojevi su robusni, imaju relativno nisku proizvodnu cijenu i male rotorske gubitke.

S druge strane, nedostatak magneta u rotoru rezultira s manjom gustoćom momenta, manjim faktorom snage i većom valovitošću momenta. Kao niša za primjenu u automobilskoj industriji je određen kamionski priključak za pokretanje vanjskih tereta (eng. *PTO - power take-off*). *PTO* priključak je tradicionalno pogonjen pomoću diesel motora na unutarnje izgaranje. Međutim s prijelazom na baterijski pogonjene električne kamione, *PTO* također mora biti pogonjen električnim putem, stoga se uvodi naziv električni *PTO* (eng. *e-PTO - electric power take-off*). Klasični *PTO* je karakterizan izraženom valovitošću momenta koje su posljedica rada dizel motora. Uzevši u obzir da sinkroni reluktantni strojevi inherentno imaju slične karakteristike, e-*PTO* je idealna niša za primjenu u automobilskom sektoru.

Optimizacijski algoritmi su danas jako popularni u projektiranju električnih strojeva. Zbog utjecaja elektromagnetske nelinearnosti i složenosti geometrije na performanse električnih strojeva, općenito se smatra da matematička optimizacija može znatno poboljšati konačni dizajn. Iznimno popularna klasa optimizacijskih algoritama su evolucijski stohastički algoritmi temeljeni na populacijama mogućih rješenja (populacija čini veći broj individualnih jedinki dizajna stroja) koje se mutiraju i kombiniraju prema pravilima odabranog algoritma za svaku sljedeću generaciju. Najbolje jedinice propagirane su kroz generacije do postizanja optimalnog rješenja.

Potreba za optimizacijom je posebno izražena zbog regulatornih zahtjeva za povećanjem korisnosti u industriji što korelira s osnovnim zahtjevima u automobilskom sektoru. Računalna zahtjevnost je proporcionalna složenosti geometrije stroja, što vodi k velikom broju optimizacijskih parametara i dužem vremenu optimizacije. Uzevši to obzir, jedan od ciljeva istraživanja bio je razvoj geometrijskog opisa sinkronog reluktantnog stroja s minimalnim brojem rotorskih parametara. Korištenje programskih alata baziranih na metodi konačnih elemenata u projektiranju sinkronih reluktantnih strojeva je nezaobilazno zbog izraženog zasićenja u rotorskim barijerama i mostićima koje ima veliki utjecaj na konačne performanse. Navedeni alati zahtijevaju veliku procesorsku moć, pri čemu evolucijska optimizacija uslijed populacija s velikim brojem jedinki (do 50) i velikog broja generacija (do 200) može zahtijevati provođenje više tisuća proračuna.

Ključni problem u projektiranju sinkronih reluktantnih strojeva odnosi se na projektiranje barijera na rotoru. To se posebice odnosi na oblik i raspodjelu zračnih barijera te željeznih mostića koji su bitni za mehaničku čvrstoću rotora. Rotorske barijere kod sinkronog reluktantnog stroja mogu biti pravokutne, kružne, hiperboličke ili izvedene iz teorije konformnih preslikavanja i teorije Žukovskog o tokovima fluida. Istražene su razne varijante konstrukcije barijera kako bi se definirale najjednostavnije metode parametrizacije koje se mogu implementirati kao automatski generirani predlošci rotorskih geometrija. Na primjer, tipična definicija rotora temeljena na barijerama Žukovskoga zahtijeva $N = 3 \cdot k$ geometrijskih parametara, gdje k predstavlja broj barijera. Predloženi pristup smanjuje broj parametara na $N = 2 \cdot k + 1$. Jedan od ciljeva istraživanja je definiranje smanjenog seta parametara za svaki tip rotorskih barijera.

Neovisno o vrsti stroja, tijekom izvršavanja optimizacije, odabrani tip optimizacijskog algoritma generira set parametara koji opisuju geometrijski oblik rotorskih barijera odnosno pojedinu jedinku u trenutnoj populaciji. Bez obzira na raspon ulaznih parametara, sustav mora moći detektirati ako je generirana geometrija neizvediva. Pojam "izvodljivost" ili "izvedivost" (eng. *feasibility*) je najčešće vezan za rezultat i znači da rješenje ispunjava sva definirana ograničenja. Postoji i drugi tip izvedivosti, tzv. geometrijska izvedivost. Model je geometrijski izvediv ako se oblici ne preklapaju, ne postoje negativne duljine ili neki drugi nekonvencionalni odnosi koji redovito uzrokuju greške pri rješavanju alatima temeljenim na metodi konačnih elemenata. Posebno je važno riješiti navedeni problem u slučaju korištenja programskih alata čije su geometrije bazirane na preddefiniranim predlošcima.

U slučaju da je geometrija neizvediva, postoje dva načina osiguravanja geometrijske izvedivosti. U prvom slučaju, cijeli set parametara se nasumično generira dok god nije postignuta geometrijska izvedivost. Alternativa je prisilna izvedivost koja mijenja parametre svakog neizvedivog dizajna do zadovoljavanja izvedivosti. Navedeni pristup može biti iznimno složen i zahtijeva naprednu parametrizaciju s minimalnim brojem uvjeta izvedivosti. S druge strane, moguća prednost ovog pristupa je skraćanje vremena optimizacije iz dva razloga. Prvo, pristup prisilne izvedivosti je vrlo brz stoga gotovo da nema čekanja da se pojavi geometrijski izvediv dizajn. Drugo, intervencija u genetsku progresiju evolucijskog algoritma je u slučaju nasumične generacije parametara značajna, dok je u slučaju prisilne izvedivosti minimalna.

Bez obzira na odabrani pristup, u slučaju da sustav ne uspije detektirati neizvediv dizajn, doći će do neželjenih posljedica. Ovisno o korištenom alatu, u najboljem slučaju sustav će dojaviti grešku i optimizacija će se zaustaviti. U najgorem slučaju, proračun će se nastaviti, a konačni rezultati neće biti upotrebljivi. Ovo je veliki problem koji se može riješiti jedino strogim definiranjem svih mogućih parametarskih ograničenja. To je jako složen zadatak, posebno u slučaju višeslojnih rotorskih geometrija i može rezultirati suboptimalnim konačnim rješenjem. Kako bi se riješio navedeni problem, istraživanje je rezultiralo razvojem i implementacijom robusnog algoritma za određivanje geometrijske izvedivosti.

Razmatrani strojevi imaju radijalni magnetski tok, što znači da se u svrhu optimizacije geometrija poprečnog presjeka rotora i statora može reducirati na 2D Euklidski prostor. Parametrizacija geometrije se izvodi u kartezijskim ili polarnim koordinatama koje određuju geometrijske primitivne elemente: točke, linije, lukove i tzv. polilinije (setove više linija koji modeliraju kompleksnu krivulju). Set međusobno spojenih primitivnih elemenata definira oblik (npr. rotorsku barijeru) koji ima matematička svojstva (površinu, opseg, težište).

Ako cijelu geometriju stroja definiramo pomoću oblika koji su ujedno i programski objekti bilo bi iznimno korisno koristiti funkcijski alat koji na jednostavan način može proračunati odnose među pojedinim oblicima (Booleove funkcije, presjeci, površine...). Spomenuti inovativni pristup određivanja izvedivosti je moguć na temelju Matlabove klase *polyshape* koja

omogućuje podizanje nivoa apstrakcije s razine primitivnih elemenata na razinu objektno opisanih oblika. Nakon definicije, objekti se mogu organizirati u obliku vektora. Funkcionalnost polylshape klase omogućava brzu analizu vektoriziranih objekata oblika. Jedna od posebno zanimljivih funkcija je funkcija Intersection koja vraća informaciju postoji li preklapanje među pojedinim elementima vektora oblika. Ovo omogućava robusnu provjeru izvedivosti bez obzira na granice inicijalnih geometrijskih parametara i na složenost geometrijskog oblika.

Dodatno, svi alati za elektromagnetski proračun strojeva zahtijevaju precizno definiranje geometrijskih područja (regija) pojedinog oblika što predstavlja problem u slučaju stohastički generiranih geometrija. Općenito, generirani oblik može biti konveksan ili konkavan (oblici koji sadrže šupljine nisu dozvoljeni). Pojednostavljeno, konveksni oblici uvijek imaju težište unutar rubova elementa, što ne mora biti slučaj kod konkavnih oblika. Tipičan primjer konveksnog oblika je pravokutnik permanentnog magneta. S druge strane, zračne barijere su uglavnom konkavne i imaju težište izvan svojih granica. Prezentirani problem je riješen razvojem algoritma za određivanje regija oblika temeljenom na Matlab polylshape klasi. Prednosti predložene pristupa objektno definiranih oblika su jednostavno povezivanje s bilo kojim elektromagnetskim alatom koji podržava skriptiranje, značajna sloboda u projektiranju složenih geometrija i jednostavno uklanjanje softverskih grešaka. Literatura ne pokriva navedeni pristup u projektiranju električnih strojeva što dokazuje znanstvenu izvornost.

Zaključno, istraživanje se koncentrira na parametrizaciju rotorskih barijera, unaprjeđivanje postizanja izvedivosti rotorskih geometrija, i razvoj algoritama za baratanje geometrijom stroja temeljenom na objektno opisanim oblicima. Primjena rezultata istraživanja nije ograničena samo na automobilsku industriju jer se stečena znanja i zaključci mogu primijeniti i u energetici te procesnoj industriji.

Sukladno navedenim koracima, doprinos provedenog istraživanja opisani kroz doktorsku disertaciju s naslovom "Optimizacija sinkronih reluktantnih strojeva temeljena na reduciranom skupu geometrijskih parametara s poboljšanom konvergencijom i robusnom provjerom geometrijske izvedivosti" sastoji se od sljedećeg:

1. Robusni algoritmi za ocjenu geometrijske izvedivosti i pronalaženje geometrijskih područja temeljeni na objektnom pristupu definiranja oblika s primjenom u geometrijskom opisu električnog stroja.
2. Poboljšanje konvergencije optimizacije temeljeno na skraćivanju vremena pronalaska izvedive geometrije električnog stroja korištenjem metode prisiljene geometrijske izvedivosti.
3. Metoda parametrizacije geometrije rotora sinkronog reluktantnog stroja sa smanjenim skupom parametara.

Modeli su razvijeni i implementirani u programskom okruženju Matlab, a za izračun karakteristika električnih strojeva je korišten programski paket Ansys Motor-CAD.

Disertacija ujedinjuje opis teorijske pozadine i implementiranih metoda. Kroz disertaciju

su opisani doprinosi te su konkretno povezani s različitim dijelovima objavljenih radova koji ih definiraju i pojašnjavaju. Pseudo kod za generiranje apsolutno izvedivih rotora sinkronih reluktantnih strojeva, te izvorni kod za robusnu detekciju izvedivosti su objavljeni u relevantnim znanstvenim časopisima.

Ključne riječi: sinkroni reluktantni stroj, optimizacija, robusna izvedivost, prisiljena izvedivost, minimalna kompleksnost

Contents

1. Introduction	1
1.1. Background and motivation.	.1
1.2. Problem statement.	.2
1.3. Objective of the Thesis.	.3
1.4. Structure of the thesis.	.4
2. Theoretical aspects and applications of Synchronous Reluctance Machines	5
2.1. General facts.	.5
2.1.1. Electromagnetic torque.	.8
2.1.2. Combination of PM and reluctance: IPM design plane.	.11
2.1.3. Rotor laminations assembly.	.11
2.2. SyRM commercial applications.	.13
2.2.1. Industry.	.13
2.2.2. Automotive traction.	.13
2.2.3. Ship propulsion and freight traction.	.13
2.2.4. Commercial vehicles.	.14
2.3. Further reading.	.15
3. SyRM rotor cross section parametrization	16
3.1. Rotor design Automation.	.17
3.2. Parametric Complexity.	.19
3.3. Pseudo-Code Validation.	.20
3.4. Further reading.	.22
4. Feasibility detection as a part of optimization strategy	23
4.1. Optimization methodology.	.23
4.1.1. Optimization workflow.	.24
4.1.2. Geometric feasibility.	.24
4.1.3. Feasibility detection importance.	.26
4.2. Standard approach for feasibility detection.	.28

4.3.	Robust feasibility detection.29
4.3.1.	Region inner-point detection.30
4.3.2.	Feasibility check.31
4.3.3.	Impact on total execution time.31
4.4.	Further reading.32
5.	Main scientific contribution of the thesis	33
5.1.	Robust feasibility and region detection algorithm based on the shape object approach in the definition of electrical machine geometry.33
5.2.	Improvement of optimization convergence through the reduction of feasible geometry search-time for synchronous reluctance machines using novel forced feasibility approach.34
5.3.	Method for synchronous reluctance machine rotor geometry parametrization with the reduced parameter set.35
6.	List of publications	37
7.	Author’s contributions to the publications	39
8.	Conclusion and Future Directions	42
9.	Publications	43
	Publication 1: Synchronous Reluctance Machines: Theory, Design and the Potential Use in Traction Applications.43
	Publication 2: Electric Multipurpose Vehicle Power Take-Off: Overview, Load Cycles and Actuation via Synchronous Reluctance Machine.56
	Publication 3: Design and optimization of Synchronous Reluctance Machine for actuation of Electric Multi-purpose Vehicle Power Take-Off.65
	Publication 4: Minimum Set of Rotor Parameters for Synchronous Reluctance Machine and Improved Optimization Convergence via Forced Rotor Barrier Feasibility.74
	Publication 5: Absolutely Feasible Synchronous Reluctance Machine Rotor Barrier Topologies with Minimal Parametric Complexity.91
	Publication 6: Robust Feasibility Verification and Region Inner-Point Detection Algorithms for Geometric Shape Objects applied to Electric Machine Optimization Workflow.112
	Publication 7: Systematic Metamodel-based Optimization Study of Synchronous Reluctance Machine Rotor Barrier Topologies.124

Bibliography	149
List of abbreviations	157
Biography	162
Životopis	165

Chapter 1

Introduction

In order to reduce emissions, air pollution, resource waste, and traffic noise, global legislation is pushing towards the increase of electric and hybrid vehicle production [1]. This has caused a tectonic change in the automotive industry, both knowledge, and production-wise. New traction components like battery, inverter, and electric machine are becoming the most important factors in vehicle design in a matter of cost and packaging (component layout within the vehicle) [2,3]. The battery is usually modular component and inverter is small in size, which means they can in most cases be packed efficiently within the vehicle. On the other hand, the electric machine is usually integrated within some sort of transmission system, which is inherently space-consuming [2]. To reduce the size of the drivetrain, electric machine size must be minimized, while efficiency and power density must be kept on the sufficient level.

1.1 Background and motivation

Currently, electric automobiles are predominantly powered by interior permanent magnet electric machines (IPM) which possess high efficiency and torque density in comparison to alternative machine types. Although the performance benefits are undisputed, the use of rare earth permanent magnet (PM) materials, such as neodymium or dysprosium, has raised concerns in several areas. In 2011 and 2012, China reportedly threatened to cut off international supplies of these materials [4], leading to dramatic, though short-term, increase in the material price, increasing as much as 3000% in case of dysprosium [5]. These volatilities have forced the automotive industry to search for the alternative electric machine design, which will either use none or minimal amount of rare earth material. The risk can potentially increase as electric vehicles (EVs) start to penetrate the market on a large scale Fig.1.1.

One of the magnet-free alternatives are synchronous reluctance machines (SyRM) and their derivatives [6]. These solutions rely on high reluctance torque, thus theoretically needing no PM material in the rotor structure. They have relatively low material costs, low rotor losses

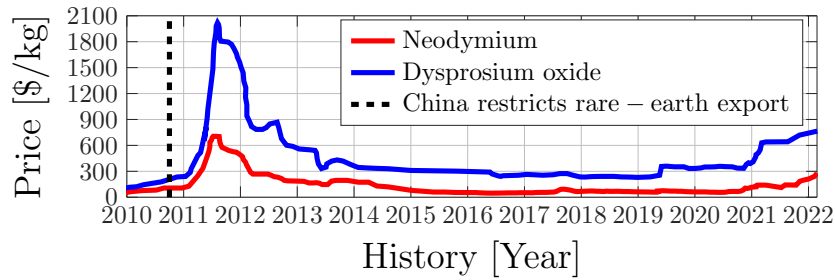


Figure 1.1: Historical rare-earth material prices

and are considered as robust [7,8]. On the other hand, the lack of permanent magnet field in the rotor is penalized with lower torque density, lower power factor, and higher torque ripple [9,10]. Up to now, SyRM machines have not been considered for automotive applications which presents a niche for academic research.

1.2 Problem statement

Nowadays, optimization algorithms enjoy high popularity among electrical machine designers [11,12,13,14,15,16,17,18]. Due to the influence of electromagnetic nonlinearity and geometrical complexity of electrical machines on their performance, it is commonly understood that mathematical optimization can significantly improve the final design. Very popular class of optimization algorithms are evolutionary stochastic algorithms that are based on populations of possible solutions (population is a number of individual machine designs) which are mutated and combined according to selected algorithm rules for the next generation. The best machine designs are propagated through generations until reaching the optimal solution. Optimization necessity is especially noticeable in the problem of increasing efficiency [19,20,21]. Currently, there is a substantial focus on optimization tool-chain improvements, especially in design of traction drives, where high efficiency within limited packaging space is an absolute imperative [22].

According to Pellegrino [23,24], computational load is proportional to the geometrical complexity. This is inherently the case for IPM and SyRM machines, leading to a high number of optimization variables and longer optimization time. The utilization of the finite element analysis (FEA) is practically unavoidable in the case of SyRM and IPM machines due to the significant influence of saturation in rotor barrier bridges and posts on machine performance. FEA is computationally intensive and may naturally require thousands of calculations through evolution-based optimisation due to large population size (up to 50) and large number of generations (up to 200). Having this in mind, one of the research goals is the definition of SyRM geometries with a minimal set of rotor parameters.

SyRM rotor barrier profiles can be rectangular, circular, hyperbolic [25] or derived from

the conformal mapping theory and the Zhukovsky air-flow potential formulation [26]. Barrier design variants have been studied to define the simplest parametrization approach which can be implemented as automated geometry templates.

During the design process on any electric machine type, the selected optimization procedure generates a set of parameters which describe the geometric shape of rotor barriers of a candidate motor in the current population. Regardless of the range of input parameters and the machine type, the system must be able to detect if the geometry is infeasible. The term feasibility is usually related to the solution and it denotes that the solution satisfies all the given constraints. There is another type of feasibility, so-called "geometrical or model feasibility". Geometrically feasible model is valid for solving if: there are no overlapping edges, negative lengths or non-conventional geometric relations that will inevitably create issues after the start of the FEA solver.

This is a cumbersome issue that can be solved only by strictly defining all parameter constraints. This is an extremely complicated process, especially in the case of complex multi-layer rotor geometries and can result in suboptimal designs. To mitigate the problem, the research has resulted with a robust feasibility verification and material region detection procedure. The proposed method is applicable to any type of electric machine.

1.3 Objective of the Thesis

The objective of the research is to improve the optimization process for synchronous reluctance machine (SyRM) regarding geometrical definition complexity and software implementation for the geometry feasibility validation. After selecting the geometry and commencing optimization, the optimization system (software code) must be able to detect if generated geometry is unfeasible (i.e. rotor barriers are overlapping).

The first part of the research concentrates on a novel approach of defining rotor geometry on a shape object level, instead of classical approach which uses geometrical primitives like points, lines, arcs. This methodology allows robust determination of at least one point inside every object which is extremely important for assigning the material to different regions in finite element analysis tool. Additionally, the introduction of shapes enables the development of a global feasibility detection procedure.

An alternative solution to shape-based feasibility detection is a novel concept of forced feasibility (the second part of research), which forces every unfeasible design to change parameters until reaching feasibility. The expected benefit is again overall optimization time reduction.

The final part of the research is the definition of SyRM rotor geometries using a minimal set of parameters in order to reduce design complexity. Consequently, a reduction of overall optimization time is expected due to the smaller number of parameters that define the optimization

problem.

The objectives of the research were:

1. Development of innovative software algorithms for accurate and fast design compatible with any finite element analysis software. When implemented and proven, the source code will be published online and shared with the electrical machine design community.
2. Implementation of forced feasibility approach in the optimization of synchronous reluctance machines with the aim of convergence improvement and consequently reduction of optimization time.
3. Development of rotor geometries for synchronous reluctance machine with a reduced set of parameters.

The robust rotor feasibility and region detection algorithms fall into software implementation domain, and their contributions to electric machine design community will be significant because the proposed method can be easily implemented in any FEA software package. Another hypothesis is that forced feasibility subroutine will yield a reduction of optimization time. This needs to be proven by consecutive optimization runs on the selected example. In the domain of geometry parametrization, the hypothesis is that Zhukovsky barriers have a minimal number of parameters and yet yield optimal machines with the best performance. This needs to be proven by comparison with circular and hyperbolic barrier designs.

1.4 Structure of the thesis

The thesis is organized as follows. Chapter 2 provides an introduction to theoretical aspects of synchronous reluctance machines and discusses potential applications. The emphasis is placed on comparison of IPM and SyRMs. Chapter 3 summarizes the automated rotor geometry scripting of smooth-barrier SyRMs, and validation of corresponding pseudo-code. Chapter 4 presents the robust feasibility detection method and inner-point detection algorithm as a part of optimization framework. Chapters 3-5 are designed to summarize the background for the thesis contributing publications. Further reading section is added at the end of each chapter referring to the relevant publications. Chapter 5 summarized the scientific contributions of the thesis. Chapter 6 provides a list of all related publications that contain different segments of the research contributions. The author's contributions to the publications included in the thesis are summarized in Chapter 7. Finally, Chapter 8 concludes the thesis and provides a potential direction of the future research.

Chapter 2

Theoretical aspects and applications of Synchronous Reluctance Machines

2.1 General facts

Currently, due to the inherently high torque and power density, rare earth based IPM synchronous machines are predominantly used for automotive traction (Fig.2.1a-b). A landmark for IPM machines in automotive hybrid/electric traction was the adoption by both Toyota and Honda, for the first generation of Prius and Insight, respectively [27,28]. Due to the mechanical limitations for high speed operation, surface permanent magnet machines (SPM) are currently not used by any major vehicle manufacturer. On the other hand, some vehicle producers have considered alternative machine designs, which either use none or a minimal amount of rare earth material. Notable passenger vehicle examples are 1th gen. Tesla Model S and Audi e-tron which use induction machines (IM), and 2nd gen. Chevrolet Volt which uses rare-earth-free Ferrite IPM.

The alternatives which have not been in recent automotive focus are synchronous reluctance machines (SyRM) and its derivatives [6].

One advantage of SyRM compared to IM and IPM is the lack of squirrel cage and magnets, which results in reduced material and manufacturing costs (Fig.2.2). This feature leads to SyRM having minimal rotor losses compared to both alternatives [29], and higher efficiency compared to IM [30]. Furthermore, the SyRM control algorithm is very similar to IPM, meaning that the same drive can be used in both cases. Obviously, there are no issues with demagnetization. And finally, SyRM does not produce open-circuit back electromotive force, which secures fault tolerance and can simplify the electric vehicle drive train (mechanical disconnect is not required), resulting in a cheaper transmission system.

On the other hand, lack of the permanent magnetic field in the rotor is penalized with lower torque density, lower power factor, and higher torque ripple.

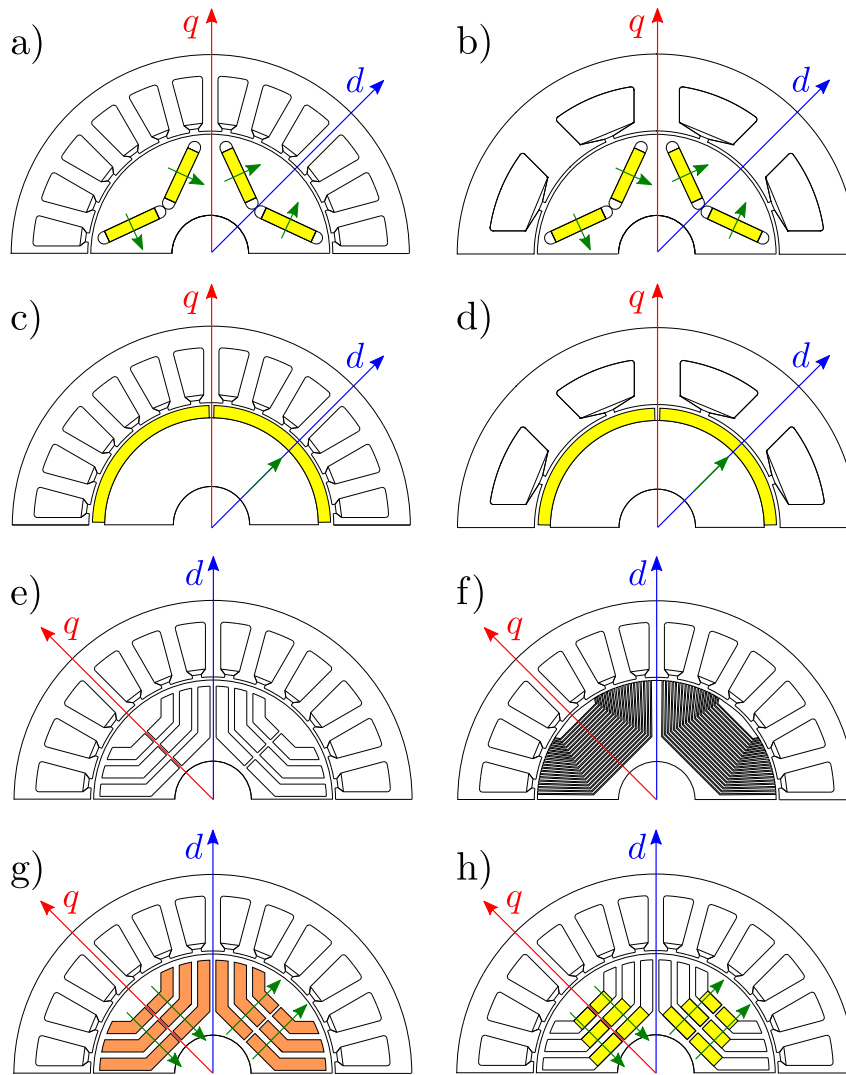


Figure 2.1: Example of four pole machine families with corresponding dq axes: IPM with a) distributed and b) concentrated winding stator; SPM with c) distributed and d) concentrated winding stator; e) SyRM; f) Axially laminated SyRM (AxLam); g) "weak" PM material PMASR; and h) "strong" PM material PMASR. Green arrows indicate PM magnetization direction, Pub.1

The main SyRM disadvantage compared to IPM is reduced power and torque density. The situation can be improved by using hairpin stator technology which increases the fill factor [31], or by improvements in rotor design. Rotor has to be designed for high-speed operation [30], ideally without barrier posts [32], with minimal barrier bridge thickness [33,34], Fig.2.2. This will obviously compromise mechanical integrity. Nevertheless, the issue can be solved by the use of "smooth barrier" topologies (e.g. circular, hyperbolic...) with injected epoxy resin [32], and carefully applied barrier corner fillets [33,34,35].

The next SyRM disadvantage compared to IM and IPM is higher torque ripple [9,10]. Depending on the application, ripple has to be reduced to an acceptable level which is usually 2-4% for vehicle traction or $\approx 10\%$ in industrial applications.

Typical *a posteriori* (post optimization) method for torque ripple reduction is rotor (or stator)

skewing. The disadvantage of the approach is the reduction of average torque and increased production cost.

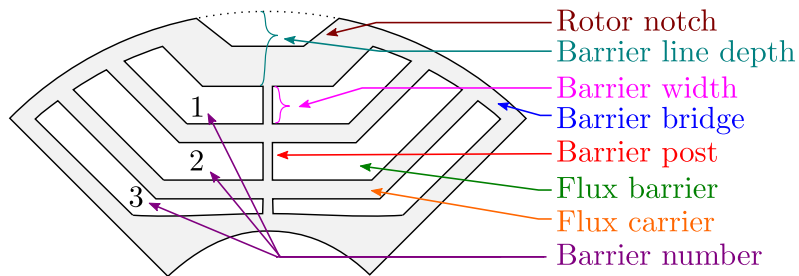


Figure 2.2: SyRM rotor nomenclature

On the other hand, *a priori* (prior to optimization) ripple reduction methods are: increasing the number of poles, application of barrier corner fillets [35], use of barrier notch (Fig.2.2), and use of asymmetric pole designs [36]. Considering that the high pole number has a strong negative impact on power factor, SyRM machines typically have 4 or 6 poles (more than 6 poles correspond to power factors ≤ 0.6). In case inverter size is not a design constraint, higher pole number combinations can be investigated. Nevertheless, implementation of other *a priori* methods will effectively reduce torque ripple without major design penalties. Asymmetric pole design is especially interesting because it can significantly reduce torque ripple [37] and potentially eliminate the need for *a posteriori* skewing, thus making SyRM the cheapest machine variant on the market. Detailed comparison of different SyRM skewing strategies is available in [38].

The unavoidable disadvantage of SyRM is the lowest power factor compared to IM and IPM. The only solution to compensate for this drawback is in mass production of inverter switching modules which will enable cheaper technology, with higher current ratings. This will most likely happen when electric vehicles (EVs) penetrate the market on a large scale.

SyRM design can theoretically be upgraded by adding permanent magnet material to the rotor structure, thus creating an assisted synchronous reluctance machine (PMASR, Fig.2.1g-h). The performance effects of adding different grades of PM materials to the rotor are available on Fig.2.3. The detailed comparison is available in Pub.1.

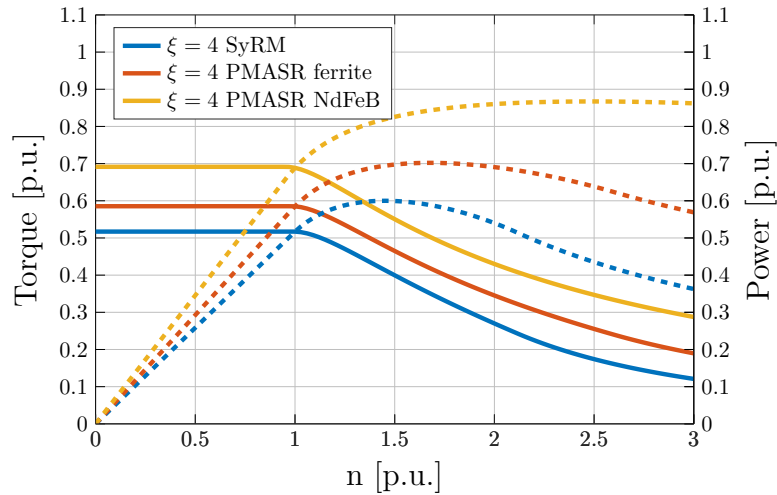


Figure 2.3: Theoretical performance comparison of SyRM, ferrite and NdFeB PMASR at fixed saliency ratio, Pub.1

The purpose of the magnets in PMASR is to saturate barrier bridges, to increase the torque and especially the power factor, which reduces the size of the attached variable frequency drive [9].

As previously mentioned, a penalty of SyRM is the inability to have a large number of poles (in practice, pole numbers are limited to 4 and 6). Obviously, if the number of poles is increased, magnetic bridges and posts must be reduced to maintain the saliency ratio, which is directly related to electromagnetic performance. This puts pressure on rotor structural integrity with increase of operational speed. On the other hand, PMASR technology is well suited for high pole-number designs because magnet flux saturates the barrier bridges and posts (12 poles in case of Chevrolet Volt [39]). In this way, bridges can be thicker, which increases structural robustness of the rotor.

2.1.1 Electromagnetic torque

Machines listed in Fig.2.1 can be divided in two families. First is alignment torque component dominant group, which includes IPM and SPM machines where PM magnetization direction is aligned with positive d axis (Fig.2.1a-d). Second is reluctance torque component dominant group, which includes SyRM and PMASR machines. It is important to emphasize that PMASR magnetization direction is opposing positive q axis (Fig.2.1g-h), [9].

In general, there are two different rotor paths for the flux (Fig.2.1). A distinction of the reluctance machines is a switch of rotor d and q axes in relation to alignment torque dominant family. High permeability path (high magnetic conductivity, d -axis path) is parallel to the flux-barriers. Low permeability path (low magnetic conductivity, q -axis path), is vertical to the rotor flux barriers [9].

For both families, torque output consists of alignment and reluctance component and can

be written as (2.1), (2.3), where L_d, L_q are inductances, i_d, i_q currents in d and q axis, p is the number of pole pairs and λ_m is magnet flux. In case there is no PM material (SyRM, $\lambda_m = 0$), the relation between L_d and L_q will determine the machine torque capability (2.1). The inductance ratio is referred as saliency ratio ξ , whose formula depends on the machine family (2.2), (2.4), [9]. Detailed equation list is available on Fig.2.5.

Dominant reluctance component machine family	}	$T_{em} = \frac{3}{2}p \left[\underbrace{\lambda_m i_d}_{\text{Alignment}} + \underbrace{(L_d - L_q) i_q i_d}_{\text{Reluctance}} \right]$ $\xi = L_d / L_q$	(2.1) (2.2)
Dominant alignment component machine family	}	$T_{em} = \frac{3}{2}p \left[\underbrace{\lambda_m i_q}_{\text{Alignment}} + \underbrace{(L_d - L_q) i_q i_d}_{\text{Reluctance}} \right]$ $\xi = L_q / L_d$	(2.3) (2.4)

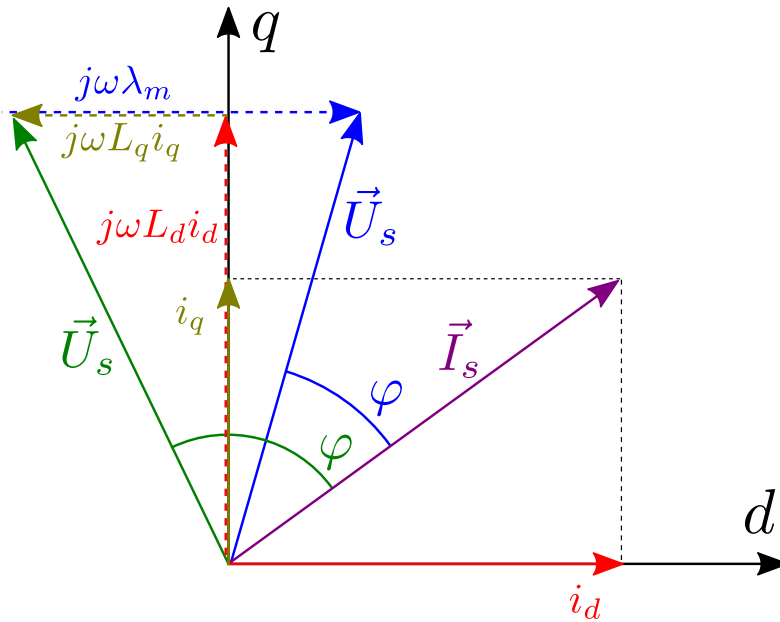


Figure 2.4: Voltage phasor diagram of SyRM (green) and PMASR (blue) for a given stator current (stator resistance is neglected $R_s = 0$) [9].

A high number of cavity layers in each pole combined with a small air-gap typically leads to saliency ratios higher than 3,5 [40]. Lipo and Matsuo report that $\xi = 7 - 8$ can be expected [41], usually achieving power densities in the order of 5.5 – 7.5 kW/l [42], [43]. Apart from the stator and rotor cross-section design, lamination steel selection has an impact on final saliency ratio ($\Delta\xi = \pm 7\%$) [44].

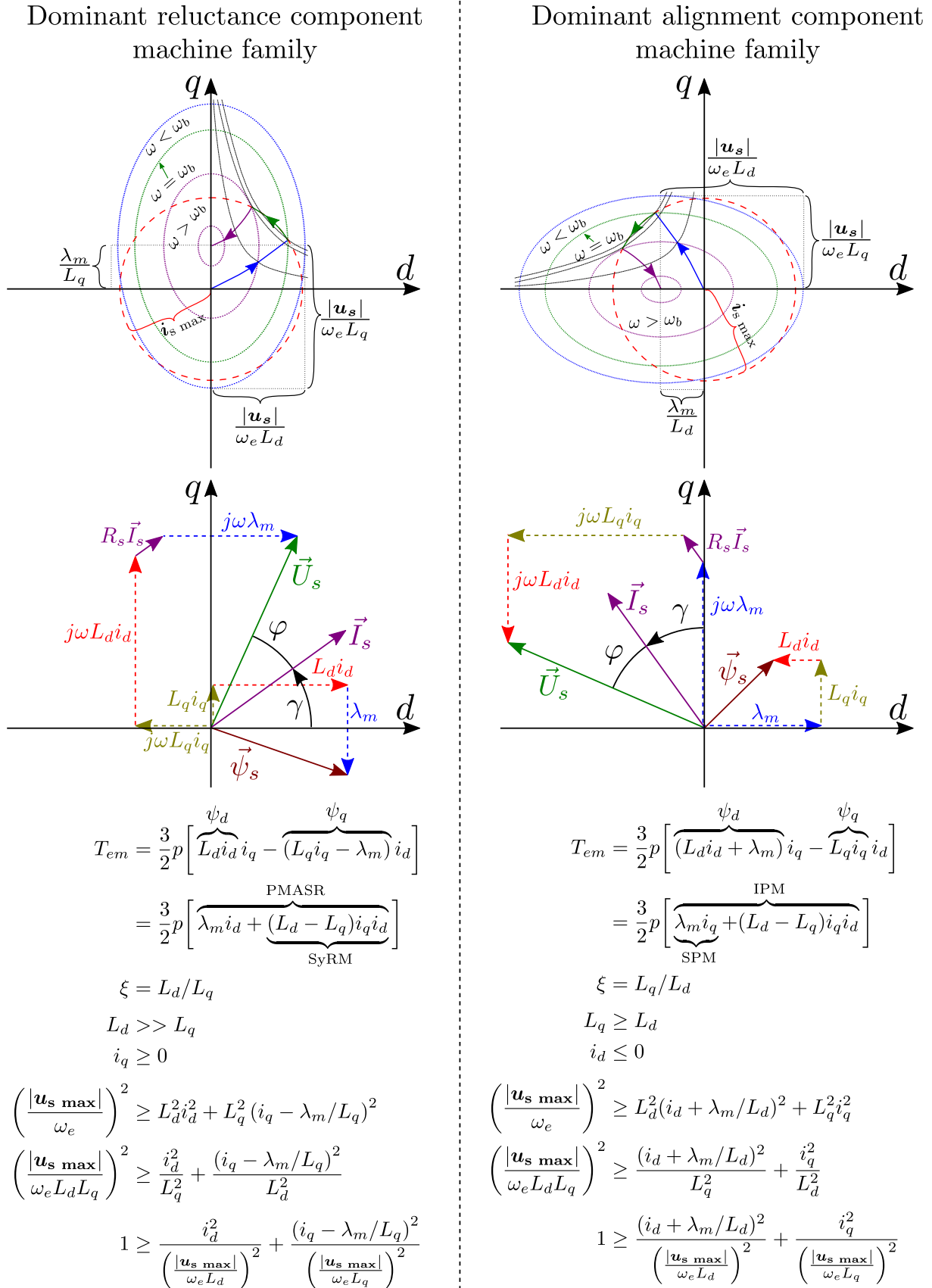


Figure 2.5: Voltage and current constraints, voltage vector diagrams and equations for dominant reluctance torque component family (left) and dominant alignment torque component family (right).

2.1.2 Combination of PM and reluctance: IPM design plane

Depending on the amount of the rotor PM material and rotor cross-section, IPM and PMASR properties can often overlap and one can argue that IPM is actually PMASR and vice versa. According to the informal rule, if reluctance torque component is greater than 50% of maximum torque at base speed, the machine is considered PMASR. To further differentiate machine families, Soong [45] introduces "IPM design plane" (Fig.2.6). From left to right, the plane starts with SyRMs ($\lambda_m = 0$, high saliency, only reluctance torque, Fig.2.1e-f) and ends with SPM machines (no saliency $\xi = 1$, only magnet torque, Fig.2.1c-d). In between, all IPM machines and PMASR combinations are included.

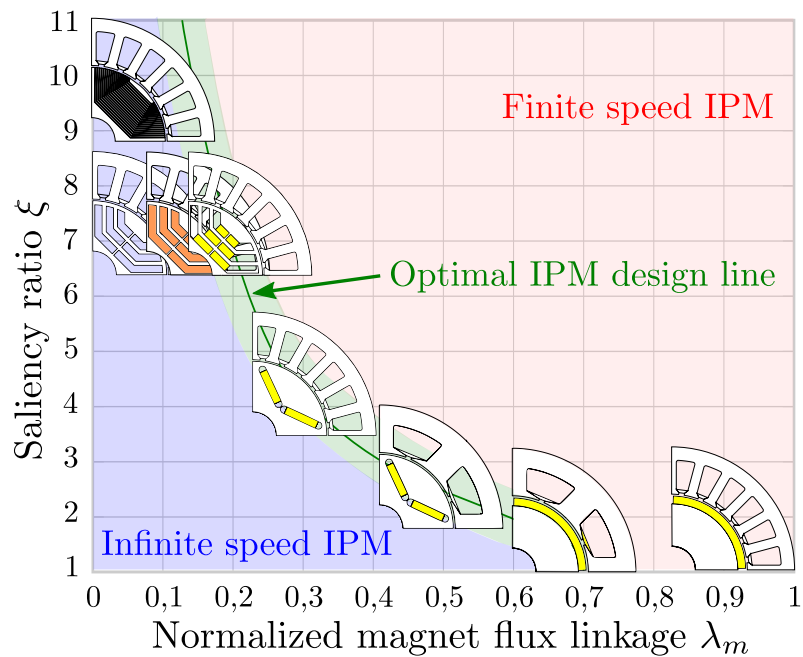


Figure 2.6: IPM design plane [9].

The optimal IPM design line defines special matches of PM flux and saliency ratios resulting in optimal field weakening (FW) capability, indicating infinite constant power speed range under limited voltage and current constraints (this is valid for ideal machine [45]). SyRM is out of the optimal design line, whereas PMASR fall into the optimal FW area when the appropriate quantity of magnets is added to a baseline synchronous reluctance design.

2.1.3 Rotor laminations assembly

SyRM with transversally (conventionally) laminated rotor (TrLam) has been proposed in early nineties [46], [47], [48], (Fig.2.7a). Machine laminates are produced by punching tool or laser cutting, which removes extra material. The other, non standard production technique is rotor lamination mounting alongside shaft axis (AxLam, Fig.2.7b). Theoretically, this method increases the saliency ratio above the levels achievable with TrLam machines ($\xi > 10$, [39])

using fixed strips of steel separated by thin layers of insulating material [49].

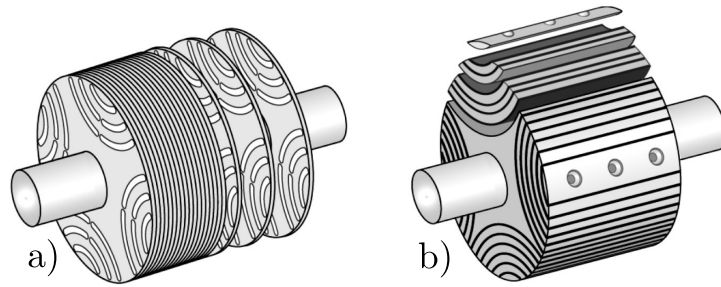


Figure 2.7: a) Transversally laminated rotor (TrLam) and b) Axially laminated rotor (AxLam) [50].

According to Vagati [48], the better suitability of TrLam structure for industrial manufacturing is evident from several aspects: the laminates can be punched with conventional methods, assembly process is straightforward and either constant (in case of PM injection molding), or segmental skewing can be applied on the rotor. In large scale machine manufacturing, stator skewing is normally avoided in favor of using automatic winding devices [51].

On the other hand, AxLam structure theoretically enables high saliency ratio by increasing the number of laminate layers n_l (Fig.2.8a). However, this is only true for a two-pole structure ($p = 1$) [48], while for $p > 1$, Bianchi et al. [52] shows that due to the saturation effects, the ideal structure should have a variable ratio between the depths of magnetic and non-magnetic structures where $k_1 < k_2 < k_3$, which reduces saliency ratio (Fig.2.8b). To summarize, production difficulties of AxLam rotors are:

- Every laminate segment has different design and size.
- Inter-segment insulation thickness k_i has to vary in-between layers.
- There is no straightforward skewing possibility.
- Rotor circumference needs to be machined after laminate mounting, which can change the material properties and increase iron losses [53].

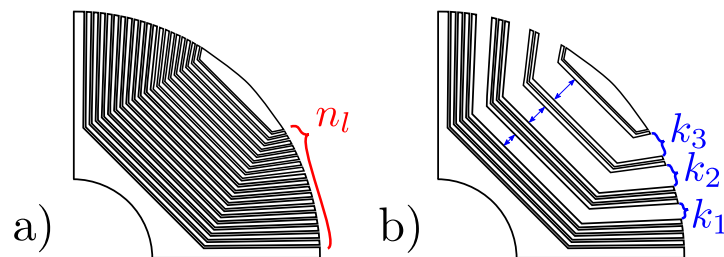


Figure 2.8: Sketch of rotor with uniform, and non-uniform distribution of the AxLam laminations.

Due to the rotor magnetic reaction to stator slot harmonics, both TrLam and AxLam options face problems with torque ripple, which makes either rotor or stator skewing a necessity [54]. As mentioned, TrLam rotor can be easily skewed, which is not the case for AxLam rotors, leaving stator skewing as the only option.

2.2 SyRM commercial applications

2.2.1 Industry

The first notable modern industrial commercialization of the SyRM was done by ABB in 2012. As an example, 90 kW machine measured nominal efficiency of 96.1% at $\cos \varphi = 0.73$, illustrating both the strengths and challenges of this technology [55], [9]. Today, in addition to ABB, various manufacturers such as Kaiser Motoren, REEL, SIEMENS, and Končar MES provide solutions in the 0.55 – 315 kW range [7], [56]. The main reason SyRM designs came in to spotlight is the introduction of the new IEC 60034-30-1 standard with harsher efficiency constraints. Introduction of IE4 super-premium efficiency class [57], and better efficiency in comparison to IMs, makes SyRM attractive for industrial use.

2.2.2 Automotive traction

Up to today, SyRM has not been commercialized in large scale automotive traction. One of the rare examples adapted for the electric vehicle is Ricardo 85 kW 6ph SyRM [58]. MotorBrain project [59] has investigated an inverter power module integration with SyRM stator for automotive application. The project resulted in 97.6% efficiency inverter and 93.6% efficiency 6ph 60 kW SyRM (overall system 91.6%).

The conclusion is that the current low volume production of electric/hybrid in comparison to internal combustion vehicles still favors the use of IPM machines.

On the other hand, PMASR machines are a direct competitor to IPM machines and have already been commercialized in the automotive industry. The example is second generation Chevrolet Volt which uses ferrite [39] and BMW i3 which mounts NdFeB magnets [60], [61], [6]. Second-generation Toyota Prius machine [62] is slightly on the side of the IPM family (alignment torque component at base speed is slightly above 50% of maximum torque).

2.2.3 Ship propulsion and freight traction

SyRM is considered to be a direct competitor of IMs which are often used in railway and ship propulsion. This has been confirmed by [29], concluding that both IM and SyRM have similar electric, magnetic, and thermal performance, with SyRM having lower rotor losses. Germishuizen et al. emphasize that SyRM compared to IM have lower stator winding temperature rise, which allows an increase of the power rating by 5 - 10% [63]. All authors agree that the main drawbacks of the SyRM solution is low torque in FW range and inherently large variable frequency drive.

Although SyRM in relation to PMASR has a lower power factor, its main benefit is high overload capability, without any demagnetization problems [64].

2.2.4 Commercial vehicles

To power the special equipment (cranes, refuse system, refrigerators, etc.), the commercial vehicle must be fitted with an extra means of a power supply, a power take-off (PTO). One or more PTOs transfer power from the engine to drive attachments or load handling equipment. The PTO provides a mechanical link (output shaft) towards load (usually some sort of hydraulic system) with most of the systems having power demand < 80 kW [65]. Historically, the PTO output shaft has been a part of the combustion engine or transmission (Fig.2.9a-d). With recent commercial vehicle electrification trends [66], [67], PTO will probably be an extra electric machine (ePTO) mounted on the vehicle chassis (Fig.2.9e-h) powered via stand-alone inverter attached to the traction battery.

Most commercial vehicle manufacturers have strategy of reusing components when possible to increase volume which leads to price reduction. The presumption is that ePTO inverter will have the same part number as traction inverter. The obvious conclusion is that the inverter will be oversized for ePTO application which effectively eliminates low power factor issue. Considering price, overload capability and production simplicity, SyRM can be a viable ePTO solution [68,69]. More details about the ePTO SyRM design is available in Pub.3,2and [38].

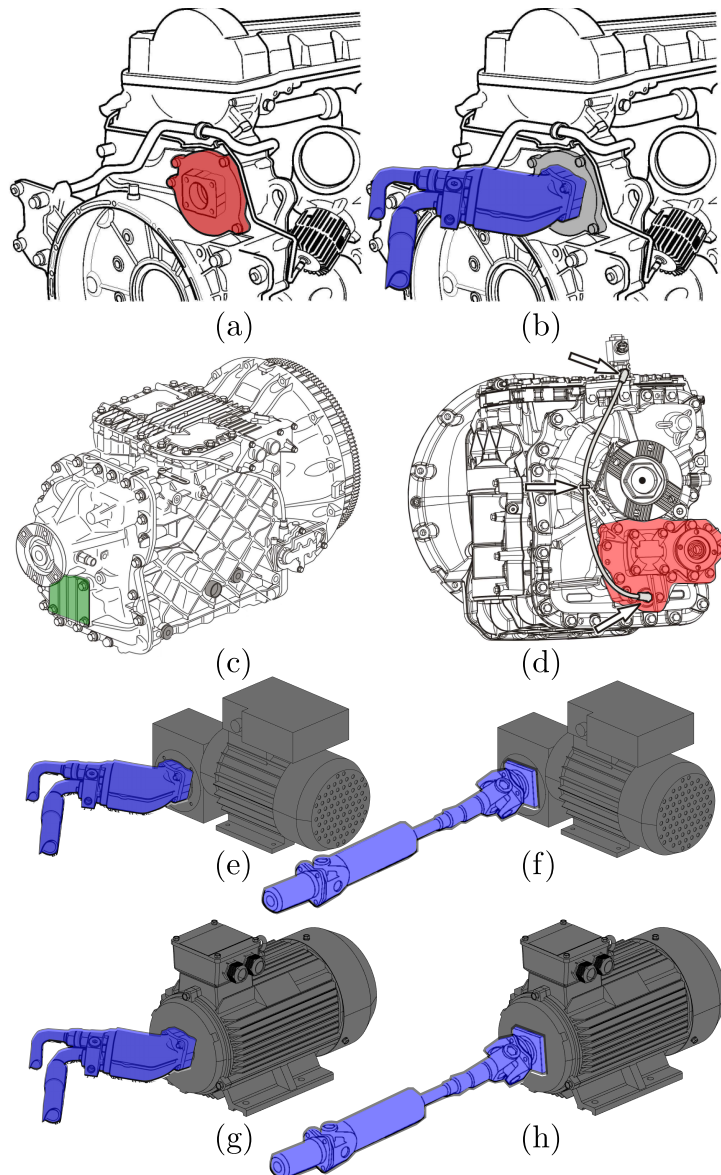


Figure 2.9: a) Diesel engine rear PTO mount; b) diesel engine with mounted hydraulic pump; c) Transmission with direct PTO mount; d) transmission with geared PTO [70]; geared PTO propelling hydraulic pump e) and universal joint shaft f); direct PTO propelling hydraulic pump g) and universal joint shaft h).

2.3 Further reading

More detailed information about SyRM design criteria and theoretical performance is available in Pub.1. ePTO load cases for different electric multi purpose vehicle types are covered in Pub.2. SyRM optimization strategies for the ePTO use are presented in Pub.3and7, while [38] elaborates torque ripple mitigation strategies.

Chapter 3

SyRM rotor cross section parametrization

In recent decades, SyRM research has focused on improving the rotor barrier design, minimizing the torque ripple, and increasing the power factor [71]. Literature provides references to several barrier topologies: circular [72,73], hyperbolic [25,74], Zhukovsky fluid type [26,75], segmented, etc. Open-source SyRE project offers more details and instructions on geometry generation [76].

The common goal in barrier construction strategy is the reduction of parametric complexity. However, too simplified rotor topologies can lead to decreased performance, while too complex geometries yield better performance, but also tend to increase optimization time (increase is proportional to the parametric complexity). By merging both approaches, the research presented in Pub.5 formulates a set of flux barrier construction methods with an increased degree of freedom and minimal parametric complexity, based on non-dimensional rotor parameters. Four rotor topologies based on smooth analytical functions have been analyzed and implemented in a form of pseudo-code:

1. Circular variable depth (CrVD), Figure 3.1b
2. Variable eccentricity hyperbolic (HyVE), Figure 3.1c
3. Original Zhukovsky (Zh), Figure 3.1d (red)
4. Modified Zhukovsky variable depth (MZhVD), Figure 3.1d (blue).

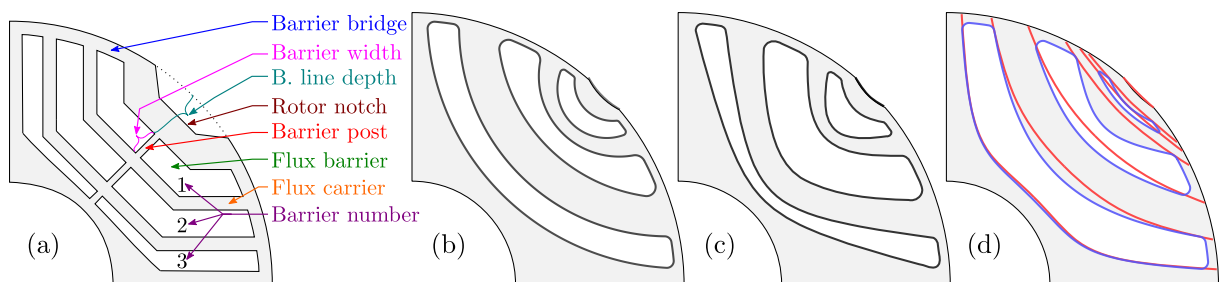


Figure 3.1: (a) SyRM terminology; SyRM rotor barrier types: (b) Circular variable depth; (c) Hyperbolic variable eccentricity; (d) Modified Zhukovsky (blue), original Zhukovsky (red).

3.1 Rotor design Automation

The initial step in electric machine optimization is the development of automated geometry generation. An example of the procedure is provided in Figure 3.2. Design automation functions are covered in detail in Pub.5. The same strategy is applied to all rotor geometries.

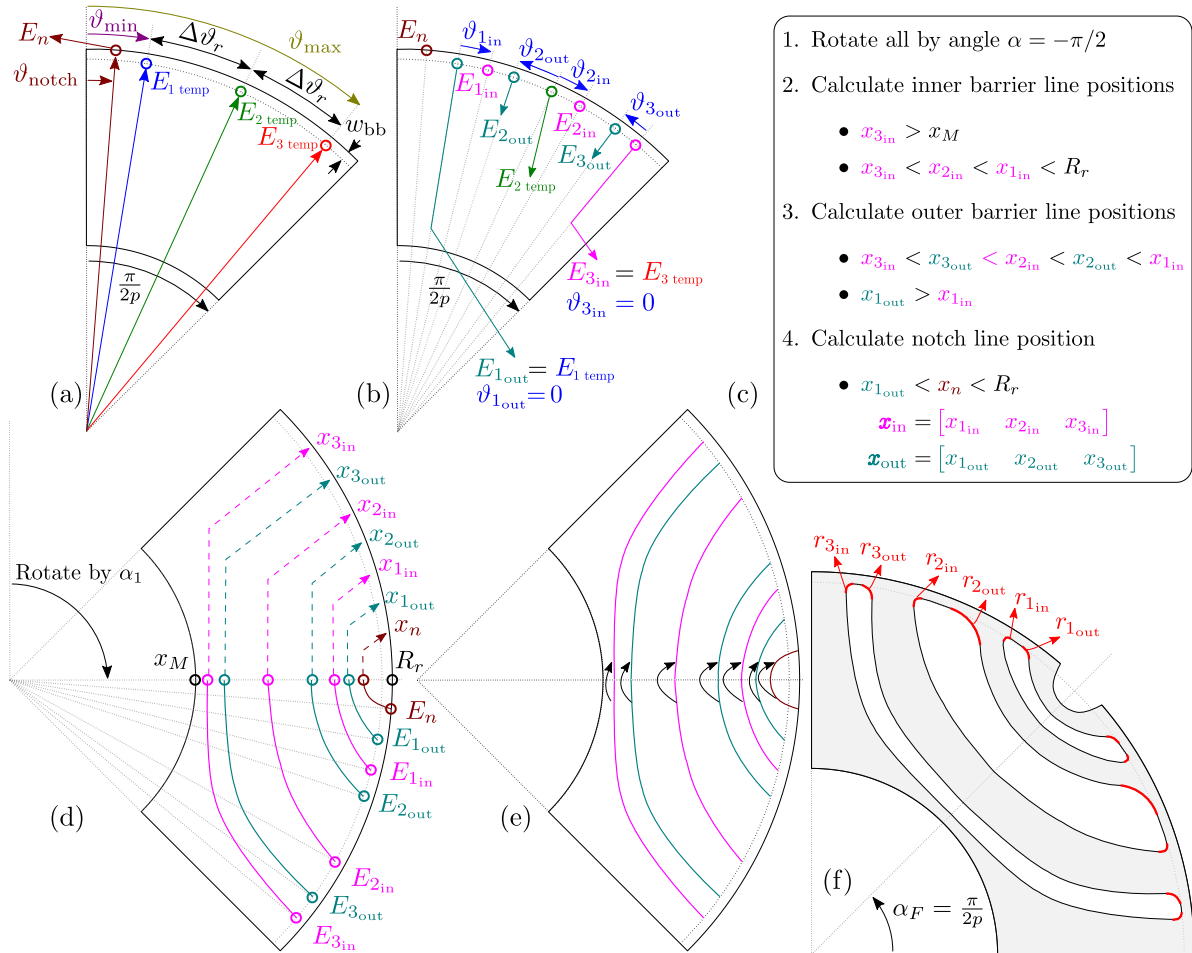


Figure 3.2: Rotor barrier construction procedure. Initial rotor construction step (a); Construction of inner and outer barrier line starting points (b); calculation of barrier intersection points (c); calculation of barrier vertices (d); vertex mirroring (e); rotation around center and addition of barrier fillets (f);

All bolded variables in the further text represent arranged vectors. Upon completion of the steps illustrated on Figure 3.2a-c, the function returns all inner and outer barrier line vertices $\mathbf{X}_{in}, \mathbf{Y}_{in}, \mathbf{X}_{out}, \mathbf{Y}_{out}, \mathbf{X}_n, \mathbf{Y}_n$, Figure 3.2d. Variables $\mathbf{X}_{in}, \mathbf{Y}_{in}, \mathbf{X}_{out}, \mathbf{Y}_{out}, \mathbf{X}_n, \mathbf{Y}_n$ specifically, represent the arranged vertices, a set of x, y coordinates which form an inner, outer and notch barrier poly-line. The next step is mirroring line vertices around the horizontal axis (Figure 3.2e). The final step is the rotation around the center point by the angle $\alpha_F = \pi/(2p)$. Barrier fillets ($\mathbf{r}_{1..k_{in}}, \mathbf{r}_{1..k_{out}}$) responsible for securing mechanical integrity of the rotor are added to the geometry, and final rotor geometry is exported as to the FEA tool (Figure 3.2f). Adding precise fillets to the discrete lines is a complex problem which is planned to be explained in the future publications.

Barrier Depth Variation

Considering that the barrier width has a substantial impact on the machine performance, this section will explain how inner and outer barrier depth coefficients affect each of the studied topologies, with a simplified presumption of equal line starting points.

Width of the each barrier depends on initial inner and outer line starting points E_{in} , E_{out} , and depth coefficients D_{in} , D_{out} . Depending on the depth parameter combination, barrier width can be variable, or uniform. Uniform width is a special case where CrVD barriers are concentric (Figure3.3a, green). HyVE barriers can be approximately uniform when they have equal eccentricity (Figure3.3b, green). These special cases are covered by CrVD and HyVE pseudo-code (Pub.5), and will not be studied in detail.

In general, CrVD and HyVE depth variation is unconstrained resulting in variable barrier width (Figure3.3a,b, blue).

Zh barrier type (Figure3.3c) is a special case because it does not support any depth variation. Barrier line depths are defined directly from starting points and cannot be modified. In order to explore the possible benefits of depth variation, Zh type has been modified as MZhVD where barrier depths have full freedom (Figure3.3d).

An example of different barrier line depth parameter combinations is provided in the (Table 3.1).

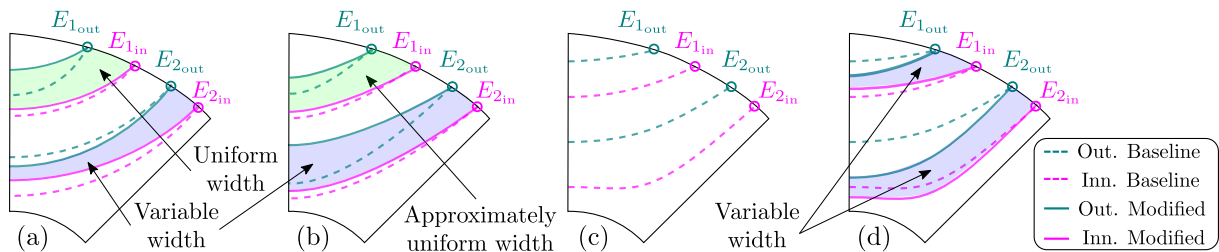


Figure 3.3: Barrier depth variation influence on different 2-barrier ($k = 2$) SyRM topologies. Circular (a); Hyperbolic (b), Zhukovsky (c) and Modified Zhukovsky barrier types (d).

Table 3.1: Illustrative depth coefficient table for Figure3.3.

		Baseline Barrier Depths				Modified Barrier Depths			
	Abbr.	D_{1out}	D_{1in}	D_{2out}	D_{2in}	D_{1out}	D_{1in}	D_{2out}	D_{2in}
(a)	CrVD	0.35	0.50	0.65	0.90	0.40	0.55	0.70	0.80
(b)	HyVE	0.40	0.50	0.80	0.90	0.35	0.45	0.60	0.85
(c)	Zh	0.10	0.45	0.60	0.85	-	-	-	-
(d)	MZhVD	0.10	0.45	0.60	0.85	0.20	0.40	0.80	0.90

3.2 Parametric Complexity

A high number of optimization variables is associated with a longer optimization time [77,78], so the imperative is to simplify barrier topology parametrization. Gamba et al. [26] state that three parameters per barrier (total complexity of $3k$, where k is the number of barriers) are the appropriate number for a fast yet accurate description of multi-barrier SyRM (barrier fillet parameters are not included). In the first iteration of automated rotor design (Pub.4), our group of authors has reduced the complexity to $2 \cdot k + 1$ per barrier [79].

The final, further simplified pseudo-code version of automated rotor design strategy is implemented in the Pub.5. Table 3.2 shows the calculation of total number of SyRM parameters. Note that the parameters $\vartheta_{1_{out}}$, $\vartheta_{k_{in}}$ are subtracted from the count because they are constant and equal to zero within the pseudo-code.

Table 3.3 lists the complexity comparison of the presented procedures and similar approaches in [26,73,79]. The examples in [26,73,79] do not have a notch feature, so to have a fair comparison, the notch is not included in the complexity calculation (Table 3.2). Compared to [26], and [79], Zh, respectively, yields smaller complexity ($2k$), while CrVD, HyVE, MZhVD have the same complexity as in [73].

Overall, the construction principle explained in Section 3.1 enables the higher degree of design freedom. Considering that the simple barrier topologies are sub-optimal compared to more complex types, developing the set of different parametrization methods with equal parametric complexity is certainly a novel contribution.

Table 3.2: Calculation of total parameter number. Color coding is according to Fig. 3.2 variables.

Sum:	Description	Symbol	Topology
1	Min. angle	ϑ_{min}	
2	Max. angle	ϑ_{max}	
$k + 2$	Barrier angle in	$\vartheta_{1..k_{in}}$	
$2k + 2$	Barrier angle out	$\vartheta_{1..k_{out}}$	
$2k + 2 - 2$	Remove constants	$\vartheta_{1_{out}} = \vartheta_{k_{in}} = 0$	
$2k$	-	-	Zh
$4k$	Barrier depths	$D_{1..k_{in}}$	HyVE
	Barrier depths	$D_{1..k_{out}}$	CrVD
			MZhVD

Table 3.3: Summary of parametric complexity presented in Pub.5.

Topology	Complexity	$k = 2$	$k = 3$	$k = 4$
Zhukovsky; Gamba et.al. [26]	$3k$	6	9	12
Circular; Stipetic et.al. [73]	$4k$	8	12	16
Zhukovsky; Ban et.al. [79]	$2k + 1$	5	7	9
Zh	$2k$	4	6	8
HyVE				
CrVD	$4k$	8	12	16
MZhVD				

3.3 Pseudo-Code Validation

After the implementation of the proposed pseudo-code, a set of questions naturally arises. Which barrier topology yields the best performance for the given requirements? Is Modified Zhukovsky barrier type better than alternative topologies? For this reason, a detailed optimization study based on meta-modeling (surrogate modeling) approach which compared the different barrier topologies was conducted (details are available in Pub.7).

The optimization process couples automated geometry generation (Matlab), electromagnetic finite element analysis (Ansys Motor-CAD), and metamodel optimization (Ansys OptiSlang). Seven rotor topologies have been derived from circular, hyperbolic, and Zhukovsky barrier types:

1. Circular concentric (CrC)
2. Circular variable depth (CrVD)
3. Hyperbolic with fixed eccentricity (HyFE)
4. Hyperbolic with variable eccentricity (HyVE)
5. Original Zhukovsky (Zh)
6. Modified Zhukovsky variable depth (MZhVD)
7. Modified Zhukovsky with equal barrier depth (MZhED)

The same optimization strategy (maximize torque per volume (TPV), minimize losses) has been applied to all variants, and results prove that barrier type substantially affects the final machine performance. For easier comparison, seven designs (one per topology) with approximately the same losses (5200 W) have been selected (Figure 3.4, Table 3.4).

Performance wise, HyFE topology yields the worst results and is considered as baseline design (Gain = 0%). Performance gain is calculated via: $\text{Gain} = (T_{\text{avg}}/T_{\text{HyFE avg}} - 1) \cdot 100\%$. The best results are achieved by MZhVD topology. In relation to the worst (baseline) topology, the performance gain is 14.9% and the power factor is increased from 0.61 to 0.69. It is important to note that these comparisons are valid for design requirements presented in Pub.7. Other

combinations of optimization objectives and requirements might yield a different results.

HyFE, CrC and MZhed are special case topologies covered in CrVD, HyVE and MzVD pseudo-code. The summary of the optimized cross-sections are provided on Figure3.5. It is important to note that optimization was conducted on the entire machine cross section (rotor and stator).

Table 3.4: Optimization result comparison table, Pub.7.

Name	Unit	HyFE	CrC	HyVE	CrVD	Zh	MZhed	MZhd
TPV	Nm/dm ³	32.5	33.1	34.3	35.4	36.2	36.4	37.3
V_{active}	dm ³	6.47	6.47	6.47	6.47	6.47	6.47	6.47
P_{loss}	kW	5188	5199	5209	5182	5188	5197	5184
P_{mech}	kW	37.4	38.1	39.5	40.8	41.7	41.9	43.0
T_{avg}	Nm	210.1	214.2	221.9	229.0	234.1	235.6	241.3
$T_{\text{ripp.}}$	%	12.1	14.1	11.7	12.7	9.7	9.3	13.7
n	rpm	1700	1700	1700	1700	1700	1700	1700
l_s	mm	180	180	180	180	180	180	180
γ	°	57.9	60.3	61.4	62.5	61.8	61.8	62.9
I_{max}	A _{rms}	95.6	95.6	94.3	94.1	95.9	95.7	95.7
$\cos \varphi$	-	0.61	0.62	0.66	0.67	0.67	0.67	0.69
Gain	%	0.0	1.9	5.6	9.0	11.4	12.1	14.9

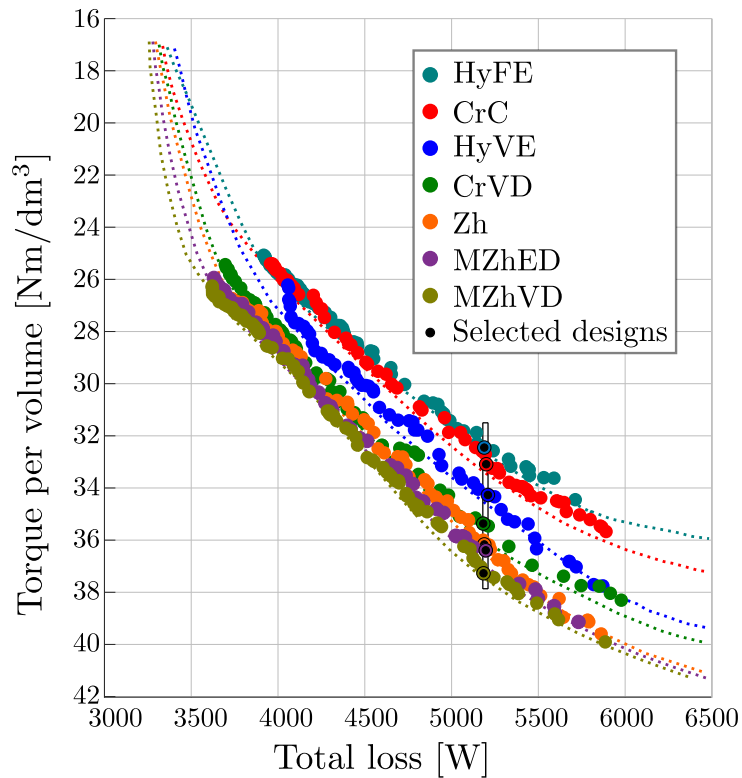


Figure 3.4: Validated Pareto fronts for each design variant, Pub.7

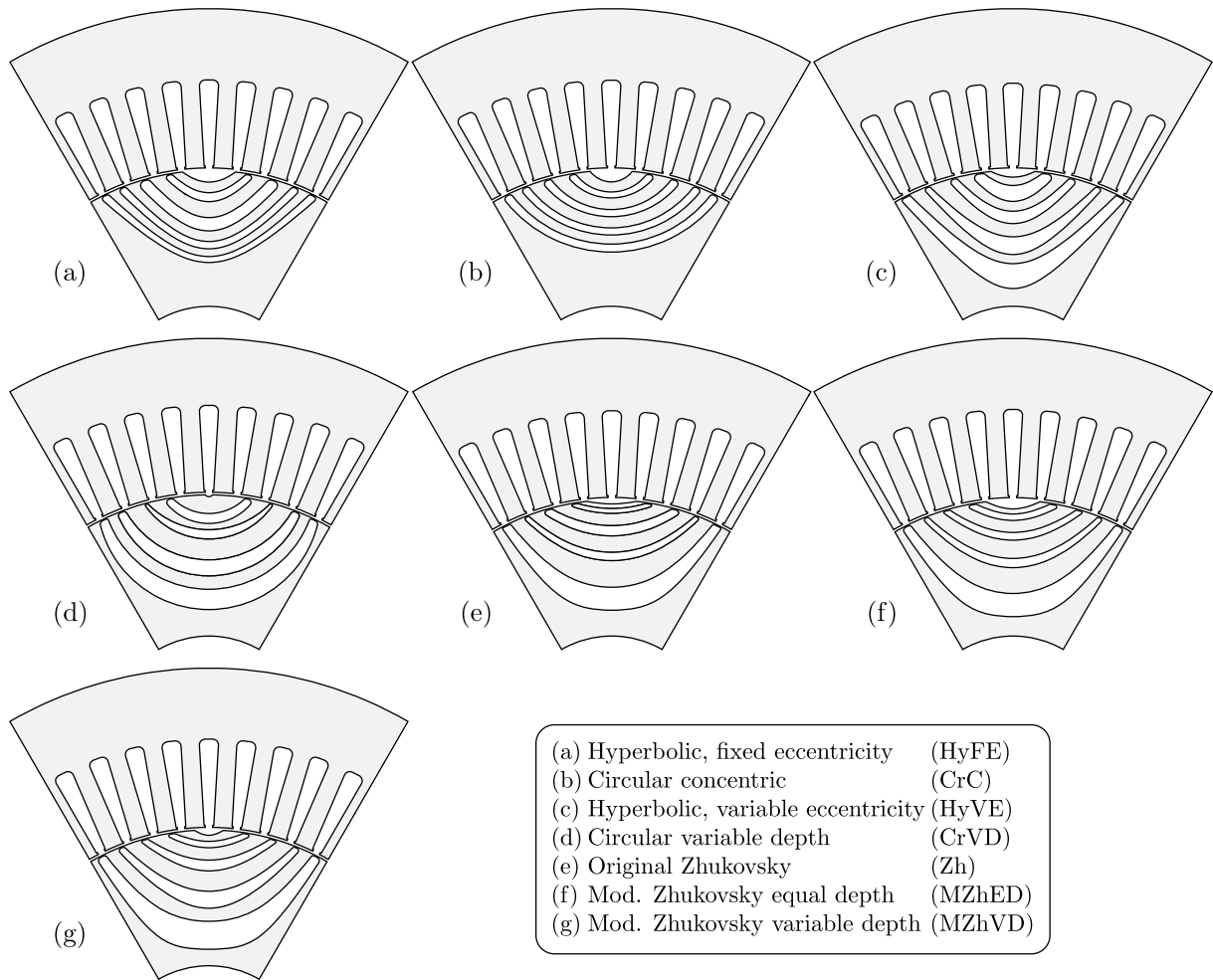


Figure 3.5: Optimized cross sections per topology, Pub.7.

3.4 Further reading

The first iteration of automated design procedure (not covered in this chapter) inspired by [26] is covered in Pub.4. The refinement of the procedure led to further geometrical complexity reduction. More detailed information about final SyRM rotor design automation strategy, including the pseudo-code is available in Pub.5. Overall, the presented pseudo-code provides a valuable starting point for the designer who wants to investigate different SyRM smooth barrier topologies.

Finally, the optimization, performance analysis and comparison of all considered design variants is available in Pub.7. As expected, SyRM rotor barrier topology substantially affects the final machine performance. The consequence of barrier depth variation is variable flux carrier thickness which has a positive impact on performance and mechanical integrity. The novelty of the proposed approach reflects in the systematic comparison of different "smooth barrier" SyRM topologies via metamodel-based optimization. This offers a fair topology comparison and finally proves that modified Zhukowsky-based topologies yield the best results in terms of TPV and higher power factor.

Chapter 4

Feasibility detection as a part of optimization strategy

In most cases, the search for the optimal design of an electrical machine is closely related to its 2D radial cross section. When optimizing a 2D cross section, special attention must be paid to the geometry and to the definition of the parameters along with their boundaries. Even if properly bounded, complex geometries generated by optimization algorithms can lead to geometrically infeasible candidates. These cannot be manufactured because they contain generally undesirable geometric relationships between air, magnets, and steel. Different commercial and open-source finite element analysis (FEA) design tools treat the infeasible designs in various ways. The results vary from simulation stop to successful FEA calculation of the infeasible candidate, which wastes time by producing useless data. To prevent the infeasible designs from entering the optimization competition and possibly appearing incorrectly as optimal solutions, and to reduce optimization time, it is important to capture the infeasible designs during optimization. Moreover, the FEA tool requires a precisely determined interior point to assign the material to each closed region (air, steel, epoxy, magnet...). This can be very challenging for complex geometries.

Pub.6 provides a solution to both problems through a novel robust feasibility verification procedure and inner-point detection using Matlab polyshape objects. The generality of approach is demonstrated through a set of simple, but extremely robust algorithms. The approach elevates geometric design analysis from geometric primitives (points, lines and arcs) to the level of objects (shapes), applicable to any type of machine geometry as an upgrade to existing code.

4.1 Optimization methodology

Most of the requirements for the design of electric machines are in conflict with each other (reduction of volume or mass, increase of efficiency, etc.). Therefore, a manual design that satisfies

all constraints can be an overwhelming task due to a large number of coupled parameters that affect the performance and quality of the machine. The solution is in the use of mathematical optimization.

Optimization algorithms can be divided into gradient based methods and stochastic or meta-heuristic methods. Gradient-based methods converge quickly but have difficulty with global optima. Usually they require feasible starting point which can be a problematic task in complex problems (Quasi Newton method [80]). Stochastic methods are heavily used in electrical machine optimization (Powell's method [80]). Popular metaheuristic methods are based on natural behaviour (Genetic algorithm, Differential evolution [81,82], Particle swarm [83]), but they can also be iterative [84], or based on approximation [85]. The disadvantage is that convergence can take days and the global optimum cannot be mathematically proven. On the other hand, from the engineer's point of view, these methods can find a satisfactory global result.

All methods are generally set to solve a multi-objective problem, which is mathematically defined as follows: find the vector of parameters (4.1), subject to D parameter boundary constraints (4.2) and subject to m inequality constraint functions (4.3), that will minimize (or maximize) n objective functions (4.4). A vector \vec{x} of D variables specifies dimensions, dimensionless ratios, current densities, material types used, etc. The goal of design optimization is to have a chosen objective function $f(\vec{x})$ reach its minimum or maximum value while keeping other engineering indices within an acceptable range.

$$\vec{x} = [x_1, x_2, \dots, x_D], \quad \vec{x} \in R^D \quad (4.1)$$

$$x_i^{(L)} \leq x_i \leq x_i^{(U)}, \quad i = 1, \dots, D \quad (4.2)$$

$$g_j(\vec{x}) \leq 0, \quad j = 1, \dots, m \quad (4.3)$$

$$\min(f_k(\vec{x})), \quad k = 1, \dots, n \quad (4.4)$$

4.1.1 Optimization workflow

A typical optimization workflow is a series of computations consisting of: optimization algorithm that generates optimization variables according to the given parameter boundaries, geometry generation block that passes the design to the selected FEA tool for performance calculations, and finally post-processing block that returns the computed data to the optimization algorithm for further evaluation (Fig.4.1, black). Additionally, a geometric feasibility checking (FC) block can be part of the optimization workflow (Fig.4.1, red).

4.1.2 Geometric feasibility

The term feasibility usually refers to the solution and means that the solution satisfies all given constraints. In other words, the region enclosed by $\forall g_j(\vec{x}) = 0$ is called a feasible region.

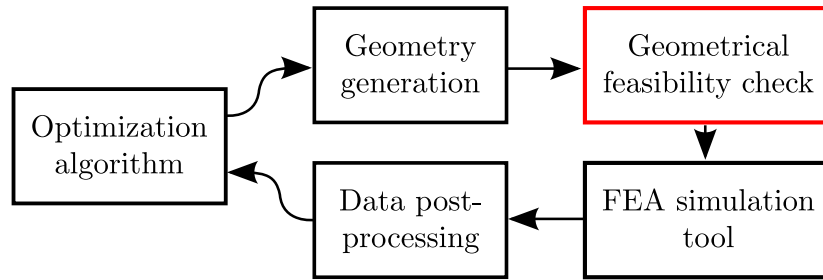


Figure 4.1: Feasibility detection as an optimization workflow add-on feature

The research concentrates on another type of feasibility called *geometric or model feasibility*. Geometrically feasible model is valid for solving if there are no overlapping edges or non-conventional geometric relations. Infeasible candidate is the one that cannot be produced as a real machine because there are overlapping magnets, non-rectangular shaped magnets, air pockets overlapping magnets etc. Infeasible candidates should not be evaluated for performance because theoretically they can falsely appear as optimal solutions but can never be considered for manufacturing/production.

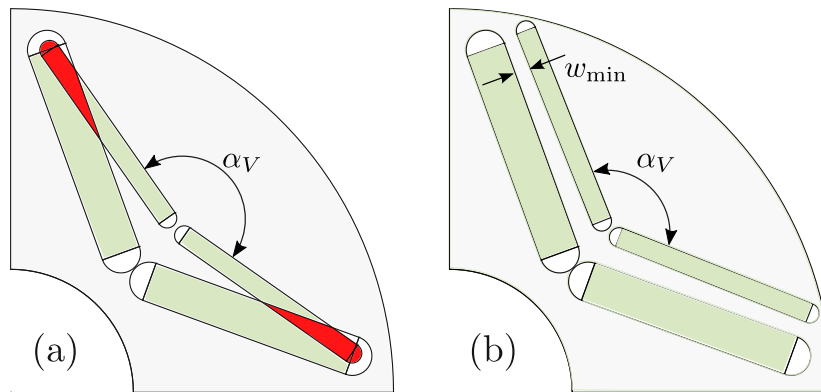


Figure 4.2: Infeasible geometry (a) and forced feasibility (b)

Optimization workflow without FC

If the optimization software does not include a feasibility check (FC), two different scenarios may occur during the FEA calculation (depending on the selected FEA tool).

In the first case, the FEA tool detects that the design is erroneous and throws an error. In this case, the designer must implement a try-catch procedure which will capture the event, otherwise the optimization procedure will fail (try-catch adds $t_{\text{extra}} \geq 4\text{s}$ per design evaluation). In the second case, the FEA tool does not detect the infeasibility and a full FEA calculation is performed. This is the worst case scenario which will produce useless results and cause significant increase of optimization time (e.g., detailed transient electromagnetic simulations can take $t_{\text{extra}} \geq 15\text{min}$).

Optimization workflow with FC

However, if the optimization software includes a feasibility detection procedure, the designer can either attempt to correct the problematic instance or skip it. There are two typical ways to correct the optimization candidate prior to performance evaluation (passing it to the FEA calculation).

First, the entire set of optimization variables for that candidate is reinitialized randomly within the specified parameter bounds until geometric feasibility is achieved. This is a brute-force approach, but it is mandatory since evolutionary optimization algorithms (e.g. Genetic Algorithm, Differential Evolution) must have the same number of members in each population of optimization candidates. This is due to the fact that each generation must be equal or better than the previous as the algorithm advances towards the optimum.

The alternative is forced feasibility, where each infeasible design is subjected to minimal parameter modification until feasibility is reached (e.g., the magnetic layer angle α_V is modified until w_{\min} is reached, Fig.4.2b). This approach can be complicated and requires an advanced parameterization with minimal feasibility constraints. Benefits of the method are covered in the Pub.4.

Depending on the complexity of the design, both methods may increase execution time ($t_{\text{extra}} = 2 - 15\text{s}$). On the other hand, detecting and skipping the infeasible design actually does not impact execution time ($t_{\text{extra}} = 0$).

4.1.3 Feasibility detection importance

If feasibility detection is not considered, or if it fails because the method is not robust enough, there are two possible scenarios.

First case: the FEA tool (computation engine) outputs an error when it tries to solve an infeasible candidate. This error can be easily handled in the optimization code with the typical *try-catch* structure so that the whole optimization code does not crash. The presence of the error and catching it is actually a good thing because it is not desirable to waste time on evaluating infeasible candidates and to consider them valid in optimization competition. However, from the programming point of view, it is better to recognize the infeasible design by having an algorithm to analyze it, rather than relying on the FEA tool error and try-catch procedure. Depending on how the optimization algorithm application is connected to the FEA software (via a Python script, a Visual Basic script, or Windows ActiveX interface), model creation and data transfer from the optimizer to the FEA tool can also take an unnecessary amount of time that adds up in long-term optimization. To explain this more precisely: some FEA tools require drawing line by line and arc by arc for each object which requires individual function calls. Even if the geometry (usually in *.dxf* format) is transferred from optimizer to FEA software, creation of

regions, assigning materials and defining coils is usually done programatically line-by-line (e.g. Tools 1,4) and this can last a few seconds depending on the geometry complexity.

Second case: the FEA tool does not report an error, the design is evaluated, but the final result is useless because such an optimization candidate is infeasible and therefore not valid. This case is very problematic because it unnecessarily increases the optimization time with regard to the previous case due to the full duration of the calculation (Table4.2) and potentially misleads the optimization algorithm towards impossible and non-manufacturable practical solutions.

For both cases, just as in the case of detected infeasibility, this means that an optimization candidate is wasted and has to be reinitialized randomly within specified parameter boundaries or the forced feasibility approach must be applied. However, second case yields an additional computational cost because an useless design is evaluated, which again proves that feasibility detection is important. Moreover, some sensitivity analysis and optimization tools prefer to know which combination of parameters leads to an infeasible geometry (e.g., Ansys OptiSlang [86],[87]). When such an event is reported, the tool can adjust the creation of the optimization metamodel to avoid the infeasible parameter space. If the optimization is based on the use of such advanced tools, the information about the infeasibility of the colliding regions can be a valuable upgrade, with minimal impact on the overall computation time increase (0.5-2 seconds per feasibility evaluation).

To prove that the two different cases exist, various open-source and commercial electromagnetic tools were fed with intentionally generated infeasible IPM and SyRM geometries (.dxf cross-sections, material regions, and magnetization directions were generated according to Fig.4.3b,d. Table4.1 summarizes the results of the single load point calculation, where some tools report an error (Tools 1-3), while others continue the simulation, waste optimization time and give an unusable result (Tools 3-5).

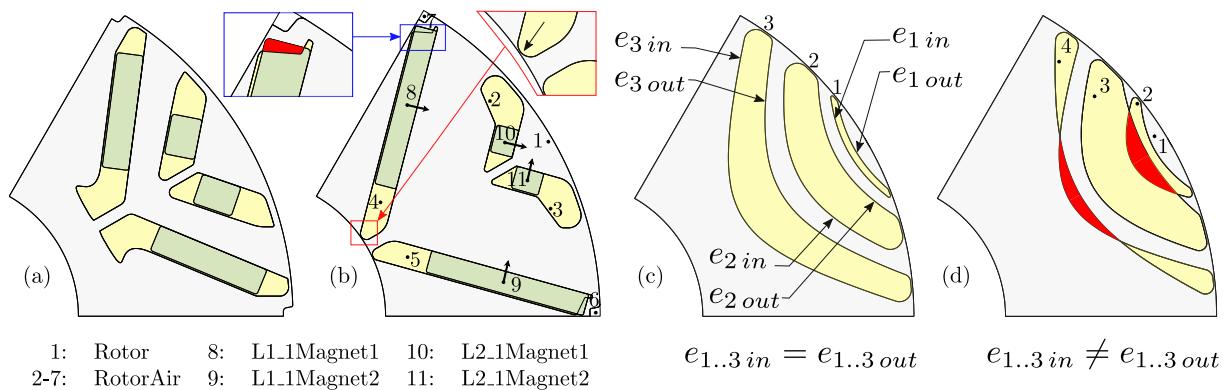


Figure 4.3: Illustration of feasible (a,c) and infeasible geometry (b,d)

Table 4.1: Analysis of infeasibility detection in different FEA tools

No.	FEA software	Category	.dxf Fig.4.3b	.dxf Fig.4.3d
1	FEMM	Open-source	Error reported	Error reported
2	Ansys Motor-CAD	Commercial	Error reported	Error reported
3	Ansys Maxwell	Commercial	No error	Error reported
4	Infolytica Magnet	Commercial	No error	No error
5	JMAG	Commercial	No error	No error

4.2 Standard approach for feasibility detection

The standard approach to feasibility detection is specific to each parameterized template, which typically requires immense programming/development resources for research groups engaged in electric machine design optimization. Not only are top-level differences between templates relevant, e.g., a single-layer V-shape geometry compared to spoke interior permanent magnet machine (IPM), but also peculiarities such as air-pockets around magnets and curvature of posts and bridges have a significant impact on potential geometric feasibility. This means that an extensive study of the mathematical geometry dependencies has to be performed between arcs and lines that are either adjacent or have the possibility to touch or intersect during optimization process.

However, when it comes to IPM rotors, especially multi-layered configurations as in Fig. 4.4, the mathematical description is much more complicated and, more importantly, it needs to be refined after each intervention in the template change.

Algorithm 1 Feasibility verification example for 2-layer V-shape IPM geometry

```

1: function CHECK FEASIBILITY
2:   for all points do
3:     verify whether radial coordinates are inside rotor
4:     verify whether angular coordinates are inside one pole
5:   for all layers do
6:     verify whether x-coordinates of all points are sorted
7:     verify that arcs do not cross interpolar line
8:     verify layer disposition
9:     verify possible intersection between two layers

```

The procedures for feasibility verification are specific and different for each different geometry. The pseudocode for a 2-layer V-shape IPM is shown in Algorithm 1. It is difficult to tackle all possible geometry failure cases so sometimes the algorithm can let the infeasible geometry further down the optimization pipeline.

It can be seen that this method is not robust and needs to be modified even for small changes in the geometry features of the topology under study. Therefore, a novel feasibility handling algorithm is presented in the next chapter.

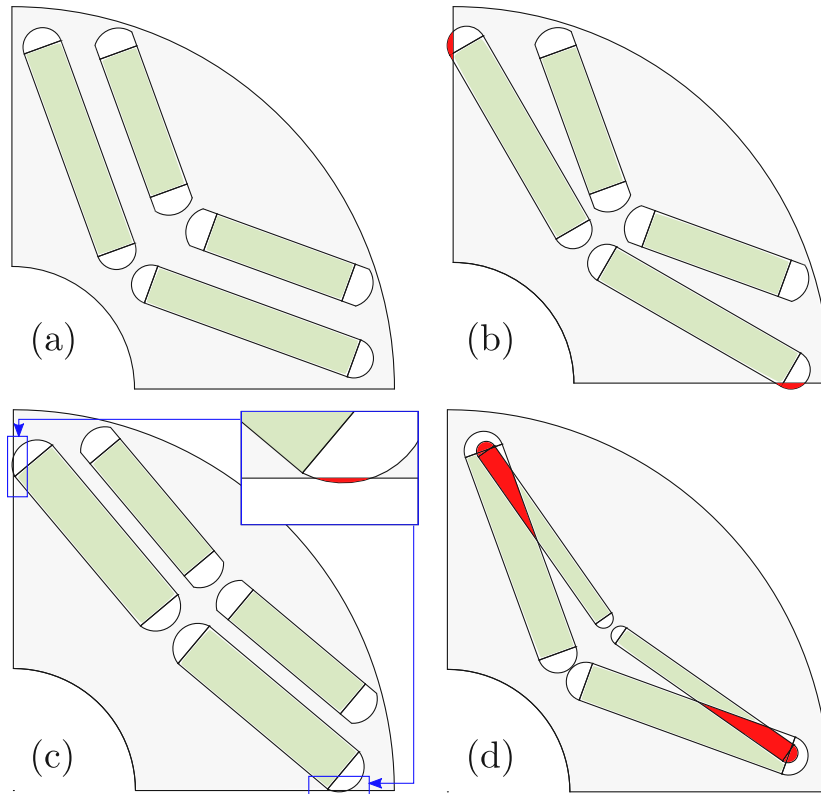


Figure 4.4: Example of 2-layer V-shape IPM: (a) feasible case, (b) barrier definition point crossing polar lines, (c) barrier arc crossing polar lines, (d) barrier collision

4.3 Robust feasibility detection

For optimization purposes, the cross-sectional geometry of the stator and rotor of the machine can be reduced to 2D Euclidean space. Geometry parameterization is performed in either Cartesian or polar coordinates, specifying all geometric primitives: Points, Lines, Arcs, and Polylines, which are sets of multiple lines that model a complex curve (polyline can be approximated with series of arcs and lines before sending a drawing *.dxf* to FEA solver). A set of connected primitives forms an object as a shape, such as a rotor barrier, which has mathematical properties: Area, Perimeter, Centroid etc. If the entire machine geometry can be defined by shapes - software objects, it would be very convenient to have some sort of functional tool to determine the correlation between different shapes. Correlations include Boolean functions, intersections, areas etc. This novel approach is made possible by the Matlab Polyshape class [88], which enables elevation of primitives to an object (shape) level. Once created, the shape objects can be organized in the form of a vector. The polyshape functionality allows a quick analysis of vectorized shape objects. One of the functions is *Intersection*, which returns information when there is an intersection between members of the shape vector. This provides a robust feasibility check regardless of parameter boundaries and regardless of the complexity of the geometry shape.

The main advantage of this approach is moving away from strict mathematical feasibility

verification to shape object level which allows great design freedom, instead of relying on the rather complicated procedure described in the previous chapter.

4.3.1 Region inner-point detection

A robust region detection algorithm was developed in combination with the existing *polyshape* functions and applied to all objects.

E.g., the selected polyshape (Fig.4.5a green). Polyshape vertex limits are extracted resulting in a 4x4 vectorized polyshape rectangle mesh (Fig.4.5b). Each rectangle is intersected with the polyshape to form an output vector of intersection points (Fig.4.5b). The intersection element with the largest area is then identified with (Fig.4.5c).

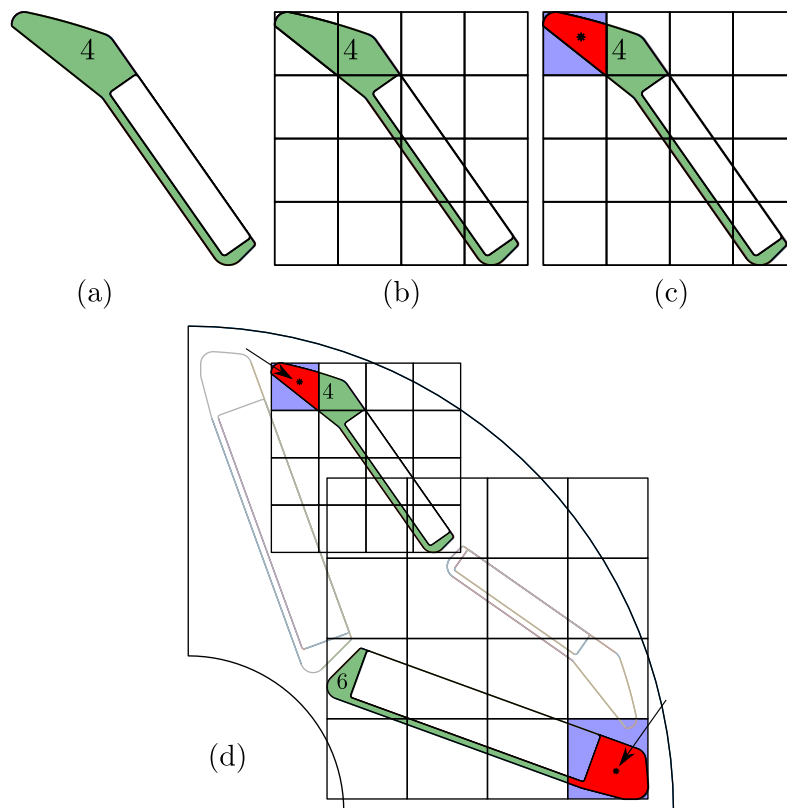


Figure 4.5: Shape robust region detection meshing example (a-d)

4.3.2 Feasibility check

The complete machine cross section with all polyshapes and assigned material regions including the rectangular mesh intersections is shown in Fig.4.6a. In this example, a total of 15 polyshapes are stored in a vector form. The polyshape vector is passed to the overlap detection function which returns overlaps matrix M_{ovl} . If M_{ovl} is a unitary matrix, the design is feasible and there are no overlaps (Fig.4.6a,b), otherwise the generated design is infeasible (Fig. 4.6c,d).

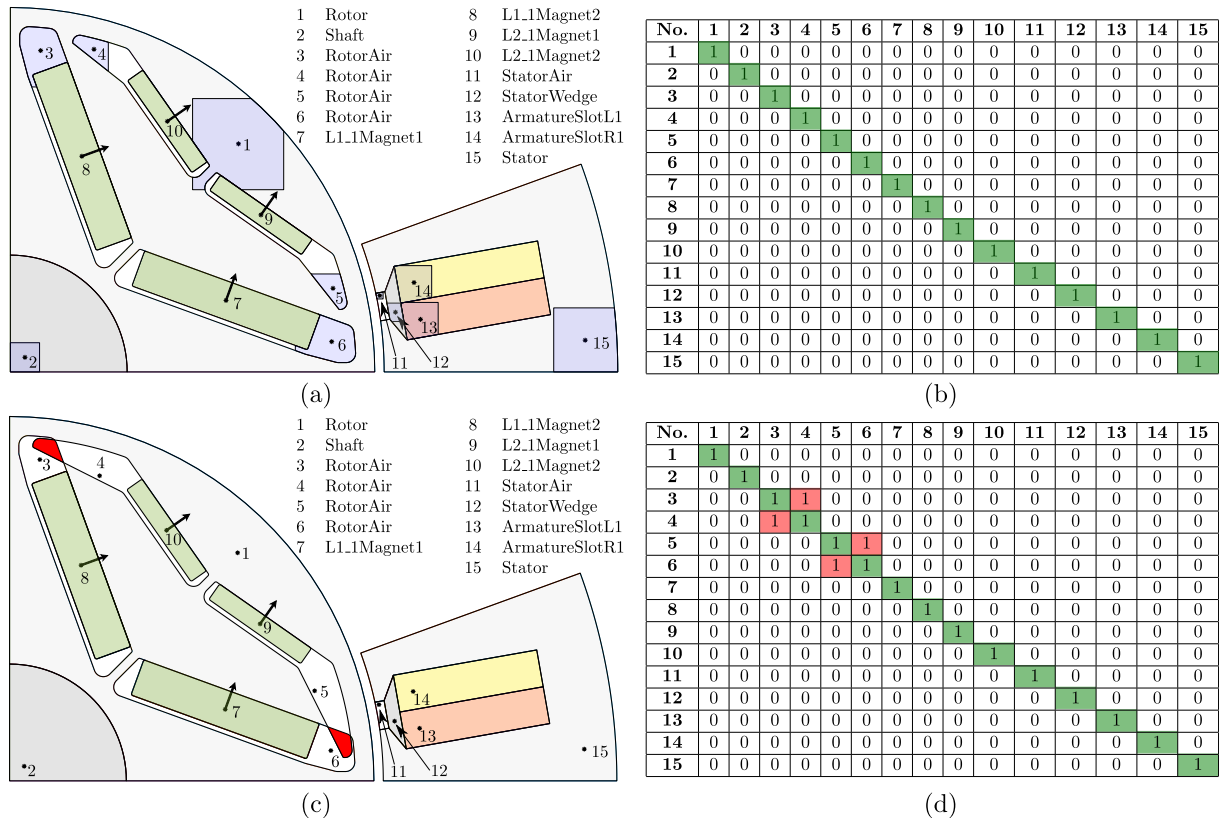


Figure 4.6: Feasible (a,b) and infeasible geometry (c,d)

4.3.3 Impact on total execution time

The feasibility and region detection procedure is performed only once during geometry generation, with a typical duration of 0.5-2 seconds. The transient calculation of a single operating point in ANSYS Motor-CAD for a two-layer IPM machine geometry typically takes between 30-60 seconds. If additional calculations are performed during the design evaluation (thermal transients, drive cycle analysis, etc.), the cumulative time can increase to 10-15 minutes.

As an experiment, a sensitivity analysis with 4 consecutive runs of 1000 iterations was performed for a well-defined two-layer V-shape rotor geometry with 44 parameters (Table4.2).

The design space has been specified by defining upper and lower bounds of all design parameters. A set of parameters for each design has been generated by scanning the multidimensional

Table 4.2: FC impact on total optimization time

Run	1	2	3	4
Feasible designs	758	749	731	749
Infeasible designs	242	251	269	251
Total	1000	1000	1000	1000
Calculation time using try-catch, without FC [h]	64.0	63.2	61.7	63.2
Calculation time with FC [h]	63.6	62.8	61.3	62.8
Calculation time worst case [h]	83.3	83.3	83.3	83.3
Time saving, try-catch to worst case [%]	23.2	24.1	25.9	24.1
Time saving, FC to worst case [%]	23.6	24.6	26.4	24.6

space via Space filling Latin Hypercube sampling method using Ansys OptiSlang surrogate modelling tool.

The average design evaluation time is 300 seconds (5 minutes). Using try-catch adds 4 seconds (304s per design evaluation), while using feasibility check adds 2 seconds (302s per design evaluation).

Let us first consider the worst-case scenario without try-catch or FC (FEA tool runs the entire simulation). This approach leads to a maximum duration of 83.3h per run. On the other hand, the try-catch procedure detects all possible errors, leading to an average execution time of 63.1h (here we assume the scenario where the FEA tool outputs an error for each infeasible design). Finally, using FC results in an average execution time of 62.6 hours.

As expected, the try-catch and FC procedures result in virtually the same execution time and a significant overall time savings (25% or 20h shorter execution time). The conclusion is that the use of FC has no impact on the total execution time. Unlike the try-catch procedure, FC can provide the information about the colliding regions and parameters that can be exploited in surrogate (metamodel) optimization, or tools such as Ansys OptiSlang [86,87].

4.4 Further reading

Pub.6 contains detailed extended elaboration of this chapter.

Chapter 5

Main scientific contribution of the thesis

The emphasis of the research described in this thesis is on developing a software framework that would allow higher design freedom for any machine cross-section, exploring SyRM optimization improvement potential via forced feasibility strategy, and finally, developing an automated SyRM rotor generation strategy with minimal parameter number. The research was conducted in 3 steps. As previously stated, after selecting the geometry and commencing optimization, the optimization system (software code) must be able to detect if generated geometry is unfeasible (i.e. rotor barriers are overlapping). The first step included the development of robust geometry feasibility and region detection algorithms using the Matlab software package. The second step is development of an alternative approach of forced feasibility, where every unfeasible design is forced to change parameters until reaching feasibility. The benefit is an overall optimization time reduction. Finally, the third step is the definition of SyRM rotor geometries using a minimal set of parameters in order to reduce design complexity. Consequently, a reduction of overall optimization time is expected due to the smaller number of parameters that define the optimization problem.

The achieved scientific contribution of the research described in this doctoral thesis is briefly summarized in the following sections:

5.1 Robust feasibility and region detection algorithm based on the shape object approach in the definition of electrical machine geometry

Optimization is an important and inevitable part of the modern electric machine design process. When properly applied, optimization leads to a design that satisfies all imposed requirements.

Even when properly constrained, complex geometries generated by optimization algorithm can lead to infeasible designs that in worst case increase optimization time or propagate non-

manufacturable candidates. In addition, the accurate detection of interior points for each closed region in order to assign material can be a serious challenge.

The proposed scientific contribution provides a solution to both problems through a novel robust feasibility verification procedure and inner-point detection using Matlab polyshape objects. The generality of the approach allows application in any other script language. The polyshape approach elevates geometric design analysis from geometric primitives (points, lines and arcs) to the level of objects (shapes), applicable to any type of machine geometry as an upgrade to existing code. In addition to geometrical properties (vertex coordinates), elevation to shapes allows severely simplified surface area, mass and Boolean calculations. When implemented, the method represents a paradigm shift in electric machine design.

The main benefits of robust feasibility checking are: preventing infeasible (non-manufacturable) candidates to be propagated or to win in the optimization competition, gathering information about which shapes and parameters cause problems and finally, greater freedom in defining geometry parameter boundaries when describing complex geometries. The procedure can be used with any electric machine type. The scientific contribution is covered in Pub.6.

5.2 Improvement of optimization convergence through the reduction of feasible geometry search-time for synchronous reluctance machines using novel forced feasibility approach

Considering that the previous scientific contribution currently depends on the Matlab software package (*polyshape* class), I wanted to explore an alternative approach applicable in open-source optimization algorithms.

A traditional way of securing geometrical feasibility is the application of strict parameters bounds to completely avoid the occurrence of infeasible models. The solution is well suited for simple problems. On the other hand, in complex problems, the issues cannot be avoided, but still, the method reduces the probability of the occurrence of the infeasible candidates. For this reason, optimization algorithms must include a method for dealing with geometrically infeasible candidates.

In general, a geometrically infeasible candidate is discarded while the new candidate takes its place. To generate a replacement candidate, Žarko et al. [82,89] randomly initialize the entire parameter set until a geometrically feasible replacement candidate appears. The drawback of this method is a possible rejection of candidates with some good properties. Moreover, this method may lead to slow convergence to the optimal solution if the optimal candidate is on the boundary of the feasible space.

The alternative approach is forced feasibility, where each infeasible design (Figure5.1a)

is subjected to parameter modification until feasibility is achieved (i.e., barrier 1 (blue) and barrier 2 (yellow) are modified until the candidate achieves the specified flux carrier width w_{goal} , Figure 5.1b). This approach requires smart parametrization with minimum feasibility constraints and can potentially be extremely complex. On the other hand, potential benefits include reduced optimization time (no need to wait for a random feasible design to emerge) and faster convergence to the final result.

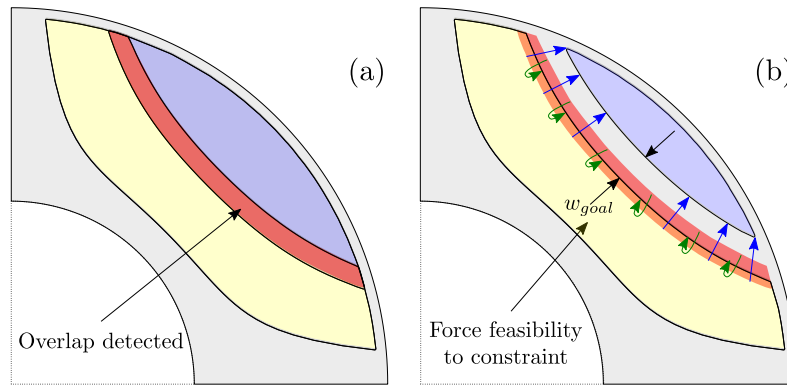


Figure 5.1: Infeasible geometry (a) and forced feasibility (b).

The second part of the scientific contribution is the introduction of novel forced feasibility concept which improves optimization convergence proved by successive comparative optimization runs with randomly generated rotor barrier geometries. The results show that properly implemented forced feasibility leads to a reduction in optimization time (12.3% shorter). Pub.1 concentrates on theoretical aspects of SyRM design. Pub.2 develops the ePTO design requirements used in Pub.3,4,7. The scientific contribution is covered in Pub.4.

5.3 Method for synchronous reluctance machine rotor geometry parametrization with the reduced parameter set

The third scientific contribution is the definition of smooth-barrier SyRM rotor geometries using a minimal set of parameters in order to reduce design complexity. Consequently, a reduction of overall optimization time is expected due to the smaller number of parameters that define the optimization problem.

SyRM barrier generation procedure was studied in detail. A pseudo-code solution that secures absolute feasibility, barrier topology complexity minimization, and simple implementation is provided. Four smooth barrier types have been presented: circular variable depth (CrVD), hyperbolic with variable eccentricity (HyVE), original Zhukovsky (Zh) and modified Zhukovsky with variable depth (MZhVD). MZhVD is contracted by applying a conformal mapping based modifications of the original Zh topology. Absolute feasibility is a very important

feature because it enables the use of dimensionless parameters which secure code robustness and design scalability to any physical dimension. Barrier topology complexity has been minimized via a systematic approach to design automation and careful analysis of construction features of each topology. The scientific contribution is covered in Pub.5. The proposed pseudo-code is validated in Pub.7.

Chapter 6

List of publications

The main publications related to the thesis are specified in the following list.

Conference papers

- Pub 1.** B. Ban, S. Stipetić and M. Klanac "Synchronous Reluctance Machines: Theory, Design and the Potential Use in Traction Applications", in International Conference on Electrical Drives & Power Electronics (EDPE), The High Tatras, 24-26 September 2019.
Available at:<https://doi.org/10.1109/EDPE.2019.8883905>
- Pub 2.** B. Ban and S. Stipetić, "Electric Multipurpose Vehicle Power Take-Off: Overview, Load Cycles and Actuation via Synchronous Reluctance Machine", in International Aegean Conference on Electrical Machines and Power Electronics (ACEMP) & International Conference on Optimization of Electrical and Electronic Equipment (OPTIM), Istanbul, 27-29 August 2019.
Available at:<https://doi.org/10.1109/ACEMP-OPTIM44294.2019.9007187>
- Pub 3.** B. Ban and S. Stipetić, "Design and optimization of Synchronous Reluctance Machine for actuation of Electric Multi-purpose Vehicle Power Take-Off", in International Conference on Electrical Machines (ICEM), Gothenburg, 23-26 Aug. 2020.
Available at:<https://doi.org/10.1109/ICEM49940.2020.9270784>

Journal papers

- Pub 4.** B. Ban, S. Stipetić and T. Jerčić "Minimum Set of Rotor Parameters for Synch. Reluctance Machine and Improved Optimization Convergence via Forced Rotor Barrier Feasibility", in Special Issue Optimization and Simulation of Permanent Magnet Motors, Energies, 2021, 14(10), 2744. April 2021.
Available at:<https://doi.org/10.3390/en14102744>
- Pub 5.** B. Ban and S. Stipetić "Absolutely Feasible Synchronous Reluctance Machine Rotor Barrier Topologies with Minimal Parametric Complexity", in Special Issue Synchronous Reluctance Motor-

Drive Advancements, *Machines* 2022, 10(3), 206. January 2022.

Available at:<https://doi.org/10.3390/machines10030206>

Pub 6. B. Ban and S. Stipetić, "Robust Feasibility Verification and Region Inner-Point Detection Algorithms for Geometric Shape Objects applied to Electric Machine Optimization Workflow", in *Journal of Structural and Multidisciplinary Optimization*. June 2022.

Available at:<https://doi.org/10.1007/s00158-022-03263-4>

Pub 7. B. Ban and S. Stipetić, "Systematic Metamodel-based Optimization Study of Synchronous Reluctance Machine Rotor Barrier Topologies", in Special Issue Synchronous Reluctance Motor-Drive Advancements, *Machines* 2022, 10(8), 712. August 2022.

Available at:<https://doi.org/10.3390/machines10080712>

Chapter 7

Author's contributions to the publications

The author of the thesis is the main contributor (the first author) on every listed publication.

- Pub 1.** In the conference paper titled "**Synchronous Reluctance Machines: Theory, Design and the Potential Use in Traction Applications**" [69] the author has explored the theoretical aspects of SyRM machines, rotor parametrization, design alternatives, structural analysis, performance and optimization. Commercial applications of SyRM have been investigated. Marine and freight traction and commercial vehicle PTO have been selected as application niches. The decision was made to further investigate ePTO use cases. The author performed the study, processed the results, discussed them with the coauthors, and written the manuscript.
- Pub 2.** In the conference paper titled "**Electric Multipurpose Vehicle Power Take-Off: Overview, Load Cycles and Actuation via Synchronous Reluctance Machine**" [68] the author has concentrated on investigation of PTO load cycles for various commercial electric multipurpose vehicles. This paper provides load cycle approximations of ePTO load cycles (refuse, concrete mixer, hook-loader and vacuum trucks). These can be used for continuous and peak requirement calculation and optimal ePTO machine sizing. The study was crucial for the development of the ePTO SyRM design requirements used as a starting point of Pub.2,3,4,5,7. The author performed the study, processed the results, discussed them with the coauthor, written and revised the manuscript.
- Pub 3.** In the conference paper titled "**Design and optimization of Synchronous Reluctance Machine for actuation of Electric Multi-purpose Vehicle Power Take-Off**" [90] the author designed the SyRM for ePTO application. This paper presents the SyRM parametrization, design constraints and optimization via improved differential evolution algorithm. The most important research outcome was the first iteration of Zhukovsky rotor cross-section parametrization (later presented in Pub.4). The author developed the rotor parametrization, performed the optimization, processed the results, discussed them with the coauthor, written and revised the manuscript.

- Pub 4.** In the journal paper "**Minimum Set of Rotor Parameters for Synchronous Reluctance Machine and Improved Optimization Convergence via Forced Rotor Barrier Feasibility**" [91] the author documented the first iteration of novel SyRM rotor parametrization with reduced number of parameters. Furthermore, the paper introduced the novel forced feasibility concept, applied on rotor barrier parameters, resulting in improved optimization convergence with overall optimization time reduced by 12.3%. Proposed approaches were demonstrated using optimization procedure based on the existing differential evolution algorithm framework. The author developed the rotor parametrization, performed the SyRM optimization using the forced feasibility approach, processed the results, discussed them with the coauthors, and written and revised the manuscript.
- Pub 5.** In the journal paper "**Absolutely Feasible Synchronous Reluctance Machine Rotor Barrier Topologies with Minimal Parametric Complexity**" [92] the author presented a final iteration of automated SyRM rotor barrier construction with an increased degree of freedom and minimal geometrical complexity. The paper proposes four topologies based on circular, hyperbolic, and original Zhukovsky lines. Furthermore, a novel Modified Zhukovsky variable depth type geometry was introduced. The step-by-step construction of each topology was presented in a form of pseudo-code with detailed comments and illustrations. The author developed the rotor parametrization, created the pseudo-code, written and revised the manuscript.
- Pub 6.** In the journal paper "**Robust Feasibility Verification and Region Inner-Point Detection Algorithms for Geometric Shape Objects applied to Electric Machine Optimization Workflow**" [93] the author introduced the novel software framework which solves one of the most cumbersome electric machine design issues, determining if generated cross-section is feasible or not. Additional novelty is an introduction of geometric shape objects instead of classic point, line and arc primitives. Furthermore, a set of functions for calculation of shape inner-points for assigning the material to each closed region (air, steel, epoxy, magnet...) was developed. The author implemented the shape-based parametrization and all related software functions in Matlab, created the figures and pseudo-code, discussed them with the coauthor, written and revised the manuscript.
- Pub 7.** In the journal paper "**Systematic Metamodel-based Optimization Study of Synchronous Reluctance Machine Rotor Barrier Topologies**" [91] the author validated the pseudo-code from Pub.5. Nine rotor topologies with different complexities have been compared via novel metamodel-based strategy, which enables systematic and fair comparison of different rotor topologies. The approach significantly reduces total optimization time from several weeks to a few days. Additionally, the study confirms that a Modified Zhukovsky variable depth topology yield the best results for the given requirements. The author im-

plemented metamodel optimization framework in Matlab and OptiSlang tools, processed the results, discussed them with the coauthor, written and revised the manuscript.

All the papers in their final versions are included in the “Publications” section of the Thesis.

Chapter 8

Conclusion and Future Directions

Nowadays, especially in the automotive sector, electric machine designers primarily rely on simulation. This is both cost and time effective. There is a substantial confidence in FEA modelling compared with the experiment, especially for machine topologies like SyRM. The FEA simulations for SyRMs are becoming a standard proof, almost a virtual prototyping validation of the machine performance. Another benefit of FEA based design of experiments is the reduction of prototype variant number.

Having this in mind, the main thesis objective is the improvement of the optimization process for synchronous reluctance machines. Considering that SyRM rotor parametrization can be designed for absolute feasibility, and that IPM machines are currently the automotive industry standard when it comes to traction application, the research was expanded to development of robust feasibility detection methods.

The novel research results are described through three achieved scientific contribution. The first contribution is of the thesis is the development of the framework for robust feasibility detection and material inner-point calculation of any electric machine type. The second contribution is the forced feasibility method which shortens the optimization time. The third contribution is achieved through development of novel absolutely feasible rotor geometries with minimum set of parameters. All three contributions create a unique optimization framework aimed at optimization of SyRM and IPM machines. The research is shared with the community through pseudo-code for the construction of absolutely SyRM rotors, and open-source code for robust feasibility detection.

Further research will concentrate on developing fast methods for SyRM torque ripple reduction and further development of SyRM rotor parametrization. Several follow-up projects are planned to be derived from the presented work:

1. Asymmetric rotor topologies with the purpose of torque ripple reduction without skewing.
2. Torque ripple mitigation methods based on non-uniform rotor skew angles and variable segment lengths.
3. Algorithm for the addition of precise corner fillets to arbitrary poly-line curves.

Chapter 9

Publications

Publication 1: Synchronous Reluctance Machines: Theory, Design and the Potential Use in Traction Applications

Paper details:

B. Ban, S. Stipetić and M. Klanac "Synchronous Reluctance Machines: Theory, Design and the Potential Use in Traction Applications", in International Conference on Electrical Drives & Power Electronics (EDPE), The High Tatras, 24-26 September 2019.

Available at:<https://doi.org/10.1109/EDPE.2019.8883905>

Synchronous Reluctance Machines: Theory, Design and the Potential Use in Traction Applications

Branko Ban

Dept. of El. Machines and Automation
FER; University of Zagreb;
Unska 3, 10000 Zagreb, Croatia
branko.ban@outlook.com

Stjepan Stipetić

Dept. of El. Machines and Automation
FER; University of Zagreb;
Unska 3, 10000 Zagreb, Croatia
stjepan.stipetic@fer.hr

Mario Klanac

Dept. of El. Machines and Automation
FER; University of Zagreb;
Unska 3, 10000 Zagreb, Croatia
mario.klanac@fer.hr

Abstract—The volatilities in the permanent magnet price have raised interest within the automotive industry for finding substitute electric machine designs. The proposed alternatives are synchronous reluctance machines (SyRM) and its derivatives, assisted synchronous reluctance (PMASR) machines. These solutions rely on high reluctance torque thus theoretically needing no magnet material in the rotor structure. This paper covers reluctance machine theoretical background, rotor parametrization, design alternatives, structural analysis, and optimization. Commercially available traction reluctance machines applications have been investigated. Marine and freight traction and commercial vehicle power take-off have been selected as application niches. Finally, a performance comparison for different saliency ratios of the ideal SyRM, ferrite and neodymium PMASR has been conducted.

Keywords—electric machine; traction; permanent magnet; synchronous reluctance; assisted; optimization; comparison; axially laminated; design; power take-off; commercial vehicles; rare earth free.

TABLE I. Abbreviation list

Abbreviation:	Description:
CFD	Computational fluid dynamics
DE	Differential evolution
FEM	Finite element method
FW	Field weakening
FOS	Factor of safety
IM	Induction machine
IPM	Interior permanent magnet
NdFeB	Neodymium iron boron magnet
PM	Permanent magnet
PMASR	Permanent magnet assisted synchronous reluctance
PTO	Power take-off
SPM	Surface permanent magnet
SyRM	Synchronous reluctance machine

I. INTRODUCTION

In order to reduce emissions, air pollution, resource waste, and traffic noise, EU government legislation is pushing towards the increase of electric and hybrid vehicle production [1]. This has caused a tectonic change in the automotive industry, both knowledge, and production wise. New traction

components like battery, inverter, and electric machine are becoming the most important factors in vehicle design in a matter of cost and packing (component layout within the vehicle) [2], [3]. The battery is usually modular component and inverter is small in size, which means they can in most cases be packed efficiently within the vehicle. On the other hand, the electric machine is usually integrated within some sort of transmission system, which is inherently space consuming [2]. To reduce the size of the drivetrain, electric machine size must be minimized, while efficiency and power density must be kept on the sufficient level.

Currently, due to the inherently high torque and power density, interior rare earth permanent magnet synchronous machines (IPM) are predominantly used for automotive traction (Fig. 2a-b). A notable landmark for IPM machines in automotive hybrid/electric traction was the adoption by both Toyota and Honda, for the first generation of Prius and Insight, respectively [4], [5].

Although the performance benefits are undisputed, the use of rare earth permanent magnet (PM) materials, such as neodymium or dysprosium, has raised concerns in a number of areas. In 2011 and 2012, China reportedly threatened to cut off international supplies of these materials [6], leading to dramatic, though short-term, increase in the material price, increasing as much as 3000% in case of dysprosium [7]. These volatilities have forced the automotive industry to search for the alternative electric machine design, which will either use none or minimal amount of rare earth material.

The alternatives which have not been in recent industry focus are synchronous reluctance machines (SyRM) and its derivatives [8]. These solutions rely on high reluctance torque, thus theoretically needing no PM material in the rotor structure. They have relatively low material costs, low rotor losses and are considered as robust [9], [10]. On the other hand, lack of the permanent magnetic field in the rotor is penalized with lower torque density, lower power factor, and higher torque ripple [11], [12]. This paper will present the theory, state of the art trends in reluctance machine technology and potential applications in vehicle traction. The survey will be performed on pure synchronous reluctance machines (SyRM), and its derivative designs improved by adding permanent magnet material, assisted synchronous reluctance machines (PMASR).

II. SYRM AND PMASR THEORY AND DESIGN ASPECTS

A. General facts

The stator of the SyRM or PMASR machines is not different from other machine types, therefore, to be able to evaluate and compare different designs, only rotor cross sections will be discussed. Furthermore, this paper will consider only machines for traction applications which are coupled to multi-phase variable frequency drive.

In 1923, Kostko [13] has calculated that if properly designed and manufactured, SyRM performance is comparable with induction machine (IM) of the same volume. During the years SyRM concept evolved from simple squirrel cage, to complex design implementations (Fig. 2e-h), [14], [15].

All of the concepts rely on rotor anisotropic properties designed to produce high reluctance torque. Rotor anisotropy is achieved by large magnetic conductivity differences in d and q axis caused by several flux barriers, and saturation effects in different parts of the rotor core. The purpose of the barriers is to create high resistance path for the flux along the q axis to achieve high saliency ratio, thus producing a high reluctance torque component (Fig. 2e-f). However, barrier bridges and posts are required (at the ends and sometimes in the middle of each barrier) for sustaining rotor structural integrity. A portion of flux flows through these bridges causing a consequent reduction of the torque. Another downside is limited operation in FW area and inherently low power factor (Fig. 3), which requires large variable frequency drive.

If permanent magnets are inserted in each rotor flux barrier (Fig. 2g-h), SyRM is transformed to PMASR. The purpose of the magnets is to saturate barrier bridges, to increase the torque and especially the power factor, which reduces the size of the attached variable frequency drive [11].

Two most commonly used types of PM material are "strong" neodymium (NdFeB) and "weak" ferrite. PM material properties are a function of remanent flux density, coercive force (demagnetization field proportional to demagnetization current) and temperature. Fig. 1 demonstrates operational contrast of NdFeB and ferrite PMs.

At -40°C , NdFeB have remanent flux density around 1,17 T and large coercive force (large current is required for demagnetization) while ferrites have approx. flux density of 0,42 T and smallest coercive force [16]. The main ferrite PM disadvantage is demagnetization at low temperatures [17] which can be an issue (-40°C is the minimal operational temperature of most road vehicles). At high temperatures ($> 150^\circ\text{C}$), similar phenomena happen with NdFeB magnets where rapid reduction of coercive force makes them vulnerable to demagnetization (in practice max. operational temperature of NdFeB magnets is 150°C). Here ferrites demonstrate their unique advantage, increasing coercive force with temperature rise, a feature that makes them more resilient to demagnetization. Both PM materials remanent flux density decreases with temperature increase.

Another benefit of ferrite PMs is rotor injection molding, which allows complete filling of the rotor structure (Fig. 2g).

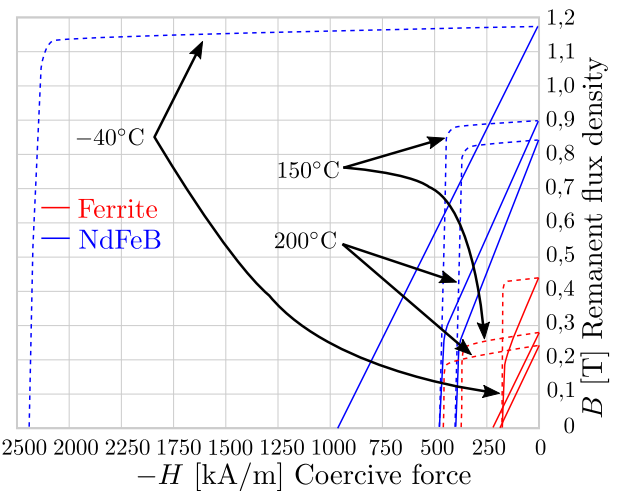


Fig. 1: Comparison of ferrite and NdFeB PM curves at different temperatures [16].

This is not the case with NdFeB PMs, which are produced in specific shapes (Fig. 2h), thus leaving empty space in the rotor flux barriers [18]. This method can further increase power output and reduce losses.

A penalty of SyRM is the inability to have a large number of poles (in practice maximum pole pair number is $p = 2$). Obviously, if the number of poles is increased, magnetic bridges and posts must be reduced to maintain the saliency ratio. This puts pressure on rotor structural integrity. On the other hand, PMASR technology is well suited for high pole-number designs because magnet flux saturates the barrier bridges and posts ($p = 6$ in case of Chevrolet Volt [19]). In this way, bridges can be thicker, which increases structural robustness of the rotor. As an example, in-wheel 12-pole PMASR machine with an external rotor is presented in [20], achieving a 30% reduction of the torque ripple compared with the reference design. In [21], a 16-pole design with a double stator and 3D air-gap concept is presented, improving the efficiency by 5% when compared to a conventional design.

B. Electromagnetic torque

Machines listed in Fig. 2 can be divided in two families. First is alignment torque component dominant group, which includes IPM and SPM machines where PM magnetization direction is aligned with positive d axis (Fig. 2a-d). Second is reluctance torque component dominant group, which includes SyRM and PMASR machines. It is important to emphasize that PMASR PM magnetization direction is opposing positive q axis (Fig. 2g-h), [11].

In general, there are two different rotor paths for the flux (Fig. 2). A distinction of the reluctance machines is a switch of rotor d and q axes in relation to alignment torque dominant family. High permeability path (high magnetic conductivity, d -axis path) is parallel to the flux-barriers. Low permeability path (low magnetic conductivity, q -axis path), is vertical to the rotor flux barriers [11].

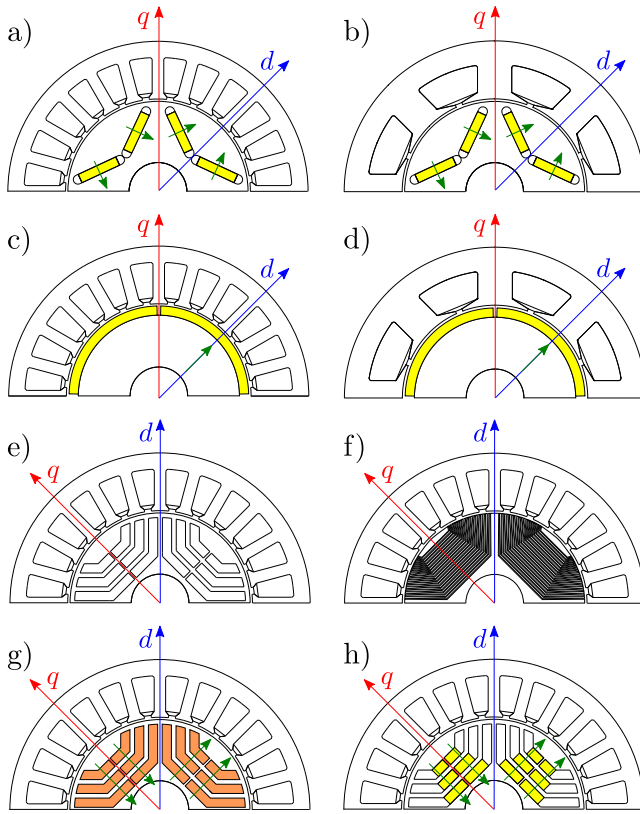


Fig. 2: Example of four pole machine families with corresponding dq axes: IPM with a) distributed and b) concentrated winding stator; SPM with c) distributed and d) concentrated winding stator; e) SyRM; f) AxLam SyRM; g) "weak" PM material PMASR; and h) "strong" PM material PMASR. Green arrows indicate PM magnetization direction.

For both families, torque output consists of alignment and reluctance component and can be written as (1), (3), where L_d, L_q are inductances, i_d, i_q currents in d and q axis, p is the number of pole pairs and λ_m is magnet flux. In case there is no PM material (SyRM, $\lambda_m = 0$), the relation between L_d and L_q will determine the machine torque capability (1). The inductance ratio is referred as saliency ratio ξ , whose formula depends on the machine family (2), (4), [11].

A high number of cavity layers in each pole combined with a small air-gap typically leads to saliency ratios higher than 3,5 [22]. Lipo and Matsuo report that $\xi = 7 - 8$ can be expected [23], power densities in the order of 5, 5-7, 5 kW/l can usually be achieved [24], [25]. Apart from the stator and rotor cross-section design, lamination steel selection has an impact on final saliency ratio ($\Delta\xi = \pm 7\%$) [26].

$$\text{Dominant reluctance component machine family} \begin{cases} T_{em} = \frac{3}{2}p \left[\underbrace{\lambda_m i_d}_{\text{Alignment}} + \underbrace{(L_d - L_q) i_q i_d}_{\text{Reluctance}} \right] & (1) \\ \xi = L_d/L_q & (2) \end{cases}$$

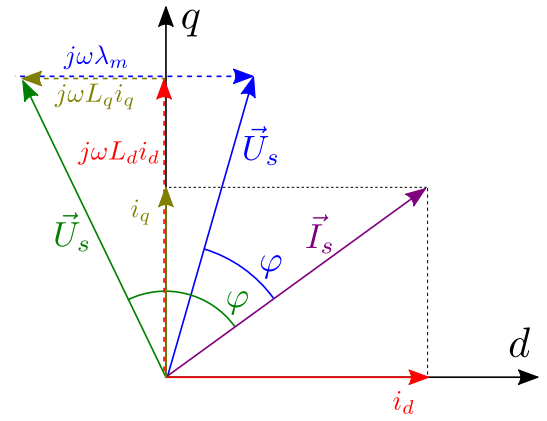


Fig. 3: Voltage phasor diagram of SyRM (green) and PMASR (blue) for a given stator current (stator resistance is neglected $R_s = 0$) [11].

$$\text{Dominant alignment component machine family} \begin{cases} T_{em} = \frac{3}{2}p \left[\underbrace{\lambda_m i_q}_{\text{Alignment}} + \underbrace{(L_d - L_q) i_q i_d}_{\text{Reluctance}} \right] & (3) \\ \xi = L_q/L_d & (4) \end{cases}$$

C. Combination of PM and reluctance: IPM design plane

Depending on the amount of the rotor PM material and rotor cross-section, IPM and PMASR properties can often overlap and one can argue that IPM is actually PMASR and vice versa. According to the informal rule, if reluctance torque component is greater than 50% of maximum torque at base speed, the machine is considered PMASR. To further differentiate machine families, Soong [27] introduces "IPM design plane" (Fig. 5). From left to right, the plane starts with SyRMs ($\lambda_m = 0$, high saliency, only reluctance torque, Fig. 2e-f) and ends with SPM machines (no saliency $\xi = 1$, only magnet torque, Fig. 2c-d). In between, all IPM machines and PMASR combinations are included.

The optimal IPM design line defines special matches of PM flux and saliency ratios resulting in optimal field weakening (FW) capability, indicating infinite constant power speed range under limited voltage and current constraints (this is valid for ideal machine [27]).

SyRM is out of the optimal design line, whereas PMASR fall into the optimal FW area when the appropriate quantity of magnets is added to a baseline synchronous reluctance design.

D. Rotor laminations assembly

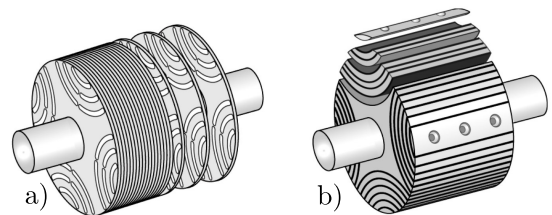


Fig. 4: a) Transversally laminated rotor (TrLam) and b) Axially laminated rotor (AxLam) [28].

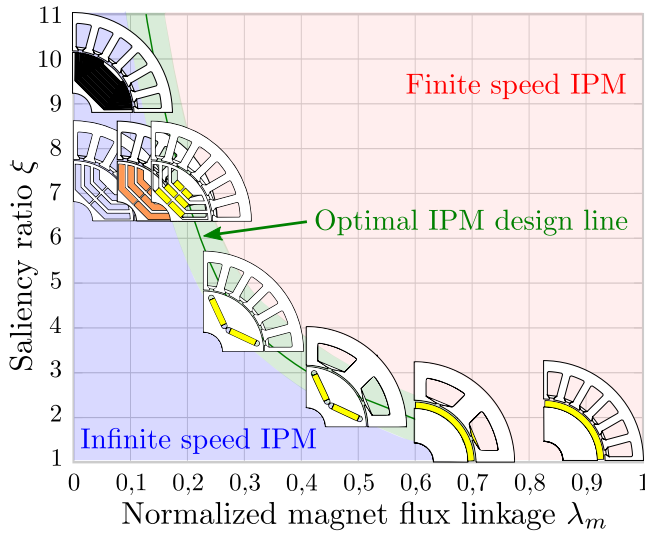


Fig. 5: IPM design plane [11].

SyRM with transversally (conventionally) laminated rotor (TrLam) has been proposed in early nineties [14], [29], [30], (Fig. 4a). Machine laminates are produced by punching tool or laser cutting, which removes extra material. The other, non standard production technique is rotor lamination mounting alongside shaft axis (AxLam, Fig. 4b). Theoretically, this method increases the saliency ratio above the levels achievable with TrLam machines ($\xi > 10$, [19]) using fixed strips of steel separated by thin layers of insulating material [31].

According to Vagati [30], the better suitability of TrLam structure for industrial manufacturing is evident from several aspects: the laminates can be punched with conventional methods, assembly process is straightforward and either constant (in case of PM injection molding), or segmental skewing can be applied on the rotor. In large scale machine manufacturing, stator skewing is normally avoided in favor of using automatic winding devices [32].

On the other hand, AxLam structure theoretically enables high saliency ratio by increasing the number of laminate layers n_l (Fig. 6a). However, this is only true for a two-pole structure ($p = 1$) [30], while for $p > 1$, Bianchi et al. [33] shows that due to the saturation effects, the ideal structure should have a variable ratio between the depths of magnetic and non-magnetic structures where $k_1 < k_2 < k_3$, which reduces saliency ratio (Fig. 6b). To summarize, production difficulties of AxLam rotors are:

- Every laminate segment has different design and size.
- Inter-segment insulation thickness k_i has to vary in-between layers.
- There is no straightforward skewing possibility.
- Rotor circumference needs to be machined after laminate mounting, which can change the material properties and increase iron losses [34].

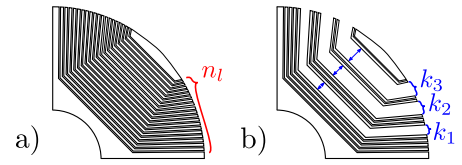


Fig. 6: Sketch of rotor with uniform, and non-uniform distribution of the AxLam laminations.

Due to the rotor magnetic reaction to stator slot harmonics, both TrLam and AxLam options face problems with torque ripple, which makes either rotor or stator skewing a necessity [35]. As mentioned, TrLam rotor can be easily skewed, which is not the case for AxLam rotors, leaving stator skewing as the only option.

Furthermore, when comparing TrLam machine of similar rotor volume, AxLam machines have increased iron losses (Tab. II).

TABLE II. TrLam and AxLam iron loss comparison

Variable	TrLam [36]	AxLam [37]	Unit
n	1500	1500	rpm
p	2	2	-
Rotor diameter	140	136	mm
Stack length	134	160	mm
Power at the shaft @ 1500 rpm	3,6	2,5	kW
Power density @ 1500 rpm	1,7	1,1	kW/l
Iron loss	119	665	W
ξ	8,1	12,5	-

These can be explained in different ways, Maronghiu and Vagati [29] suggest that these losses are due to flux oscillations in stator teeth. A different explanation is given in [37], where losses are caused by rotor eddy currents. Anyway, the additional losses are considerable and represent a further drawback for the AxLam setup [38].

The above-cited reasons are largely sufficient to choose the TrLam rotor type. However, interest on the AxLam type is probably due to the belief that this solution gives a better saliency. This is not correct as comparable anisotropy values are obtained from both rotors, with condition that the pole number is the same. Saliency ratio $\xi = 10$ is a typical, non saturated value for four-pole ($p = 2$) AxLam machine [32].

E. Rotor flux barrier design and number

According to Bianchi [11] and Pellegrino [18], there are multiple parameters which define basic rotor structure in both SyRM and PMASR. Also, asymmetric rotor structures are possible [11], [39], but they are complicated to parametrize and will not be covered in this paper. To simplify the process, several terms are defined (Fig. 7): flux barriers (air cavities in q axis direction), flux carriers (steel guides alternated to flux barriers), barrier bridges (flux barrier ends, whose angular positions at the air-gap are key to minimize torque ripple and

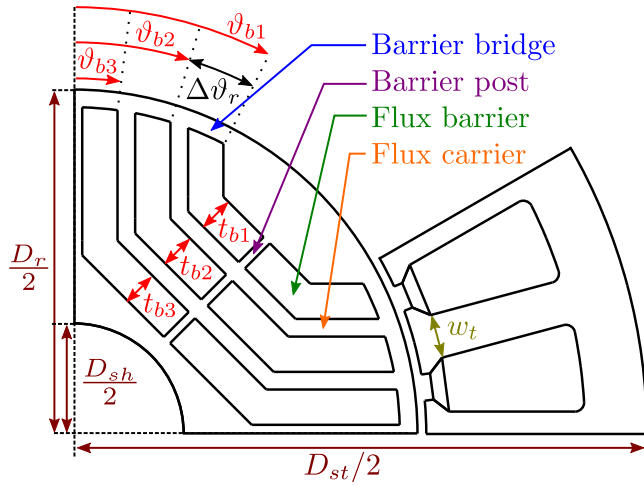


Fig. 7: SyRM/PMASR rotor geometry parameters.

iron losses) and barrier posts (steel reinforcements between flux carriers).

The fundamental rotor design variable is the number of flux barriers (n_l), which can be calculated from (6), where n_r is the number of stator slots (N_s) per pole pair (p), (5). The example machine from Fig. 7 has $N_s = 24$, $p = 2$ meaning $n_l \leq 24/(4 \cdot 2) \leq 3$. In this case, barrier bridges have been designed angularly equidistant (e.g. barrier bridge pitches are: $\vartheta_{b1} : \vartheta_{b2} : \vartheta_{b3} = 3 : 2 : 1$), barrier bridge pitch ($\Delta\vartheta_r$) is considered regular and can be calculated from eq. (7). In practice this does not need to be the case [18]. Obata et al. reports that non uniform pitch distribution can reduce torque ripple [17].

$$n_r = N_s/p \quad (5)$$

$$n_l \leq n_r/4 \quad (6)$$

$$\Delta\vartheta_r = 360/n_r \quad [\text{el. deg.}] \quad (7)$$

A second important set of parameters is barrier thickness distribution (t_{bi}) which correlates to rotor saturation [18]. Referring to Fig. 7, Bianchi defines two coefficients for determining optimal barrier size. $k_{\text{air } r}$ is calculated by eq. (8) where, t_{bi} are the flux barriers thickness, D_r is rotor diameter and D_{sh} is the shaft diameter. Too large $k_{\text{air } r}$ can cause saturation of flux carriers, thus reducing torque output [39]. Second coefficient $k_{\text{air } s}$, is related to the stator geometry (10), where p_s is the stator slot pitch (9) and w_t is tooth width. To keep machine equally saturated coefficients $k_{\text{air } r}$ and $k_{\text{air } s}$ should be kept as equal as possible [11], [23].

$$k_{\text{air } r} = \left[\sum_{i=1}^{n_l} t_{bi} \right] / [(D_r - D_{sh})/2] \quad (8)$$

$$p_s = (\pi D_{st})/N_s \quad [\text{rad}] \quad (9)$$

$$k_{\text{air } s} = (p_s - w_t)/p_s \quad (10)$$

According to [34], the optimal design of a PMASR has to consider PM demagnetization. To avoid demagnetization,

ferrite PMASR flux barriers thickness are recommended to be the same along their length. Alternatively, short NdFeB magnets may be placed on the bottom of rotor flux barriers.

F. Barrier bridges and posts reduction methods

In practice, barrier bridge (Fig. 8c) and post (Fig. 8b) thickness is minimized to reduce torque ripple and losses, while keeping the structural integrity of the rotor.

After a preliminary design is done, mechanical structural finite element method (FEM) and fatigue analysis have to be performed. If rotor design is angularly symmetrical, only one rotor pole has to be considered. Rotor material properties are key inputs for mechanical analysis. In case of SyRMs, only laminate steel data is required (Fig. 8d). PMASR calculation requires additional PM mechanical data. PMs are considered to be a part of the rotor mass without any load-carrying capacity. To avoid calculation issues, a good practice is to "glue" PMs to the laminate surface within FEM software.

Static resistance (one operating point, i.e. at 5220 rpm) to centrifugal load is assessed by using a classic approach based on the average stress over the reduced section [40]. Vibrations and shaft dynamical forces are neglected. The analysis result is often presented in a form of Von Mises stress distribution (Fig. 8b-c), and maximum material displacement (Fig. 8a). The common way of determining design quality is the factor of safety (FOS), which measures how much load will the designed part actually be able to withstand (Fig. 8e). FOS is calculated by equation (11), where σ_{max} is maximal simulated Von Mises stress, and $\sigma_{0,2}$ is yield strength at 0,2 strain, which represents material elastic deformation limit. Typically, it is required that the maximum rotor stress calculated at maximum over-speed ($1,2 \cdot n_{\text{max}}$ [41]) is approximately 2 times lower than the nominal yield strength of the rotor lamination (FOS ≈ 2).

$$\text{FOS} = \sigma_{0,2}/\sigma_{\text{max}} \quad (11)$$

Fatigue analysis is performed to assess the iron bridge lifetime, resulting from cyclic loading. It requires careful considerations due to the reduced value of the tip radii at the corners of the flux barriers and cavities. FEM mesh needs to be sufficiently dense in these areas for a valid result. Extreme operating conditions have to be considered, consisting of repeated start and stop cycles (zero to maximum speed, [40]).

Apart from barrier bridges and posts minimization through electromagnetic and mechanical optimization, Reddy et al. [25], [42] propose a rotor retaining sleeve. The sleeve reduces laminate stress, allowing smaller bridge dimensions. Another approach in [24] proposes a magnetic material which allows the selective introduction of non-magnetic regions in the barrier bridges and posts. This is achieved by local heat treatment of laminations.

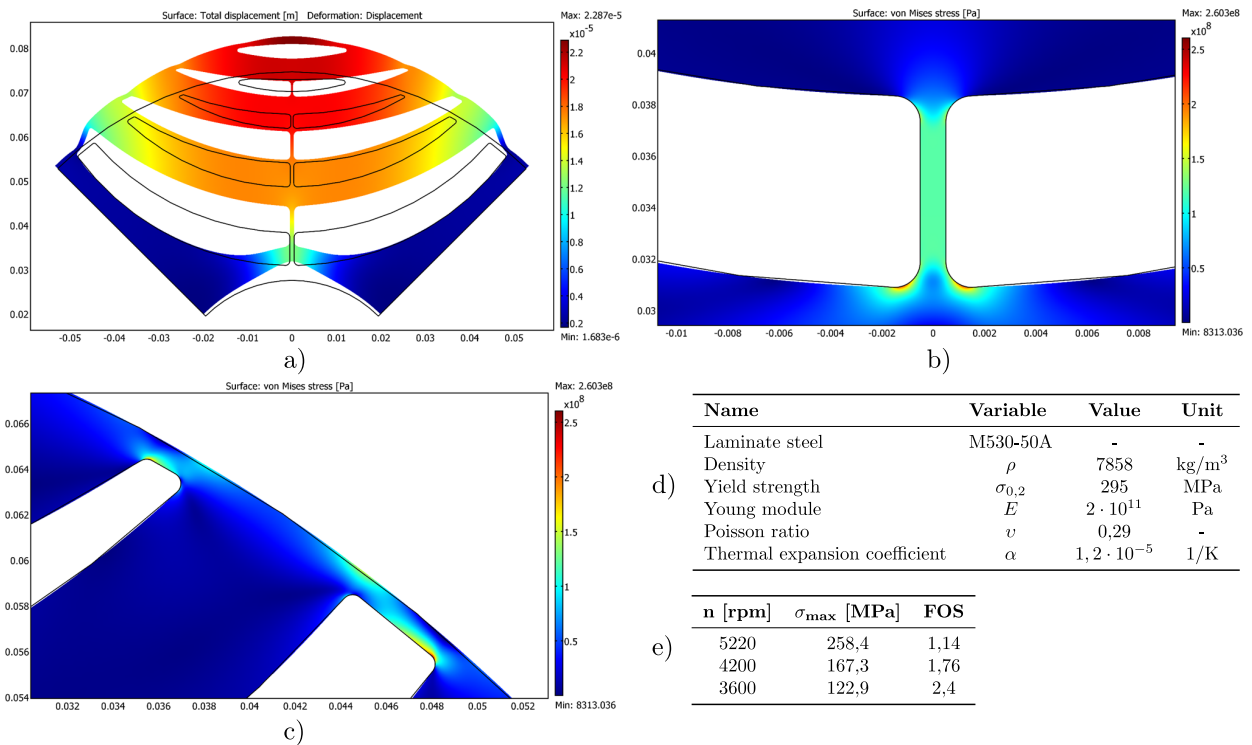


Fig. 8: a) Exaggerated pole displacement; b) Barrier post stress detail; c) Barrier bridge stress detail; d) Material properties table; e) FOS calculation table;

G. Machine design and rotor optimization

The machine design is performed in several steps. Each step usually requires multiple iterations until satisfying results are obtained [43], [44].

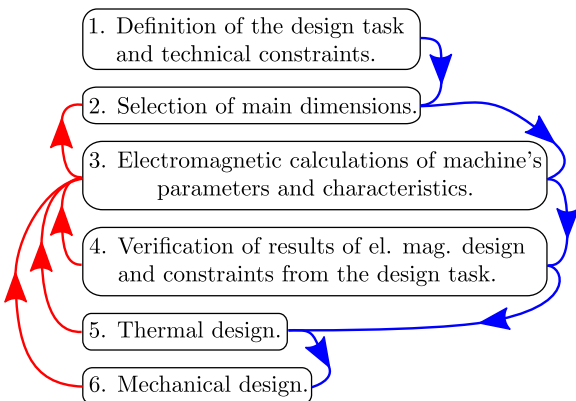


Fig. 9: Electric machine design algorithm example [43].

If the machine volume envelope is defined, the performance will be determined by electromagnetic and thermal design (cooling capability) [45]. There are two approaches to electromagnetic and thermal design. First is lumped parameter modeling which allows fast iterative computations with a precision penalty (especially in case of thermal design). The

second approach is based on FEM where electromagnetic design can be downsized to a 2D problem, while precise thermal modeling requires 3D computational fluid dynamics (CFD) simulations (the penalty is prolonged simulation time). In practice, a combination of both approaches together with empiric methods yields acceptable results [45].

This paper concentrates only on SyRM and PMASR electromagnetic performance which is mostly determined by rotor topology optimization. According to Pellegrino [18], a golden rule for a good PMASR is a SyRM baseline which is then gradually modified towards optimal design.

As previously stated, there are many parameters (Fig. 7) which define the rotor cross section and machine performance. In example, Liu et al. in [46] reports that PMASR efficiency can be improved by 6% with optimal magnet placement. Finding the optimal parameters is a classic Pareto multi-objective optimization problem [47].

Some of the optimization methods are genetic algorithms, differential evolution (DE), and simulated annealing [48]. DE is stochastic evolutionary optimization algorithm [49], [50], [51], which gives the best results in terms of convergence time and repeatability [48]. Together with the machine parameters, the optimization algorithm requires one or several goal functions, which provide a parameter selection boundary (i.e. maximize torque [52], minimize torque ripple, minimize material cost, etc.).

In comparison to other machine types, SyRM and PMASR

can have a large number of rotor parameters. Reduction of parameter numbers will simplify the design and reduce computational time. The recommended compromise between output performance and computational time is to limit the number of degrees of freedom for two [53], or three [54] per rotor barrier.

III. COMMERCIAL APPLICATIONS

A. Industry

The first notable modern industrial commercialization of the SyRM was done by ABB in 2012. As an example, 90 kW machine measured nominal efficiency of 96,1% @ $\cos \varphi = 0,73$, illustrating both the strengths and challenges of this technology [55], [11]. Today, in addition to ABB, various manufacturers such as Kaiser Motoren, REEL, SIEMENS, and Končar MES provide solutions in the 0,55 – 315 kW range [9], [56]. The main reason SyRM designs came in to spotlight is the introduction of the new IEC 60034-30-1 standard with harsher efficiency constraints. Introduction of IE4 super-premium efficiency class [57], and better efficiency in comparison to IMs, makes SyRM attractive for industrial use.

B. Automotive traction

Up to today, SyRM has not been commercialized in large scale automotive traction. One of the rare examples adapted for the electric vehicle is Ricardo 85 kW 6ph SyRM [58]. MotorBrain project [59] has investigated an inverter power module integration with SyRM stator for automotive application. The project resulted in 97,6% efficiency inverter and 93,6% efficiency 6ph 60 kW SyRM (overall system 91,6%).

The conclusion is that the current low volume production of electric/hybrid in comparison to internal combustion vehicles still favors the use of IPM machines.

On the other hand, PMASR machines are a direct competitor to IPM machines and have already been commercialized in the automotive industry. The example is second generation Chevrolet Volt which uses ferrite [19] and BMW i3 which mounts NdFeB magnets [60], [61], [8]. Second-generation Toyota Prius machine [62] is slightly on the side of the IPM family (alignment torque component at base speed is slightly above 50% of maximum torque).

C. Ship propulsion and freight traction

SyRM is considered to be a direct competitor of IMs which are often used in railway and ship propulsion. This has been confirmed by [63], concluding that both IM and SyRM have similar electric, magnetic, and thermal performance, with SyRM having lower rotor losses. Germishuizen et al. emphasize that SyRM compared to IM have lower stator winding temperature rise, which allows an increase of the power rating by 5 - 10% [64]. All authors agree that the main drawbacks of the SyRM solution is low torque in FW range and inherently large variable frequency drive.

Although SyRM in relation to PMASR has a lower power factor, its main benefit is high overload capability, without any demagnetization problems [65].

D. Commercial vehicles

To power the special equipment (cranes, refuse system, refrigerators, etc.), the commercial vehicle must be fitted with an extra means of a power supply, a power take-off (PTO). One or more PTOs transfer power from the engine to drive attachments or load handling equipment. The PTO provides a mechanical link (output shaft) towards load (usually some sort of hydraulic system) with most of the systems having power demand < 80 kW [66]. Historically, the PTO output shaft has been a part of the combustion engine or transmission (Fig. 10a-d). With recent commercial vehicle electrification trends [67], [68], PTO will most likely be an extra electric machine mounted on the vehicle chassis (Fig. 10e-h). The PTO machine will be powered via inverter attached to the traction battery.

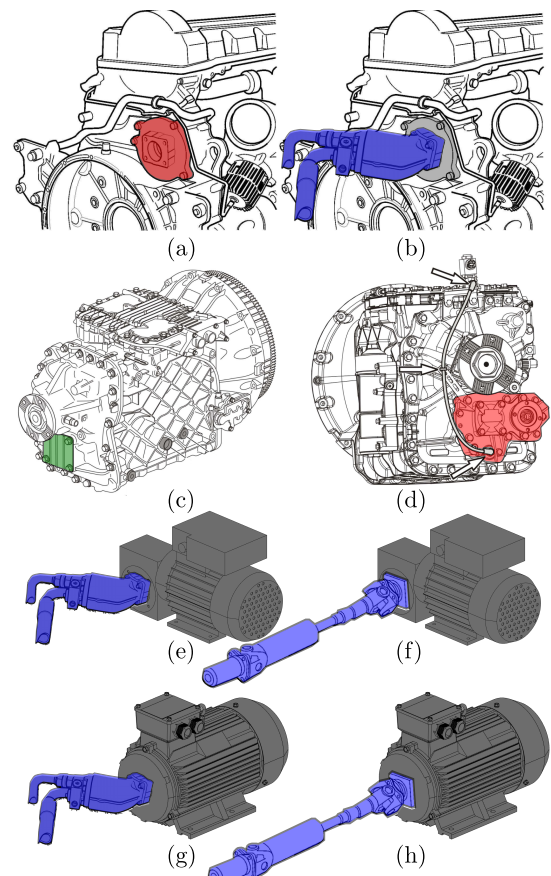


Fig. 10: a) Diesel engine rear PTO mount; b) diesel engine with mounted hydraulic pump; c) Transmission with direct PTO mount; d) transmission with geared PTO [69]; geared PTO propelling hydraulic pump e) and universal joint shaft f); direct PTO propelling hydraulic pump g) and universal joint shaft h).

IV. THEORETICAL SYRM AND PMASR PERFORMANCE

This section examines theoretical limitations of the SyRM, and ferrite and NdFeB PMASR for different saliency ratios ($\xi = 4 - 10$). The calculations are assuming lossless linear machine ($R_s = 0$), driven from inverter with limited voltage and current [16], [70], [71]. All machines have the same

cross section for the given saliency ratio (L_d is fixed and $L_q = L_d/\xi$). In case of SyRM, magnet flux is zero, in ferrite PMASR $\lambda_m = 0,095$ [11], and NdFeB PMASR $\lambda_m = 2,5 \cdot 0,095 = 0,2375$ [65]. Theoretical maximum performance has been calculated using Matlab based MTPA optimization method described in [72]. All inputs variables are listed in Table III in normalized form.

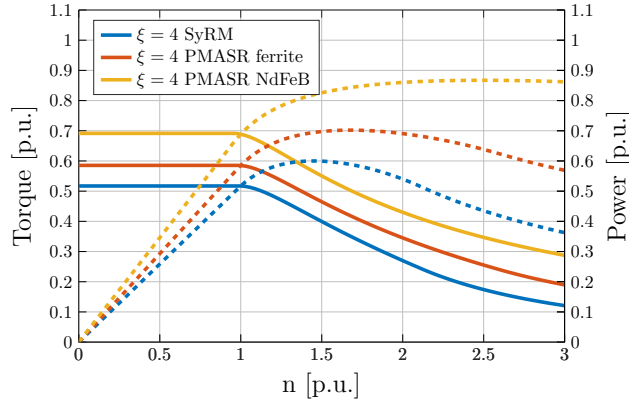


Fig. 11: Performance comparison of SyRM, ferrite and NdFeB PMASR at fixed saliency ratio.

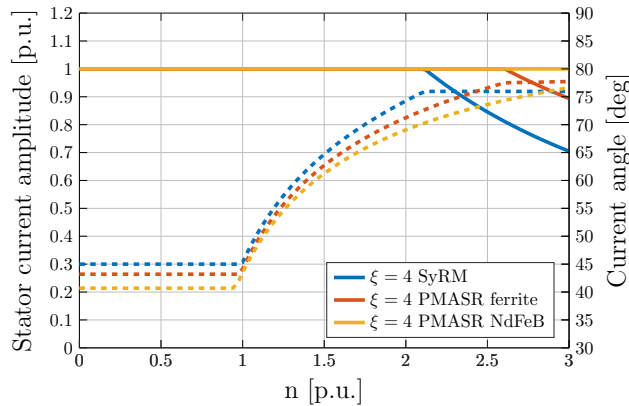


Fig. 12: Current amplitude and angle comparison of SyRM, ferrite and NdFeB PMASR at fixed saliency ratio.

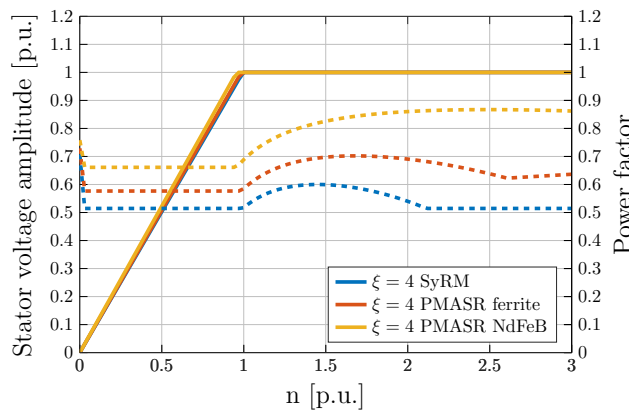


Fig. 13: Voltage amplitude and power factor comparison of SyRM, ferrite and NdFeB PMASR at fixed saliency ratio.

A. Comparison at fixed saliency

If saliency ratio is kept constant at $\xi = 4$, by adding PM material, base torque increases from 0,5 to 0,6 (ferrite PMASR) and 0,7 (NdFeB PMASR) (Fig. 11). There is a large power difference in FW operation. SyRM and ferrite PMASR power rapidly drops, while NdFeB PMASR remains constant up to the maximum speed. Such NdFeB PMASR behavior is due to the fact that the λ_m has been chosen to achieve the characteristic current I_c close to the maximum inverter current $I_{s \max}$. The characteristic current (also known as short circuit current) is defined as $I_c = \lambda_m/L_q$ [11].

Fig. 12 confirms that inverter is operating on the current limit (current amplitude is always 1 in case of NdFeB PMASR) and voltage limit is not reached. Prior to FW, SyRM current angle is fixed to 45° which follows constant torque hyperbola vertex. Adding the PMs reduces the angle which is always $< 45^\circ$ in case of PMASRs. As SyRM and ferrite PMASR reach voltage limit, the current amplitude reduces and angle becomes constant.

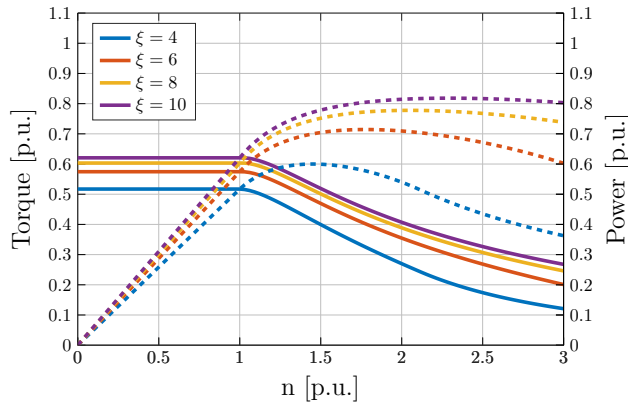
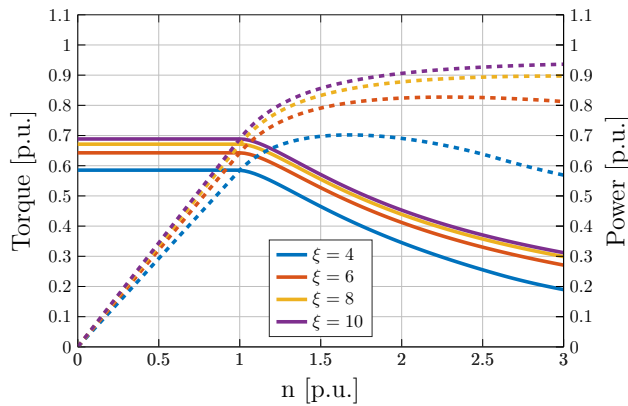
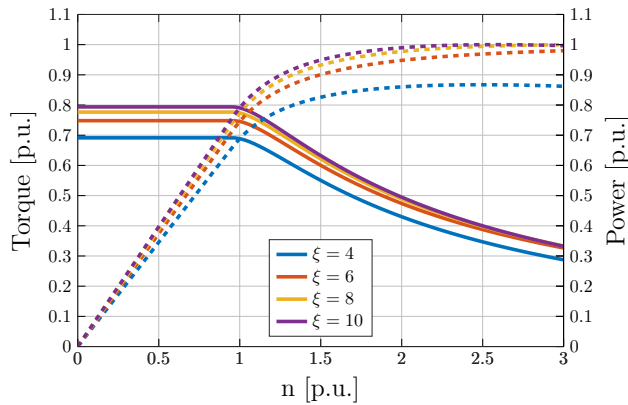
Fig. 13 shows another important effect of adding PMs, the increase of the power factor in the whole operating region. The power factor increases with PM strength and it is always higher than in the case of SyRM machine. The power factor improvement is more beneficial as the speed increases. In the case of PMASR solution, it means that the size of the inverter could be decreased for the same performance requirement.

TABLE III. Parameters of SyRM and ferrite/NdFeB PMASR

Variable	[SyRM; Fe PMASR; NdFeB PMASR]	Unit
ξ	[4 6 8 10]	-
λ_m	[0; 0,095; 0,2375;]	-
L_d	1,379	-
L_q	L_d/ξ	-
p	2	-
$\omega_{el \text{ base}}$	1	-
$U_{s \max}$	1	-
$I_{s \max}$	1	-
n_{base}	$\omega_{el \text{ base}} \cdot 30/(\pi p)$	p.u.
U_{base}	$U_{s \max}$	p.u.
I_{base}	$I_{s \max}$	p.u.
S_{base}	$3/2 \cdot I_{\text{base}} \cdot U_{\text{base}}$	p.u.
Z_{base}	$U_{\text{base}}/I_{\text{base}}$	p.u.
L_{base}	$Z_{\text{base}}/\omega_{el \text{ base}}$	p.u.
T_{base}	$S_{\text{base}}/(p \cdot \omega_{el \text{ base}})$	p.u.
ψ_{base}	$U_{\text{base}}/\omega_{el \text{ base}}$	p.u.

B. Saliency ratio variation effects to maximum performance

Higher saliency ratio by large margin improves SyRM (Fig. 14) and ferrite PMASR (Fig. 15) performance in FW range. NdFeB PMASR (Fig. 16) has satisfactory performance trough whole FW range. Table IV summarizes the performance at $n = 1, 5$.

Fig. 14: Performance curves of SyRM for $\xi = 4 - 10$ Fig. 15: Performance curves of ferrite PMASR for $\xi = 4 - 10$ Fig. 16: Performance curves of NdFeB PMASR for $\xi = 4 - 10$ TABLE IV. Comparison of peak performance values of SyRM, ferrite and NdFeB PMASR at $n = 1, 5$ and $\xi = 4 - 10$.

ξ	n	T_{SyRM}	T_{Fe}	T_{NdFeB}	P_{SyRM}	P_{Fe}	P_{NdFeB}
4	1,5	0,40	0,46	0,55	0,60	0,70	0,83
6	1,5	0,47	0,52	0,60	0,71	0,79	0,90
8	1,5	0,50	0,55	0,62	0,75	0,83	0,93
10	1,5	0,52	0,57	0,63	0,78	0,86	0,95

V. CONCLUSION

The paper has covered the SyRM and PMASR theory, design aspects, and prospective commercial applications. Special attention has been addressed to differentiate reluctance and alignment torque component dominant families, and to list all PM machine theory equations and principles in one paper.

In comparison to the alignment torque component dominant machine family, reluctance machines have a large number of rotor parameters, which increases the duration of the electromagnetic design process and create issues for rotor mechanical analysis. Nevertheless, when properly designed, reluctance machines can be robust and contain no rare earth PM material, making them attractive from the cost point of view.

Replacing high-performance IPMs with rare-earth-free machines poses difficult challenges above all in terms of power density. A number of drawbacks, such as the demagnetization risk of the ferrite magnets at low temperatures, and reduced rotor mechanical strength, should be taken into account for the successful introduction of the technology.

Considering all available information, reluctance machine technology seems promising. However, each particular application has to be analyzed to find out which design variant (SyRM or PMASR, etc.) should be used.

VI. ACKNOWLEDGMENT

This work was partially supported by the Croatian Science Foundation under the project IP-2018-01-5822 - HYDREL.

APPENDIX A

SUMMARY OF FIGURES AND EQUATIONS TO DIFFERENTIATE RELUCTANCE AND ALIGNMENT TORQUE COMPONENT DOMINANT FAMILIES

A detailed review of the literature has confirmed that reluctance and alignment torque component machine families are still not strictly separated in the scientific community. Depending on the author, different dq reference frame approaches can be used, leading to PMASRs being described with IPM equations. This is mathematically correct, but differs from dq frame convention described in section II-A. This appendix summarizes the approaches used for different machine families. Equations valid for both families are listed in (12-14), while current and voltage constraint, constant torque hyperbolas, torque and saliency ratio equations are listed in Fig. 17.

$$\underbrace{\begin{bmatrix} u_d \\ u_q \end{bmatrix}}_{\mathbf{u}_s} = R_s \underbrace{\begin{bmatrix} i_d \\ i_q \end{bmatrix}}_{\mathbf{i}_s} + \omega_e \begin{bmatrix} 0 & -1 \\ 1 & 0 \end{bmatrix} \underbrace{\begin{bmatrix} \psi_d \\ \psi_q \end{bmatrix}}_{\boldsymbol{\psi}_s} + \underbrace{\begin{bmatrix} \dot{\psi}_d \\ \dot{\psi}_q \end{bmatrix}}_{\dot{\boldsymbol{\psi}}_s} \quad (12)$$

$$|\mathbf{u}_s|^2 = u_d^2 + u_q^2 \quad (13)$$

$$\left(\frac{|\mathbf{u}_s|}{\omega_e}\right)^2 = \psi_d^2 + \psi_q^2 \quad (14)$$

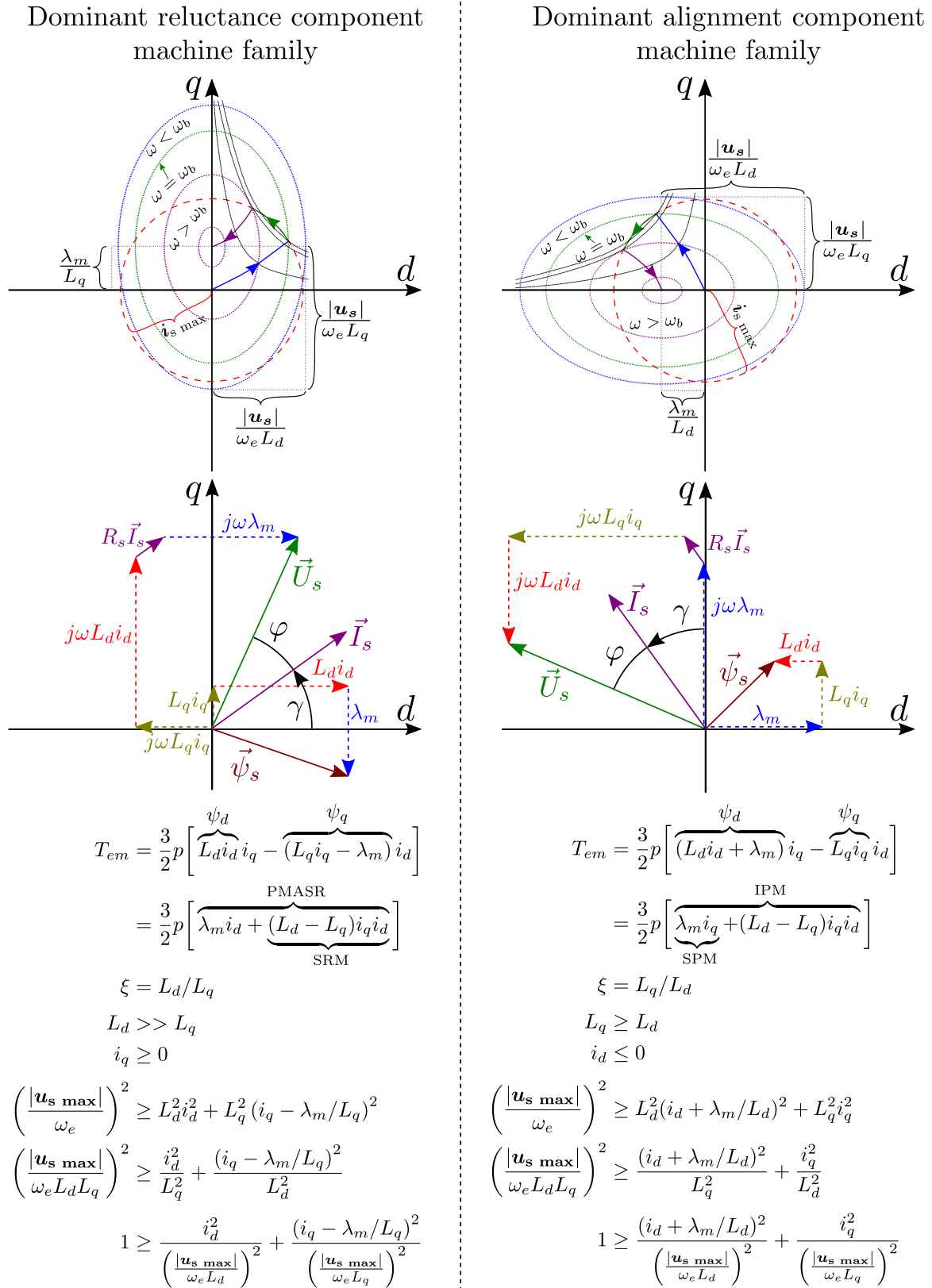


Fig. 17: Voltage and current constrains, voltage vector diagrams and equations for dominant reluctance torque component family (left) and dominant alignment torque component family (right).

REFERENCES

- [1] European Environment Agency, "Electric Vehicles in Europe," p. 60, 2016. [Online]. Available: <https://www.eea.europa.eu/publications/electric-vehicles-in-europe>
- [2] M. Eshani, Y. Gao, S. Gay, and A. Emadi, *Modern electric, hybrid electric and fuel cell vehicles 2nd. Edition*. CRC Press, 2010.
- [3] H. Z. De La Parra, F. Magnussen, and S. Bosga, "Challenges for electric machines and power electronics in automotive applications," *International Conference on Ecological Vehicles and Renewable Energies, (EVER'09)*, pp. 1–9, 2009.
- [4] J. S. Hsu, C. Ayers, and C. Coomer, "Report on Toyota/Prius motor design and manufacturing assessment," Tech. Rep., 2010. [Online]. Available: <https://goo.gl/fuEtvS>
- [5] A. Kabasawa and K. Takahashi, "Development of the IMA motor for the V6 hybrid midsize sedan," *SAE transactions*, vol. 2005, no. 724, p. 8, 2005.
- [6] K. Bourzac, "The Rare-Earth Crisis," 2011. [Online]. Available: <https://www.technologyreview.com/s/423730/the-rare-earth-crisis/>
- [7] J. Rowlatt, "Rare earths: Neither rare, nor earths," 2014. [Online]. Available: <http://www.bbc.com/news/magazine-26687605>
- [8] U. Department of Energy, "Annual Progress Report Electric Drive Technologies Program," Tech. Rep. July, 2011.
- [9] J. R. Riba, C. López-Torres, L. Romeral, and A. Garcia, "Rare-earth-free propulsion motors for electric vehicles: A technology review," *Renewable and Sustainable Energy Reviews*, vol. 57, pp. 367–379, 2016.
- [10] S. Estenlund, M. Alaküla, and A. Reinap, "PM-less machine topologies for EV traction: A literature review," *2016 International Conference on Electrical Systems for Aircraft, Railway, Ship Propulsion and Road Vehicles and International Transportation Electrification Conference, ESARS-ITEC 2016*, 2016.
- [11] G. Pellegrino, T. M. Jahns, N. Bianchi, W. L. Soong, and F. Cupertino, *The Rediscovery of Synchronous Reluctance and Ferrite Permanent Magnet Motors Tutorial Course Notes*. Springer, 2016.
- [12] P. Duck, J. Jurgens, and B. Ponick, "Calculation of Synchronous Reluctance Machines Used as Traction Drives," *2015 IEEE Vehicle Power and Propulsion Conference, VPPC 2015 - Proceedings*, pp. 0–4, 2015.
- [13] J. K. Kostko, "Polyphase reaction synchronous motors," *Journal of the American Institute of Electrical Engineers*, vol. 42, no. 11, pp. 1162–1168, 1923.
- [14] A. Fratta and A. Vagati, "A Reluctance Motor Drive for High Dynamic Performance Applications," *IEEE Transactions on Industry Applications*, vol. 28, no. 4, pp. 873–879, 1992.
- [15] D. Staton, T. Miller, and S. Wood, "Maximising the saliency ratio of the synchronous reluctance motor," *IEE Proceedings B Electric Power Applications*, vol. 140, no. 4, pp. 249–259, 1993.
- [16] D. Žarko, "Modern electric machine design methods course materials: "Design of PMSM series motor"," 2014.
- [17] M. Obata, S. Morimoto, M. Sanada, and Y. Inoue, "Performance of PMASynRM with ferrite magnets for EV/HEV applications considering productivity," *IEEE Transactions on Industry Applications*, vol. 50, no. 4, pp. 2427–2435, 2014.
- [18] G. Pellegrino, "Permanent Magnet Machine Design and Analysis with a Focus to Flux-switching PM and PM-assisted Synchronous Reluctance Machines Part II: PM-assisted Synch Rel Machines," *ICEM*, 2016.
- [19] T. Jahns, "Getting Rare-Earth Magnets Out of EV Traction Machines: A review of the many approaches being pursued to minimize or eliminate rare-earth magnets from future EV drivetrains," *IEEE Electrification Magazine*, vol. 5, no. 1, pp. 6–18, 2017.
- [20] S. S. Reddy Bonthu, A. Arafat, and S. Choi, "Comparisons of Rare-Earth and Rare-Earth-Free External Rotor Permanent Magnet Assisted Synchronous Reluctance Motors," *IEEE Transactions on Industrial Electronics*, vol. 64, no. 12, pp. 9729–9738, 2017.
- [21] K. Kondo, S. Kusase, T. Maekawa, and K. Hanada, "A new PM-assisted synchronous reluctance motor with three-dimensional trench air gap," *IEEE Transactions on Industry Applications*, vol. 50, no. 4, pp. 2485–2492, 2014.
- [22] C. T. Liu, H. Y. Chung, and S. Y. Lin, "On the Electromagnetic Steel Selections and Performance Impact Assessments of Synchronous Reluctance Motors," *IEEE Transactions on Industry Applications*, vol. 53, no. 3, pp. 2569–2577, 2017.
- [23] T. Lipo and T. Matsuo, "Rotor Design Optimization of Synchronous Reluctance Machine," *IEEE Transactions on Energy Conversion*, vol. 9, no. 2, pp. 359–365, 1994.
- [24] P. B. Reddy, A. M. El-Refai, S. Galioto, and J. P. Alexander, "Design of Synchronous Reluctance Motor Utilizing Dual-Phase Material for Traction Applications," *IEEE Transactions on Industry Applications*, vol. 53, no. 3, pp. 1948–1957, 2017.
- [25] A. El-Refai, T. Raminoso, P. Reddy, S. Galioto, D. Pan, K. Grace, J. Alexander, and K. K. Huh, "Comparison of traction motors that reduce or eliminate rare-earth materials," *IET Electrical Systems in Transportation Research*, vol. 7, no. 3, pp. 207–214, 2016.
- [26] M. N. Ibrahim, P. Sergeant, and E. M. Rashad, "Synchronous Reluctance Motor Performance Based on Different Electrical Steel Grades," *IEEE Transactions on Magnetics*, vol. 51, no. 11, pp. 1–4, 2015.
- [27] W. L. Soong and T. J. E. Miller, "Field-weakening performance of brushless synchronous AC motor drives," *IEEE Elec. Power Appl.*, pp. 331–340, 1994.
- [28] T. Fukami, M. Momiyama, K. Shima, R. Hanaoka, and S. Takata, "Steady-State Analysis of a Dual-Winding Reluctance Generator With a Multiple-Barrier Rotor," *IEEE Transactions on Energy Conversion*, vol. 23, no. 2, pp. 492–498, 2008.
- [29] I. Marongiu and A. Vagati, "Improved modelling of a distributed anisotropy synchronous reluctance machine," *IEEE Industry Applications Society Annual Meeting*, pp. 239–243, 1991.
- [30] A. Vagati, "The synchronous reluctance solution: a new alternative in AC drives," *Proceedings of IECON'94 - 20th Annual Conference of IEEE Industrial Electronics*, vol. 1, pp. 1–13, 1994.
- [31] W. L. Soong, D. A. Staton, and T. J. E. Miller, "Design of a New Axially-laminated Interior Permanent Magnet Motor," *IEEE Transactions on Industry Applications*, vol. 31, no. 2, pp. 358–367, 1995.
- [32] R. R. Moghaddam, F. Magnussen, and C. Sadarangani, "Synchronous Reluctance Machine (SynRM) Design," Ph.D. dissertation, KTH, 2007.
- [33] N. Bianchi and B. J. Chalmers, "Axially laminated reluctance motor: Analytical and finite-element methods for magnetic analysis," *IEEE Transactions on Magnetics*, vol. 38, no. 1 II, pp. 239–245, 2002.
- [34] I. Boldea and L. Tutelea, *Reluctance Electric Machines Design and Control*. CRC Press, 2019, vol. 91.
- [35] A. Vagati, M. Pastorelli, G. Franceschini, and S. C. Petracche, "Design of low-torque-ripple synchronous reluctance motors," *IEEE Transactions on Industry Applications*, vol. 34, no. 4, pp. 758–765, 1998.
- [36] M. J. Kamper, F. S. Van Der Merwe, and S. Williamson, "Direct Finite Element Design Optimisation of the Cageless Reluctance Synchronous Machine," *IEEE Transactions on Energy Conversion*, vol. 11, no. 3, pp. 547–553, 1996.
- [37] B. J. Chalmers and L. Musaba, "Design and field-weakening performance of a synchronous reluctance motor with axially laminated rotor," *IEEE Transactions on Industry Applications*, vol. 34, no. 5, pp. 1035–1041, 1998.
- [38] A. Vagati, M. Pastorelli, P. Guglielmi, and A. Canova, "Synchronous reluctance motor based sensorless drive for general purpose application," Politecnico di Torino, Torino, Tech. Rep., 2002.
- [39] M. Ferrari, N. Bianchi, and E. Fornasiero, "Analysis of rotor saturation in synchronous reluctance and PM-assisted reluctance motors," *IEEE Transactions on Industry Applications*, vol. 51, no. 1, pp. 169–177, 2015.
- [40] M. Barcaro, G. Meneghetti, and N. Bianchi, "Structural analysis of the interior PM rotor considering both static and fatigue loading," *IEEE Transactions on Industry Applications*, vol. 50, no. 1, pp. 253–260, 2014.
- [41] IEEE-SA Standards Board, "IEEE Standard for Rotating Electric Machinery for Rail and Road Vehicles," IEEE Power Engineering Society, Tech. Rep., 2000.
- [42] P. B. Reddy, K. Grace, and A. El-Refai, "Conceptual design of sleeve rotor synchronous reluctance motor for traction applications," *Proceedings - 2015 IEEE International Electric Machines and Drives Conference, IEMDC 2015*, vol. 10, pp. 195–201, 2016.
- [43] D. Žarko, "Design of Synchronous Permanent Magnet Motors Manual," Zagreb, p. 88, 2016.
- [44] S. Taghavi and P. Pillay, "A Sizing Methodology of the Synchronous Reluctance Motor for Traction Applications," *IEEE Journal of Emerging and Selected Topics in Power Electronics*, vol. 2, no. 2, pp. 329–340, 2014.
- [45] D. Stanton and M. Popescu, "Motor-CAD Manual V11," 2018.
- [46] H. C. Liu, I. G. Kim, Y. J. Oh, J. Lee, and S. C. Go, "Design of Permanent Magnet-Assisted Synchronous Reluctance Motor for Max-

- imized Back-EMF and Torque Ripple Reduction,” *IEEE Transactions on Magnetics*, vol. 53, no. 6, pp. 2015–2018, 2017.
- [47] P. Di Barba, *Multiobjective Shape Design in Electricity and Magnetism*. Springer, 2010.
- [48] F. Cupertino, G. Pellegrino, and C. Gerada, “Design of Synchronous Reluctance Machines with Multi-Objective Optimization Algorithms,” *IEEE Transactions on Industry Applications*, vol. 50, no. c, pp. 3617–3627, 2014.
- [49] S. Stipetić, “Optimization of electromagnetic design of synchronous permanent magnet motor series,” Ph.D. dissertation, Zagreb, 2014.
- [50] R. Storn and K. Price, “Differential Evolution – A Simple and Efficient Heuristic for Global Optimization over Continuous Spaces,” *Journal of Global Optimization*, vol. 11, pp. 341–359, 1997.
- [51] S. Das and P. N. Suganthan, “Differential Evolution: A Survey of the State of the Art,” *IEEE Transactions on Evolutionary Computation*, no. May 2014, pp. 1–28, 2010.
- [52] D. Zarko, D. Ban, and T. Lipo, “Design optimization of interior permanent magnet (IPM) motors with maximized torque output in the entire speed range,” *2005 European Conference on Power Electronics and Applications*, no. 1, pp. 1–10, 2005.
- [53] G. Pellegrino, F. Cupertino, and C. Gerada, “Automatic Design of Synchronous Reluctance Motors Focusing on Barrier Shape Optimization,” *IEEE Transactions on Industry Applications*, vol. 51, no. 2, pp. 1465–1474, 2015.
- [54] M. Gamba, G. Pellegrino, and F. Cupertino, “Optimal Number of Rotor Parameters for the Automatic Design of Synchronous Reluctance Machines,” *Proceedings - 2014 International Conference on Electrical Machines, ICEM 2014*, pp. 1334–1340, 2014.
- [55] ABB, “DOLSynRM Concept introduction up to IE5 efficiency,” p. 5, 2015. [Online]. Available: <https://bit.ly/2PwSuym>
- [56] REEL, “REEL SuPremE® – The IE5* magnet-free synchronous reluctance motor datasheet,” p. 36, 2019. [Online]. Available: <https://goo.gl/t2GgTW>
- [57] ABB, “IEC 60034-30-1 standard on efficiency classes for low voltage AC motors,” 2019. [Online]. Available: <https://goo.gl/qvLUzr>
- [58] Ricardo, “Ricardo develops next-generation electric vehicle motor,” 2015. [Online]. Available: <https://goo.gl/CGH8tH>
- [59] R. John, “MotorBrain summary report: Nanoelectronics for Electric Vehicle Intelligent Failsafe PowerTrain,” Tech. Rep., 2015. [Online]. Available: <http://www.motorbrain.eu/>
- [60] M. Kimiabeigi, J. D. Widmer, R. Long, Y. Gao, J. Goss, R. Martin, T. Lisle, J. M. Soler Vizan, A. Michaelides, and B. Mecrow, “High-performance low-cost electric motor for electric vehicles using ferrite magnets,” *IEEE Transactions on Industrial Electronics*, vol. 63, no. 1, pp. 113–122, 2016.
- [61] J. Merwerth, J. Halbedel, and G. Schlangen, “Electrical drive motor for a vehicle,” 2012. [Online]. Available: <https://goo.gl/WiLsMq>
- [62] I. Boldea, L. Tutelea, L. Parsa, and D. Dorrell, “Automotive electric propulsion systems with reduced or no permanent magnets: An overview,” *IEEE Transactions on Industrial Electronics*, vol. 61, no. 10, pp. 5696–5711, 2014.
- [63] S. M. De Pancorbo, G. Ugalde, J. Poza, and A. Egea, “Comparative study between induction motor and Synchronous Reluctance Motor for electrical railway traction applications,” *2015 5th International Conference on Electric Drives Production, EDPC 2015 - Proceedings*, pp. 2–6, 2015.
- [64] J. J. Germishuizen, F. S. Van Der Merwe, K. Van Der Westhuizen, and M. J. Kamper, “Performance comparison of reluctance synchronous and induction traction drives for electrical multiple units,” *IEEE Transactions on Industry Applications*, pp. 316–323, 2000.
- [65] N. Bianchi, S. Bolognani, E. Carraro, M. Castiello, and E. Fornasiero, “Electric Vehicle Traction Based on Synchronous Reluctance Motors,” *IEEE Transactions on Industry Applications*, vol. 52, no. 6, pp. 4762–4769, 2016.
- [66] VOLVO, “Power take-offs: Fields of application and Calculation guide,” 2018. [Online]. Available: [http://productinfo.vtc.volvose/files/pdf/lo/PowerTake-off\(PTO\)_Eng_08_580114.pdf](http://productinfo.vtc.volvose/files/pdf/lo/PowerTake-off(PTO)_Eng_08_580114.pdf)
- [67] —, “Volvo Trucks - Premiere for our first all-electric truck,” 2018. [Online]. Available: <https://www.youtube.com/watch?v=zAbbulKiX-o>
- [68] —, “Premiere for Volvo Trucks first all-electric truck,” 2018. [Online]. Available: <https://www.volvogroup.com/content/dam/volvo/volvo-group/markets/global/en-en/news/2018/apr/180412-volvo-all-electric-truck--en-2018-04-12-08-30-54.pdf>
- [69] —, “Body builder instructions: PTO and pumps,” 2018. [Online]. Available: <https://www.volvotrucks.ca/en-ca/parts-and-services/service/body-builder/manuals/>
- [70] W. L. Soong, “Design and Modelling of Axially-Laminated Interior Permanent Magnet Motor Drives for Field-Weakening Applications,” Ph.D. dissertation, University of Glasgow, 1993.
- [71] A. K. Adnanes, “Torque Analysis of Permanent Magnet Synchronous Motors,” *IEEE Transactions on Industry Applications*, pp. 695–701, 1991.
- [72] J. Goss, “The Design of AC Brushless Permanent Magnet Motors for Electric Vehicle Traction Applications,” Ph.D. dissertation, University of Bristol, 2015.



Branko Ban was born in Šibenik (Croatia) in 1991. He completed Bachelor (2012.) and Master (2015.) studies in Electrical Engineering at the University of Zagreb (Faculty of electrical engineering and computing) and Chalmers University of Technology. Since 2015. he is a part of the ALTEN consultancy team working in the automotive sector as electric machine specialist in areas related to design, advanced engineering, quality assurance, and root cause analysis. He is currently enrolled in the University of Zagreb PhD program covering next-generation electric machines.



Stjepan Stipetić was born in Ogulin (Croatia) in 1985. He received Dipl.Eng. and PhD degrees in electrical engineering from the University of Zagreb, Croatia, in 2008 and 2014, respectively. Currently, he is an Assistant Professor at the University of Zagreb Faculty of Electrical Engineering and Computing, Department of Electrical Machines Drives and Automation, Croatia where his research activities are related to design, modelling, analysis and optimization of electrical machines.



Mario Klanac was born in Zadar, Croatia. He received M.Sc. degree in electrical engineering from the University of Zagreb, Croatia in 2018. Currently, he is a research assistant at the University of Zagreb, Faculty of Electrical Engineering and Computing, Department of Electrical Machines, Drives and Automation, Croatia. His research interests include design, modeling, analysis and optimization of electrical machines.

Publication 2: Electric Multipurpose Vehicle Power Take-Off: Overview, Load Cycles and Actuation via Synchronous Reluctance Machine

Paper details:

B. Ban and S. Stipetić, "Electric Multipurpose Vehicle Power Take-Off: Overview, Load Cycles and Actuation via Synchronous Reluctance Machine", in International Aegean Conference on Electrical Machines and Power Electronics (ACEMP) & International Conference on Optimization of Electrical and Electronic Equipment (OPTIM), Istanbul, 27-29 August 2019.

Available at:<https://doi.org/10.1109/ACEMP-OPTIM44294.2019.9007187>

Electric Multipurpose Vehicle Power Take-Off: Overview, Load Cycles and Actuation via Synchronous Reluctance Machine

Branko Ban

Dept. of Electric Machines and Automation
FER; University of Zagreb;
Unska 3, 10000 Zagreb, Croatia
branko.ban@outlook.com

Stjepan Stipetić

Dept. of Electric Machines and Automation
FER; University of Zagreb;
Unska 3, 10000 Zagreb, Croatia
stjepan.stipetic@fer.hr

Abstract—While electric vehicle (EV) technology has been established in passenger vehicle sector, commercial multipurpose vehicle (MPV) penetration is strictly related to the niche end-markets, like medium-duty, short-haul and last mile applications. Some of the examples of short-haul applications are electric multipurpose vehicles (eMPV) like refuse, hook-loader or vacuum trucks. This paper will concentrate on eMPVs, which apart from electric traction, have to actuate additional body systems by the means of electric power take-off (ePTO).

This paper provides load cycle approximations of ePTO load cycles (refuse, concrete mixer, hook-loader and vacuum trucks). These can be used for continuous and peak requirement calculation and optimal ePTO machine sizing. Taking into consideration that the machine needs to be affordable and reliable, synchronous reluctance machine (SyRM) ePTO is proposed for future evaluation.

Keywords—electric machine; traction; synchronous reluctance; optimization; comparison; refuse truck; concrete mixer; vacuum truck; hook-loader truck; design; power take-off; commercial; multipurpose; electric; vehicle; rare-earth free; neodymium.

TABLE I. Abbreviation list

Abbreviation:	Description:
ePTO	Electric power take-off
EV	Electric Vehicle
ICE	Internal combustion engine
IPM	Interior permanent magnet
OEM	Original equipment manufacturer
MPV	Multipurpose vehicle
eMPV	Electric multipurpose vehicle
PTO	Power take off
SyRM	Synchronous reluctance machine

I. INTRODUCTION

In order to reduce emissions, air pollution, resource waste, and traffic noise, government legislation is pushing towards the

increase of electric vehicle (EV) production [1]. In addition to legal requirements, shippers and consumers demand cleaner and safer vehicles. This has caused a tectonic change in the automotive industry, both knowledge, and production wise, forcing the industry into a quick development curve. Additionally, the increasing number of start-ups is likely to upset the economics for the traditional original equipment manufacturers (OEM) and suppliers.

Passenger vehicles like Tesla and BMW are well ahead in technology development, which can be used in commercial vehicle industry as leverage (particularly in battery segment) to penetrate niche end-markets like medium-duty, short-haul and last mile applications. Long-haul applications are likely to take more time and be more sensitive to economics.

Short-haul and last mile applications seem to be best suited for immediate EV adoption, with large fleets such as Amazon, UPS and FedEx already making sizable orders for local EV delivery vehicles. Furthermore, the purchasing decisions on these smaller multipurpose vehicles (MPV) face fewer uncertainties than in the case of larger heavy-duty vehicles.

Some of the examples of short-haul applications are electric multipurpose vehicles (eMPV) like refuse, hook-loader or vacuum trucks. This paper concentrates on eMPVs, which apart from electric traction, have to actuate additional body systems (usually powered by some sort of hydraulic pump). Traditionally, this actuation is done via diesel engine or gearbox mounted output shaft, referred as power take-off (PTO). In case of electric trucks, to reduce space claim, weight, and price, the additional electric machine (ePTO) can be the interface to the hydraulic pump shaft. Due to the hydraulic pump and diesel engine operational characteristics, PTO operation is limited to narrow speed range with high torque.

When switching to eMPV, diesel engine does not exist, which creates a big challenge for single size ePTO design. Additionally, hydraulic system load characteristics vary between the applications. This paper will concentrate on providing comprehensive background in eMPV applications including PTO performance requirements and load cycles.

II. PTO PERFORMANCE AND REQUIREMENTS

A. General PTO facts

To power the special equipment (cranes, refuse systems, refrigerators, etc.), the MPV must be fitted with an extra means of a power supply, a power take-off (PTO). One or more PTOs transfer power from the engine to drive attachments or load handling equipment. The PTO provides a mechanical link (output shaft) towards load (usually some sort of hydraulic system) with most of the systems having power demand < 90 kW [2]. Historically, the PTO output shaft has been a part of the combustion engine or transmission (Fig. 1a-d). With recent MPV electrification trends [3], [4], PTO will most likely be an extra electric machine mounted on the vehicle chassis (Fig. 1e-h). The ePTO machine will be powered via inverter attached to the traction battery.

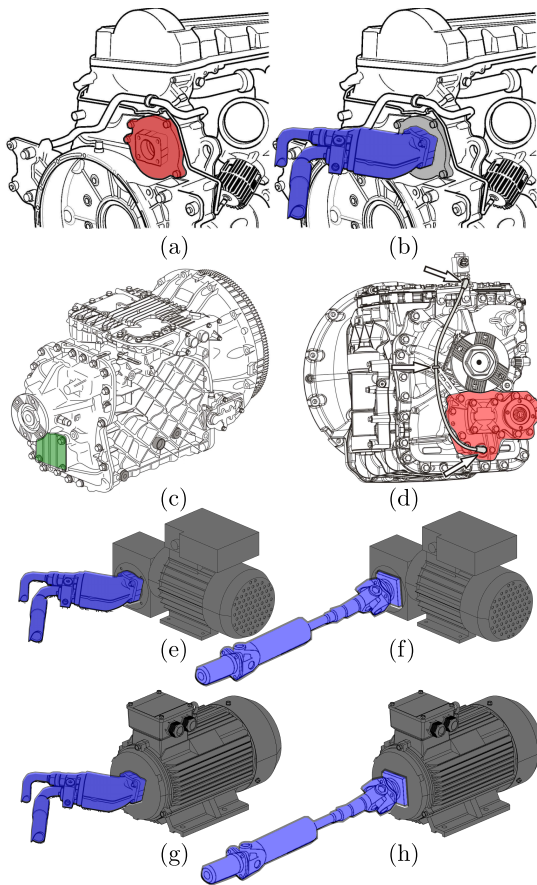


Fig. 1: a) Diesel engine rear PTO mount; b) diesel engine with mounted hydraulic pump; c) Transmission with direct PTO mount; d) transmission with geared PTO [5]; geared ePTO propelling hydraulic pump e) and universal joint shaft f); direct ePTO propelling hydraulic pump g) and universal joint shaft h).

B. Hydraulic pumps

In the applications covered by this paper, the PTO actuates a hydraulic pump (the most common type of PTO attachment). This enables the transmission of mechanical force through the hydraulic system, to any location around the vehicle.

Depending on the application, the hydraulic flow can be finally transformed to linear motion via the piston (e.g. refuse compression), or to torque via a hydraulic motor (e.g. concrete mixer drum rotation) [6].

The main parameters for the pump selection are the required system flow Q_{pump} in l/min and pressure p_{pump} in bars. Pump shaft speed n_{pump} depends on the PTO output speed, which varies depending on the ICE or gearbox gear ratio. For the applications listed in figure 3, PTO output speed can be defined by the referent speed range described by (1) [7].

$$n_{\text{PTO}} \in [1500, 3000] \text{ rpm} \quad (1)$$

Furthermore, the pump type is system related. The most common types are bent axis piston pump 2a), and variable displacement pump 2b). Bent axis piston pump has fixed displacement, meaning that output flow is proportional to the shaft revolution (more flow requires higher shaft speed). These pumps are considered simple and robust, but the disadvantage is a higher level of vibrations in comparison to other alternatives [8]. Variable displacement pumps, as their name indicates, have variable displacement, regulated via special pressure valve, which changes the angle of the piston swash plate. This feature enables more freedom in output flow regulation at different pump shaft speeds. The disadvantage is increased pump weight and system complexity (due to external pressure sensor) [8].

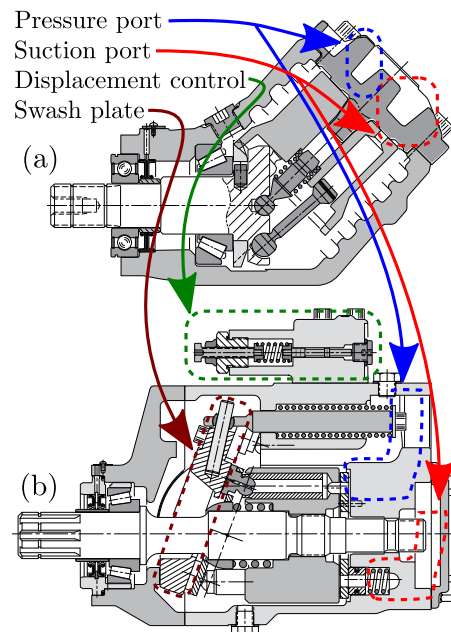


Fig. 2: Example cross-section of truck hydraulic pumps: a) fixed displacement bent axis pump and b) variable displacement pump [8].

C. ICE powered MPV and eMPV PTO requirements

The commercial success of eMPV will depend on the operational range and adaptation to different special body systems. In theory, these systems should have the same functionality

as an internal combustion engine (ICE) powered PTO. This assumes the same hydraulic pump size and operational speed range as in (1). Reference [2] provides PTO power range tables for different MPVs. With the assumption of pump speed range (1), and data from [2], peak torque versus power operational areas are calculated in Fig. 3.

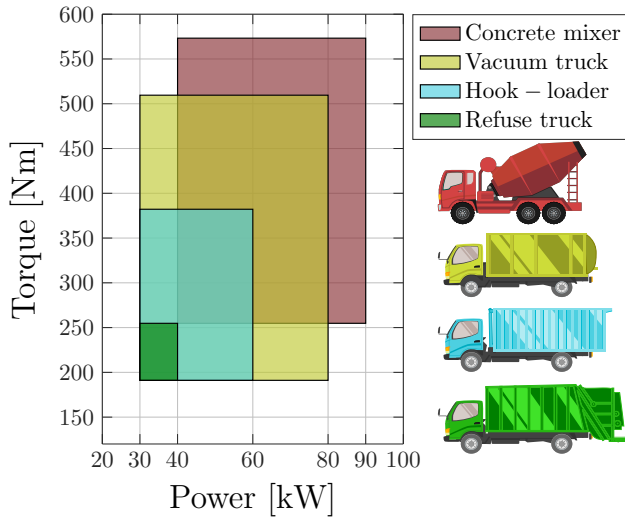


Fig. 3: Torque and power operational areas of some eMPVs.

The most critical MPV types for PTO sizing are: concrete mixer, vacuum truck, hook-loader and refuse truck. Fig. 3 shows that PTO performance requirements are approx. 30-90 kW and 190-570 Nm.

III. PTO LOAD CYCLE FOR DIFFERENT EMPV

A. Refuse truck



Fig. 4: Refuse truck example [9]

Refuse collection applications have a high degree of utilization and are equipped with complex hydraulic circuits. This makes big demands on the reliability of the PTO and requires quiet operation in urban areas [5].

The load cycle has been approximated based on the data from [7] and table II [10]. The cycle consists of three subcycles. Subcycle 1: the opening of the refuse doors and lowering of the bin mounting system, bin loading, and closing of the

refuse doors. The vehicle then drives to the next bin and the subcycle 1 is repeated. As the bins are being loaded, the refuse volume (V_{loaded}) is increasing until the truck container is full (V_{truck}). The next step is subcycle 2, in which refuse volume is compacted proportionally to the compaction factor (k_c). The compaction reduces the volume of the loaded refuse, and subcycle 1 repetition starts again. These two subcycles are repeated until no more compactations are possible. The vehicle then begins subcycle 3: driving to the landfill, dumping of the refuse and driving back for another bin collection. Refuse cycle calculation diagram is described in figure 5, subcycle illustrations and real-time cycle are shown in figure 10a.

TABLE II. Refuse truck parameters

Description	Variable	Value	Unit
Max. truck refuse volume	V_{truck}	40	m^3
Max. refuse bin volume	V_{bin}	2	m^3
Compaction factor	k_c	0,5	-
Number of compactations	N_c	> 0	-

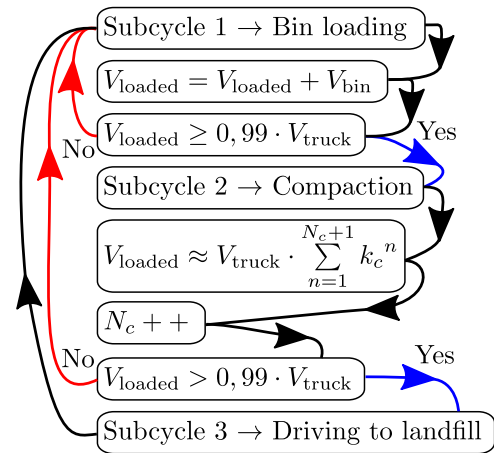


Fig. 5: Refuse cycle calculation diagram.

B. Concrete mixer



Fig. 6: Example concrete mixer truck [11]

Concrete mixers (Fig. 6) come in different sizes differentiated by the payload volume. The calculated load cycle is based on 8 m³ concrete drum volume. This is the most demanding eMPV ePTO application because concrete must be constantly mixed (even while driving), with relatively high torque demand across the PTO load cycle.

The load cycle consists of three subcycles approximated from the data available at [6], [12], [13]. Subcycle 1 describes initial concrete mixing, subcycle 2 is driving to the construction site, while subcycle 3 represents concrete unloading and driving back for another fill. Subcycle illustrations and real-time cycle are shown in figure 10b.

C. Hook-loader



Fig. 7: Hook-loader truck example [14].

Hook-loader (Fig. 7) is a type of MPV with a mounted hydraulic hook-lift hoist. This attachment enables quick swapping of flatbeds, dumpster bodies, and similar containers. Hook-loaders are mostly used for the transportation of materials in the logistic, waste, scrap and demolition industries.

The load cycle consists of two subcycles approximated from [14]. Subcycle 1 describes pushing the container off the the vehicle body, unloading via hook and driving for another container loading. Subcycle 2 represents hook positioning, loading the container and driving to the destination. Subcycle illustrations and real-time cycle are shown in figure 10c.

D. Vacuum truck



Fig. 8: Vacuum truck example [15].

Vacuum truck (Fig. 8) or tanker is a tank hauling MPV with a mounted vacuum pump. The pump is designed for pneumatic suction/unloading of liquids, sludges, slurries, or similar. The payload is transported to the treatment or disposal site (e.g. sewage treatment plant). Data used for load cycle calculation is listed in table III [16].

TABLE III. Vacuum pump parameters

Description	Variable	Value	Unit
Vacuum pressure	V_{vac}	96	kPa
Suction rate	Q_{vac}	40	m ³ /min
Tank volume	V_{tank}	25	m ³
Suction power	P_{vac}	64	kW

The load cycle consists of two subcycles. Subcycle 1 describes the initial tank filling and driving to the disposal site. Subcycle 2 represents tank unloading and driving to another fill site. Subcycle illustrations and real-time cycle is shown in figure 10d.

E. MPV PTO load comparison

Considering the load duration (energy usage), the concrete mixer is the most demanding application and will be setting the continuous (crucial variable for thermal design) and peak ePTO performance requirements. Refuse truck load duration comes second with a distinctive dynamic profile caused by frequent refuse bin loading. This will cause mechanical stress to ePTO bearings, leading to the conclusion that this cycle should be used for rotor cross-section fatigue analysis. Hook-loader and vacuum truck dynamics and load duration are much shorter and do not affect the setting of peak and continuous performance requirements.

IV. EPTO MACHINE SIZING CONSIDERATIONS

A. Peak torque envelope

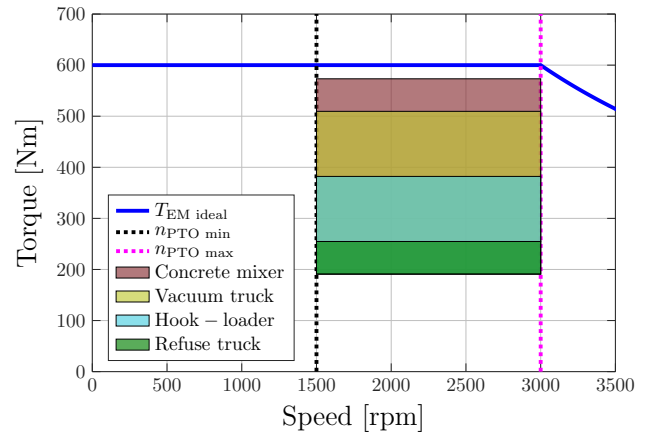


Fig. 9: Torque-speed diagram of PTO operation area for different eMPV and ideal ePTO peak torque envelope (blue line).

Fig. 9 illustrates MPV PTO operational areas in a form of torque-speed graph. The blue line represents the ideal peak torque envelope of ePTO machine.

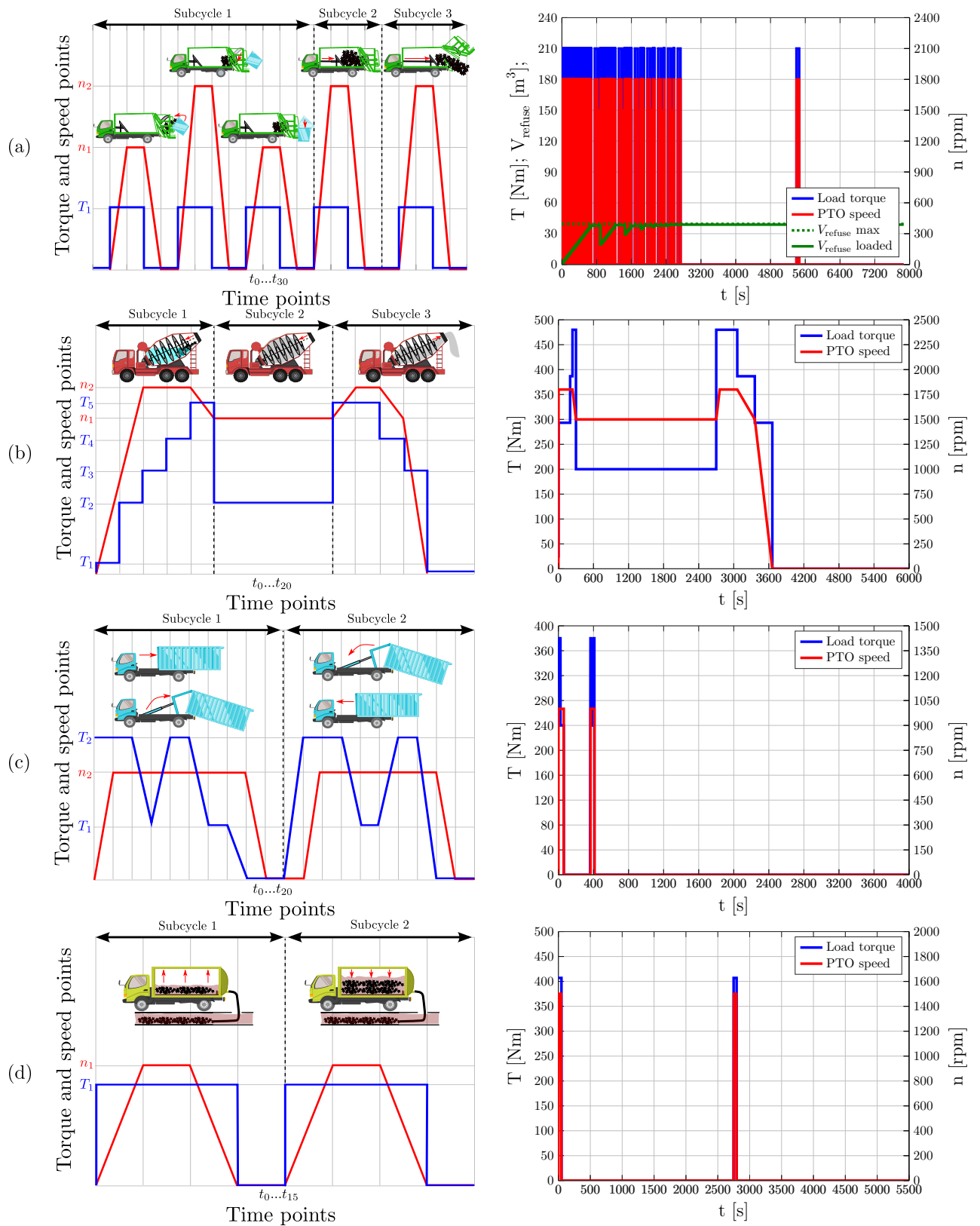


Fig. 10: Illustration of load subcycles (left), and corresponding real-time plots (right) for: a) Refuse truck; b) Concrete mixer; c) Hook-loader truck; d) Vacuum truck.

TABLE IV. eMPV ePTO load cycles

	Refuse truck*			Concrete mixer			Vacuum truck			Hook-loader		
	t [s]	T [Nm]	n [rpm]	t [s]	T [Nm]	n [rpm]	t [s]	T [Nm]	n [rpm]	t [s]	T [Nm]	n [rpm]
t_0	0,0	210,0	0,0	0,0	25,0	0,0	0,0	407,0	0,0	0,0	380,0	0,0
t_1	1,0	210,0	1500,0	1,0	25,0	450,0	5,0	407,0	1500,0	0,5	380,0	1000,0
t_2	3,0	210,0	1500,0	1,5	200,0	900,0	5,5	407,0	1500,0	2,0	380,0	1000,0
t_3	3,5	0,0	1500,0	2,0	200,0	1800,0	42,5	407,0	1500,0	20,0	240,0	1000,0
t_4	4,5	0,0	0,0	2,5	293,3	1800,0	43,0	407,0	1500,0	21,0	380,0	1000,0
t_5	6,5	0,0	0,0	200,0	293,3	1800,0	47,5	407,0	0,0	23,0	380,0	1000,0
t_6	7,0	210,0	0,0	200,5	386,7	1800,0	48,0	0,0	0,0	24,0	240,0	1000,0
t_7	8,0	210,0	1800,0	240,0	386,7	1800,0	2747,5	0,0	0,0	60,0	240,0	1000,0
t_8	12,0	210,0	1800,0	240,5	480,0	1800,0	2748,0	407,0	0,0	61,0	0,0	1000,0
t_9	12,5	0,0	1800,0	300,0	480,0	1500,0	2752,5	407,0	1500,0	61,5	0,0	0,0
t_{10}	13,5	0,0	0,0	300,5	200,0	1500,0	2753,0	407,0	1500,0	361,5	0,0	0,0
t_{11}	15,5	0,0	0,0	2700,0	200,0	1500,0	2790,0	407,0	1500,0	365,5	380,0	0,0
t_{12}	16,0	210,0	0,0	2700,5	480,0	1500,0	2790,5	407,0	1500,0	366,0	380,0	1000,0
t_{13}	17,0	210,0	1500,0	2760,0	480,0	1800,0	2795,0	407,0	0,0	371,0	380,0	1000,0
t_{14}	19,0	210,0	1500,0	3060,0	480,0	1800,0	2795,5	0,0	0,0	375,0	240,0	1000,0
t_{15}	19,5	0,0	1500,0	3060,5	386,7	1800,0	5495,0	0,0	0,0	400,0	240,0	1000,0
t_{16}	20,5	0,0	0,0	3360,0	386,7	1500,0	-	-	-	401,0	380,0	1000,0
t_{17}	80,5	0,0	0,0	3360,5	293,3	1500,0	-	-	-	410,0	380,0	1000,0
t_{18}	81,0	210,0	0,0	3660,0	293,3	0,0	-	-	-	410,5	0,0	1000,0
t_{19}	83,0	210,0	1800,0	3660,5	0,0	0,0	-	-	-	411,0	0,0	0,0
t_{20}	143,0	210,0	1800,0	6060,0	0,0	0,0	-	-	-	4011,0	0,0	0,0
t_{21}	143,5	0,0	1800,0	-	-	-	-	-	-	-	-	-
t_{22}	145,5	0,0	0,0	-	-	-	-	-	-	-	-	-
t_{23}	205,5	0,0	0,0	-	-	-	-	-	-	-	-	-
t_{24}	2605,5	0,0	0,0	-	-	-	-	-	-	-	-	-
t_{25}	2606,0	210,0	0,0	-	-	-	-	-	-	-	-	-
t_{26}	2608,0	210,0	1800,0	-	-	-	-	-	-	-	-	-
t_{27}	2668,0	210,0	1800,0	-	-	-	-	-	-	-	-	-
t_{28}	2668,5	0,0	1800,0	-	-	-	-	-	-	-	-	-
t_{29}	2670,5	0,0	0,0	-	-	-	-	-	-	-	-	-
t_{30}	5070,5	0,0	0,0	-	-	-	-	-	-	-	-	-

*Refuse truck load points are valid only for illustrated subcycle in Fig. 10a) (left), real time load can be calculated following the Fig. 5 diagram.

B. SyRM as a potential ePTO

Currently, due to the inherently high torque and power density, interior rare earth permanent magnet synchronous machines (IPM) are predominantly used for automotive traction. Although the performance benefits are undisputed, the use of rare earth permanent magnet (PM) materials, such as neodymium or dysprosium, has raised concerns in a number of areas. In 2011 and 2012, China reportedly threatened to cut off international supplies of these materials [17], leading to dramatic, though short-term, increase in the material price, increasing as much as 3000% in case of dysprosium [18]. These volatilities have forced the automotive industry to search for the alternative electric machine design, which will either

use none or minimal amount of rare earth material.

The alternatives which have not been in recent industry focus are synchronous reluctance machines (SyRM), and its derivatives [19]. These solutions rely on high reluctance torque, thus theoretically needing no PM material in the rotor structure. They have relatively low material costs, low rotor losses and are considered as robust [20], [21]. On the other hand, lack of the permanent magnetic field in the rotor is penalized with lower torque density, lower power factor, and higher torque ripple [22], [23].

SyRM is considered to be a direct competitor of induction machines which are often used in railway and ship propulsion. This has been confirmed by [24], concluding that both IM

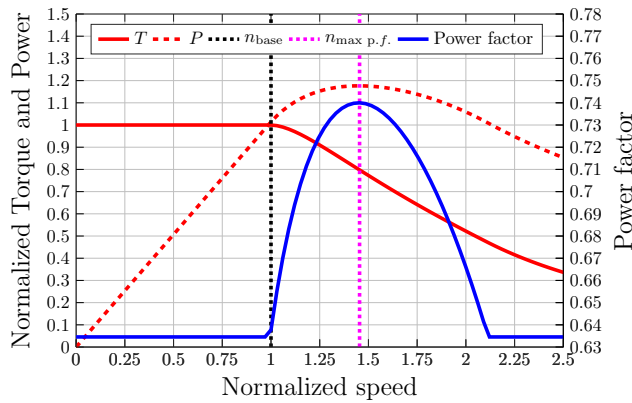


Fig. 11: Example normalized SyRM performance and power factor.

and SyRM have similar electric, magnetic, and thermal performance, with SyRM having lower rotor losses. Germishuizen et al. emphasize that SyRM compared to IM have lower stator winding temperature rise, which allows an increase of the power rating by 5 - 10% [25].

Considering price, overload capability and production simplicity, SyRM can be a viable ePTO solution. Fig. 11 illustrates the normalized performance and power factor achievable by 4 pole, inverter regulated SyRM. It is important to note that the power factor is quite low below the base speed. To increase inverter utilization and increase peak power, ePTO machine should be designed for operation in the area between base speed n_{base} and maximum power factor speed $n_{max\ p.f.}$. The following chapter will assume that SyRM ePTO $n_{base} = n_{PTO\ min} = 1500\ rpm$ and $n_{max\ p.f.} = n_{PTO\ max} = 3000\ rpm$.

C. Direct or geared ePTO machine considerations and future work

Figure (Fig. 12, 13, blue) indicates the ideal ePTO output torque should be 600 Nm. This requirement can be achieved in two ways.

The first approach is high torque (and low speed) machine which does not require a gearbox and can be more easily packaged (Fig. 1g-h). The disadvantage is increased machine volume and weight.

The second approach is a high speed (and low torque) machine with integrated gearbox (Fig. 1e-f). The benefits of this approach are minimized machine volume and weight and increased rotational inertia (traditionally, ICE PTO operates in speed control mode with one or two fixed reference speeds, high rotational inertia comes from ICE crankshaft). The disadvantages are increased system complexity and more complicated packaging. To cover both approaches, two SyRM variants will be investigated in future work.

High torque (low speed) variant performance is illustrated in Fig. 12. It is important to note that output base speed is lower than ideal requirement (Fig. 12, blue). This compromise will maximize SyRM power factor and output power in n_{PTO} (1) speed range. The disadvantage is limitation in pump selection

options, mainly in concrete mixer application. It must be noted that even with this performance adjustment, ePTO can successfully complete concrete mixer cycle.

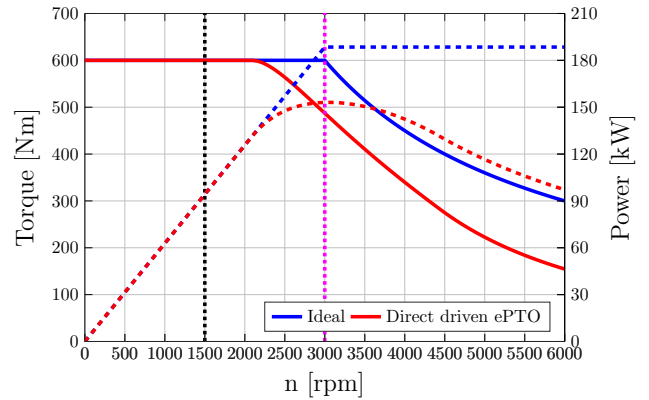


Fig. 12: Ideal (blue) and directly driven ePTO performance.

High speed (low torque) variant (Fig. 13, green), will be coupled to reduction gearbox with transfer ratio $i = 2$, leading to output performance profile (Fig. 13, red). Gear ratio has been selected so that the geared ePTO (Fig. 13, red) has the same output performance as the direct ePTO (Fig. 12, red).

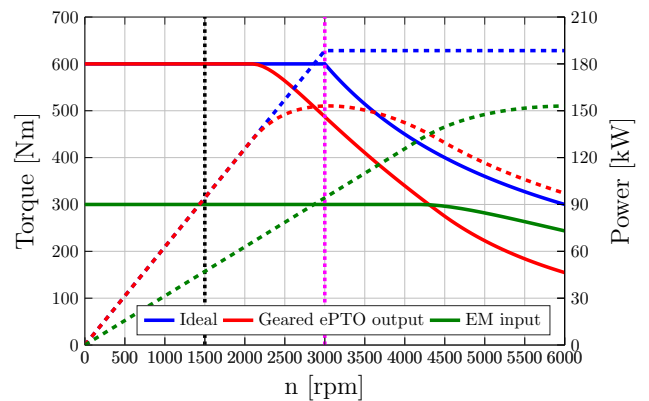


Fig. 13: Ideal performance (blue), input performance before gearbox (green), and ePTO output performance including gearbox (red).

V. CONCLUSION

This paper has covered PTO theory, applications, and recent MPV industry status with emphasis on eMPV e-PTO.

Special attention has been addressed to PTO load cycle definition and calculation. As a next step, this data will be used for the calculation of continuous and peak performance requirements as inputs for optimal ePTO machine design.

Considering robustness, price and reliability, a synchronous reluctance machine (SyRM) has been selected as target ePTO technology. Future work will concentrate on the validation of two concepts, directly driven, or gearbox integrated SyRM design.

REFERENCES

[1] European Environment Agency, "Electric Vehicles in Europe," p. 60, 2016. [Online]. Available: <https://www.eea.europa.eu/publications/electric-vehicles-in-europe>

[2] VOLVO, "Power take-offs: Fields of application and Calculation guide," 2018. [Online]. Available: [http://productinfo.vtc.volvose/files/pdf/lo/PowerTake-off\(PTO\)_Eng_08_580114.pdf](http://productinfo.vtc.volvose/files/pdf/lo/PowerTake-off(PTO)_Eng_08_580114.pdf)

[3] —, "Volvo Trucks - Premiere for our first all-electric truck," 2018. [Online]. Available: <https://www.youtube.com/watch?v=zAbbulKiX-o>

[4] —, "Premiere for Volvo Trucks first all-electric truck," 2018. [Online]. Available: <https://www.volvogroup.com/content/dam/volvo/volvo-group/markets/global/en-en/news/2018/apr/180412-volvo-all-electric-truck--en-2018-04-12-08-30-54.pdf>

[5] —, "Body builder instructions: PTO and pumps," 2018. [Online]. Available: <https://www.volvotrucks.ca/en-ca/parts-and-services/service/body-builder/manuals/>

[6] M. H. Bae, T. Y. Bae, and D. J. Kim, "The Strength Analysis of Differential Planetary Gears of Gearbox for Concrete Mixer Truck," *IOP Conference Series: Materials Science and Engineering*, vol. 317, no. 1, pp. 0–8, 2018. [Online]. Available: <https://iopscience.iop.org/article/10.1088/1757-899X/317/1/012010/pdf>

[7] VOLVO Trucks Canada, "mDrive PTO Pump Speed Calculator - Volvo Trucks Canada," 2019. [Online]. Available: <https://bit.ly/2lhGBZ8>

[8] Parker Hannifin, "Series GPA, GP1, F1, T1, F2, F3, VP1, Fixed and Variable Displacement Pumps, Motors and Accessories," p. 80, 2019. [Online]. Available: https://www.parker.com/Literature/PMDE/Catalogs/Truck_Hydraulics/MSG30-8200_UK.pdf

[9] ShinMaywa Industries, "Refuse Compactor (Garbage Compactor Truck)." [Online]. Available: https://www.shinmaywa.co.jp/truck/english/products/refuse_compactor.html

[10] Veolia, "Veolia commercial waste containers," 2019. [Online]. Available: http://veolia.co.uk/birmingham/sites/g/files/dvc501/t/assets/documents/2014/10/Commercial_Waste_Containers.pdf

[11] Construction Equipment, "Putzmeister Redesigns Pro Series, Bridge Maxx Mixers," 2019. [Online]. Available: <https://www.constructionequipment.com/putzmeister-redesigns-pro-series-bridge-maxx-mixers>

[12] C. Ferraris, "Concrete mixing methods and concrete mixers: State of the art," *Journal of Research of the National Institute of Standards and Technology*, vol. 106, no. 2, p. 391, 2012.

[13] J. Yang, H. Zeng, T. Zhu, and Q. An, "Study on the dynamic performance of concrete mixer's mixing drum," *Mechanical Sciences*, vol. 8, no. 1, pp. 165–178, 2017.

[14] HIAB, "HIAB multilift systems," 2019. [Online]. Available: <https://www.hiab.com/>

[15] PUMPER, "8 Tips for Vacuum Truck Shoppers," 2019. [Online]. Available: https://www.pumper.com/online_exclusives/2014/09/8_tips_for_vacuum_truck_shoppers

[16] K. vacuum trucks, "Mobile Vac," 2019. [Online]. Available: <http://www.kanematsu-eng.jp/english/products/mobile-vac.html>

[17] K. Bourzac, "The Rare-Earth Crisis," 2011. [Online]. Available: <https://www.technologyreview.com/s/423730/the-rare-earth-crisis/>

[18] J. Rowlatt, "Rare earths: Neither rare, nor earths," 2014. [Online]. Available: <http://www.bbc.com/news/magazine-26687605>

[19] U. Department of Energy, "Annual Progress Report Electric Drive Technologies Program," Tech. Rep. July, 2011.

[20] J. R. Riba, C. López-Torres, L. Romeral, and A. Garcia, "Rare-earth-free propulsion motors for electric vehicles: A technology review," *Renewable and Sustainable Energy Reviews*, vol. 57, pp. 367–379, 2016.

[21] S. Estenlund, M. Alaküla, and A. Reinap, "PM-less machine topologies for EV traction: A literature review," *2016 International Conference on Electrical Systems for Aircraft, Railway, Ship Propulsion and Road Vehicles and International Transportation Electrification Conference, ESARS-ITEC 2016*, 2016.

[22] G. Pellegrino, T. M. Jahns, N. Bianchi, W. L. Soong, and F. Cupertino, *The Rediscovery of Synchronous Reluctance and Ferrite Permanent Magnet Motors Tutorial Course Notes*. Springer, 2016.

[23] P. Duck, J. Jurgens, and B. Ponick, "Calculation of Synchronous Reluctance Machines Used as Traction Drives," *2015 IEEE Vehicle Power and Propulsion Conference, VPPC 2015 - Proceedings*, pp. 0–4, 2015.

[24] S. M. De Pancorbo, G. Ugalde, J. Poza, and A. Egea, "Comparative study between induction motor and Synchronous Reluctance Motor for electrical railway traction applications," *2015 5th International Conference on Electric Drives Production, EDPC 2015 - Proceedings*, pp. 2–6, 2015.

[25] J. J. Germishuizen, F. S. Van Der Merwe, K. Van Der Westhuizen, and M. J. Kamper, "Performance comparison of reluctance synchronous and induction traction drives for electrical multiple units," *IEEE Transactions on Industry Applications*, pp. 316–323, 2000.



Branko Ban was born in Šibenik (Croatia) in 1991. He completed Bachelor (2012.) and Master (2015.) studies in Electrical Engineering at the University of Zagreb (Faculty of electrical engineering and computing) and Chalmers University of Technology. Since 2015. he is a part of the ALTEN consultancy team working in the automotive sector as electric machine specialist in areas related to design, advanced engineering, quality assurance, and root cause analysis. He is currently enrolled in the University of Zagreb PhD program covering next-generation electric machines.



Stjepan Stipetić was born in Ogulin (Croatia) in 1985. He received Dipl.Eng. and PhD degrees in electrical engineering from the University of Zagreb, Croatia, in 2008 and 2014, respectively. Currently, he is an Assistant Professor at the University of Zagreb Faculty of Electrical Engineering and Computing, Department of Electrical Machines Drives and Automation, Croatia where his research activities are related to design, modelling, analysis and optimization of electrical machines.

Publication 3: Design and optimization of Synchronous Reluctance Machine for actuation of Electric Multi-purpose Vehicle Power Take-Off

Paper details:

B. Ban and S. Stipetić, "Design and optimization of Synchronous Reluctance Machine for actuation of Electric Multi-purpose Vehicle Power Take-Off", in International Conference on Electrical Machines (ICEM), Gothenburg, 23-26 Aug. 2020.

Available at:<https://doi.org/10.1109/ICEM49940.2020.9270784>

Design and Optimization of Synchronous Reluctance Machine for actuation of Electric Multi-purpose Vehicle Power Take-Off

Branko Ban, and Stjepan Stipetić, *Senior member, IEEE*

Abstract—While electric vehicle (EV) technology has been established in passenger vehicle sector, commercial multipurpose vehicle (MPV) penetration is strictly related to the niche end-markets, like medium-duty, short-haul and last mile applications. Some of the examples of short-haul applications are electric multipurpose vehicles (eMPV) like refuse, hook-loader or vacuum trucks. eMPVs, apart from electric traction, have to actuate additional body systems by the means of electric power take-off (ePTO). Taking into consideration that the machine needs to be affordable and reliable, synchronous reluctance machine (SyRM) has been selected for ePTO actuation. This paper will present SyRM parametrization, design constraints and optimization via improved differential evolution (DE) algorithm.

Index Terms—electric machine; synchronous reluctance; optimization; comparison; differential-evolution; design; power take-off; commercial; multipurpose; electric; vehicle; rare-earth free; neodymium.

I. INTRODUCTION

A. Electric multipurpose vehicles

IN order to reduce environmental impact, government legislation is pushing towards the increase of electric vehicle (EV) production [1]. In addition to legal requirements, shippers and consumers demand cleaner and safer vehicles. This has caused a tectonic change in the automotive industry, both knowledge, and production wise, forcing the industry into a quick development curve. Additionally, the increasing number of start-ups is likely to upset the economics for the traditional original equipment manufacturers (OEM) and suppliers.

Passenger vehicle industry is currently leading the market development (Tesla, Nissan, Toyota, BMW), mainly because of lighter vehicles, which require fewer batteries for traction. On the other hand, the commercial vehicle industry is forced to penetrate niche end-markets like medium-duty, short-haul and last mile applications. Long-haul applications are likely to take more time and be more sensitive to economics.

Some of the examples of short-haul applications are electric multipurpose vehicles (eMPV) like refuse, hook-loader or vacuum trucks. eMPVs, apart from electric traction,

This work was partially supported by the Croatian Science Foundation under the project IP-2018-01-5822 - HYDREL.

Branko Ban and Stjepan Stipetić are affiliated with University of Zagreb, Faculty of electrical engineering and computing (FER), Department of Electric Machines, Drives and Automation (e-mail: branko.ban@outlook.com, stjepan.stipetic@fer.hr).

have to actuate additional body systems (usually powered by some sort of hydraulic pump). Traditionally, this actuation is done via diesel engine or gearbox mounted output shaft (Fig. 1a-d), referred to as power take-off (PTO). In case of electric trucks, to reduce space claim, weight, and price, the additional electric machine (ePTO) can be the interface to the hydraulic pump shaft (Fig. 1e-g). To conclude, the commercial success of eMPV will depend on the operational range and adaptation to different special body systems. Fig. 2 shows the most critical MPV types for PTO sizing with performance requirements range of approx. 30-90 kW and 190-570 Nm [2].

B. ePTO machine type

Currently, due to the inherently high torque and power density, interior rare earth permanent magnet synchronous machines (IPM) are predominantly used for automotive traction. Although the performance benefits are undisputed, the use of rare earth permanent magnet (PM) materials, such as neodymium or dysprosium, has historically been a commercial risk [4], [5]. Additional penalty of PM material is the risk of demagnetization at higher temperatures. This have forced the industry to search for the alternative electric machine design, which will either use none or minimal amount of rare earth material.

The alternatives which have not been in recent industry focus are synchronous reluctance machines (SyRM) [6]. These solutions rely on high reluctance torque, thus theoretically needing no PM material in the rotor structure (Fig. 3). They have relatively low material costs, higher overload capacity (no demagnetization issues), low rotor losses and are considered as robust [7]–[9]. On the other hand, lack of the permanent magnetic field in the rotor is penalized with lower torque density, lower power factor, and higher torque ripple if no skewing is applied [10], [11]. Most OEMs have strategy of reusing components when possible to increase volume which leads to price reduction. The presumption is that ePTO inverter will have the same part number as traction inverter. The obvious conclusion is that the inverter will be oversized for ePTO application which effectively eliminates low power factor issue.

Considering price, overload capability and production simplicity, SyRM can be a viable ePTO solution [12]. This

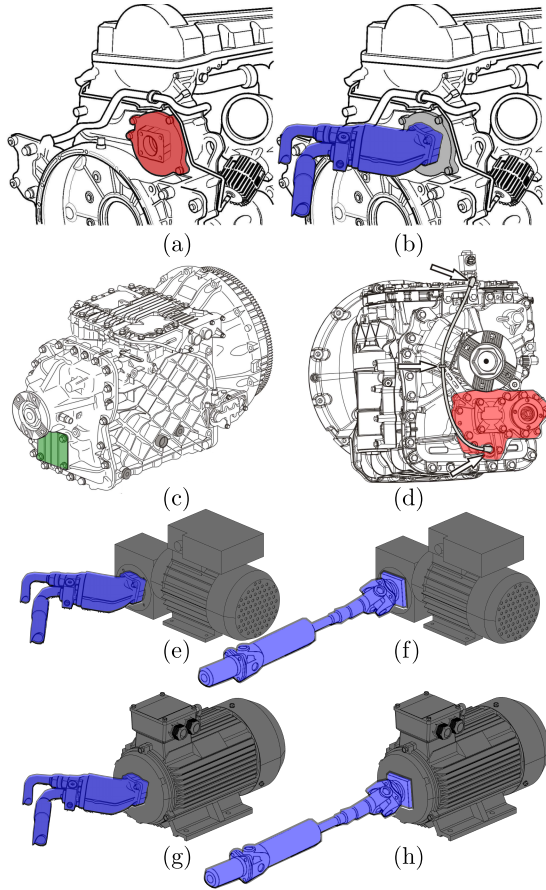


Fig. 1: a) Diesel engine rear PTO mount; b) diesel engine with mounted hydraulic pump; c) Transmission with direct PTO mount; d) transmission with geared PTO [3]; geared ePTO propelling hydraulic pump e) and universal joint shaft f); direct ePTO propelling hydraulic pump g) and universal joint shaft h).

paper will concentrate on the SyRM parametrization and optimization for eMPV ePTO applications.

II. EPTO DESIGN

A. Peak performance requirements

Reference [12] in detail describes peak ePTO torque requirements for different eMPV types. The decision has been to design direct driven high torque (and low speed) ePTO machine. Due to the hydraulic pump and diesel engine operational characteristics, PTO operation is limited to narrow speed range with high torque. To reduce machine size and adapt peak performance to tougher applications (concrete mixer), pump operating range has been limited to:

$$n_{PTO} \in [1500, 1700] \text{ rpm} \quad (1)$$

Varying PTO speed outside of the selected window with purpose of efficiency increase would be counter productive because of the increased pump noise and reduced volumetric efficiency. Peak PTO operating range can be calculated with

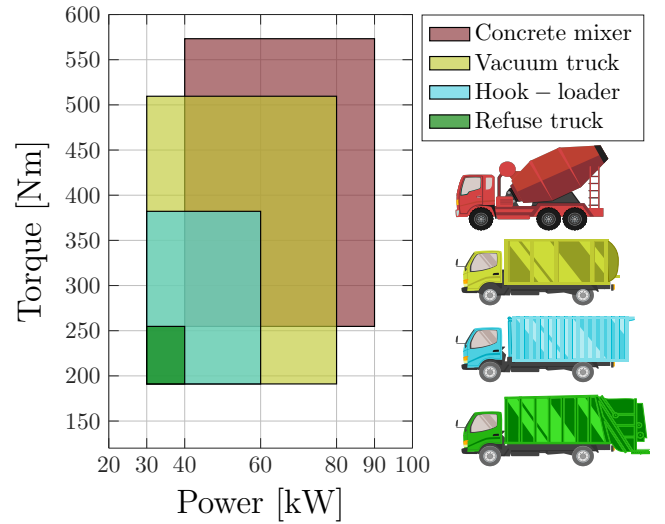


Fig. 2: Torque and power operational areas of some eMPVs [2].

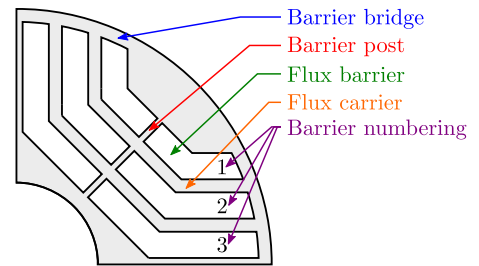


Fig. 3: SyRM rotor nomenclature

the assumption of pump speed range (1), and data listed in Fig. 2. Fig. 4 illustrates different PTO operational areas in a form of torque-speed graph. The blue line represents the ideal peak torque envelope of ePTO machine.

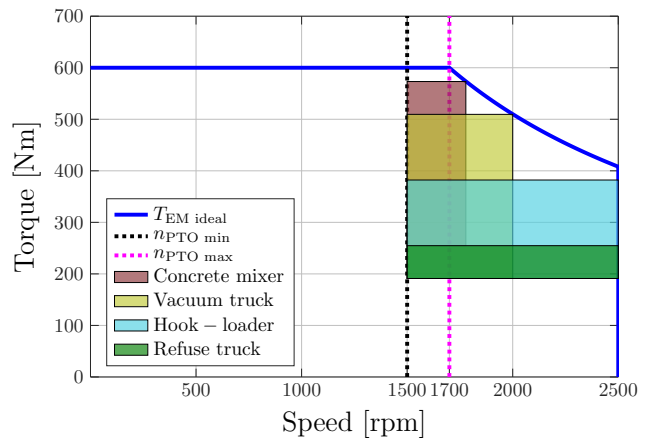


Fig. 4: Torque-speed diagram of PTO operation area for different eMPV and ideal ePTO peak torque envelope (blue line).

All peak performance requirements are listed in table I.

Peak machine torque within selected speed range has been set to $T_{\max} = 600$ Nm with required base speed $n_b = 1700$ rpm. To expand hydraulic pump selection base for lower torque applications (hook-loader, refuse truck), maximum operational speed has been set to $n_{\max} = 2500$ rpm. This automatically sets maximum (non operational) over-speed requirement to $1.2 \cdot n_{\max} = 3000$ rpm. Initial assumptions are that battery voltage is $U_{\text{DC}} = 610$ V with maximum inverter phase current $I_{s \max} = 310$ A_{rms}. Assumed current density is within $J \in [18, 20]$ A/mm² range.

TABLE I: Peak operation requirements at base speed

Description	Symbol	Value	Unit
Base speed	n_b	1700	rpm
Max. operating speed	n_{\max}	2500	rpm
Max. over speed	$1.2 \cdot n_{\max}$	3000	rpm
Max. torque	T_{\max}	600	Nm
Battery voltage	U_{DC}	610	V
Max. phase current	$I_{s \max}$	310	A _{rms}
RMS current density	J	[18, 20]	A/mm ²

B. Optimization method

Nowadays, optimization algorithms enjoy high popularity among electrical machine designers [13]–[20]. Designer’s personal experience should not be underestimated, but due to non-linearity and complexity of the relations between the geometry of electrical machines and their performance, it is commonly understood that only the mathematical optimization can push the boundaries towards better designs.

This is especially noticeable in the problem of increasing efficiency [21]–[24] due to worldwide legislation initiatives [1], [25]. In the case of traction drives, high efficiency within limited packaging space is absolute imperative [26].

According to Pellegrino [27], [28], computational load is proportional to the geometrical complexity. This is inherently the case for IPM and SyRM machines, leading to a high number of optimization variables and longer optimization time.

The utilization of the finite element method is practically unavoidable in the case of SyRM’s due to the significant influence of saturation in rotor barrier bridges and posts on machine performance. Finite element analysis (FEA) is computationally intensive and the optimization may require thousands of calculations through generations. Significant time savings can be achieved if all calculations are performed using magnetostatic simulations with fixed rotor position. Detailed explanation of various approaches to calculation of IPM machine parameters and performance using only magnetostatic simulations is available in [29].

This paper uses improved version of DE algorithm derived by Žarko et. al. [30] based on Lampinen’s constraint function approach [31]–[33].

III. OPTIMIZATION PROCEDURE DETAILS

The optimization of the 2D cross-section is set up as a multi-objective problem which is mathematically defined as:

find the vector of parameters (2), subject to D parameter boundary constraints (3) and subject to m inequality constraints functions (4), which will minimize (or maximize) n objective functions (5).

$$\vec{x} = [x_1, x_2, \dots, x_D], \quad \vec{x} \in R^D \quad (2)$$

$$x_i^{(L)} \leq x_i \leq x_i^{(U)}, \quad i = 1, \dots, D \quad (3)$$

$$g_j(\vec{x}) \leq 0, \quad j = 1, \dots, m \quad (4)$$

$$f_k(\vec{x}) \leq 0, \quad k = 1, \dots, n \quad (5)$$

The applied optimization workflow is shown in Fig. 5. The optimization process starts with problem definition (boundaries, constraints, objectives, model type) and a preset of constant model parameters (slots, poles, active diameter, etc.). FEM model solver is Motor-CAD, connected to Matlab via ActiveX link. Matlab source-code handles black, Motor-CAD blue and ActiveX interface red boxes on Fig. 5.

After entering the optimization loop, the following steps are performed iteratively:

- 1) optimization algorithm generates vector \vec{x}
- 2) variables are converted to model parameters
- 3) model generation
- 4) model solving
- 5) performance extraction
- 6) constraint and objective function calculation
- 7) constraints and objectives are passed to the optimization algorithm

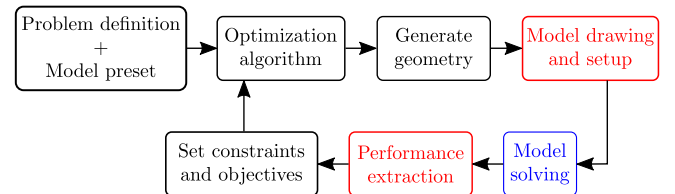


Fig. 5: Optimization workflow

A. Preset model

The number of slots and poles is selected to be 36/4 with 4 rotor flux barriers which yields two-layer integer slot winding with distributed overlapping coils. This combination has a good trade-off between inherent capability for mitigation of torque pulsations, susceptibility to noise and possibility of using multiple parallel paths. To maximize the torque output, the windings have been connected in a star configuration.

Initial design is limited with constant parameters (Table II) and peak performance at base speed (Table I). A set of parameters which are subject to optimization are listed in Table III, colors and numbering correspond to Fig. 6. Independent variables have limits in square brackets (e.g. slot corner radius can be between 1,5 and 5 mm), dependent variables (e.g. tooth width) are calculated from constants, multiplied with perunitized limits derived from sensitivity analysis [34].

All flux barriers share fillet corner radius parameter (r_f). Maximum barrier angle (ϑ_{\max}) is calculated from end carrier thickness (e_c). Discrete variable e_p specifies how many barriers will not have a center post, always starting from most outer barrier (1 \rightarrow only the first barrier, 2 \rightarrow first and second barrier, 3 \rightarrow the first, second and third barrier). The ideal number of turns (N_c) and parallel paths (a_p) for matching the base speed are automatically calculated based on winding feasibility [35] and ultra-fast scaling laws [36].

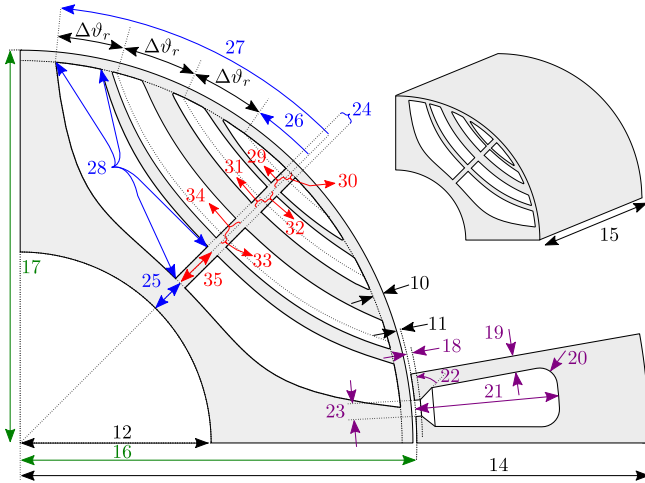


Fig. 6: List of parametrization variables

TABLE II: Constant parameters

No:	Description	Symbol	Value	Unit
1	Stator diameter	D_s	240	mm
2	Shaft diameter	D_{sh}	65	mm
3	Phase number	N_{ph}	3	-
4	No. of turns	N_c	Auto calculated	-
5	Parallel paths	a_p	Auto calculated	-
6	Coil pitch	y_c	6	-
7	Barrier number	N_{bar}	4	-
8	Pole pairs	p	2	-
9	Slot number	N_s	36	-
10	Barrier bridge	w_{bb}	0.5	mm
11	Airgap	δ	0.65	mm
12	Shaft radius	$D_{sh}/2$	32.5	mm
13	Barrier offset	$\Delta r_{4\ in}$	0	mm
14	Stator radius	$D_s/2$	120	mm
15	Max. active length	$l_{s\ max}$	450	mm

B. Handling of inequality constraints

Inequality constraints normally arise from different electromagnetic, thermal, mechanical, manufacturing, economic or standard limits such as maximum flux density in the stator tooth, maximum magnet temperature, the maximum stress in the rotor bridge, minimum dimensions of the magnet, the maximum cost of the active material, maximum noise etc. [37].

The traditional approach for handling constraint functions uses penalty functions to penalize the solutions which violate constraints. This principle is implemented in the form of

TABLE III: Complete list of optimization parameters

No:	Description	Symbol	Boundaries	Unit
16	Stator bore	D_b	$[0.54, 0.58]D_s$	mm
17	Rotor radius	$\frac{D_b - 2\delta}{2}$	Calc. from 11 and 16mm	
18	Tooth tip depth	d_t	$[0.5, 2]$	mm
19	Tooth width	w_t	$[0.3, 0.8] \left(\frac{D_b \pi}{N_s} - w_{op} \right)$	mm
20	Slot corner rad.	r_{sc}	$[1.5, 5]$	mm
21	Slot depth	d_s	$\frac{D_s - D_b}{2} [0.4, 0.7]$	mm
22	Tooth tip angle	α_t	$[27, 50]$	$^\circ$
23	Slot opening	w_{op}	$[2, 3.13]$	mm
24	Barrier post	w_p	$[0.5, 1]$	mm
25	End carrier	e_c	$\frac{D_b - 2\delta - D_{sh}}{2} [0.08, 0.3]$	mm
26	Min. angle	ϑ_{\min}	$\pi/p/2 [0.1, 0.35]$	$^\circ$
27	Max. angle	ϑ_{\max}	Calc. from 25	$^\circ$
28	Fillet radius	r_f	$[0.2, 0.5]$	mm
29	Barrier offset	$\Delta r_{1\ in}$	Variablemm	
30	Barrier offset	$\Delta r_{1\ out}$	Variablemm	
31	Barrier offset	$\Delta r_{2\ in}$	Variablemm	
32	Barrier offset	$\Delta r_{2\ out}$	Variablemm	
33	Barrier offset	$\Delta r_{3\ in}$	Variablemm	
34	Barrier offset	$\Delta r_{3\ out}$	Variablemm	
35	Barrier offset	$\Delta r_{4\ out}$	Variablemm	
36	Exclude posts	e_p	$[1\ 2\ 3]$	-

weighted sums which modify each objective function. Despite the popularity of penalty functions, they have several drawbacks. The main one is the requirement for careful fine tuning of the penalty factors responsible for efficient approach to the feasible region. In addition, this method can suffer from problems related to poor choice of the weight factors which can affect the convergence.

This paper uses an improved constraint function algorithm proposed by Žarko et. al. [38].

C. Inequality constraints

Inequality constraints for this particular case are defined in Table IV. The constraint function g_1 checks rotor structural factor of safety at maximum over-speed ($1.2 \cdot n_{\max}$).

The procedure related to constraint function g_2 contains several subfunctions designed according to ultra-fast scaling laws [36]. Multiple magnetostatic FEA calculations are conducted to find the maximum of torque vs. current phase advance curve thus determining the optimal maximum torque per ampere (MTPA) control angle through polynomial fit (initial machine has one turn and one parallel path). The machine number of turns and parallel paths is adjusted towards required base speed. Initially, the optimization assumes maximum stack length (table III, parameter $l_{s\ max}$), if calculated magnetostatic torque is larger than the limit, the machine active length is reduced. If calculated torque at $l_{s\ max}$ is less than required, the machine design does not fulfil the constraint. Finally, stator phase current is checked to be less than maximum inverter current, otherwise, the constraint is not fulfilled. After this stage, all magnetostatic computations are completed. The results are extracted and evaluated in the following constraint functions.

Constraint g_3 checks maximum stator yoke flux density, while g_4 checks maximum tooth flux density. The purpose is

to penalize the designs with increased iron losses. g_5 checks power factor.

Finally, transient FEA calculation is performed at base speed to determine the power factor, average torque, torque ripple and terminal voltage (g_6). The transient is run on the skewed machine, if torque ripple ($T_{rip,skew}$) is greater than the limit, the machine does not fulfil the constraint. The calculation includes segment with an angle of one stator slot $360^\circ/36 = 10^\circ$ (mechanical degrees).

If all constraints are fulfilled, the final step is the calculation of goal functions (table V). First goal (f_1) is to maximize efficiency calculated in magnetostatic conditions. The second function (f_2) maximizes torque density calculated from transient torque with applied skewing $T_{trans,skew}$ and active volume $V_{active} = (D_s/2)^2 \pi l_s$. It is important to emphasize that the described goal functions are evaluated simultaneously (multi-objective optimization).

TABLE IV: List of inequality constraints

No:	Constraint description	Symbol	Limit
g_1	Stress yield factor at $1.2 \cdot n_{max}$	FOS_{min}	≥ 2
g_2	Magnetostatic torque at n_b	T_{static}	≥ 600 Nm
g_3	Flux density in stator yoke	$B_{sy,max}$	≤ 1.6 T
g_4	Flux density in stator tooth	$B_{st,max}$	≤ 1.8 T
g_5	Power factor	$\cos \varphi_{min}$	≥ 0.6
g_6	Torque ripple with skewing	$T_{ripple,max}$	≤ 10 %

TABLE V: Optimization goal functions

No:	Goal function description	Formula	Unit
f_1	Maximize efficiency	η	-
f_2	Maximize torque density	$T_{trans,skew}/V_{active}$	Nm/dm ³

IV. OPTIMIZATION RESULTS

Optimization consists of 250 iterations (generations) of DE algorithm with population size $NP = 110$. In total $NP \cdot 250 = 27500$ designs have been evaluated out of which 647 fulfil all constraint functions. The optimization resulted in a Pareto front (Fig. 7), consisting of 16 designs (by definition any front member is not dominated by any other design). Considering that the machine has been designed for overload condition, selection of higher torque per volume has been prioritized over efficiency. Finally, design marked with blue dot in Fig. 7 has been selected as the best overall member (drawing is shown on Fig. 13a).

Considering that the machine diameter is 230 mm, with length of 344 mm and that it has Zhukovsky flux barrier profile, the machine is named EM230-344-Zhukovsky (Fig. 13a).

Only one post within the final barrier is enough to withstand centrifugal stress. Mechanical safety factor at over-speed conditions is $FOS = 2.287$ with maximum displacement of $33 \mu\text{m}$ occurring within third flux carrier (Fig. 13b). Maximum stress levels are approximately 196 MPa in the barrier bridge area (Fig. 13c). At base speed and phase current of $254 A_{rms}$ (corresponding to current density of

$18.43 A/\text{mm}^2$), stator saturation levels are very close to the inequality constraint limits. Stator yoke flux density is $B_{sy} = 1.59$ T while stator tooth flux density is $B_{st} = 1.79$ T (Fig. 13d).

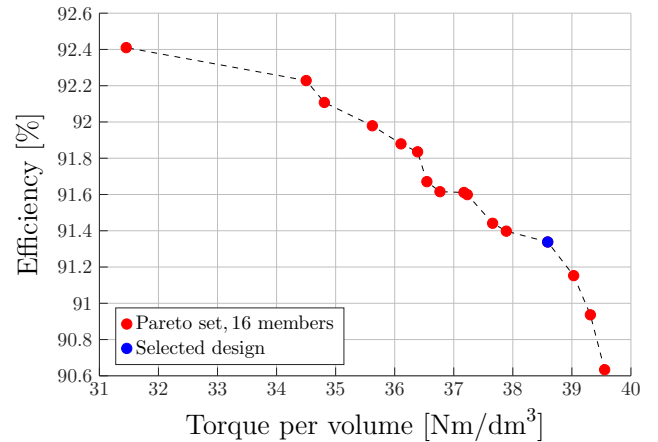


Fig. 7: Pareto front of Zhukovsky SyRM ePTO machine

V. PERFORMANCE GRAPHS

As described in section III-C, machine optimization has been conducted in a single operating point. To extract peak performance, EM230-344-Zhukovsky has been simulated in Motor-LAB environment [35] at 150, 202 and 254 A_{rms} .

Considering that magnetostatic calculations have been used to determine the machine length and that the machine has higher torque after running transient calculations, Motor-LAB has calculated that the base speed at MTPA conditions has been shifted to 1800 rpm at maximum current (instead of the original constraint of 1700 rpm). This is not considered a drawback because it expands the operation area of the ePTO machine (Fig. 8).

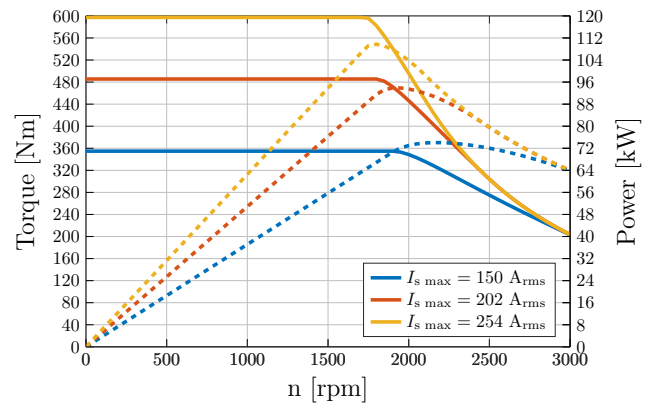


Fig. 8: Peak torque-speed curves

It is interesting to observe that at phase current of 254 A_{rms} phase advance is approx. 72° el. (due to the high saturation) with maximum $\cos \varphi = 0.66$. If the phase current is decreased to 150 A_{rms} , phase advance drops to approx. 64° el. and maximum power factor increases to $\cos \varphi = 0.72$.

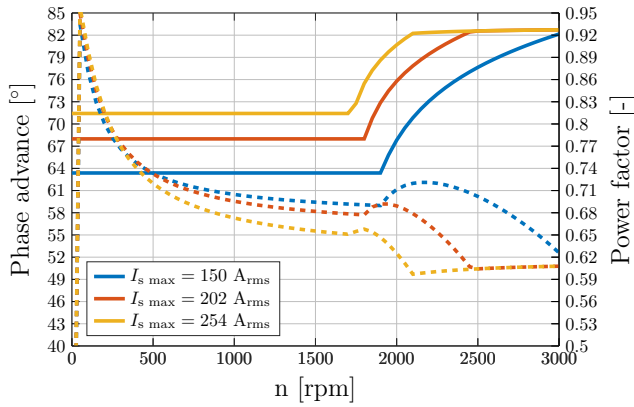


Fig. 9: Phase advance (full line) and power factor versus speed (dashed line)

Transient simulation (at base speed and 254 A_{rms}) has been conducted with the assumption of sinusoidal phase currents which yield flux linkage shown on Fig. 10. Furthermore, the results show that unskewed machine would have very high torque ripple (35 %), this is greatly improved by 5 segment rotor skewing which reduces torque ripple to 4,5 % (Fig. 11). Calculated line terminal voltage THD is 7,1 % (Fig. 12).

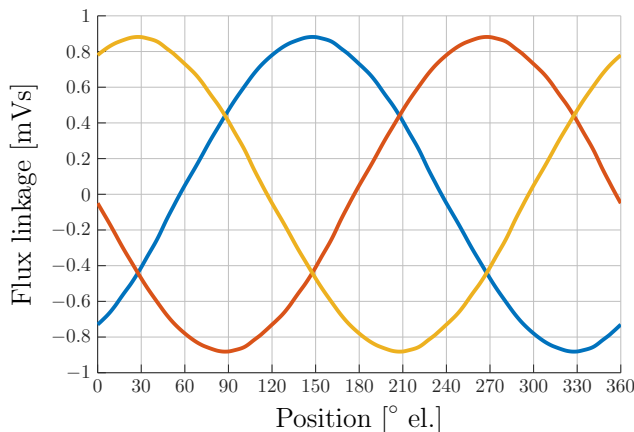


Fig. 10: Phase flux during transient conditions

VI. CONCLUSION

Considering robustness, price and reliability, a synchronous reluctance machine (SyRM) has been selected as target ePTO technology. The paper presents SyRM design and optimization via improved DE optimization algorithm. This approach interrupts computationally intensive FEA procedures if the inequality constraint is violated, therefore saving computational time. Furthermore, the paper shows how to efficiently perform geometrical parametrization of SyRM machine with the minimal number of parameters. This approach simplifies automatic design generation and reduces optimization time. The overall approach has been demonstrated as a case study of design optimization of a SyRM machine for eMPV ePTO.

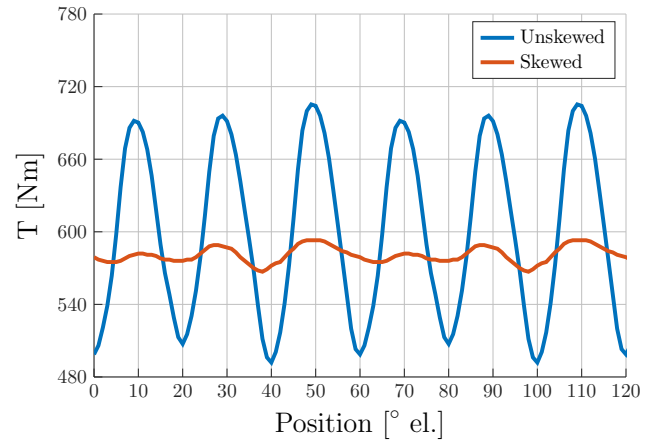


Fig. 11: Torque during transient conditions

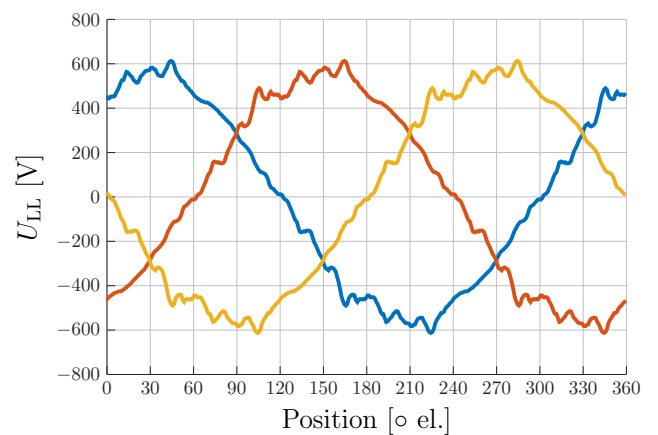


Fig. 12: Terminal line voltages during transient conditions

REFERENCES

- [1] European Environment Agency, "Electric Vehicles in Europe," p. 60, 2016. [Online]. Available: <https://www.eea.europa.eu/publications/electric-vehicles-in-europe>
- [2] VOLVO, "Power take-offs: Fields of application and Calculation guide," 2018. [Online]. Available: [http://productinfo.vtc.volvose/files/pdf/lo/PowerTake-off\(PTO\){_}Eng{_}08{_}580114.pdf](http://productinfo.vtc.volvose/files/pdf/lo/PowerTake-off(PTO){_}Eng{_}08{_}580114.pdf)
- [3] —, "Body builder instructions: PTO and pumps," 2018. [Online]. Available: <https://www.volvotrucks.ca/en-ca/parts-and-services/service/body-builder/manuals/>
- [4] K. Bourzac, "The Rare-Earth Crisis," 2011. [Online]. Available: <https://www.technologyreview.com/s/423730/the-rare-earth-crisis/>
- [5] J. Rowlett, "Rare earths: Neither rare, nor earths," 2014. [Online]. Available: <http://www.bbc.com/news/magazine-26687605>
- [6] U. Department of Energy, "Annual Progress Report Electric Drive Technologies Program," Tech. Rep. July, 2011.
- [7] J. J. Germishuizen, F. S. Van Der Merwe, K. Van Der Westhuizen, and M. J. Kamper, "Performance comparison of reluctance synchronous and induction traction drives for electrical multiple units," *IEEE Transactions on Industry Applications*, pp. 316–323, 2000.
- [8] R. Riba, C. López-Torres, L. Romeral, and A. Garcia, "Rare-earth-free propulsion motors for electric vehicles: A technology review," *Renewable and Sustainable Energy Reviews*, vol. 57, pp. 367–379, 2016.
- [9] S. Estenlund, M. Alaküla, and A. Reinap, "PM-less machine topologies for EV traction: A literature review," *2016 International Conference on Electrical Systems for Aircraft, Railway, Ship Propulsion and Road*

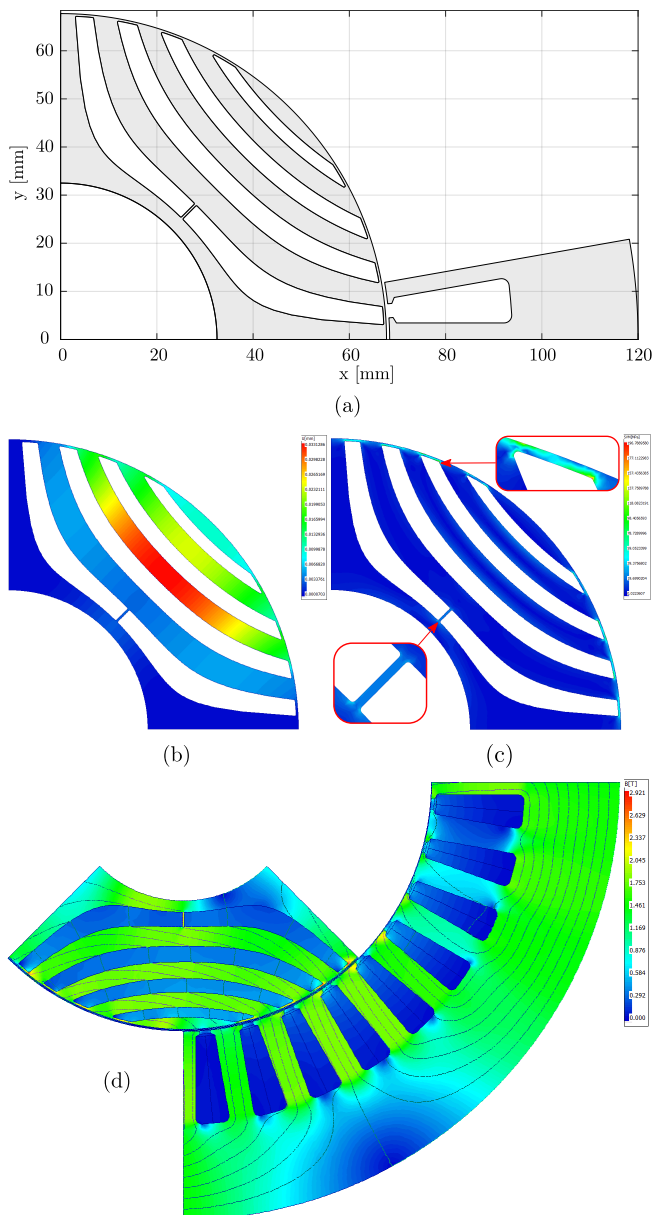


Fig. 13: a) Selected geometry (EM230-344-Zhukovsky); b) mechanical displacement at maximum over-speed; c) mechanical stress map at maximum over-speed; d) flux density map at base speed, peak phase current (254 A_{rms})

Vehicles and International Transportation Electrification Conference, ESARS-ITEC 2016, 2016.

[10] G. Pellegrino, T. M. Jahns, N. Bianchi, W. L. Soong, and F. Cupertino, *The Rediscovery of Synchronous Reluctance and Ferrite Permanent Magnet Motors Tutorial Course Notes*. Springer, 2016.

[11] P. Duck, J. Jurgens, and B. Ponick, "Calculation of Synchronous Reluctance Machines Used as Traction Drives," *2015 IEEE Vehicle Power and Propulsion Conference, VPPC 2015 - Proceedings*, pp. 0-4, 2015.

[12] B. Ban and S. Stipetić, "Electric Multipurpose Vehicle Power Take-Off: Overview, Load Cycles and Actuation via Synchronous Reluctance Machine," *ACEMP-OPTIM*, 2019.

[13] F. Parasiliti, M. Villani, S. Lucidi, and F. Rinaldi, "Finite-element-based multiobjective design optimization procedure of interior permanent

magnet synchronous motors for wide constant-power region operation," *IEEE Transactions on Industrial Electronics*, 2012.

[14] M. Barcaro, N. Bianchi, and F. Magnussen, "Permanent-magnet optimization in permanent-magnet-assisted synchronous reluctance motor for a wide constant-power speed range," *IEEE Transactions on Industrial Electronics*, 2012.

[15] H. I. Lee and M. D. Noh, "Optimal design of radial-flux toroidally wound brushless DC machines," *IEEE Transactions on Industrial Electronics*, 2011.

[16] G. Lei, J. G. Zhu, Y. G. Guo, J. F. Hu, W. Xu, and K. R. Shao, "Robust design optimization of PM-SMC motors for six sigma quality manufacturing," *IEEE Transactions on Magnetics*, 2013.

[17] W. Q. Chu, Z. Q. Zhu, and J. T. Chen, "Simplified analytical optimization and comparison of torque densities between electrically excited and permanent-magnet machines," *IEEE Transactions on Industrial Electronics*, 2014.

[18] H. M. Hasanien, "Particle swarm design optimization of transverse flux linear motor for weight reduction and improvement of thrust force," *IEEE Transactions on Industrial Electronics*, 2011.

[19] J. A. Tapia, J. Pyrhönen, J. Puranen, P. Lindh, and S. Nyman, "Optimal design of large permanent magnet synchronous generators," *IEEE Transactions on Magnetics*, 2013.

[20] J. A. Tapia, A. Parviainen, J. Pyrhonen, P. Lindh, and R. R. Wallace, "Optimal design procedure for an external rotor permanent-magnet machine," in *Proceedings - 2012 20th International Conference on Electrical Machines, ICEM 2012*, 2012.

[21] L. Alberti, N. Bianchi, A. Boglietti, and A. Cavagnino, "Core axial lengthening as effective solution to improve the induction motor efficiency classes," in *IEEE Energy Conversion Congress and Exposition: Energy Conversion Innovation for a Clean Energy Future, ECCE 2011, Proceedings*, 2011.

[22] A. Boglietti, A. Cavagnino, L. Ferraris, M. Lazzari, and G. Luparia, "No tooling cost process for induction motors energy efficiency improvements," *IEEE Transactions on Industry Applications*, 2005.

[23] G. Bramerdorfer, A. Cavagnino, and S. Vaschetto, "Impact of IM pole count on material cost increase for achieving mandatory efficiency requirements," in *IECON Proceedings (Industrial Electronics Conference)*, 2016.

[24] E. B. Agamloh, A. Boglietti, and A. Cavagnino, "The incremental design efficiency improvement of commercially manufactured induction motors," *IEEE Transactions on Industry Applications*, 2013.

[25] T. H. E. Commission, O. F. The, and E. Communities, "Commission Regulation (EC) 640/2009 Implementing Directive 2005/32/EC of the European Parliament and of the Council with regard to ecodesign requirements for electric motors," *Official Journal of the European Union*, 2009.

[26] A. M. El-Refai, "Motors/generators for traction/propulsion applications: A review," 2013.

[27] G. Pellegrino, F. Cupertino, and C. Gerada, "Automatic Design of Synchronous Reluctance Motors Focusing on Barrier Shape Optimization," *IEEE Transactions on Industry Applications*, 2015.

[28] C. Lu, S. Ferrari, and G. Pellegrino, "Two Design Procedures for PM Synchronous Machines for Electric Powertrains," *IEEE Transactions on Transportation Electrification*, 2017.

[29] S. Stipetic, D. Zarko, and M. Kovacic, "Optimised design of permanent magnet assisted synchronous reluctance motor series using combined analytical-finite element analysis based approach," *IET Electric Power Applications*, 2016.

[30] D. Zarko, S. Stipetic, M. Martinovic, M. Kovacic, T. Jercic, and Z. Hanic, "Reduction of computational efforts in finite element-based permanent magnet traction motor optimization," *IEEE Transactions on Industrial Electronics*, vol. 65, no. 2, pp. 1799-1807, 2017.

[31] J. Lampinen, "Multi-Constrained Nonlinear Optimization by the Differential Evolution Algorithm," in *Soft Computing and Industry*, 2002.

[32] R. Storn and K. Price, "Differential Evolution - A Simple and Efficient Heuristic for Global Optimization over Continuous Spaces," *Journal of Global Optimization*, 1997.

[33] K. Price and R. Storn, "Matlab code for differential evolution." [Online]. Available: <http://www1.icsi.berkeley.edu/~storn/code.html>

[34] D. Zarko, "A Systematic Approach To Optimized Design Of Permanent Magnet Motors With Reduced Torque Pulsations," Ph.D. dissertation, University Of Wisconsin-Madison, 2004.

[35] Motor Design Ltd., "Motor-CAD / Motor-LAB software." [Online]. Available: <http://www.motor-design.com/motorlab.php>

Publications

- [36]S. Stipetic, D. Zarko, and M. Popescu, "Ultra-fast axial and radial scaling of synchronous permanent magnet machines," *IET Electric Power Applications*, vol. 10, no. 7, pp. 658–666, 2016.
- [37]S. Stipetic, W. Miebach, and D. Zarko, "Optimization in design of electric machines: Methodology and workflow," *Joint International Conference - ACEMP 2015: Aegean Conference on Electrical Machines and Power Electronics, OPTIM 2015: Optimization of Electrical and Electronic Equipment and ELECTROMOTION 2015: International Symposium on Advanced Electromechanical Moti*, pp. 441–448, 2016.
- [38]D. Zarko and S. Stipeti ć, "Criteria for optimal design of interior permanent magnet motor series," in *Proceedings - 2012 20th International Conference on Electrical Machines, ICEM 2012*, 2012.



Branko Ban was born in Šibenik (Croatia) in 1991. He completed Bachelor (2012.) and Master (2015.) studies in Electrical Engineering at the University of Zagreb (Faculty of electrical engineering and computing) and Chalmers University of Technology. Since 2015. he is a part of the ALTEN consultancy team working in the automotive sector as electric machine specialist in areas related to design, R&D, and quality assurance. He is currently enrolled in the University of Zagreb PhD program covering next-generation electric machines.



Stjepan Stipetić was born in Ogulin (Croatia) in 1985. He received Dipl.Eng. and PhD degrees in electrical engineering from the University of Zagreb, Croatia, in 2008 and 2014, respectively. Currently, he is an Assistant Professor at the University of Zagreb Faculty of Electrical Engineering and Computing, Department of Electrical Machines Drives and Automation, Croatia where his research activities are related to design, modelling, analysis and optimization of electrical machines.

Publication 4: Minimum Set of Rotor Parameters for Synchronous Reluctance Machine and Improved Optimization Convergence via Forced Rotor Barrier Feasibility

Paper details:

B. Ban, S. Stipetić and T. Jerčić "Minimum Set of Rotor Parameters for Synch. Reluctance Machine and Improved Optimization Convergence via Forced Rotor Barrier Feasibility", in Special Issue Optimization and Simulation of Permanent Magnet Motors, *Energies*, 2021, 14(10), 2744. April 2021.

Available at:<https://doi.org/10.3390/en14102744>

Article

Minimum Set of Rotor Parameters for Synchronous Reluctance Machine and Improved Optimization Convergence Via Forced Rotor Barrier Feasibility [†]

Branko Ban ¹, Stjepan Stipetic ^{1,*} and Tino Jercic ²

¹ Faculty of Electrical Engineering and Computing (FER), Department of Electric Machines, Drives and Automation, University of Zagreb, Unska 3, 10000 Zagreb, Croatia; branko.ban@fer.hr

² Cognitio Elektronika, Bani ul. 73A, 10010 Zagreb, Croatia; tino@cognitio-elektronika.hr

* Corresponding author: stjepan.stipetic@fer.hr

[†] This paper is an extended version of our paper “Design and Optimization of Synchronous Reluctance Machine for actuation of Electric Multi-purpose Vehicle Power Take-Off” published in 2020 International Conference on Electrical Machines (ICEM).



Citation: Ban, B.; Stipetic, S.; Jercic, T. Minimum Set of Rotor Parameters for Synchronous Reluctance Machine and Improved Optimization Convergence Via Forced Rotor Barrier Feasibility [†]. *Energies* **2021**, *14*, 2744. <https://doi.org/10.3390/en14102744>

Academic Editor: Chunhua Liu

Received: 6 April 2021

Accepted: 6 May 2021

Published: 11 May 2021

Publisher's Note: MDPI stays neutral with regard to jurisdictional claims in published maps and institutional affiliations.



Copyright: © 2021 by the authors. Licensee MDPI, Basel, Switzerland. This article is an open access article distributed under the terms and conditions of the Creative Commons Attribution (CC BY) license (<https://creativecommons.org/licenses/by/4.0/>).

Abstract: Although rare earth materials are the critical component in high torque density permanent magnet machines, their use has historically been a commercial risk. The alternatives that have been in the recent industry focus are synchronous reluctance machines (SyRM). They have lower torque density but also relatively low material cost and higher overload capability. Multi-layer IPM and SyRM machines have significant geometric complexity, resulting in a high number of parameters. Considering that modern machine design requires the use of optimization algorithms with computational load proportional to the number of parameters, the whole design process can take several days. This paper presents novel SyRM parameterization with reduced number of parameters. Furthermore, the paper introduces the novel forced feasibility concept, applied on rotor barrier parameters, resulting in improved optimization convergence with overall optimization time reduced by 12.3%. Proposed approaches were demonstrated using optimization procedure based on the existing differential evolution algorithm (DE) framework.

Keywords: electric machine; synchronous reluctance; optimization; comparison; differential-evolution; design; electric; rare-earth free; forced feasibility

1. Introduction

To reduce environmental impact, global legislation is pushing to increase electric vehicle (EV) production [1]. In addition to regulatory requirements, consumers are demanding cleaner and safer vehicles. This has led to a tectonic shift in the automotive industry, both in terms of knowledge and production, forcing the industry to evolve rapidly.

At the moment, passenger vehicles are leading the market development (Tesla, Toyota, BMW), mainly because of lighter vehicles that require smaller traction batteries. On the other hand, commercial vehicles are much heavier and require large battery capacity, resulting in significant production costs. Therefore, the commercial vehicle industry is forced to move into niche markets, such as medium-duty, short-haul, and last mile applications. Long-haul vehicle development is likely to take more time and have even more sensitive financing.

Examples of commercial vehicles suitable for SyRM adoption include electric multi-purpose vehicles (eMPVs), such as refuse trucks, hook loader trucks, or vacuum trucks [2]. eMPVs must actuate additional body systems (usually through some type of hydraulic pump) in addition to electric propulsion. Traditionally, this actuation is done by a diesel engine or a gearbox-mounted output shaft referred to as power take-off (PTO). Considering price, overload capability, and production simplicity, SyRM can be a viable ePTO solution [2,3].

This paper presents novel SyRM parameterization with a reduced number of parameters (rotor nomenclature according to Figure 1). During the optimization process, infeasible models may occur. Depending on the designer's choice, the infeasible models can be rejected or modified until they become feasible. The idea is that the procedure does not discard randomly generated infeasible geometry but modifies it until feasibility is achieved (hence the name "forced" feasibility).

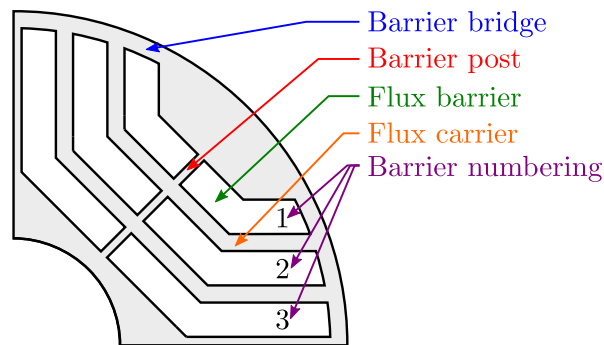


Figure 1. SyRM rotor nomenclature [3].

2. SyRM Design

2.1. Peak Performance Requirements

The machine requirements in this paper are derived from Reference [3]. All peak performance requirements are listed in Table 1.

Table 1. Peak operation requirements at base speed.

Description	Symbol	Value	Unit
Base speed	n_b	1700	rpm
Max. operating speed	n_{max}	2500	rpm
Max. over speed	$1.2 \cdot n_{max}$	3000	rpm
Max. torque	T_{max}	600	Nm
Battery voltage	U_{DC}	610	V
Max. phase current	$I_{s \ max}$	310	A _{rms}
RMS current density	J	18.4	A/mm ²

2.2. Optimization Method

Most of the requirements for the design of electrical machines are in conflict with each other (reduction of volume or mass, increase of efficiency, etc.). This is evident in the problem of increasing efficiency [4–6] through global legislative initiatives [1]. For traction drives, high efficiency in limited packaging space is an absolute imperative [7]. Therefore, a manual design that satisfies all constraints can be an overwhelming task due to a large number of coupled parameters that affect the performance and quality of the machine.

According to Pellegrino [8,9], the computational load increases proportionally with the number of geometric parameters. This is inherently the case for IPM and SyRM machines, leading to a high number of optimization variables and a longer optimization time.

Today, optimization algorithms enjoy great popularity among designers of electrical machines [10–16]. The personal experience of the designer should not be underestimated, but, due to the non-linearity and complexity of the relationships between the geometry of electrical machines and their performance, it is generally believed that only mathematical optimization can push the boundaries to better designs.

Optimization algorithms can be divided to gradient based methods and stochastic or metaheuristic methods (PyOpt provides several open-source algorithms [17]). Gradient type methods converge fast but have difficulties with global optima. Usually they require feasible starting point which can be a problematic task in complex problems (Quasi Newton method [18]). Stochastic methods are heavily used in electrical machine optimization (Pow-

ell's method [18], Nelder-Mead method [19]). The disadvantage is that the convergence can last for days, and global optimum cannot be mathematically proven. On the other hand, from engineer's point of view, these methods can find a satisfying global result. Popular metaheuristic methods are based on natural behavior (Evolutionary algorithm [20], Differential evolution [21], Particle Swarm [22]).

All methods are generally set to solve a single or multi-objective problem. The goal of design optimization is to have a chosen objective function $f(\vec{x})$ reach its minimum or maximum value while keeping other engineering indices within an acceptable range [23].

The use of finite element analysis (FEA) is inevitable in the case of SyRM's because saturation in the rotor bridges and posts significantly affects the final performance. FEA is computationally intensive and optimization can require thousands of calculations through generations. Significant time savings can be achieved if all calculations are performed using magnetostatic simulations with fixed rotor position. Detailed explanation of different approaches for calculation of IPM machine parameters and performance using only magnetostatic simulations is available in Reference [24].

This paper uses an improved version of DE algorithm proposed by Žarko et al. [25] based on Lampinen's constraint function approach [21,26,27].

2.3. Preset Model

The number of slots and poles is chosen to be 36/4 with 4 rotor flux barriers, resulting in a two-layer integer slot winding with distributed overlapping coils. This combination provides a good compromise between the inherent ability to mitigate torque pulsations, susceptibility to noise, and the ability to use multiple parallel paths.

The ideal number of turns per coil (N_c) and parallel paths (a_p) for matching the base speed is automatically calculated based on winding feasibility [28] and ultra-fast scaling laws [29].

The goal of this paper is to prove that the forced feasibility approach (which will be discussed in later sections) yields a shorter optimization time. Considering that the selected machine has a relatively large number of parameters, all non-rotor parameters are taken from the optimized machine design in Reference [3] (Table 2). In addition, the initial design is constrained by peak performance requirements at the base speed (Table 1).

A set of parameters which are subject to optimization are listed in Table 3; colors and numbering in Tables 2 and 3 correspond to Figure 2.

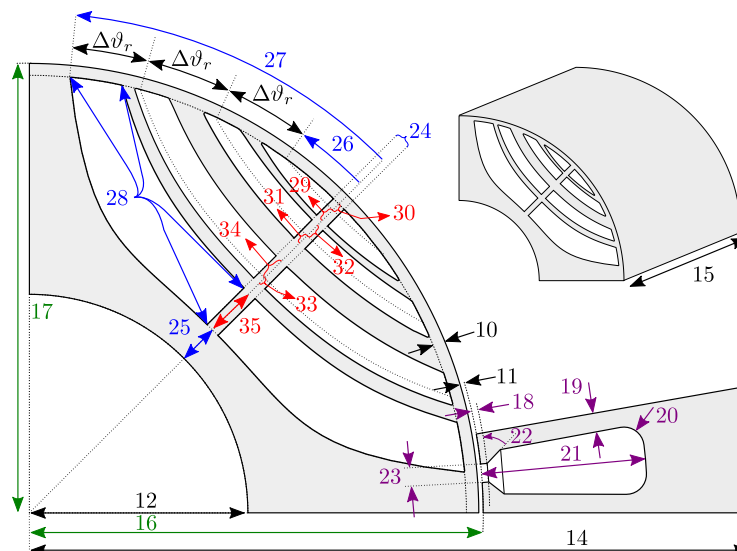


Figure 2. List of parametrization variables.

Table 2. Constant parameters.

No:	Symbol	Description	Value	Unit
1	D_s	Stator diameter	240	mm
2	D_{sh}	Shaft diameter	65	mm
3	N_{ph}	Phase number	3	-
4	N_c	No. of turns	Auto calculated	-
5	a_p	Parallel paths	Auto calculated	-
6	y_c	Coil pitch	6	-
7	N_{bar}	Barrier number	4	-
8	p	Pole pairs	2	-
9	N_s	Slot number	36	-
10	w_{bb}	Barrier bridge	0.500	mm
11	δ	Airgap	0.650	mm
12	$D_{sh}/2$	Shaft radius	32.500	mm
13	$\Delta r_{4\ in}$	Barrier offset	0	mm
14	$D_s/2$	Stator radius	120	mm
15	$l_{s\ max}$	Active length	344.141	mm
16	D_b	Stator bore	136.751mm	
17	$\frac{D_b - 2\delta}{2}$	Rotor radius	67.725mm	
18	d_t	Tooth tip depth	0.857mm	
19	w_t	Tooth width	6.874mm	
20	r_{sc}	Slot corner rad.	1.588mm	
21	d_s	Slot depth	25.491mm	
22	α_t	Tooth tip angle	31.699	°
23	w_{op}	Slot opening	2.935mm	
24	w_p	Barrier post	0.511mm	
25	e_c	End carrier	3.122mm	
26	ϑ_{min}	Min. angle	15.069	°
27	ϑ_{max}	Max. angle	42.383	°
28	r_f	Fillet radius	0.240mm	

Table 3. Complete list of optimization parameters.

No:	Symbol	Description	Boundaries	Unit
29	$\Delta r_{1\ in}$	Barrier offset	[0 1]	mm
30	$\Delta r_{1\ out}$	Barrier offset	[0 1]	mm
31	$\Delta r_{2\ in}$	Barrier offset	[0 1]	mm
32	$\Delta r_{2\ out}$	Barrier offset	[0 1]	mm
33	$\Delta r_{3\ in}$	Barrier offset	[0 1]	mm
34	$\Delta r_{3\ out}$	Barrier offset	[0 1]	mm
35	$\Delta r_{4\ out}$	Barrier offset	[0 1]	mm

3. Automated Geometry Construction

Any optimization requires automatic design generation. As mentioned earlier, a higher number of optimization variables is associated with a longer optimization time. Gamba et al. [30] have shown that three variables per barrier ($3 \cdot k$, where k is the number of barriers) is the appropriate number of parameters to use for a fast yet accurate description of multi-barrier SyRM. To reduce this even further, the $2 + (2 \cdot k - 1)$ alternative is proposed in this paper. Several rotor barrier types are commonly used in SyRM design: circular, hyperbolic, fluid (Zhukovsky), segmented, etc. (open-source SyRE project offers more details and instructions on geometry generation [31]).

Within this paper, barrier line profiles (Figure 2) are derived from conformal mapping theory and the Zhukovsky airflow potential formulation [30,31]. This was originally developed to describe the flow paths of fluids channeled by two infinite plates forming an

angle π/p , and a plug centered at the origin of the reference frame (p is the number of pole pairs). In the solid rotor context, the plug represents the non-magnetic shaft with a radius of $D_{sh}/2$. Equations (1) and (2) express the magnetic field potential lines in parametric form.

$$C(\vartheta, r, \Delta r) = \sin(p\vartheta) \frac{\left(\frac{r+\Delta r}{D_{sh}/2}\right)^{2p} - 1}{\left(\frac{r+\Delta r}{D_{sh}/2}\right)^p}, \tag{1}$$

$$r(\vartheta, C) = \frac{D_{sh}}{2} \sqrt[p]{\frac{C + \sqrt{C^2 + 4 \sin^2(p\vartheta)}}{2 \sin(p\vartheta)}}; 0 \geq \vartheta \geq \pi/p. \tag{2}$$

3.1. Single Barrier Construction

The first step in creating the flux barrier is to select the point E_k in polar coordinates. E_k consists of two components, the radial component $r_k = (D_b - 2\delta)/2 - w_{bb}$, which has a fixed value, and the variable angle ϑ_k (5). The centerline parameter C_k is computed by solving the Equation (6). Virtual center barrier line is then computed by solving Equation (7). It is important to note that the angle vector should be generated in the range $\vartheta \in [\vartheta_k - \frac{\pi}{2p}, \vartheta_k]$; otherwise, if the angle is close to $\frac{\pi}{2p}$, the radial component will be weighted to infinity, leading to a computational error. The point G_k (8) is the center barrier coordinate (always lies at angle $\frac{\pi}{2p}$) and a reference point for calculating the inner and outer barrier line.

The barrier is constructed from a virtual centerline, which is modified by adding offsets Δr_{in} and Δr_{out} to form inner and outer flux lines (Figure3). Offsets in millimeters are calculated from per-unitized input offset parameters according to expressions (4), (3), where d_{kin} and d_{kout} represent distance between G_k points according to Figure4.

$$\overbrace{\Delta r_{kout}}^{[mm]} = \overbrace{\Delta r'_{kout}}^{\text{Per unit} \in [0 \ 1]} \cdot d_{kout}, \tag{3}$$

$$\overbrace{\Delta r_{kin}}^{[mm]} = \overbrace{\Delta r'_{kin}}^{\text{Per unit} \in [0 \ 1]} \cdot d_{kin}, \tag{4}$$

$$E_k = r_k / \vartheta_k, \tag{5}$$

$$C_k(\vartheta_k, r_k, \Delta r = 0), \tag{6}$$

$$r_k \left(\vartheta \in \left[\vartheta_k - \frac{\pi}{2p}, \vartheta_k \right], C_k \right), \tag{7}$$

$$G_k = r \left(\frac{\pi}{2p}, C_k \right) / \frac{\pi}{2p}. \tag{8}$$

The next step in the construction of the barrier is to compute C_{kout} (9) and C_{kin} (11), which completely define the equations of the inner and outer barriers. Solving the Equation (2) = r_k with the arguments C_{kin}, C_{kout} gives the intersection point angles $\vartheta_{kin}, \vartheta_{kout}$. The last step is the calculation of barrier lines r_{out} (10) and r_{in} (12) over the given angles.

$$C_{kout} \left(\frac{\pi}{2p}, r_{G_k}, \Delta r_{kout} \right), \tag{9}$$

$$r_{out} \left(\vartheta \in \left[\vartheta_{kout} - \frac{\pi}{2p}, \vartheta_{kout} \right], C_{kout} \right), \tag{10}$$

$$C_{kin} \left(\frac{\pi}{2p}, r_{G_k}, -\Delta r_{kin} \right), \tag{11}$$

$$r_{in} \left(\vartheta \in \left[\vartheta_{kin} - \frac{\pi}{2p}, \vartheta_{kin} \right], C_{kin} \right). \tag{12}$$

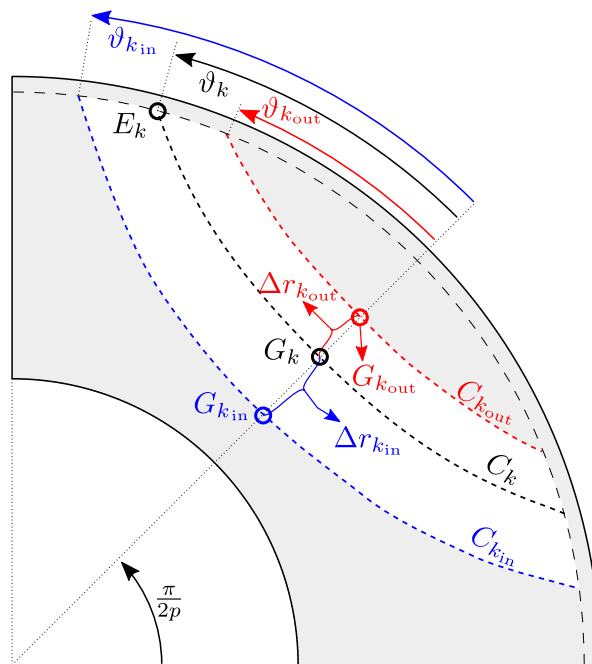


Figure 3. Construction of single barrier.

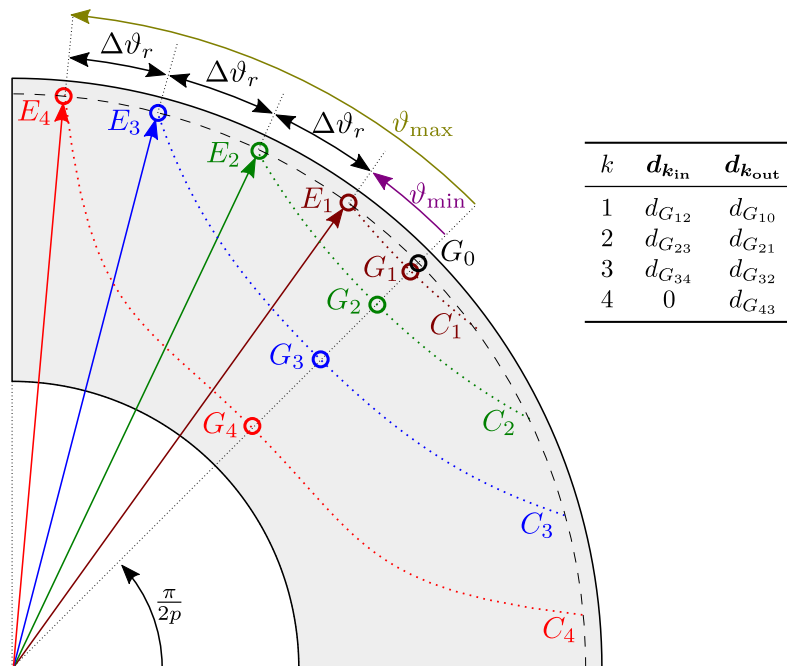


Figure 4. Construction of all flux barriers.

3.2. Construction of All Rotor Flux Barriers

The previous section described the flux barrier construction based on three parameters: variable angle ϑ_k , inner (Δr_{in}) and outer (Δr_{out}) barrier offsets. If all barriers were constructed according to this principle, the total parameter number would be $3 \cdot k$. Considering that center virtual barrier line is not part of the final barrier, there is a way to reduce the total number of parameters. Two angles, ϑ_{min} and ϑ_{max} , indicate the allowed center barrier line range. Depending on the number of barriers k , they define angles $\vartheta_{1..k}$ with equidistant angular offsets $\Delta\vartheta_r$ defining points $E_{1..k}$ used to construct each virtual center barrier line (Figure 4). To make the procedure robust, and to avoid clashes with the shaft, final barrier

(closest to the shaft) inner offset value is always zero. This procedure reduces the total number of barrier parameters to $2 + (2 \cdot k - 1)$. The constant 2 refers to the parameters ϑ_{\min} and ϑ_{\max} , -1 refers to the constant $\Delta r_{\text{final in}} = 0$, which can be removed from the total number of parameters.

The choice of equidistant virtual flux line angle offset ($\Delta\vartheta_r$) might appear to be a design-limiting constraint, but this is not the case. The virtual lines are used only as a reference for calculating the inner and outer barriers. Only in the special case, they represent flux barrier middle line when $\forall \Delta r_{k_{\text{out}}} = \forall \Delta r_{k_{\text{in}}}$. Optimization results proved that $\forall \Delta r_{k_{\text{out}}} \neq \forall \Delta r_{k_{\text{in}}}$ (Table 4). Furthermore, $\forall \Delta r_{k_{\text{out}}} \neq 0$ and $\forall \Delta r_{k_{\text{in}}} \neq 0$ (except in the final barrier, where $\Delta r_{\text{final in}} = 0$ by default). This proves that the assumption of equidistant virtual line offset angles has no effect on the final rotor design and can be used in the case of the Zhukovsky flux barrier type.

Table 4. Optimized rotor parameters and final result comparison.

Result	Unit	Random Generated							Forced Feasibility					Diff. [%]
		89	91	106	132	160	AVG	77	87	88	94	132	AVG	
$\Delta r_{1 \text{ in}}$	mm	2.26	1.29	1.64	1.87	2.51	1.91	2.53	2.58	2.75	1.26	2.76	2.37	
$\Delta r_{1 \text{ out}}$	mm	0.46	1.00	1.24	0.87	0.37	0.79	0.54	0.39	0.03	0.79	0.42	0.43	
$\Delta r_{2 \text{ in}}$	mm	2.06	2.13	1.77	1.70	1.00	1.73	1.40	1.30	0.81	1.03	2.12	1.33	
$\Delta r_{2 \text{ out}}$	mm	1.18	1.80	1.70	1.36	1.46	1.50	1.05	1.36	1.73	2.50	0.56	1.44	
$\Delta r_{3 \text{ in}}$	mm	2.91	2.11	2.69	2.15	3.07	2.59	2.98	1.76	1.99	2.36	1.29	2.08	
$\Delta r_{3 \text{ out}}$	mm	1.45	1.71	1.24	1.87	2.06	1.67	1.85	1.95	2.19	2.10	2.30	2.08	
$\Delta r_{4 \text{ out}}$	mm	3.73	4.52	4.26	4.58	3.41	4.10	3.64	4.71	4.41	4.23	4.65	4.33	
η	-	0.91	0.91	0.91	0.91	0.91	0.91	0.91	0.91	0.91	0.91	0.91	0.91	0.00
$T_{\text{trans,skew}}$	Nm	603.7	602.9	603.3	603.6	603.2	603.3	604.1	605.2	604.5	604.0	604.9	604.5	0.20
$B_{\text{sy,max}}$	T	1.60	1.60	1.60	1.60	1.59	1.60	1.60	1.60	1.60	1.60	1.60	1.60	0.00
$B_{\text{st,max}}$	T	1.79	1.79	1.80	1.79	1.79	1.79	1.79	1.79	1.79	1.79	1.80	1.79	0.00
$\cos \varphi$	-	0.66	0.66	0.66	0.66	0.66	0.66	0.66	0.66	0.66	0.66	0.66	0.66	0.00
T_{ripple}	%	2.65	3.25	1.64	1.72	3.46	2.54	2.88	2.86	2.41	1.93	2.89	2.59	1.95

4. Optimization Procedure Details

The optimization of the 2D cross-section is set up as a single-objective problem mathematically defined as: Find the vector of parameters (13), subject to D parameter boundary constraints (14) and subject to m inequality constraint functions (15), which will maximize objective function (16).

$$\vec{x} = [x_1, x_2, \dots, x_D], \quad \vec{x} \in R^D, \quad (13)$$

$$x_i^{(L)} \leq x_i \leq x_i^{(U)}, \quad i = 1, \dots, D \quad (14)$$

$$g_j(\vec{x}) \leq 0, \quad j = 1, \dots, m, \quad (15)$$

$$\max f(\vec{x}). \quad (16)$$

The applied optimization workflow is shown in Figure 5. The optimization process starts with the problem definition (boundaries, constraints, objectives, etc.) and a preset of constant parameters (slots, poles, active diameter, etc.).

After entering the optimization loop, the following steps are performed iteratively:

1. the optimization algorithm generates the vector \vec{x} (optimization variables);
2. variables are converted to model parameters;
3. model is generated based on the model parameters;
4. model is solved;
5. performance is extracted from the solution (values for constraints and objective functions are calculated from the solution);
6. data is passed to the optimization algorithm.

Single-objective optimization has only one objective function, which may have multiple variables and scaling factors. When the optimization converges, the value of the objective function saturates around a certain value. Without stopping criteria, the objective function will improve in infinitesimal steps for a very long time without any significant design improvement. In this paper, the following stopping criteria are used: after each generation, the last four objective function increments $f_{1..4}$ are checked; if the difference between f_1 and f_4 is less than 0.2%, the optimization is stopped; otherwise, it continues until the 160th generation.

5. Model and Solution Feasibility

In optimization problems, the notion of feasibility is related to the acceptance criteria of the solution. A solution is declared feasible if it satisfies certain criteria (15). The feasibility of a solution implies that a solution exists, i.e., the problem or model that provides this solution is solvable. During the optimization process, models may occur that are not solvable. These models have no solution and can be declared infeasible without solving them, which can decrease computational burden in the case of FEA-based solver. The models that are not solvable are declared as infeasible considering the model feasibility criteria.

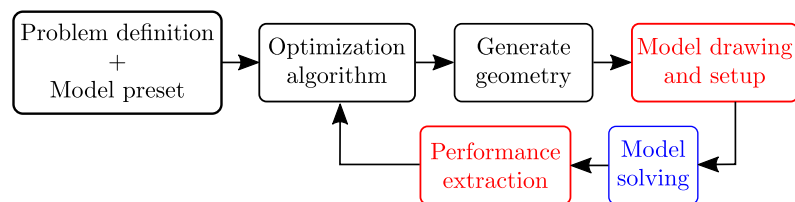


Figure 5. Optimization workflow.

5.1. Geometrical Feasibility

A special subset of model feasibility criteria is geometric feasibility, which characterizes whether the model geometry satisfies certain criteria (e.g., mechanical integrity, physicality, overlaps, etc.). In some cases, trying to solve a geometrically infeasible model with external solvers can lead to a crash of the whole optimization routine, a problem that highlights the need for detection methods to deal with geometrically infeasible models (e.g., barrier 1 (blue) collides with barrier 2 (yellow), the overlap is marked in red, Figure 6c).

To avoid the construction of such an invalid model, a geometric feasibility procedure can be performed within the optimization algorithm for each candidate vector. Regardless of the method of handling and detecting geometric infeasibility, it is always beneficial to reduce the occurrence of infeasible models. The simplest method for reducing the occurrence of geometrically infeasible models is to introduce lower and upper parameter bounds, which can be in the form of linear (Figure 7a), non-linear function bounds (Figure 7b), or complex bounds (Figure 7c).

For simple problems, the introduction of bounds can completely avoid the occurrence of infeasible models, while for complex problems it reduces the probability of the occurrence of the infeasible candidates. For this reason, optimization algorithms must include a method for dealing with geometrically infeasible candidates.

In general, a geometrically infeasible candidate is discarded while the new candidate takes its place. To generate a replacement candidate, Žarko et al. [25,32] randomly initialize the entire parameter set (13) until a geometrically feasible replacement candidate appears. The drawback of this method is a possible rejection of candidates with some good properties. Moreover, this method may lead to slow convergence to the optimal solution if the optimal candidate is on the boundary of the feasible space.

The alternative approach is forced feasibility, where each infeasible design is subjected to parameter modification until feasibility is achieved (i.e., barrier 1 (blue) and barrier 2 (yellow) are modified until the candidate achieves the specified flux carrier width w_{goal} ,

Figure 6d). This approach requires smart parametrization with minimum feasibility constraints and can potentially be extremely complex. On the other hand, potential benefits include reduced optimization time (no need to wait for a random feasible design to emerge) and faster convergence to the final result. The substitution of infeasible candidates is implemented in the form of a projection onto the feasible space (Figure 7d).

Projection operator can be mathematically written as:

$$P = \min[(\vec{x}_{orig} - \vec{x}_{new}) \cdot Q(\vec{x}_{orig} - \vec{x}_{new})^T], \tag{17}$$

$$Q = \begin{bmatrix} q_1 & 0 & \cdots & 0 \\ 0 & q_2 & \cdots & 0 \\ \vdots & \vdots & \ddots & \vdots \\ 0 & 0 & \cdots & q_D \end{bmatrix}, \tag{18}$$

$$\forall \vec{x}_{new} \in R^D$$

where \vec{x}_{orig} represents parameter vector of original, geometrically infeasible candidate, \vec{x}_{new} is its geometrically feasible replacement/alternative, and Q is weighting matrix (18) in which its coefficients control the projection path (1, 2, and 3 in Figure 7d). If all coefficients satisfy $q_{1..D} = 1$, projection is orthogonal, and the new geometrically feasible candidate is closest to the original infeasible candidate.

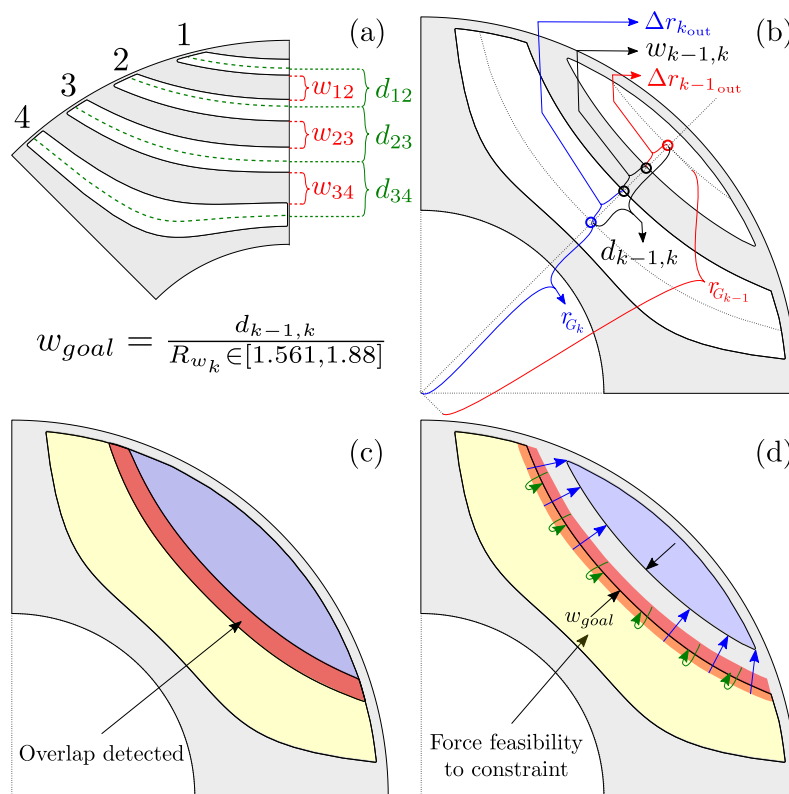


Figure 6. Empirical flux carrier width range (a); feasibility check parameters (b); infeasible geometry (c) and forced feasibility (d).

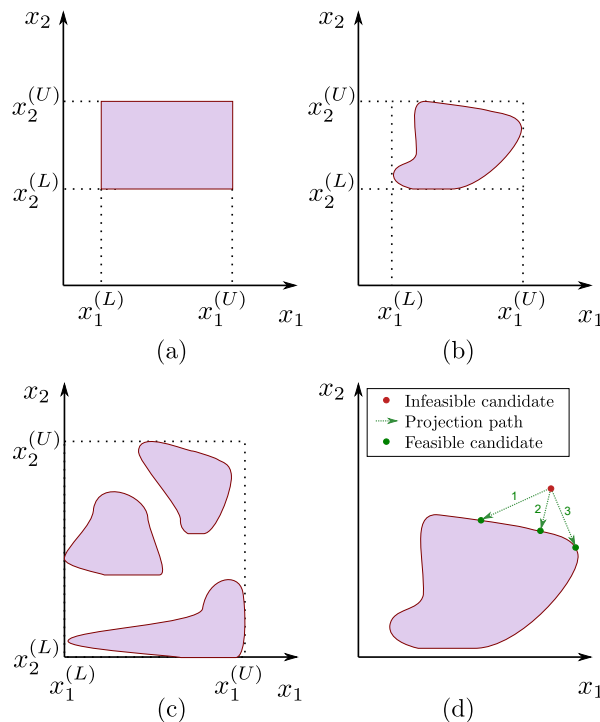


Figure 7. Optimization function bounds: (a) simple, (b) non-linear, and (c) complex. Candidate projection on feasible space (d).

5.2. Forced Feasibility Algorithm

For simplicity, the functionality is explained using two barrier SyRM (Figure6b–d). The first step is geometry generation based on the parameterization approach from Section3(Algorithm1: ln:1–5). The next step is to compute the variables $d_{k-1,k}, w_{k-1,k}, w_{goal}$ (Figure6b) and check whether the infeasibility condition is satisfied (Algorithm1: ln:11). The design may be infeasible for one of two reasons: there is a barrier conflict ($w_{k-1,k} \leq 0$) or the flux carrier width is too small ($w_{k-1,k} \leq w_{goal}$). If not feasible (Figure6c), proceed to forcing feasibility (Algorithm2).

The purpose of the force feasibility function (Algorithm2: ln:1) is to provide the current position information of the barrier ($w_{goal}, d_{k-1,k}, \Delta r_{k_{out}}, \Delta r_{k-1_{in}}$, Figure6b) and provide minimally modified barrier offsets ($\Delta r'_{k_{out}}, \Delta r'_{k-1_{in}}$), defining a new feasible design (Figure 6d). The minimal deviation is secured via MATLAB function FMINCON function [33]. FMINCON default input parameters are listed in Algorithm2: ln:2–7, where x_c represents the current barrier offset vector.

During the search, FMINCON iteratively calls COSTFCN, which is responsible for the convergence of the search (calculates the deviation of the generated x and the initial offset vector x_c), and CONSTRAINTFCN which calculates the deviation of the generated flux carrier width (w) from the carrier width (w_{goal}). When the algorithm converges, FMINCON returns $\Delta r'_{k_{out}}, \Delta r'_{k-1_{in}}$, and a new feasible geometry is generated (Figure6d).

In summary, when the system detects an infeasible case, such as in the example shown in Figure6b, where 1st and 2nd barriers overlap, $\Delta r_{2_{out}}$ and $\Delta r_{1_{in}}$ are iteratively modified until flux carrier width w_{goal} is reached (Figure6d). This prevents the generation of too thin or too wide barrier geometries and improves the optimization procedure. The flux carrier width is randomly generated according to the equation $w_{goal} = d_{k-1,k} / R_{w_k}$ in the range $R_{w_k} = [1.561, 1.88]$ (Figure6a). The range is empirically derived from several optimized designs.

Algorithm 1 Check feasibility function

```

1: Get:
2:  $r_{G_{1,k}}$  ▷ Virtual barrier mid points
3:  $\Delta r_{1,k_{out}}$  ▷ Barrier outer offsets
4:  $\Delta r_{1,k_{in}}$  ▷ Barrier inner offsets
5:  $R_{w_{1,k}} \rightarrow Rnd([1.561, 1.88])$  ▷ Flux carrier width goal ratios
6: function CHECKFEASIBILITY
7:   for  $k=2:N_{barriers}$  do
   ▷ Calculate distance between virtual barrier mid points
8:      $d_{k-1,k} = r_{G_{k-1}} - r_{G_k}$ 
   ▷ Calculate flux carrier width
9:      $w_{k-1,k} = (r_{G_{k-1}} - \Delta r_{k-1,in}) - (r_{G_k} + \Delta r_{k,out})$ 
   ▷ Calculate minimal flux carrier width
10:     $w_{goal} = d_{k-1,k} / R_{w_k}$ 
11:    if  $w_{k-1,k} \leq 0$  or  $w_{k-1,k} \leq w_{goal}$  then
   ▷ Barriers are not feasible, force feasibility
12:      function FORCEFEASIBILITY(
    $w_{goal}, d_{k-1,k}, \Delta r_{k,out}, \Delta r_{k-1,in}$ )
13:        ...
14:      return  $\Delta r'_{k,out}, \Delta r'_{k-1,in}$ 

```

Algorithm 2 Force feasibility function

```

1: function FORCEFEASIBILITY
2:    $A, B, A_{eq}, B_{eq} = []$  ▷ empty FMINCON parameters
3:    $opt \rightarrow default$  ▷ Use default FMINCON options
4:    $lb = [0 \ 0]$  ▷ Lower minimization bounds
5:    $ub = [d_{k-1,k} \ d_{k-1,k}]$  ▷ Upper minimization bounds
6:    $x_0 = 0.5 \cdot ub$  ▷ Initial guess
7:    $x_c = [\Delta r_{k,out} \ \Delta r_{k-1,in}]$  ▷ Minimization goal
   ▷ Find a solution which satisfies constraints and minimally changes input parameters  $x_c$  via
   FMINCON function
8:   function FMINCON(COSTFCN,  $x_0, B, A_{eq}, B_{eq}, lb, ub, CONSTRAINTFCN, w_{goal}, d_{k-1,k}, x_c, opt,$ 
    $k$ )
   ▷ FMINCON iteratively calls COSTFCN, CONSTRAINTFCN and returns values which satisfy
   the constraint(s) with minimal deviation from current offset vector  $x_c$ 
9:     ...
10:    return  $\Delta r'_{k,out}, \Delta r'_{k-1,in}$ 
11:   function COSTFCN( $x, x_c, k$ )
   ▷ COSTFCN is responsible for result search convergence
12:      $f = (x - x_c)^2$ 
13:      $F = Sum(f)$ 
14:   return  $F$ 
15:   function CONSTRAINTFCN( $x, w_{goal}, d_{k-1,k}$ )
   ▷ CONSTRAINTFCN calculates the deviation of generated flux carrier width from the goal
   width
16:      $x(1) \rightarrow \Delta r_{k,out}$ 
17:      $x(2) \rightarrow \Delta r_{k-1,in}$ 
18:      $w = (r_{G_{k-1}} + x(2)) - (r_{G_k} + x(1))$ 
19:      $= d_{k-1,k} - x(1) - x(2)$ 
20:      $P = w_{goal} - w$ 
21:   return  $P$ 
22: return  $\Delta r'_{k,out}, \Delta r'_{k-1,in}$ 

```

Overall, this system does not discard randomly generated infeasible geometry, but modifies it until feasibility is achieved (hence the name “forced” feasibility). A similar procedure can be implemented for any problem that can be described by smooth analytic functions implemented as user-defined CONSTRAINTFCN.

5.3. Handling of Inequality Constraints

Inequality constraints usually arise from various electromagnetic, thermal, mechanical, manufacturing, economic, or normative limits, such as maximum flux density in the stator tooth, maximum magnet temperature, maximum stress in the rotor bridge, minimum magnet dimensions, maximum active material cost, maximum noise, etc. [32].

The traditional approach to constraint handling uses penalty functions to penalize the solutions that violate the constraints. This principle is implemented in terms of weighted sums that modify each objective function. Despite the popularity of penalty functions, they have several drawbacks. The most important is the need for careful fine-tuning of the penalty factors responsible for efficiently approximating the feasible range. Moreover, this method may suffer from problems related to poor choice of weighting factors, which may affect convergence. In this paper, we use an improved constraint function algorithm developed by Žarko et al. [34].

Inequality constraints for this particular case are defined in Table 5. The constraint function g_1 checks rotor structural factor of safety at maximum over-speed ($1.2 \cdot n_{\max}$).

Table 5. List of inequality constraints.

No:	Constraint Description	Symbol	Limit
g_1	Stress yield factor at $1.2 \cdot n_{\max}$	FOS_{\min}	≥ 2
g_2	Magnetostatic torque at n_b	T_{static}	$\geq 600 \text{ Nm}$
g_3	Flux density in stator yoke	$B_{\text{sy,max}}$	$\leq 1.6 \text{ T}$
g_4	Flux density in stator tooth	$B_{\text{st,max}}$	$\leq 1.8 \text{ T}$
g_5	Power factor	$\cos \varphi_{\min}$	> 0.6
g_6	Torque ripple with skewing	$T_{\text{ripple,max}}$	$\leq 10 \%$

The procedure related to constraint function g_2 contains several subfunctions designed according to ultra-fast scaling laws [29]. Multiple magnetostatic FEA calculations are performed to find the maximum torque versus current phase advance curve and to determine the optimal maximum torque-per-ampere (MTPA) control angle by polynomial fitting (the input machine has one turn per coil and one parallel path). The number of turns per coil and the number parallel paths of the machine is then matched to the required base speed. The optimization initially assumes a fixed stack length (Table 2, parameter $l_{s \max}$). If the calculated torque at $l_{s \max}$ is smaller than required, the machine design does not satisfy the constraint. Finally, it is checked whether the stator phase current is smaller than the maximum inverter current; otherwise, the constraint is not satisfied. After this step, all magnetostatic calculations are completed. The results are extracted and evaluated in the following constraint functions. Constraint g_3 checks the maximum stator yoke flux density, while g_4 checks the maximum tooth flux density. The purpose is to penalize the high saturation and the designs with increased iron losses.

Finally, a transient FEA calculation is performed at base speed to determine the power factor, average torque, torque ripple, and terminal voltage. Constraint g_5 checks the power factor. The primary goal in this ePTO optimization case study was maximization of the average torque, while torque ripple was of secondary importance, therefore being handled in the constraint (g_6). As a torque-ripple mitigation option, a rotor skew was selected. Skewing angle is one stator slot or $360^\circ / 36 = 10^\circ$ mechanical degrees [35]. Without loss of generality, other more affordable, or more practical, torque-ripple mitigation techniques can be applied to this problem [36,37]. In addition, torque ripple can be included as another

optimization objective so that the design trade-off is made on the Pareto front of torque versus torque ripple.

If all constraints are satisfied, the final step is to compute the objective function f (19). η is the efficiency, and $T_{\text{trans,skew}}$ is the transient torque with applied rotor skew. The constants 700 and 0.96 represent scaling coefficients, which are used for combining torque and efficiency within a single objective function. Furthermore, these values are important for proper optimization convergence and were intentionally chosen to be larger than the peak torque and efficiency at the base speed to constrain the objective function to values ≤ 2 (important for the final comparison of the optimization convergence of forced feasibility and randomly generated geometries).

$$f = \frac{T_{\text{trans,skew}}}{700} + \frac{\eta}{0.96}. \quad (19)$$

6. Optimization Results

Five consecutive optimization runs of the DE algorithm with population size $NP = 24$ of geometries generated both randomly and with forced feasibility were performed (results in Tables 4 and 6).

To reduce optimization time and compare both approaches, most of the design parameters were taken from a previously optimized design [3]. Twenty-eight parameters were frozen (Table 2), and only 7 parameters were used for optimization (Table 3). This trade-off yields the same average objective function result (difference is +0.05%).

The average number of generations required to achieve convergence in the random generation case is 115.6, and 95.6 in the forced feasibility case, which is a reduction of 17.3%. In addition, in terms of computation time, the average convergence of forced feasibility is 3.34 h shorter (12.3% reduction).

When comparing the average torque results ($T_{\text{trans,skew}}$), both approaches yield practically the same outcome (Table 4). The remaining results (η , $B_{\text{sy,max}}$, $B_{\text{st,max}}$, $\cos \varphi$, T_{ripple}) are identical for forced feasibility and random generation. This is expected for two reasons: most of the parameters were taken from Reference [3], and the optimization algorithm is the same. Finally, the identical results confirm that forced feasibility does not affect negatively the optimization outcome.

Table 6. Optimization results.

Random Generated			Forced Feasibility		
Generation	f	t [h]	Generation	f	t [h]
89	1.8129	20.3	77	1.8136	18.9
91	1.8124	21.2	87	1.8145	21.2
106	1.8128	24.9	88	1.8132	21.9
132	1.8128	31.5	94	1.8133	23.8
160	1.8124	37.5	132	1.8133	32.9
Average			Average		
115.6	1.81266	27.08	95.6	1.81358	23.74

Table 4 summarizes the optimized rotor parameters for both optimization approaches. As mentioned earlier, the most important result is the fact that all parameters are greater than zero (neither the inner nor the outer blocking line sticks to the virtual centerline) and $\forall \Delta r_{k_{\text{out}}} \neq \forall \Delta r_{k_{\text{in}}}$. All optimized cross sections are shown in Figure 8, which confirms that the position of the centerline of the virtual barriers does not affect the optimization result.

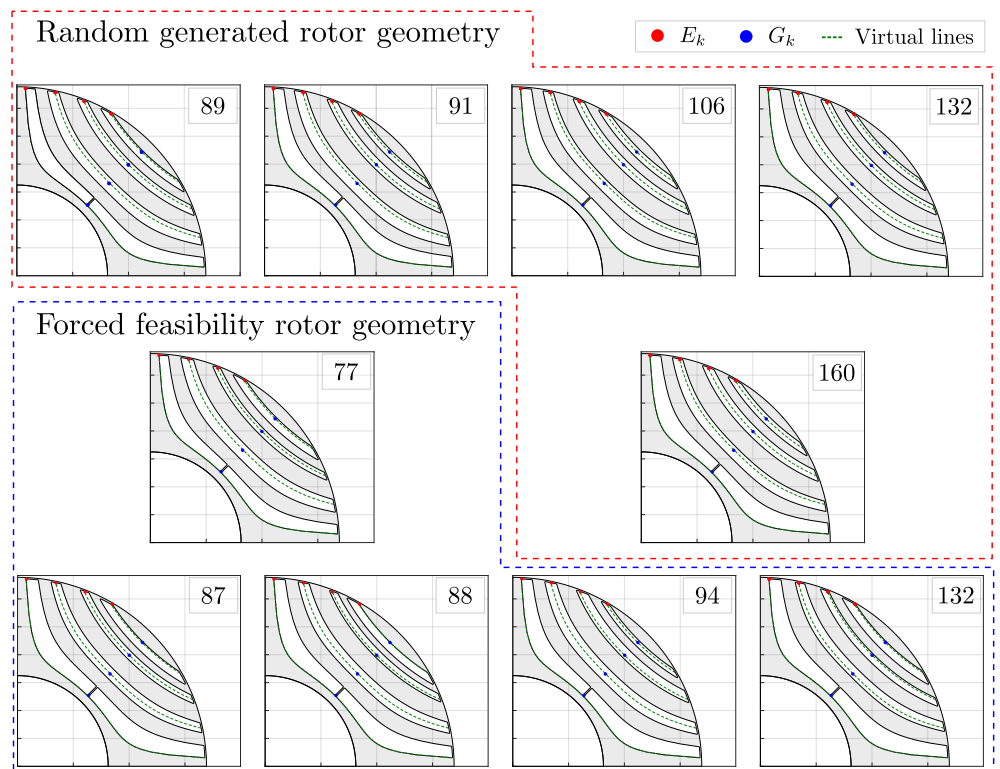


Figure 8. Comparison of optimized geometries in case of random generated and forced feasibility approach.

7. Conclusions

This paper demonstrates a novel automatic design procedure of SyRM rotor with minimum number of geometric parameters, which simplifies the design generation and reduces the optimization time. The presented procedure is implemented into an existing single objective DE optimization algorithm framework which interrupts evaluation of constraint functions when the inequality constraint is violated, thus saving computation time.

The second paper contribution is the introduction of novel forced feasibility concept which improves optimization convergence proved by successive comparative optimization runs with randomly generated rotor barrier geometries. The results show that properly implemented forced feasibility leads to a further reduction in optimization time (12.3% shorter).

The machine design originally presented in Reference [3] has 21 optimization variables. The entire optimization process took 7 days. Without the forced feasibility method, the process would be 12.3% longer (approximately 1 additional day). Considering that the optimization time is proportional to the number of parameters (i.e., a two-layer V-shape PM machine may have 44 parameters), it can be concluded that the total calculation time can be significantly reduced by using forced feasibility approach on different machine topologies.

Author Contributions: This paper is a continuation of the paper “Design and Optimization of Synchronous Reluctance Machine for actuation of Electric Multi-purpose Vehicle Power Take-Off” submitted for ICEM 2020 conference. B.B. created a preset model and automated geometry scripting with a minimal set of parameters. The original multi-objective optimization procedure was adapted to support single-objective optimization, which is easier to evaluate in terms of forced feasibility impact on optimization time reduction. B.B. adapted the original code developed by S.S., simulated the results, and prepared all tables and figures. S.S. supervised the process and formulated the contributions. T.J. worked on the mathematical formulation of the forced feasibility and the practical implementation of the algorithm through the MATLAB fmincon minimization function. All authors have read and agreed to the published version of the manuscript

Funding: This work was partially supported by the Croatian Science Foundation under the project IP-2018-01-5822 - HYDREL.

Institutional Review Board Statement: Not applicable.

Informed Consent Statement: Not applicable.

Conflicts of Interest: The authors declare no conflict of interest.

The following abbreviations are used in this manuscript:

EV	Electric vehicle
DE	Differential evolution
eMPV	Electric multipurpose vehicle
ePTO	Electric power take-off
FEA	Finite element analysis
IPM	Interior permanent magnet machine
MTPA	Maximum torque per ampere
PM	Permanent magnet
PTO	Power take-off
SyRM	Synchronous reluctance machine

References

- European Environment Agency. Electric Vehicles in Europe. <https://www.eea.europa.eu/publications/electric-vehicles-in-europe>, accessed on 2019-01-02.
- Ban, B.; Stipetić, S. Electric Multipurpose Vehicle Power Take-Off: Overview, Load Cycles and Actuation via Synchronous Reluctance Machine. *ACEMP-OPTIM* **2019**.
- Ban, B.; Stipetić, S. Design and Optimization of Synchronous Reluctance Machine for actuation of Electric Multi-purpose Vehicle Power Take-Off. *Proceedings - 2020 International Conference on Electrical Machines, ICEM 2020* **2020**, pp. 1–1.
- Alberti, L.; Bianchi, N.; Boglietti, A.; Cavagnino, A. Core axial lengthening as effective solution to improve the induction motor efficiency classes. *IEEE Energy Conversion Congress and Exposition: Energy Conversion Innovation for a Clean Energy Future, ECCE 2011, Proceedings*, 2011.
- Bramerdofer, G.; Cavagnino, A.; Vaschetto, S. Impact of IM pole count on material cost increase for achieving mandatory efficiency requirements. *IECON Proceedings (Industrial Electronics Conference)*, 2016.
- Agamloh, E.B.; Boglietti, A.; Cavagnino, A. The incremental design efficiency improvement of commercially manufactured induction motors. *IEEE Transactions on Industry Applications* **2013**.
- El-Refaie, A.M. Motors/generators for traction/propulsion applications: A review, 2013.
- Pellegrino, G.; Cupertino, F.; Gerada, C. Automatic Design of Synchronous Reluctance Motors Focusing on Barrier Shape Optimization. *IEEE Transactions on Industry Applications* **2015**.
- Lu, C.; Ferrari, S.; Pellegrino, G. Two Design Procedures for PM Synchronous Machines for Electric Powertrains. *IEEE Transactions on Transportation Electrification* **2017**.
- Zhu, X.; Wu, W.; Quan, L.; Xiang, Z.; Gu, W. Design and Multi-Objective Stratified Optimization of a Less-rare-earth Hybrid Permanent Magnets Motor with High Torque Density and Low Cost. *IEEE Transactions on Energy Conversion* **2018**.
- Bonthu, S.S.R.; Choi, S.; Baek, J. Design Optimization with Multiphysics Analysis on External Rotor Permanent Magnet-Assisted Synchronous Reluctance Motors. *IEEE Transactions on Energy Conversion* **2018**.
- Tapia, J.A.; Parviainen, A.; Pyrhonen, J.; Lindh, P.; Wallace, R.R. Optimal design procedure for an external rotor permanent-magnet machine. *Proceedings - 2012 20th International Conference on Electrical Machines, ICEM 2012*, 2012.
- Lei, G.; Bramerdorfer, G.; Ma, B.; Guo, Y.; Zhu, J. Robust Design Optimization of Electrical Machines: Multi-objective Approach. *IEEE Transactions on Energy Conversion* **2020**, pp. 1–1.
- Lei, G.; Bramerdorfer, G.; Liu, C.; Guo, Y.; Zhu, J. Robust Design Optimization of Electrical Machines: A Comparative Study and Space Reduction Strategy. *IEEE Transactions on Energy Conversion* **2020**.
- Babetto, C.; Bacco, G.; Bianchi, N. Synchronous Reluctance Machine Optimization for High-Speed Applications. *IEEE Transactions on Energy Conversion* **2018**.
- Xu, L.; Wu, W.; Zhao, W.; Liu, G.; Niu, S. Robust Design and Optimization for a Permanent Magnet Vernier Machine With Hybrid Stator. *IEEE Transactions on Energy Conversion* **2020**, pp. 1–1.
- Howard, E.; Kamper, M.J. Weighted Factor Multiobjective Design Optimization of a Reluctance Synchronous Machine. *IEEE Transactions on Industry Applications* **2016**, *52*, 2269–2279.
- Kamper, M.J.; Van Der Merwe, F.S.; Williamson, S. Direct Finite Element Design Optimisation of the Cageless Reluctance Synchronous Machine. *IEEE Transactions on Energy Conversion* **1996**, *11*, 547–553.

19. Dmitrievskii, V.; Prakht, V.; Kazakbaev, V. IE5 Energy-Efficiency Class Synchronous Reluctance Motor with Fractional Slot Winding. *IEEE Transactions on Industry Applications* **2019**, *55*, 4676–4684.
20. Yamashita, Y.; Okamoto, Y. Design Optimization of Synchronous Reluctance Motor for Reducing Iron Loss and Improving Torque Characteristics Using Topology Optimization Based on the Level-Set Method. *IEEE Transactions on Magnetics* **2020**, *56*, 36–39.
21. Storn, R.; Price, K. Differential Evolution - A Simple and Efficient Heuristic for Global Optimization over Continuous Spaces. *Journal of Global Optimization* **1997**.
22. Bramerdorfer, G.; Zavoianu, A.C.; Silber, S.; Lughofer, E.; Amrhein, W. Possibilities for Speeding Up the FE-Based Optimization of Electrical Machines-A Case Study. *IEEE Transactions on Industry Applications* **2016**.
23. Liu, X.; Slemon, G.R. An improved method of optimization for electrical machines. *IEEE Transactions on Energy Conversion* **1991**.
24. Stipetic, S.; Zarko, D.; Kovacic, M. Optimised design of permanent magnet assisted synchronous reluctance motor series using combined analytical-finite element analysis based approach. *IET Electric Power Applications* **2016**.
25. Zarko, D.; Stipetic, S.; Martinovic, M.; Kovacic, M.; Jercic, T.; Hanic, Z. Reduction of computational efforts in finite element-based permanent magnet traction motor optimization. *IEEE Transactions on Industrial Electronics* **2017**, *65*, 1799–1807.
26. Lampinen, J. Multi-Constrained Nonlinear Optimization by the Differential Evolution Algorithm. In *Soft Computing and Industry*; 2002.
27. Price, K.; Storn, R. Matlab code for differential evolution. <http://www1.icsi.berkeley.edu/~simstorn/code.html>, accessed on 2020-01-23.
28. Motor Design Ltd.. Motor-CAD / Motor-LAB software. <https://www.motor-design.com/motor-cad/>, accessed on 2020-01-23.
29. Stipetic, S.; Zarko, D.; Popescu, M. Ultra-fast axial and radial scaling of synchronous permanent magnet machines. *IET Electric Power Applications* **2016**, *10*, 658–666.
30. Gamba, M.; Pellegrino, G.; Cupertino, F. Optimal Number of Rotor Parameters for the Automatic Design of Synchronous Reluctance Machines. *Proceedings - 2014 International Conference on Electrical Machines, ICEM 2014* **2014**, pp. 1334–1340.
31. Cupertino, F.; Pellegrino, G.; Cagnetta, P.; Ferrari, S.; Perta, M. SyRE: Synchronous Reluctance (machines) - evolution. <https://sourceforge.net/projects/syr-e/>, accessed on 2021-04-23.
32. Stipetic, S.; Miebach, W.; Zarko, D. Optimization in design of electric machines: Methodology and workflow. *Joint International Conference - ACEMP 2015: Aegean Conference on Electrical Machines and Power Electronics, OPTIM 2015: Optimization of Electrical and Electronic Equipment and ELECTROMOTION 2015: International Symposium on Advanced Electromechanical Moti* **2016**, pp. 441–448.
33. Mathworks. Matlab fmincon function. <https://se.mathworks.com/help/optim/ug/fmincon.html>, accessed on 2020-01-13.
34. Žarko, D.; Stipetić, S. Criteria for optimal design of interior permanent magnet motor series. *Proceedings - 2012 20th International Conference on Electrical Machines, ICEM 2012*, 2012.
35. Bomela, X.B.; Kamper, M.J. Effect of Stator Chording and Rotor Skewing on Performance of Reluctance Synchronous Machine. *IEEE Transactions on Industry Applications* **2002**, *38*, 91–100.
36. Ferrari, S.; Armando, E.; Pellegrino, G. Torque Ripple Minimization of PM-assisted Synchronous Reluctance Machines via Asymmetric Rotor Poles. 2019 IEEE Energy Conversion Congress and Exposition (ECCE), 2019, pp. 4895–4902.
37. Ferrari, S.; Pellegrino, G.; Davoli, M.; Bianchini, C. Reduction of Torque Ripple in Synchronous Reluctance Machines through Flux Barrier Shift. 2018 XIII International Conference on Electrical Machines (ICEM), 2018, pp. 2290–2296.

Publication 5: Absolutely Feasible Synchronous Reluctance Machine Rotor Barrier Topologies with Minimal Parametric Complexity

Paper details:

B. Ban and S. Stipetić "Absolutely Feasible Synchronous Reluctance Machine Rotor Barrier Topologies with Minimal Parametric Complexity", in Special Issue Synchronous Reluctance Motor-Drive Advancements, Machines 2022, 10(3), 206. January 2022.

Available at:<https://doi.org/10.3390/machines10030206>

Article

Absolutely Feasible Synchronous Reluctance Machine Rotor Barrier Topologies with Minimal Parametric Complexity

 Branko Ban ^{1,2,*}  and Stjepan Stipetic ¹ 

¹ Faculty of Electrical Engineering and Computing (FER), Department of Electric Machines, Drives and Automation, University of Zagreb, Unska 3, 10000 Zagreb, Croatia; stjepan.stipetic@fer.hr

² Torquery Consulting, Blidvädersgatan 56, 41830 Göteborg, Sweden

* Correspondence: branko.ban@fer.hr

Abstract: The first step in the synchronous reluctance machine design is the selection of rotor flux barrier type. The literature provides various barrier construction methods with a common goal of reducing parametric complexity. However, too excessive simplification can lead to decreased performance, while overly complex geometries tend to increase optimization time. This paper presents a set of novel flux barrier construction methods with an increased degree of freedom and minimal geometrical complexity. The paper proposes four topologies based on circular, hyperbolic, and original Zhukovsky lines. When considering parametrization complexity, the original Zhukovsky type is the simplest, but it has barrier depth limitations. Other topologies have equal complexity. The paper proposes a novel Modified Zhukovsky variable depth type based on geometrical conformal mapping of the original Zhukovsky lines. The step-by-step construction of each topology is presented in a form of pseudo-code with detailed comments and illustrations. Overall, the presented research provides a valuable starting point for the designer who wants to investigate different smooth rotor barrier topologies.

Keywords: synchronous reluctance; barrier comparison; rotor topology; conformal mapping; optimization



Citation: Ban, B.; Stipetic, S. Absolutely Feasible Synchronous Reluctance Machine Rotor Barrier Topologies with Minimal Parametric Complexity. *Machines* **2022**, *10*, 206. <https://doi.org/10.3390/machines10030206>

Academic Editor: Toomas Vaimann

Received: 31 January 2022

Accepted: 10 March 2022

Published: 11 March 2022

Publisher's Note: MDPI stays neutral with regard to jurisdictional claims in published maps and institutional affiliations.



Copyright: © 2022 by the authors. Licensee MDPI, Basel, Switzerland. This article is an open access article distributed under the terms and conditions of the Creative Commons Attribution (CC BY) license (<https://creativecommons.org/licenses/by/4.0/>).

1. Introduction

In recent years, the synchronous reluctance machine (SyRM) has become commercially viable as a high-efficiency alternative to induction (IM) and interior permanent magnet machines (IPM). The main benefit of the SyRM is that the rotor has no squirrel cage, windings or magnets, just electric steel plates forming a rotor package.

Due to the highest torque and power density, interior rare earth permanent magnet synchronous machines (IPM) are preferred for automotive traction. On the other hand, the use of rare earth permanent magnet (PM) materials, such as neodymium or dysprosium, has historically been a commercial risk [1,2].

Currently, there is no commercial use of synchronous reluctance machines (SyRM) for automotive traction, but having in mind the market uncertainties and potential production cost reduction, they represent a possible alternative [3,4].

On the other hand, commercial vehicles apart from electric traction, have to actuate additional body systems (usually powered by some sort of hydraulic pump). The interface towards external systems is referred as electric power take-off (e-PTO). Considering that the e-PTO needs to be reliable, robust, and cheap, SyRM is the preferred alternative [5–7].

In recent decades, SyRM research has focused on improving the rotor barrier design, minimizing the torque ripple, and increasing the power factor [8]. Literature provides references to several barrier topologies: circular [9,10], hyperbolic [11,12], Zhukovsky fluid type [13,14], segmented, etc. Open-source SyRE project offers more details and instructions on geometry generation [15].

The common goal in barrier construction strategy is the reduction of parametric complexity. However, too simplified rotor topologies can lead to decreased performance, while

too complex geometries yield better performance, but also tend to increase optimization time (increase is proportional to the parametric complexity).

By merging both approaches, this paper presents a set of flux barrier construction methods with an increased degree of freedom and minimal parametric complexity, based on non-dimensional rotor parameters.

Considering that sharp edges tend to cause mechanical issues at high rotational speeds, only barrier topologies based on smooth analytical functions have been analyzed (circular, hyperbolic, and Zhukovsky).

By definition, Zhukovsky barrier lines are streamlines and cannot be analytically modified to secure variable barrier depth, in this case, conformal mapping is used to create a novel Modified Zhukovsky barrier type with variable depth lines. The following chapters will demonstrate automated barrier design and related pseudo-code for the following topologies:

1. Circular variable depth (CrVD), Figure 1b
2. Variable eccentricity hyperbolic (HyVE), Figure 1c
3. Original Zhukovsky (Zh), Figure 1d (red)
4. Modified Zhukovsky variable depth (MZhVD), Figure 1d (blue).

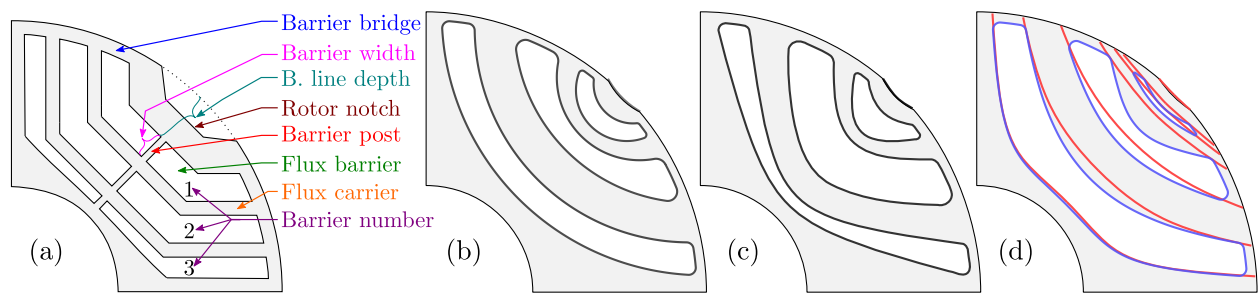


Figure 1. (a) SyRM terminology; SyRM rotor barrier types: (b) Circular variable depth; (c) Hyperbolic variable eccentricity; (d) Modified Zhukovsky (blue), original Zhukovsky (red).

2. Geometric Feasibility

The term feasibility usually refers to the solution and means that the solution satisfies all the given constraints. There is another type of feasibility called *geometric or model feasibility*. A geometrically feasible model is valid for solving if: there are no overlapping edges, negative lengths, or non-conventional geometric relations that will inevitably produce issues after optimization starts.

This is especially important when using template-based design software. The generation of such a non-valid model can be avoided in several ways (e.g., barrier 1 (blue) collides with barrier 2 (yellow), the collision is marked in red, Figure 2a). In the first case, the complete set of optimization parameters is initialized until geometric feasibility is achieved [16].

The alternative is forced feasibility, where each infeasible design is subjected to parameter modification until feasibility is reached, e.g., barrier 1 (blue) and barrier 2 (yellow) are modified until the minimum flux carrier width $w_{c \min}$ is reached, Figure 2b [7].

The final approach is to secure that the design is always feasible.

The example is a SyRM with three hyperbolic barriers where barrier depth is varied by hyperbolic eccentricity of each inner and outer barrier line (Figure 3b).

In some cases, the complete freedom in varying the eccentricity causes the inner and outer barrier collision (Figure 3a), which inevitably leads to infeasible designs.

On the other hand, if the designer wants to ensure feasibility, one solution is to parametrize the eccentricity of each outer barrier line relative to the eccentricity of each inner barrier, e.g., (1).

$$\begin{aligned}
 e_{3\text{ in}} &\in [1.2\ 1.3] & e_{3\text{ out}} &\in [e_{3\text{ in}}\ 1.35] \\
 e_{2\text{ in}} &\in [e_{3\text{ out}}\ 1.4] & e_{2\text{ out}} &\in [e_{2\text{ in}}\ 1.45] \\
 e_{1\text{ in}} &\in [e_{2\text{ out}}\ 1.5] & e_{1\text{ out}} &\in [e_{1\text{ in}}\ 1.55]
 \end{aligned}
 \tag{1}$$

Unfortunately, this option generates constantly changing parameter limits, which can lead to a suboptimal design. Considering the specifics of the SyRM rotor, the rotor geometry can be defined to always yield a feasible design thus achieving *absolute feasibility*. Instead of directly using eccentricities as parameters, a better approach is to use dimensionless inner and outer barrier depth parameters ($D_{\text{in}}, D_{\text{out}} \in [0, 1]$) for indirect calculation of respective eccentricities. The following text provides detailed instructions on absolutely feasible rotor construction with the corresponding pseudo-code which accepts any pole and barrier number.

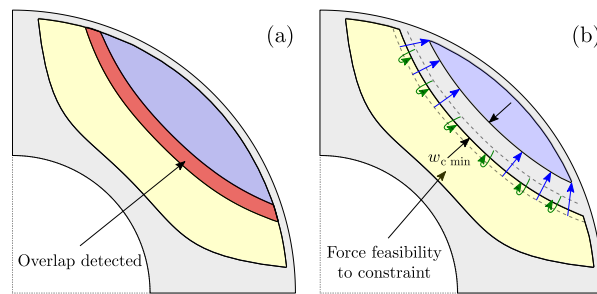
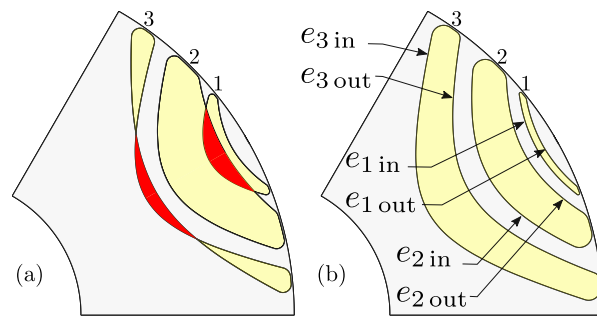


Figure 2. Infeasible geometry (a) and forced feasibility (b).



$$e_{1..3\text{ in}} \neq e_{1..3\text{ out}} \qquad e_{1..3\text{ in}} = e_{1..3\text{ out}}$$

Figure 3. Illustration of infeasible (a) and feasible geometry (b).

3. Design Automation

The following figures are drawn for illustrative purposes and valid for a three barrier rotor ($k = 3$), naming and description of all parameters is explained in Table 1. Vector variables are bolded, e.g., \mathbf{R} is a variable vector, while R represents a scalar variable.

The initial step in rotor construction (Figure 4a) is to specify number of pole pairs (p), rotor barriers (k) and barrier bridge thickness (w_{bb}). The user then specifies dimensionless $\vartheta_{\text{min}}, \vartheta_{\text{max}} \in [0, 1]$ (Table 1, 18–19). Temporary construction points vector $\mathbf{E}_{1..k\text{ temp}}$ is then created with equidistant angular spacing $\Delta\vartheta_r = (\vartheta_{\text{max}} - \vartheta_{\text{min}})/k$. Barrier notch point (E_n) is defined via additional parameter ϑ_{notch} (Table 1, 20) relative to ϑ_{min} with radial component equal to rotor radius. Note that the entire geometry is initially constructed in vertical manner (center pole axis is at the angle of 90°).

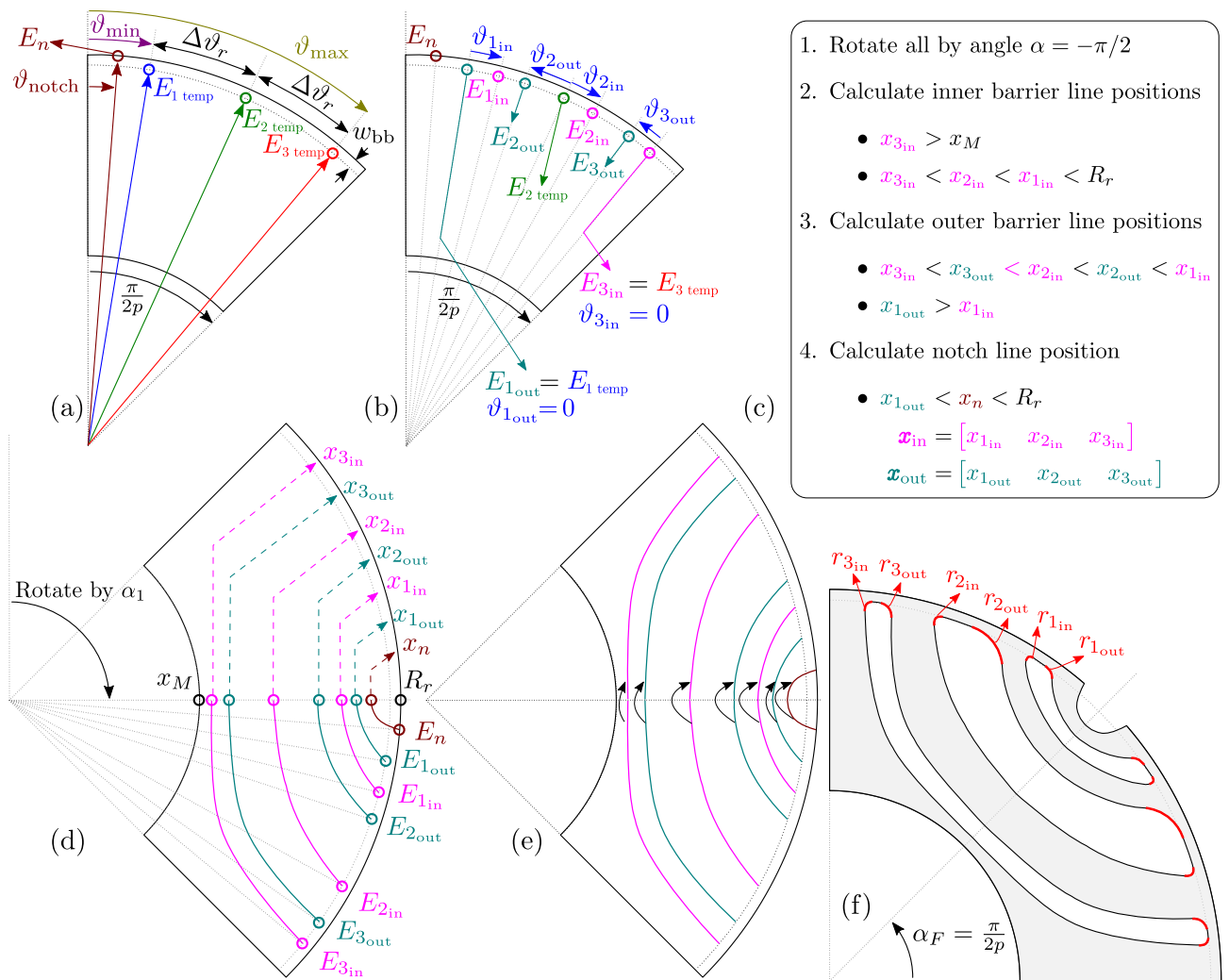


Figure 4. Rotor barrier construction procedure. Initial rotor construction step (a); Construction of inner and outer barrier line starting points (b); calculation of barrier intersection points (c); calculation of barrier vertices (d); vertex mirroring (e); rotation around center and addition of barrier fillets (f);

The second step (Figure 4b) is the construction of inner and outer barrier line starting points (E_{in}, E_{out}). The points are calculated relative to $E_{1..k temp}$, based on additional set of dimensionless parameters $\vartheta_{1..k in}, \vartheta_{1..k out} \in [0, 1]$ (Table 1, 6–11).

The third step is rotation around the center point by the specified angle (in this case $\alpha_1 = -\pi/2$). Barrier line starting points E_{in}, E_{out}, E_n (and additional depth parameters D_{in}, D_{out}, D_n depending of the barrier type) are forwarded to the selected construction function which calculates barrier line intersection points (x_{in}, x_{out}). The intersection points are calculated based on depth parameters and feasibility conditions listed in Figure 4c. The function returns all inner and outer barrier line vertices ($X_{in}, Y_{in}, X_{out}, Y_{out}, X_n, Y_n$), Figure 4d.

The next step is mirroring line vertices around the horizontal axis (Figure 4e).

The final step is the rotation around the center point by the angle $\alpha_F = \pi/(2p)$. Barrier fillets ($r_{1..k in}, r_{1..k out} \in [0, 1]$, Table 1, 12–17) responsible for securing mechanical integrity of the rotor are added to the geometry, and final rotor geometry is exported as to the FEA tool (Figure 4f). Adding precise fillets to the discrete lines is a complex problem which is planned to be explained in the future publications. Detail barrier construction steps from Figure 4b–d are discussed in the following sections.

Table 1. Example list of design parameters. Color coding is according to Fig.4 variables.

No:	Description	Symbol	Value/Range	Unit
1	Rotor diameter	D_r	100	mm
2	Shaft diameter	D_{sh}	54	mm
3	Barrier number	k	3	-
4	Pole pairs	p	2	-
5	Barrier bridge	w_{bb}	0.3	mm
6	Point angle in	ϑ_{1in}	[0.2, 0.5]	-
7	Point angle out	ϑ_{1out}	0-	-
8	Point angle in	ϑ_{2in}	[0, 0.3]	-
9	Point angle out	ϑ_{2out}	[0, 0.2]	-
10	Point angle in	ϑ_{3in}	0-	-
11	Point angle out	ϑ_{3out}	[0, 0.5]	-
12–14	Corner rad. in	$r_{1..k_{in}}$	[0, 1]	-
15–17	Corner rad. out	$r_{1..k_{out}}$	[0, 1]	-
18	Min. angle	ϑ_{min}	[0.15, 0.3]	-
19	Max. angle	ϑ_{max}	[0.9, 0.95]	-
20	Notch angle	ϑ_n	[0.1, 1]	-
22–24	Barrier depths in	$D_{1..k_{in}}$	[0.2, 1]	-
25–27	Barrier depths out	$D_{1..k_{out}}$	[0.2, 1]	-
28	Notch depth	D_n	[0, 1]	-

Barrier Depth Variation

Considering that the barrier width has a substantial impact on the machine performance, this section will explain how inner and outer barrier depth coefficients affect each of the studied topologies, with a simplified presumption of equal line starting points.

Width of the each barrier depends on initial inner and outer line starting points E_{in}, E_{out} , and depth coefficients D_{in}, D_{out} . Depending on the depth parameter combination, barrier width can be variable, or uniform. Uniform width is a special case where CrVD barriers are concentric (Figure5a, green). HyVE barriers can be approximately uniform when they have equal eccentricity (Figure5b, green). These variants are included in CrVD and HyVE pseudo-code, and will not be studied in detail.

In general, CrVD and HyVE depth variation is unconstrained resulting in variable barrier width (Figure5a,b, blue).

Zh barrier type (Figure5c) is a special case because it does not support any depth variation. Barrier line depths are defined directly from starting points and cannot be modified. In order to explore the possible benefits of depth variation, Zh type has been modified as MZhVd where barrier depths have full freedom (Figure5d).

An example of different barrier line depth parameter combinations is provided in the (Table2).

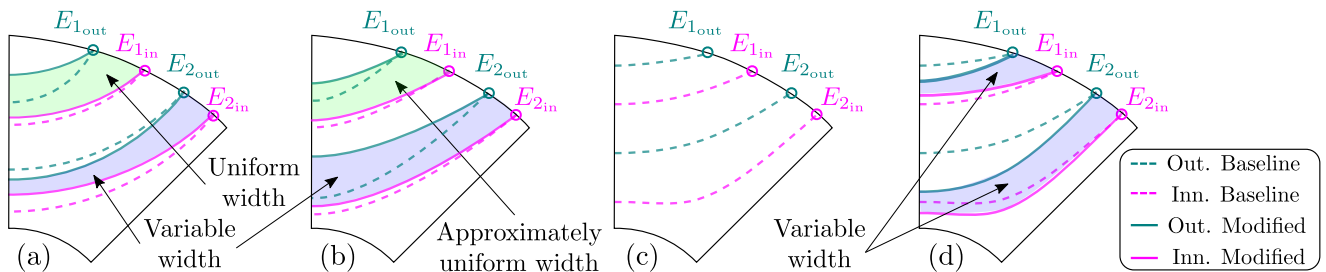


Figure 5. Barrier depth variation influence on different 2-barrier ($k = 2$) SyRM topologies. Circular (a); Hyperbolic (b), Zhukovsky (c) and Modified Zhukovsky barrier types (d).

Table 2. Illustrative depth coefficient table for Figure5.

		Baseline Barrier Depths				Modified Barrier Depths			
	Abbr.	D_{1out}	D_{1in}	D_{2out}	D_{2in}	D_{1out}	D_{1in}	D_{2out}	D_{2in}
(a)	CrVD	0.35	0.50	0.65	0.90	0.40	0.55	0.70	0.80
(b)	HyVE	0.40	0.50	0.80	0.90	0.35	0.45	0.60	0.85
(c)	Zh	0.10	0.45	0.60	0.85	-	-	-	-
(d)	MZhVD	0.10	0.45	0.60	0.85	0.20	0.40	0.80	0.90

4. Standard Rotor Barriers

4.1. Zhukovsky Barrier Construction

After definition of all inner and outer barrier line starting points (E_{in}, E_{out}, E_n), Figure6a, the entire geometry is rotated by $\alpha_{1 Zh} = -(\pi/2 - \tau_{pole}/2)$ (Algorithm1: ln:2, Figure6b, $\tau_{pole} = (2\pi)/(2p) = \pi/p$ is the angular pole step.). This partial rotation must be performed because Zhukovsky equations are defined on angular range $[0, \pi/p]$.

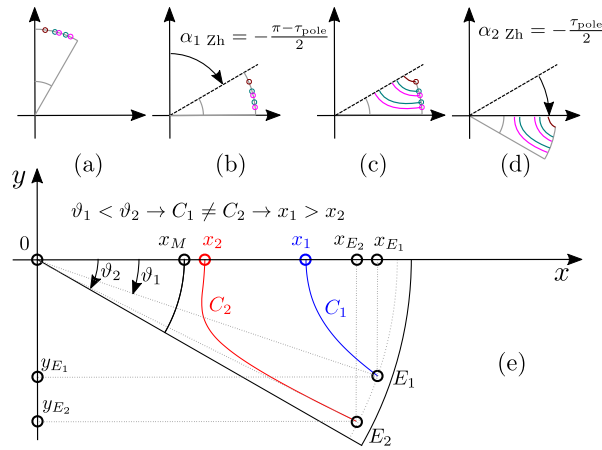


Figure 6. Zhukovsky barrier construction. Subfigures (a)–(e) are explained in the Sections4.1-4.1.3.

Algorithm 1 Construction of Zhukovsky barriers

```

1:  $\tau_{pole} = 2\pi/(2p)$ 
2: Rotate all by  $\alpha_{1 Zh} = -(\pi/2 - \tau_{pole}/2)$  and get:  $E_{in}, E_{out}, E_n$ 
3:  $\Delta r = 0$ 
4:  $[X_{in}, Y_{in}, X_{out}, Y_{out}, X_n, Y_n] = \text{GETZHUKOVSKYLINES}(E_{in}, E_{out}, E_n)$ 
5: function GETZHUKOVSKYLINES( $E_{in}, E_{out}, E_n$ )
6:    $k = N_{barrier}$   $\triangleright$  Calculate inner and outer barrier lines
7:    $[X_{in}, Y_{in}] = \text{GETZHUKLINES}(E_{in}, k)$ 
8:    $[X_{out}, Y_{out}] = \text{GETZHUKLINES}(E_{out}, k)$ 
9:    $\triangleright$  Calculate notch line
10:   $k_n = 1$   $\triangleright$  Notch has only one barrier line
11:   $[X_n, Y_n] = \text{GETZHUKLINES}(E_n, k_n)$ 
11: function GETZHUKLINES( $E, k$ )
12:    $C = \sin(p \cdot \vartheta_E) \cdot \left[ \left( \frac{r_E + \Delta r}{D_{sh}/2} \right)^{2p} - 1 \right] / \left( \frac{r_E + \Delta r}{D_{sh}/2} \right)^p$ 
13:    $\triangleright$  Calculate barrier polar angles
14:    $\varphi_{start} = \vartheta_E$ 
15:    $\varphi_{end} = \tau_{pole}/2$ 
16:   for  $i = 1 : k$  do
17:      $\vartheta(:, i) = \text{Linspace}(\varphi_{start}(i), \varphi_{end}, N_{points})$ 
18:      $\triangleright$  Calculate barrier line vertices
19:      $r = \frac{D_{sh}}{2} \sqrt[2p]{\left( C + \sqrt{C^2 + 4 \sin^2(p\vartheta)} \right) / (2 \sin(p\vartheta))}$ 
20:      $[X, Y] = \text{pol2cart}(\vartheta, r)$ 
21:   return  $X, Y$ 
22: Rotate all by  $\alpha_{2 Zh} = -\tau_{pole}/2$ 
23: return  $X_{in}, Y_{in}, X_{out}, Y_{out}, X_n, Y_n$ 

```

4.1.1. Inner Line Calculation

The first step is the calculation of GETZHUKLINES barrier line function (Algorithm1: ln:7) based on E_{in} and number of barriers k . Note that there are no depth parameters. By

definition Zhukovsky barriers are streamlines which cannot mutually intersect. Barrier line profiles (Figure6e) are derived from conformal mapping theory and the Zhukovsky airflow potential formulation [14,15]. This was originally developed to describe the flow paths of fluids channeled by two infinite plates forming an angle π/p , and a plug centred at the origin of the reference frame. In the solid rotor context, the plug represents the non-magnetic shaft with a radius of $D_{sh}/2$. Equations Algorithm1: ln:12 and Algorithm1: ln:17 express the magnetic field potential lines in parametric form [7].

Next, polar barrier vertices r, ϑ are calculated based on coefficient vector C , starting point polar coordinates ϑ_E and number of barriers k (Algorithm1: ln:12–18). Finally, GETZHUKLINES function returns X_{in}, Y_{in} vertices.

4.1.2. Outer Line Calculation

Outer barrier line vertices X_{out}, Y_{out} (Algorithm1: ln:8) are calculated in the same way as inner lines.

4.1.3. Notch Line Calculation

Notch is specific because it has only one barrier line ($k_n = 1$) (Algorithm1: ln:10). The function GETZHUKLINES returns X_n, Y_n which completes the calculation of all barrier lines (Figure6c). Finally, to be compatible with the rest of the barrier construction procedures, the geometry is rotated by $\alpha_{2Zh} = -\tau_{pole}/2$ (Algorithm1: ln:20, Figure6d).

The next steps (not described within Algorithm1) are mirroring vertices around horizontal axis (Figure4e), adding barrier fillets, and geometry rotation around center point (Figure4f).

Note that Zhukovsky construction pseudo-code is the simplest of all alternatives due to the polar streamline equations (Algorithm1: ln:12,17).

4.2. Circular Barrier Construction

After definition of all inner and outer barrier line starting points and depth parameters ($E_{in}, E_{out}, E_n, D_{in}, D_{out}, D_n$), Figure7a, the entire geometry is rotated by $\alpha_{1CrVD} = -\pi/2$ (Algorithm2: ln:1, Figure7b).

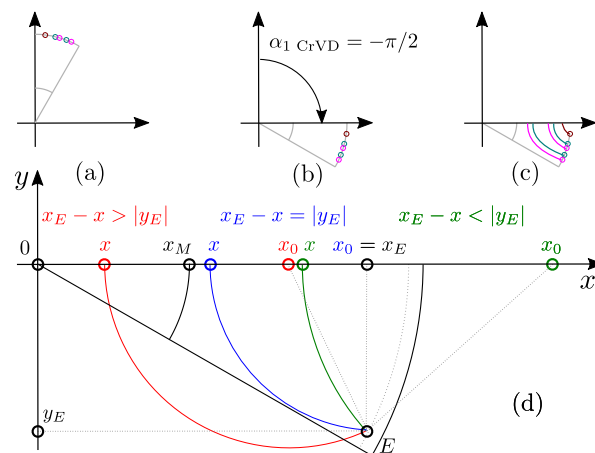


Figure 7. Circular barrier construction. Subfigures (a)–(d) are explained within the Sections4.2-4.2.3.

4.2.1. Inner line calculation

Lets first consider GETINNERLINES function which calculates inner line vertices (X_{in}, Y_{in}) and intersections (x_{in}) based on E_{in}, D_{in} and number of barriers k (Algorithm2: ln:6).

The intersections (Figure4d) are critical for barrier calculation and in case of circular barriers, they depend on the inequality $x_E - x < |y_E|$ where x represents the inner or outer intersection. If the condition is fulfilled, the constructed circle is feasible (Figure7d, green)

and the intersection can be calculated based on inner barrier limits (Algorithm2: In:15,20). Otherwise, the circle is infeasible (Figure7d, red) and the intersection point is calculated from barrier line starting point (Algorithm2: In:17,22).

In case of the most inner line ($i = k$), the feasibility limit is rotor shaft (x_M), and the intersection $x_{in}(i)$ is calculated via (Algorithm2: In:15). For the second most inner line ($i = k - 1$), feasibility limit is $x_{in}(i + 1)$ and the intersection is calculated via (Algorithm2: In:20). All inner line intersections are then iteratively calculated following the Algorithm2: In:12–22 procedure.

Next, GETCRCVTX function (Algorithm2: In:23) based on calculated intersections x_{in} , starting point coordinates $x_{E_{in}}, y_{E_{in}}$ and k , calculates the circle origins x_0 and radius R_r , and returns barrier vertices X_{in}, Y_{in} (Algorithm2: In:39–50). Finally, GETINNERLINES returns X_{in}, Y_{in}, x_{in} .

Algorithm 2 Construction of circular barriers

```

1: Rotate all by  $\alpha_1 \text{ CrVD} = -\pi/2$ 
2: Get:  $E_{in}, E_{out}, E_n, D_{in}, D_{out}, D_n$ 
3:  $[X_{in}, Y_{in}, X_{out}, Y_{out}, X_n, Y_n] = \text{GETCRCLINES}(E_{in}, E_{out}, E_n, D_{in}, D_{out}, D_n)$ 
4: function GETCRCLINES( $E_{in}, E_{out}, E_n, D_{in}, D_{out}, D_n$ )
5:    $k = N_{\text{barrier}}$   $\triangleright$  Calculate inner and outer lines
6:    $[X_{in}, Y_{in}, x_{in}] = \text{GETINNERLINES}(E_{in}, D_{in}, k)$ 
7:    $[X_{out}, Y_{out}, x_{out}] = \text{GETOUTERLINES}(E_{out}, D_{out}, x_{in}, k)$ 
8:    $\triangleright$  Calculate notch line
9:    $k_n = 1$   $\triangleright$  Notch has only one barrier line
10:   $[X_n, Y_n, x_n] = \text{GETOUTERLINES}(E_n, D_n, x_{out}(1), k_n)$ 
11: function GETINNERLINES( $E_{in}, D_{in}, k$ )
12:    $x_M = D_{sh}/2$ 
13:   for  $i = k : 1$  do
14:     if  $i = k$  then
15:       if  $x_{E_{in}}(i) - x_M < |y_{E_{in}}(i)|$  then
16:          $x_{in}(i) = x_M + (x_{E_{in}}(i) - x_M) \cdot D_{in}(i)$ 
17:       else
18:          $x_{in}(i) = x_{E_{in}}(i) - |y_{E_{in}}(i)| \cdot D_{in}(i)$ 
19:     else
20:       if  $x_{E_{in}}(i) - x_{in}(i + 1) < |y_{E_{in}}(i)|$  then
21:          $x_{in}(i) = x_{in}(i + 1) + (x_{E_{in}}(i) - x_{in}(i + 1)) \cdot D_{in}(i)$ 
22:       else
23:          $x_{in}(i) = x_{E_{in}}(i) - |y_{E_{in}}(i)| \cdot D_{in}(i)$ 
24:    $[X_{in}, Y_{in}] = \text{GETCRCVTX}(x_{in}, x_{E_{in}}, y_{E_{in}}, k)$ 
25:   return  $X_{in}, Y_{in}, x_{in}$ 
26: function GETOUTERLINES( $E_{out}, D_{out}, x_{in}, k$ )
27:   for  $i = k : 1$  do
28:     if  $i > 1$  then
29:       if  $x_{E_{out}}(i) > x_{in}(i - 1)$  then
30:          $x_{out}(i) = x_{in}(i) + (x_{in}(i - 1) - x_{in}(i)) \cdot D_{out}(i)$ 
31:       else
32:          $x_{out}(i) = x_{in}(i) + (x_{E_{out}}(i) - x_{in}(i)) \cdot D_{out}(i)$ 
33:     else
34:       if  $x_{E_{out}}(i) - x_{in}(i) < |y_{E_{out}}(i)|$  then
35:          $x_{out}(i) = x_{in}(i) + (x_{E_{out}}(i) - x_{in}(i)) \cdot D_{out}(i)$ 
36:       else
37:          $x_{out}(i) = x_{E_{out}}(i) - |y_{E_{out}}(i)| \cdot D_{out}(i)$ 
38:    $[X_{out}, Y_{out}] = \text{GETCRCVTX}(x_{out}, x_{E_{out}}, y_{E_{out}}, k)$ 
39:   return  $X_{out}, Y_{out}, x_{out}$ 
40: function GETCRCVTX( $x, x_E, y_E, k$ )
41:    $\triangleright$  Calculate barrier center
42:    $F = (x_E - x_0)^2 + y_E^2 = (x - x_0)^2$ 
43:   for  $i = 1 : k$  do
44:      $x_0 = \text{SOLVE}(F(i))$ 
45:    $R_r = |x - x_0|$ 
46:    $\triangleright$  Calculate barrier polar angles
47:    $\varphi_{\text{start}} = \pi - \text{ATAN2}(y_E, (x_0 - x_E))$ 
48:    $\varphi_{\text{end}} = \pi$ 
49:   for  $i = 1 : k$  do
50:      $\vartheta(:, i) = \text{Linspace}(\varphi_{\text{start}}(i), \varphi_{\text{end}}, N_{\text{points}})$ 
51:    $\triangleright$  Calculate barrier line vertices
52:    $X = R_r \cdot \cos(\vartheta) + x_0$ 
53:    $Y = R_r \cdot \sin(\vartheta)$ 
54:   return  $X, Y$ 
55: return  $X_{in}, Y_{in}, X_{out}, Y_{out}, X_n, Y_n$ 

```

4.2.2. Outer Line Calculation

At this point all inner barrier intersections x_{in} are defined and now present feasibility limits for outer barrier line construction (Algorithm2: In:7). The rest of the GETOUTERLINES code (Algorithm2: In:25–38) is executed in the similar manner as in GETINNERLINES. The function in the end returns $X_{out}, Y_{out}, x_{out}$.

4.2.3. Notch Line Calculation

Notch is specific because it has only one barrier line ($k_n = 1$) and depends on the most outer intersection $x_{out}(1)$ (Algorithm2: In:9). Finally, GETOUTERLINES returns X_n, Y_n, x_n which completes the calculation of all barrier lines (Figure7c).

The next steps (not described within Algorithm2) are mirroring vertices around horizontal axis (Figure4e), adding barrier fillets, and geometry rotation around center point (Figure4f).

4.3. Hyperbolic Barrier Construction

After definition of all inner and outer barrier line starting points and depth parameters ($E_{in}, E_{out}, E_n, D_{in}, D_{out}, D_n$), Figure8a, the entire geometry is rotated by $\alpha_{1\text{HyVE}} = -\pi/2$ (Algorithm3: ln:1, Figure8b).

Algorithm 3 Construction of Hyperbolic barriers

```

1: Rotate all by  $\alpha_{1\text{HyVE}} = -\pi/2$ 
2: Get:  $E_{in}, E_{out}, E_n, D_{in}, D_{out}, D_n$ 
3:  $K = 1.1$  ▷ Max eccentricity coefficient
4:  $[X_{in}, Y_{in}, X_{out}, Y_{out}, X_n, Y_n] = \text{GETHYPLINES}(E_{in}, E_{out}, E_n, D_{in}, D_{out}, D_n)$ 

5: function GETHYPLINES( $E_{in}, E_{out}, E_n, D_{in}, D_{out}, D_n$ )
6:    $k = N_{\text{barrier}}$  ▷ Calculate inner and outer barrier lines
7:    $[X_{in}, Y_{in}, x_{in}] = \text{GETINNERLINES}(E_{in}, D_{in}, k)$ 
8:    $[X_{out}, Y_{out}, x_{out}] = \text{GETOUTERLINES}(E_{out}, D_{out}, x_{in}, k)$ 
   ▷ Calculate notch line
9:    $k_n = 1$  ▷ Notch has only one barrier line
10:   $[X_n, Y_n, x_n] = \text{GETOUTERLINES}(E_n, D_n, x_{out}(1), k_n)$ 

11: function GETINNERLINES( $E_{in}, D_{in}, k$ )
12:    $x_M = D_{sh}/2$ 
13:   for  $i = k : 1$  do
14:     if  $i == k$  then
15:        $e_{\min}(i) = (r_{E_{in}}(i) - x_M) / (x_{E_{in}}(i) - x_M)$ 
16:     else
17:        $e_{\min}(i) = \frac{r_{E_{in}}(i) - x_{in}(i+1)}{x_{E_{in}}(i) - x_{in}(i+1)}$ 
18:      $e_{\max}(i) = K \cdot e_{\min}(i)$  ▷ Est. max eccentricity
19:      $e_{in}(i) = (e_{\max}(i) - e_{\min}(i)) \cdot D_{in}(i) + e_{\min}(i)$ 
20:      $x_{d_{in}}(i) = \frac{r_{E_{in}}(i)}{e_{in}(i)} - x_{E_{in}}(i)$  ▷ Left directrix
21:      $x_{in}(i) = e_{in}(i) \cdot x_{d_{in}}(i) / (1 + e_{in}(i) \cdot \text{sgn}(x_{d_{in}}(i)))$ 
22:      $[X_{in}, Y_{in}] = \text{GETHYPVTX}(x_{d_{in}}, e_{in}, \vartheta_{E_{in}}, k)$ 
23:   return  $X_{in}, Y_{in}, x_{in}$ 

24: function GETOUTERLINES( $E_{out}, D_{out}, x_{in}, k$ )
25:   for  $i = k : 1$  do
26:      $e_{\min}(i) = \frac{r_{E_{out}}(i) - x_{in}(i)}{x_{E_{out}}(i) - x_{in}(i)}$ 
27:     if  $i > 1$  then
28:        $e_{\max}(i) = \frac{r_{E_{out}}(i) - x_{in}(i+1)}{x_{E_{out}}(i) - x_{in}(i+1)}$ 
29:     else
30:        $e_{\max}(i) = K \cdot e_{\min}(i)$  ▷ Est. max eccentricity
31:      $e_{out}(i) = (e_{\max}(i) - e_{\min}(i)) \cdot D_{out}(i) + e_{\min}(i)$ 
32:      $x_{d_{out}}(i) = \frac{r_{E_{out}}(i)}{e_{out}(i)} - x_{E_{out}}(i)$  ▷ Left directrix
33:      $x_{out}(i) = \frac{e_{out} \cdot x_{d_{out}}(i)}{1 + e_{out}(i) \cdot \text{sgn}(x_{d_{out}}(i))}$ 
34:      $[X_{out}, Y_{out}] = \text{GETHYPVTX}(x_{d_{out}}, e_{out}, \vartheta_{E_{out}}, k)$ 
35:   return  $X_{out}, Y_{out}, x_{out}$ 

36: function GETHYPVTX( $x_d, e, \vartheta_E, k$ )
   ▷ Calculate barrier polar angles
37:    $\varphi_{\text{start}} = 0; \varphi_{\text{end}} = \vartheta_E$ 
38:   for  $i = 1 : k$  do
39:      $\vartheta(:, i) = \text{Linspace}(\varphi_{\text{start}}, \varphi_{\text{end}}(i), N_{\text{points}})$ 
   ▷ Calculate barrier line vertices
40:    $r = e \cdot x_d / (1 + e \cdot \text{sgn}(x_d) \cdot \cos(\vartheta))$ 
41:    $[X, Y] = \text{pol2cart}(\vartheta, r)$ 
42:   return  $X, Y$ 
43: return  $X_{in}, Y_{in}, X_{out}, Y_{out}, X_n, Y_n$ 

```

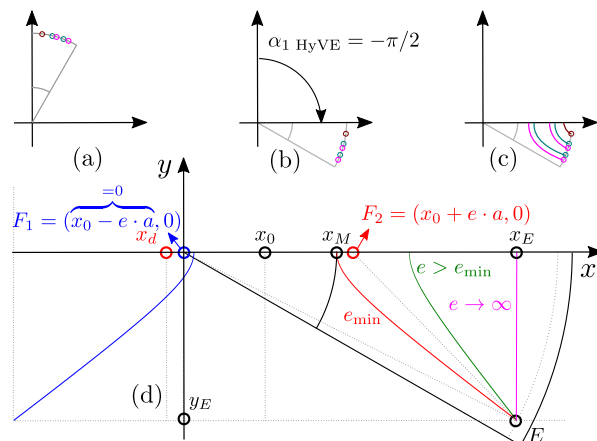


Figure 8. Hyperbolic barrier construction. Subfigures (a)–(d) are explained in the Sections4.3-4.3.3.

4.3.1. Inner Line Calculation

Lets first consider GETINNERLINES function which calculates inner lines vertices (X_{in}, Y_{in}) and intersections (x_{in}) based on E_{in}, D_{in} and number of barriers k (Algorithm3: ln:7).

To simplify the construction, the left focus is constructed in the origin of the coordinate system (Figure8d, blue). The intersections with $y = 0$ (Figure4d) are critical for barrier calculation and they depend on the minimum eccentricity Equation $e_{min} = (r_E - x)/(x_E - x)$, x is the inner or outer intersection limit.

In case of the most inner line ($i = k$), the feasibility limit is rotor shaft (x_M), the minimum eccentricity $e_{min}(i)$ is calculated via Algorithm3: ln:15. For the second most inner line ($i = k - 1$), $e_{min}(i + 1)$ is calculated via Algorithm3: ln:17.

If particular barrier has eccentricity within the limits $e \in [e_{min}, \infty]$, the construction is feasible (Figure8d, green). Otherwise the barrier is infeasible (Figure8d, red, magenta). This is why it is important to limit maximum eccentricity (Algorithm3: ln:18), where $K = 1.1$ is empirically determined coefficient. The final eccentricity is then calculated depending of the depth parameter (Algorithm3: ln:19). The next steps are calculation of the left directrix (Algorithm3: ln:20) and intersection point (x_{in}) based on polar hyperbola Equation (Algorithm3: ln:21).

All inner line intersections are then iteratively calculated following the described procedure (Algorithm3: ln:13–21).

Next, GETHYPVTX function (Algorithm3: ln:22) based on calculated directrices $x_{d_{in}}$, eccentricities e_{in} , angular starting point coordinates $\theta_{E_{in}}$ and k , calculates the hyperbolic vertices in polar coordinates r, θ , and returns barrier vertices X_{in}, Y_{in} (Algorithm3: ln:36–41).

Finally, GETINNERLINES returns X_{in}, Y_{in}, x_{in} .

4.3.2. Outer line calculation

At this point all inner barrier intersections x_{in} are defined and now present feasibility limits for outer barrier line construction (Algorithm3: ln:8). The rest of the GETOUTERLINES code (Algorithm3: ln:24–34) is executed in the similar manner as in GETINNERLINES. The function returns $X_{out}, Y_{out}, x_{out}$.

4.3.3. Notch line calculation

Notch is specific because it has only one barrier line ($k_n = 1$) and depends on the most outer intersection $x_{out}(1)$ (Algorithm3: ln:10). Finally, GETOUTERLINES returns X_n, Y_n, x_n which completes the calculation of all barrier lines (Figure7c).

The next steps (not described within Algorithm3) are mirroring vertices around horizontal axis (Figure4e), adding barrier fillets, and geometry rotation around center point (Figure4f).

5. Conformal Modifications

5.1. Conformal Mapping

A conformal or angle-preserving transformation also called conformal mapping is a transformation $w = f(z)$ that preserves local angles. An analytic function is conformal at any point where it has a nonzero derivative [17].

Conformal transformations can prove extremely useful in solving physical problems. If the selected complex function $w = f(z)$ satisfies the condition that the real and imaginary parts of w satisfy the Cauchy–Riemann equations and Laplace’s equation, they automatically provide a scalar potential and a so-called stream function [17] (e.g., Zhukovski barrier lines, Figure1d, red).

FEA is typically used for electromagnetic performance calculations in electric machine design. Depending on the complexity of the calculation and mesh density, it can take several minutes before the calculation is completed. The simulation time can be reduced if a conformal mapping is used for calculation of the analytical airgap magnetic field [16]. The method conformally transforms electric machine cross-section to w -plane thus enabling

quick analytic calculations. The w -plane results are then inversely mapped to the real plane. Compared to FEA simulation, this approach yields results within seconds [11,12,16]. On the other hand, the disadvantage is the difficult implementation on complex rotor geometries.

This paper proposes a method for geometrical modification of any SyRM barrier geometry using conformal mapping.

5.2. Mapping Workflow

Generated rotor barrier lines are defined by sorted vertices $(X_{in}, Y_{in}, X_{out}, Y_{out}, X_n, Y_n)$ containing corresponding x, y coordinates which can be drawn on a 2D real Euclidean plane (Figure9a). For easier manipulation purposes, real plain coordinates are redefined in complex z -plane $(z = x + jy)$, Figure9b. Considering that the vertices are the same in real and complex plane, this is a trivial transformation.

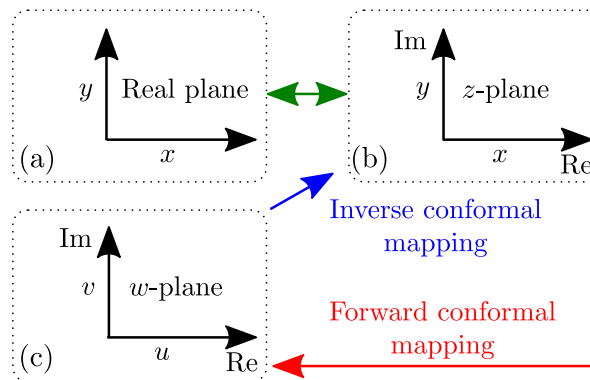


Figure 9. Mapping workflow, Subfigures (a)–(c) are explained within the Section5.2.

SyRM rotor has a circular layout which can be exploited by selecting the convenient complex function $f(z)$ and applying forward conformal mapping to a complex w -plane $(w = u + jv)$, Figure9c. Geometrical modifications of the barrier geometry are then performed in w -plane and upon completion, returned back to z (and real) plane via inverse conformal mapping. The benefit of the approach is easier barrier modification which leads to simplified software coding.

5.3. Complex Functions

The principal objects of study are complex-valued functions $f(z)$, depending on a single complex variable $z = x + jy \in \mathbb{C}$. In general, the function $f : \Omega \rightarrow \mathbb{C}$ is defined on an open subdomain, $z \in \Omega \subset \mathbb{C}$, of the complex plane. Any complex function can be uniquely written as a complex combination $f(z) = f(x + iy) = \text{Re } u(x, y) + j\text{Im } v(x, y)$ [18].

5.3.1. Forward Conformal Mapping

When working with circular shapes, it is useful to use polar form $z = re^{j\theta}$. Considering that electric machines can have an arbitrary number of pole pairs, it is very convenient to select a complex function that somehow ignores angle changes when the number of poles is increased or decreased. This kind of functionality can be achieved by a complex natural logarithm. In terms of polar coordinates, the complex logarithm has the form $w = \ln z = \ln(re^{j\theta}) = \ln r + \ln e^{j\theta} = \ln r + j\theta$.

Thus, the logarithm of a complex number has a real part which is a well-defined harmonic function save for a logarithmic singularity at the origin $x = y = 0$. The imaginary part of the complex logarithm is the polar angle, known in complex analysis as the *phase*.

$$u(x, y) = \text{Re}(\ln z) = \ln r = \frac{1}{2} \ln(x^2 + y^2) \tag{2}$$

$$v(x, y) = \text{Im}(\ln z) = \theta = \arctan \frac{y}{x} \tag{3}$$

Due to inherent symmetry, it is enough to analyze one electric machine pole. A minimum number of poles is 2, which equals to $[0, \pi]$ radian angular span in z -plane, which is mapped to the same vertical span in w -plane. Figure 10 illustrates mapping of different combination of pole geometries. To summarize, $w = \ln z$ always maps z to the upper half-plane with vertical boundaries $v \in [0, \pi/p]$ (p is the number of pole pairs) and horizontal boundaries of $u \in [\ln x_M, \ln R]$.

Note that $\ln z$ always maps SyRM barrier lines horizontally (Figure 10, w -plane), regardless of the number of poles. This feature is exploited for the creation of the Modified Zhukovsky variable depth barrier lines (MZhVD).

5.3.2. Inverse Conformal Mapping

Inverse function for return to z -plane is a complex exponential $z = e^w = e^{u+jv}$. Since $w \in \mathbb{C}$ is a non-zero complex number, the equation can be written as $z = e^u \cdot (\cos vs. + j \sin v)$ with real and imaginary parts equal to:

$$x(u, v) = \text{Re}(e^w) = e^u \cdot \cos v \tag{4}$$

$$y(u, v) = \text{Im}(e^w) = e^u \cdot \sin v \tag{5}$$

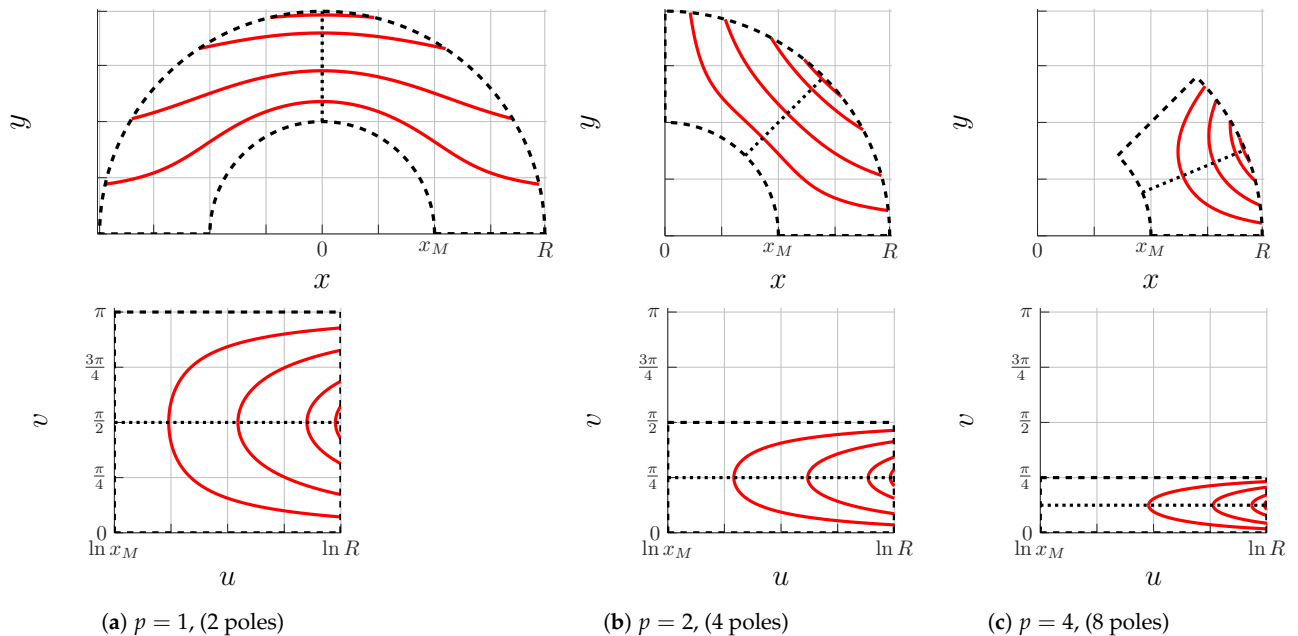


Figure 10. Real z -plane (upper row); Conformal mapping to $w = \ln z$ plane (bottom row).

5.4. Depth Modification

To summarize, original Zhukovsky barrier lines ($X_{in}, Y_{in}, X_{out}, Y_{out}, X_n, Y_n$) with corresponding x, y vertices are written as $z = x + jy$ (Figure 11a, red) and conformally transformed to w -plane via $w = \ln z$ as $w = u + jv$ (Figure 11b, red). As previously mentioned, Zhukovsky lines cannot mutually intersect. To secure barrier depth variability and improve machine performance, we are introducing Zhukovsky barrier depth modification (MZhVD) via dimensionless depth parameters D_{in}, D_{out}, D_n .

Depth variability is secured via addition of cosine offsets to the w -plane barrier lines according to Equations (6) and (7). In theory, any even function can be used for generation of Δ offset (7), cosine has been selected due to implementation simplicity.

$$T = 2 \cdot [\text{Max}(V_{Zhk}) - \text{Min}(V_{Zhk})] \tag{6}$$

$$\Delta = \Delta_{Dpth} \cdot \cos \left[\frac{\pi}{T} (V_{Zhk} - v_E) - \pi/2 \right] \tag{7}$$

Upon modification (Figure11b, blue), barrier lines are inversely mapped to z -plane via function $z = e^w$ (Figure11a, blue). The main benefit of the proposed procedure is a simplified modification of SyRM barriers without any influence on simulation time. The following section explains the modification procedure step by step.

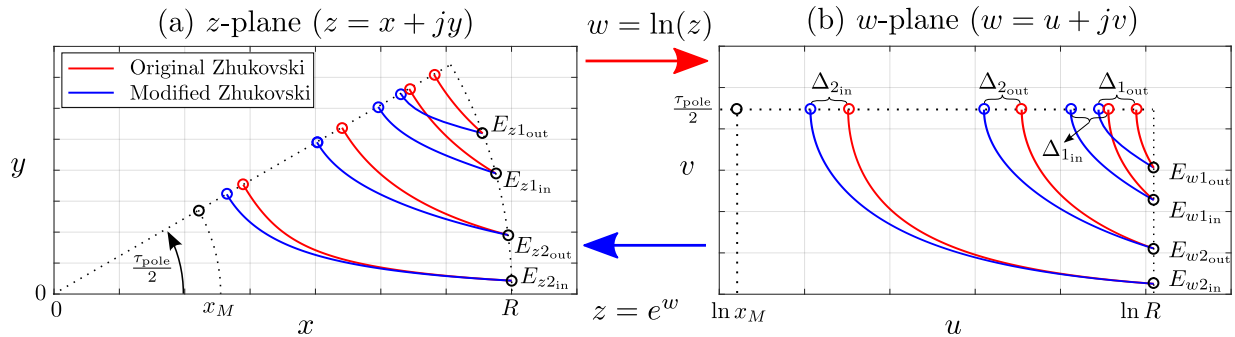


Figure 11. Modification of Zhukovski lines via conformal mapping. Subfigures (a) and (b) are explained within the Section5.4and related subsections.

5.5. Modified Zh Barrier Construction

After definition of all inner and outer barrier line starting points (E_{in}, E_{out}, E_n), Figure12a, the entire geometry is rotated by $\alpha_{1MZhVD} = -(\pi/2 - \tau_{pole}/2)$ (Algorithm4: ln:2, Figure12b).

5.5.1. Inner Line Calculation

The first step is the calculation of GETINNERLINES barrier line function (Algorithm4: ln:9). Inner line vertices (X_{in}, Y_{in}) are calculated based on E_{in}, D_{in} and number of barriers k .

Next (Algorithm4: ln:14), original Zhukovsky barrier (Zh) vertices (X_{Zhkin}, Y_{Zhkin}) are calculated in the same way as in Algorithm1, Figure12c. Original vertices (X_{Zhkin}, Y_{Zhkin}) and barrier starting points ($x_{E_{in}}, y_{E_{in}}$) are then conformally mapped to w -plane as U_{Zhkin}, V_{Zhkin} and $u_{E_{in}}, v_{E_{in}}$, Algorithm4: ln:15–16, Figure12d, dotted lines.

Intersections u_{in} are critical for Modified Zhukovsky barrier variable depth (MZhVD) calculation and they are fully tied to original Zhukovsky intersections u_{Zhkin} (calculated via Algorithm4: ln:17). As previously mentioned, original Zhukovsky barriers cannot mutually intersect which makes them absolutely feasible, but on the other hand, barrier depth variability cannot be achieved.

Modified Zhukovsky depth variation is secured by iterative recalculation of intersection points in w -plane. In case of the most inner line ($i = k$), the barrier depth limit is rotor shaft (u_M), and the original Zhukovsky intersection $u_{Zhkin}(i)$ (Algorithm4: ln:20). For the second most inner line ($i = k - 1$), depth limit is $u_{Zhkin}(i + 1)$ and the intersection is calculated via (Algorithm4: ln:22). All inner line intersections are then iteratively calculated (Algorithm4: ln:18–22).

Next, inner line depth offset is calculated based on original Zhukovsky and calculated inner intersections (Algorithm4: ln:23). CLCDPTH function (Algorithm4: ln:25) calculates modified vertices in w -plain (Figure12d, full lines), performs inverse conformal mapping, and returns z -plain vertices (Algorithm4: ln:59–64, Figure12e).

Finally, GETINNERLINES function returns X_{in}, Y_{in} vertices.

5.5.2. Outer Line Calculation

At this point all w -plane inner barrier intersections u_{in} are defined and now present limits for outer barrier line construction. The rest of the GETOUTERLINES code (Algorithm4: ln:27-40) is executed in the similar manner as in GETINNERLINES. The function at the end returns $X_{out}, Y_{out}, x_{out}$.

5.5.3. Notch Line Calculation

Notch is specific because it has only one barrier line ($k_n = 1$) and depends on the most outer w -plain intersection $u_{out}(1)$ (Algorithm4: In:12). Finally, GETOUTERLINES returns X_n, Y_n, u_n which completes the calculation of all barrier lines (Figure12e). Finally, to be compatible with the rest of the barrier construction procedures, the geometry is rotated by $\alpha_2 \text{ MZhVD} = -\tau_{pole}/2$ (Algorithm4:65, Figure12f).

The next steps (not described within Algorithm4) are mirroring vertices around horizontal axis (Figure4e), adding barrier fillets, and geometry rotation around center point (Figure4f).

Algorithm 4 Construction of Modified Zhukovsky barriers

```

1:  $\tau_{pole} = 2\pi / (2p)$ 
2: Rotate all by  $\alpha_1 \text{ MZhVD} = -(\pi/2 - \tau_{pole}/2)$ 
3: Get:  $E_{in}, E_{out}, E_n$ 
4:  $\Delta r = 0$ 
5:  $u_M = \ln(x_M)$   $\triangleright$  Shaft limit in  $w$ -plane
6:  $[X_{in}, Y_{in}, X_{out}, Y_{out}, X_n, Y_n] = \text{GETHYPLINES}(E_{in}, E_{out}, E_n, D_{in}, D_{out}, D_n)$ 
7: function GETMODZHLINES( $E_{in}, E_{out}, E_n, D_{in}, D_{out}, D_n$ )
8:    $k = N_{barrier}$   $\triangleright$  Calculate inner and outer barrier lines
9:    $[X_{in}, Y_{in}, u_{in}] = \text{GETINNERLINES}(E_{in}, D_{in}, k)$ 
10:   $[X_{out}, Y_{out}, u_{out}] = \text{GETOUTERLINES}(E_{out}, D_{out}, u_{in}, k)$ 
11:   $\triangleright$  Calculate notch line
12:   $k_n = 1$   $\triangleright$  Notch has only one barrier line
13:   $[X_n, Y_n] = \text{GETOUTERLINES}(E_n, D_n, u_{out}(1), k_n)$ 
13: function GETINNERLINES( $E_{in}, D_{in}, k$ )
14:    $[X_{Zhkin}, Y_{Zhkin}] = \text{GETZHUKLINES}(E_{in}, k)$ 
15:    $\triangleright$  Forward conformal transformation
16:    $[U_{Zhkin}, V_{Zhkin}] = \text{FRWCONF}(X_{Zhkin}, Y_{Zhkin})$ 
17:    $[u_{E_{in}}, v_{E_{in}}] = \text{FRWCONF}(x_{E_{in}}, y_{E_{in}})$ 
18:    $\triangleright$  Original Zhukovsky inner line intersection limits
19:    $u_{Zhkin} = U_{Zhkin}(\text{find}(\max(V_{Zhkin})))$ 
20:   for  $i = k : 1$  do
21:     if  $i = k$  then
22:        $u_{in}(i) = u_M + (u_{Zhkin}(i) - u_M) \cdot D_{in}(i)$ 
23:     else
24:        $u_{in}(i) = u_{Zhkin}(i+1) + (u_{Zhkin}(i) - u_{Zhkin}(i+1)) \cdot D_{in}(i)$ 
25:    $\Delta_{Dpth_{in}} = u_{Zhkin} - u_{in}$ 
26:    $[X_{in}, Y_{in}] = \text{LCDPTH}(\Delta_{Dpth_{in}}, U_{Zhkin}, V_{Zhkin}, v_{E_{in}})$ 
27:   return  $X_{in}, Y_{in}, u_{in}$ 
27: function GETOUTERLINES( $E_{out}, D_{out}, u_{in}, k$ )
28:    $[X_{Zhkout}, Y_{Zhkout}] = \text{GETZHUKLINES}(E_{out}, k)$ 
29:    $\triangleright$  Forward conformal transformation
30:    $[U_{Zhkout}, V_{Zhkout}] = \text{FRWCONF}(X_{Zhkout}, Y_{Zhkout})$ 
31:    $[u_{E_{out}}, v_{E_{out}}] = \text{FRWCONF}(x_{E_{out}}, y_{E_{out}})$ 
32:    $\triangleright$  Original Zhukovsky outer line intersection limits
33:    $u_{Zhkout} = U_{Zhkout}(\text{find}(\max(V_{Zhkout})))$ 
34:   for  $i = k : 1$  do
35:     if  $i > 1$  then
36:        $u_{out}(i) = u_{in}(i) + (u_{in}(i-1) - u_{in}(i)) \cdot D_{out}(i)$ 
37:     else
38:        $u_{out}(i) = u_{in}(i) + (u_{Zhkout}(i) - u_{in}(i)) \cdot D_{out}(i)$ 
39:    $\Delta_{Dpth_{out}} = u_{Zhkout} - u_{out}$ 
40:    $[X_{out}, Y_{out}] = \text{LCDPTH}(\Delta_{Dpth_{out}}, U_{Zhkout}, V_{Zhkout}, v_{E_{out}})$ 
41:   return  $X_{out}, Y_{out}, u_{out}$ 
41: function GETZHUKLINES( $E, k$ )
42:    $C = \sin(p \cdot \theta_E) \cdot \left[ \left( \frac{r_E + \Delta r}{D_{sh}/2} \right)^{2p} - 1 \right] / \left( \frac{r_E + \Delta r}{D_{sh}/2} \right)^p$ 
43:    $\triangleright$  Calculate barrier polar angles
44:    $\varphi_{start} = \theta_E$ 
45:    $\varphi_{end} = \tau_{pole}/2$ 
46:   for  $i = 1 : k$  do
47:      $\theta(:, i) = \text{Linspace}(\varphi_{start}(i), \varphi_{end}, N_{points})$ 
48:      $\triangleright$  Calculate barrier line vertices
49:      $r = \frac{D_{sh}}{2} \sqrt{\left( C + \sqrt{C^2 + 4 \sin^2(p\theta)} \right) / (2 \sin(p\theta))}$ 
50:      $[X, Y] = \text{pol2cart}(\theta, r)$ 
51:   return  $X, Y$ 
51: function FRWCONF( $X, Y$ )
52:    $[r, \theta] = \text{cart2pol}(X, Y)$ 
53:    $U = \ln r$ 
54:    $V = \theta$ 
55:   return  $U, V$ 
55: function INVCONF( $U, V$ )
56:    $X = e^U \cdot \cos V$ 
57:    $Y = e^U \cdot \sin V$ 
58:   return  $X, Y$ 
59: function CLCDPTH( $\Delta_{Dpth}, U_{Zh}, V_{Zh}, v_E$ )
60:    $T = 2 \cdot (\text{Max}(V_{Zh}) - \text{Min}(V_{Zh})); f = \frac{1}{2T}$ 
61:    $\Delta = \Delta_{Dpth} \cdot \cos(2\pi f(V_{Zh} - v_E) - \pi/2)$ 
62:    $U_{new} = U_{Zh} - \Delta$ 
63:    $\triangleright$  Inverse conformal transformation
64:    $[X, Y] = \text{INVCONF}(U_{new}, V_{Zh})$ 
65:   return  $X, Y$ 
65: Rotate all by  $\alpha_2 \text{ MZhVD} = -\tau_{pole}/2$ 
66: return  $X_{in}, Y_{in}, X_{out}, Y_{out}, X_n, Y_n$ 

```

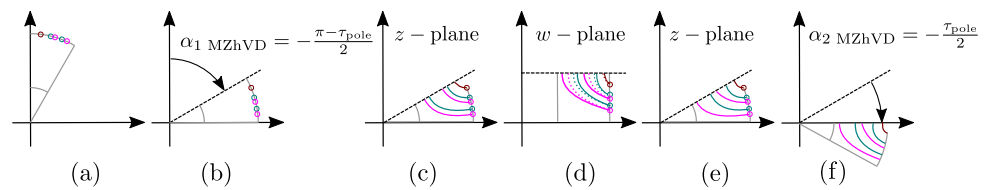


Figure 12. Modified Zhukovsky barrier construction and rotation steps. Subfigures (a)–(f) are explained within the Sections 5.5–5.5.3.

6. Parametric Complexity

A high number of optimization variables is associated with a longer optimization time [19,20], so the imperative is to simplify barrier topology parametrization. Gamba et al. [14] state that three parameters per barrier (total complexity of $3k$, where k is the number of barriers) are the appropriate number for a fast yet accurate description of multi-barrier SyRM (barrier fillet parameters are not included). In the previous publication, our group of authors has reduced the complexity to $2 \cdot k + 1$ per barrier [7].

Table 3 shows the calculation of total number of SyRM parameters for the demonstrated pseudo-code. Note that the parameters $\vartheta_{1out}, \vartheta_{k_{in}}$ are subtracted from the count because they are constant and equal to zero (Table 1).

Table 4 lists the complexity comparison of the presented procedures and similar approaches in [7,10,14]. The examples in [7,10,14] do not have a notch feature, so to have a fair comparison, the notch is not included in the complexity calculation (Table 3). Compared to [14], and [7], Zh, respectively, yields smaller complexity ($2k$), while CrVD, HyVE, MZhVD have the same complexity as in [10].

Overall, the construction principle explained in Section 3 enables the higher degree of design freedom. Considering that the simple barrier topologies are sub-optimal compared to more complex types, developing the set of different parametrization methods with equal parametric complexity is certainly a novel contribution.

Table 3. Calculation of total parameter number. Color coding is according to Fig. 4 variables.

Sum:	Description	Symbol	Topology
1	Min. angle	ϑ_{min}	
2	Max. angle	ϑ_{max}	
$k + 2$	Barrier angle in	$\vartheta_{1..k_{in}}$	
$2k + 2$	Barrier angle out	$\vartheta_{1..k_{out}}$	
$2k + 2 - 2$	Remove constants	$\vartheta_{1out} = \vartheta_{k_{in}} = 0$	
$2k$	-	-	Zh
$4k$	Barrier depths	$D_{1..k_{in}}$	HyVE
	Barrier depths	$D_{1..k_{out}}$	CrVD
			MZhVD

Table 4. Parametric complexity.

Topology	Complexity	$k = 2$	$k = 3$	$k = 4$
Zhukovsky; Gamba et.al. [14]	$3k$	6	9	12
Circular; Stipetic et.al. [10]	$4k$	8	12	16
Zhukovsky; Ban et.al. [7]	$2k + 1$	5	7	9
Zh	$2k$	4	6	8
HyVE				
CrVD	$4k$	8	12	16
MZhVD				

7. Pseudo-Code Validation

After the implementation of the proposed pseudo-code, a set of questions naturally arises. Which barrier topology yields the best performance for the given requirements? Is Modified Zhukovsky barrier type better than alternative topologies? For this reason, we have conducted a detailed optimization study based on meta-modeling (surrogate modeling) approach which compared the different barrier topologies (details are available in [21]).

The optimization process couples automated geometry generation (Matlab), electromagnetic finite element analysis (Ansys Motor-CAD), and metamodel optimization (Ansys OptiSlang). Seven rotor topologies have been derived from circular, hyperbolic, and Zhukovsky barrier types:

1. Circular concentric (CrC)
2. Circular variable depth (CrVD)
3. Hyperbolic with fixed eccentricity (HyFE)
4. Hyperbolic with variable eccentricity (HyVE)
5. Original Zhukovsky (Zh)
6. Modified Zhukovsky variable depth (MZhVD)
7. Modified Zhukovsky with equal barrier depth (MZhED)

The same optimization strategy (maximize torque per volume (TPV), minimize losses) has been applied to all variants, and results prove that barrier type substantially affects the final machine performance. For easier comparison, seven designs (one per topology) with approximately the same losses (5200 W) have been selected (Figure 13, Table 5).

Performance wise, HyFE topology yields the worst results and is considered as baseline design (Gain = 0%). Performance gain is calculated via: $\text{Gain} = (T_{\text{avg}}/T_{\text{HyFE avg}} - 1) \cdot 100\%$. The best results are achieved by MZhVD topology. In relation to the worst (baseline) topology, the performance gain is 14.9% and the power factor is increased from 0.61 to 0.69. It is important to note that these comparisons are valid for design requirements presented in [21]. Other combinations of optimization objectives and requirements might yield a different results.

HyFE, CrC and MZhED are special case topologies already covered in CrVD, HyVE and MzVD pseudo-code. Considering that stated topologies can be achieved by appropriate combination of barrier depth parameters, they are not considered in this paper. The summary of three best optimized cross-sections are provided on Figure 14.

Table 5. Optimization result comparison table [21].

Name	Unit	HyFE	CrC	HyVE	CrVD	Zh	MZhED	MZhVD
TPV	Nm/dm ³	32.5	33.1	34.3	35.4	36.2	36.4	37.3
V_{active}	dm ³	6.47	6.47	6.47	6.47	6.47	6.47	6.47
P_{loss}	kW	5188	5199	5209	5182	5188	5197	5184
P_{mech}	kW	37.4	38.1	39.5	40.8	41.7	41.9	43.0
T_{avg}	Nm	210.1	214.2	221.9	229.0	234.1	235.6	241.3
$T_{\text{ripp.}}$	%	12.1	14.1	11.7	12.7	9.7	9.3	13.7
n	rpm	1700	1700	1700	1700	1700	1700	1700
l_s	mm	180	180	180	180	180	180	180
γ	°	57.9	60.3	61.4	62.5	61.8	61.8	62.9
I_{max}	A _{rms}	95.6	95.6	94.3	94.1	95.9	95.7	95.7
$\cos \varphi$	-	0.61	0.62	0.66	0.67	0.67	0.67	0.69
Gain	%	0.0	1.9	5.6	9.0	11.4	12.1	14.9

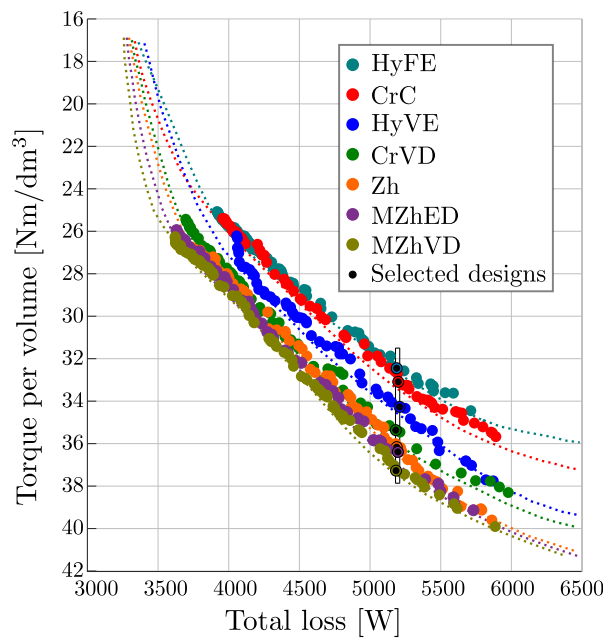


Figure 13. Validated Pareto fronts for each design variant [21].

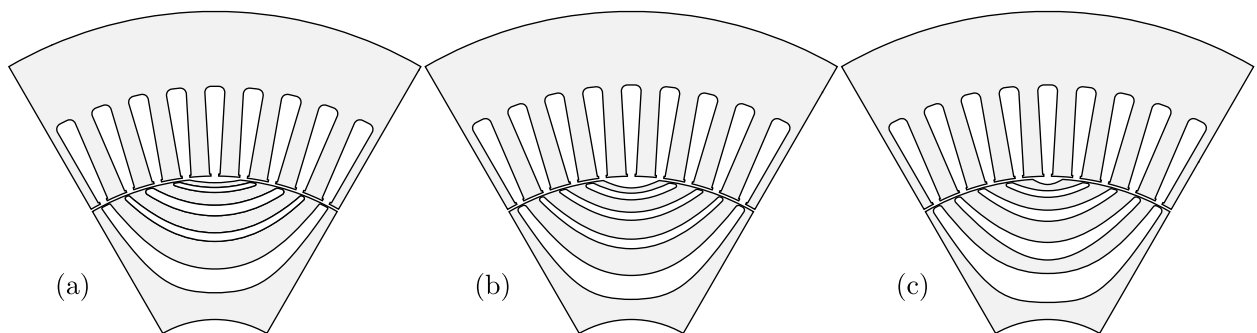


Figure 14. Optimized cross section of three best topologies: (a) Zh; (b) MZhED; (c) MZhVD [21].

8. Conclusions

SyRM barrier generation procedure was studied in detail. A pseudo-code solution that secures absolute feasibility, barrier topology complexity minimization, and simple implementation is provided. Four smooth barrier types have been presented: circular variable depth (CrVD), hyperbolic with variable eccentricity (HyVE), original Zhukovsky (Zh) and modified Zhukovsky with variable depth (MZhVD). Absolute feasibility is a very important feature because it enables the use of dimensionless parameters which secure code robustness and design scalability to any physical dimension. Barrier topology complexity has been minimized via a systematic approach to design automation (Section 3) and careful analysis of construction features of each topology.

HyVE and CrVD topologies are more complex $4k$ while Zh has smaller complexity $2k$. On the other hand, in its original form, Zh type does not support barrier depth variability which can be a design drawback. Therefore, we introduce a novel MZhVD topology based on geometrical conformal mapping of the original Zh design. This modification provides greater design freedom and sets MZhVD complexity to $4k$ (same as HyVE and CrVD).

Compared with other referenced topologies, the presented solutions offer higher design freedom with smaller or equal parametric complexity.

It should be noted that construction of barrier fillets (Figure 4f) has not been covered in this paper. Adding a precise fillet between two discrete intersecting lines is a rather

complex problem, which deserves a stand-alone publication. A minimum example code with detailed instructions is planned to be published in the near future.

Overall, the presented pseudo-code provides a valuable starting point for the designer who wants to investigate different SyRM smooth barrier topologies.

The description and list of used variables has been added in the Appendix A.

Author Contributions: Conceptualization, B.B.; methodology, B.B.; validation, B.B. and S.S.; original draft preparation, B.B.; review and editing, S.S.; visualization, B.B.; supervision, S.S.; funding acquisition, S.S. All authors have read and agreed to the published version of the manuscript.

Funding: This work was partially supported by the Croatian Science Foundation under the project IP-2018-01-5822 - HYDREL.

Institutional Review Board Statement: Not applicable.

Informed Consent Statement: Not applicable.

Data Availability Statement: Not applicable.

Acknowledgments: This paper is an extension of Branko Ban's Ph.D. research work on Synchronous Reluctance machines mentored by Stjepan Stipetic.

Conflicts of Interest: The authors declare no conflict of interest.

Abbreviations

The following abbreviations are used in this manuscript:

Abbreviation	Description
EV	Electric vehicle
FEA	Finite element analysis
IPM	Interior permanent magnet
IM	Induction machine
CrC	Circular concentric barrier
CrVD	Circular variable depth barrier
HyFE	Hyperbolic fixed eccentricity barrier
HyVE	Hyperbolic variable eccentricity barrier
Zh	Original Zhukovsky barrier
MZhED	Modified Zhukovsky equal depth barrier
MZhVD	Modified Zhukovsky variable depth barrier
PM	Permanent magnet
PTO	Power take off
e-PTO	Electric power take off
SyRM	Synchronous reluctance machine
TPV	Torque per volume

Appendix A. Variable list

All variables have been listed by the order of appearance within text. Vector variables are bolded. e.g., \mathbf{R} is a variable vector, while R represents a scalar variable.

Table A1. List of variables.

No.	Variable	Description	No.	Variable	Description
1	$w_{c \min}$	Minimum flux carrier width	33	$\alpha_1 \text{ Zh}$	First rotation angle in Zh generation
2	D_{in}	Inner barrier depth parameters	34	$\alpha_2 \text{ Zh}$	Second rotation angle in Zh generation
3	D_{out}	Outer barrier depth parameters	35	$\alpha_1 \text{ CrVD}$	First rotation angle in Zh generation
4	D_n	Notch depth parameter	36	$\alpha_1 \text{ HyVE}$	First rotation angle in Zh generation
5	p	Number of pole pairs	37	$\alpha_1 \text{ MZhVD}$	First rotation angle in MZhVD generation
6	k	Number of flux barriers	38	$\alpha_2 \text{ MZhVD}$	Second rotation angle in MZhVD generation
7	ϑ_{\min}	Minimum angular barrier span	39	r	Radial Zhukovsky line coordinate vector
8	ϑ_{\max}	Maximum angular barrier span	40	ϑ	Angular Zhukovsky line coordinate vector
9	τ_{pole}	Angle of one pole	41	C	Zhukovsky line coefficient
10	α_1	First rotation angle in example figure	42	ϑ_E	Line starting point angular coordinates
11	$E_{1..k \text{ temp}}$	Initial construction points	43	$x_{E_{in}}$	Inner line starting point horizontal coordinates

Table A1. Cont.

No.	Variable	Description	No.	Variable	Description
12	$\Delta\theta_r$	Available angular space	44	$y_{E_{in}}$	Inner line starting point vertical coordinates
13	$w_{bb\ 1..k}$	Barrier bridge vector	45	x_0	Circular barrier center coordinate vector
14	E_n	Notch line starting point	46	R_r	Circular barrier radius vector
15	θ_{notch}	Notch line starting point angular coordinate	47	e_{min}	Minimal eccentricity vector
16	E_{in}	Inner barrier line starting point vector	48	r_E	Line starting point radial coordinate vector
17	E_{out}	Outer barrier line starting point vector	49	x_E	Line starting point angular coordinate vector
18	$\theta_{1..k\ temp}$	Initial barrier construction angular coord.	50	e	Eccentricity vector
19	r_{in}	Inner barrier line starting point radial coord.	51	x_d	Left directrix of hyperbola
20	r_{out}	Outer barrier line starting point radial coord.	52	u	Horizontal w -plane coordinate vector
21	θ_{in}	Inner barrier line starting point angular coord.	53	v	Vertical w -plane coordinate vector
22	θ_{out}	Outer barrier line starting point angular coord.	54	X_{Zhk}	z -plane Zh horizontal vertex vector
23	x_{in}	Inner barrier line intersection point vector	55	Y_{Zhk}	z -plane Zh vertical vertex vector
24	x_{out}	Outer barrier line intersection point vector	56	U_{Zhk}	w -plane Zh horizontal vertex vector
25	X_{in}	Inner barrier line horizontal vertex vector	57	V_{Zhk}	w -plane Zh vertical vertex vector
26	Y_{in}	Inner barrier line vertical vertex vector	58	u_{Zhk}	w -plane Zh intersections vector
27	X_{out}	Outer barrier line horizontal vertex vector	59	u_M	w -plane shaft limit
28	Y_{out}	Outer barrier line vertical vertex vector	60	u_{in}	w -plane MZhVD inner barrier intersections
29	X_n	Notch horizontal vertex vector	61	u_{out}	w -plane MZhVD outer barrier intersections
30	Y_n	Notch vertical vertex vector	62	T	Period vector of MZhVD cosine offset
31	$r_{1..k_{in}}$	Inner barrier fillet vector	63	f	Frequency vector of MZhVD cosine offset
32	$r_{1..k_{out}}$	Outer barrier fillet vector	64	Δ_{Dpth}	Barrier depth offset maximum vector
33	α_F	Final rotation angle	65	Δ	MZhVD Barrier depth offset vector

References

- Bourzac, K. The Rare-Earth Crisis. *Technol. Rev.* **2011**, *114*, 58–63.
- Justin, R. Rare earths: Neither rare, nor earths. *BBC News*, 23 March 2014.
- Hong, H.S.; Liu, H.C.; Cho, S.Y.; Lee, J.; Jin, C.S. Design of High-End Synchronous Reluctance Motor Using 3-D Printing Technology. *IEEE Trans. Magn.* **2017**, *53*, 4–8.
- Yamashita, Y.; Okamoto, Y. Design Optimization of Synchronous Reluctance Motor for Reducing Iron Loss and Improving Torque Characteristics Using Topology Optimization Based on the Level-Set Method. *IEEE Trans. Magn.* **2020**, *56*, 36–39.
- Ban, B.; Stipetić, S. Electric Multipurpose Vehicle Power Take-Off: Overview, Load Cycles and Actuation via Synchronous Reluctance Machine. In Proceedings of the 2019 International Aegean Conference on Electrical Machines and Power Electronics (ACEMP) & 2019 International Conference on Optimization of Electrical and Electronic Equipment (OPTIM), Istanbul, Turkey, 27–29 August 2019.
- Ban, B.; Stipetić, S. Design and optimization of synchronous reluctance machine for actuation of electric multi-purpose vehicle power take-off. In Proceedings of the 2020 International Conference on Electrical Machines (ICEM), Göteborg, Sweden, 23–26 August 2020; pp. 1750–1757.
- Ban, B.; Stipetić, S.; Jercic, T. Minimum set of rotor parameters for synchronous reluctance machine and improved optimization convergence via forced rotor barrier feasibility. *Energies* **2021**, *14*, 16.
- Hubert, T.; Reinlein, M.; Kremser, A.; Herzog, H.G. Torque ripple minimization of reluctance synchronous machines by continuous and discrete rotor skewing. In Proceedings of the 2015 5th International Electric Drives Production Conference (EDPC), Nürnberg, Germany, 15–16 September 2015.
- Ferrari, S. Doctoral thesis: Design, Analysis and Testing Procedures for Synchronous Reluctance and Permanent Magnet Machines. Politecnico di Torino, Torino, Italy 2020.
- Stipetić, S.; Zarko, D.; Cavar, N. Design Methodology for Series of IE4/IE5 Synchronous Reluctance Motors Based on Radial Scaling. In Proceedings of the 2018 23rd International Conference on Electrical Machines (ICEM), Alexandroupoli, Greece, 3–6 September 2018; pp. 146–151.
- Mirazimi, M.S.; Kiyoumarsi, A. Magnetic Field Analysis of Multi-Flux-Barrier Interior Permanent-Magnet Motors Through Conformal Mapping. *IEEE Trans. Magn.* **2017**, *53*, 7002512.
- Mirazimi, M.S.; Kiyoumarsi, A. Magnetic Field Analysis of SynRel and PMA SynRel Machines with Hyperbolic Flux Barriers Using Conformal Mapping. *IEEE Trans. Transp. Electr.* **2020**, *6*, 52–61.
- Taghavi, S.; Pillay, P. Design aspects of a 50hp 6-pole synchronous reluctance motor for electrified powertrain applications. In Proceedings of the IECON 2017—43rd Annual Conference of the IEEE Industrial Electronics Society, Beijing, China, 29 October–1 November 2017; pp. 2252–2257.
- Gamba, M.; Pellegrino, G.; Cupertino, F. Optimal number of rotor parameters for the automatic design of Synchronous Reluctance machines. In Proceedings of the 2014 International Conference on Electrical Machines (ICEM 2014), Berlin, Germany, 2–5 September 2014; pp. 1334–1340.
- Cupertino, F.; Pellegrino, G.; Cagnetta, P.; Ferrari, S.; Perta, M. SyRE: Synchronous Reluctance (Machines)—Evolution. url: <https://sourceforge.net/projects/sy-re/> (accessed 11 March 2021).

16. Zarko, D. A Systematic Approach To Optimized Design of Permanent Magnet Motors with Reduced Torque Pulsations. Ph.D. Thesis, University Of Wisconsin-Madison, Madison, WI, USA, 2004.
17. Weisstein, E.W. Conformal Mapping, url:<https://mathworld.wolfram.com/ConformalMapping.html>(accessed 11 March 2021).
18. Olver, P.J. Complex Analysis and Conformal Mapping, Chapter 6. In *Complex Analysis and Conformal Mapping*; University of Minnesota: Minneapolis, MN, USA, 2011.
19. Pellegrino, G.; Cupertino, F.; Gerada, C. Automatic Design of Synchronous Reluctance Motors Focusing on Barrier Shape Optimization. *IEEE Trans. Ind. Appl.* **2015**, *51*, 1465–1474.
20. Lu, C.; Ferrari, S.; Pellegrino, G. Two Design Procedures for PM Synchronous Machines for Electric Powertrains. *IEEE Trans. Transp. Electrif.* **2017**, *3*, 98–107.
21. Ban, B.; Stipetić, S. Systematic Metamodel-based Optimization Study of Synchronous Reluctance Machine Rotor Barrier Topologies *Struct. Multidiscipl. Optim.* 2022, *in review*

Publication 6: Robust Feasibility Verification and Region Inner-Point Detection Algorithms for Geometric Shape Objects applied to Electric Machine Optimization Workflow

Paper details:

B. Ban and S. Stipetić, "Robust Feasibility Verification and Region Inner-Point Detection Algorithms for Geometric Shape Objects applied to Electric Machine Optimization Workflow", in *Journal of Structural and Multidisciplinary Optimization*. June 2022.

Available at:<https://doi.org/10.1007/s00158-022-03263-4>



Robust feasibility verification and region inner-point detection algorithms for geometric shape objects applied to electric machine optimization workflow

Branko Ban^{1,2} · Stjepan Stipetic¹

Received: 17 November 2021 / Revised: 28 February 2022 / Accepted: 26 April 2022
© The Author(s) 2022

Abstract

In most cases, the search for the optimal design of an electrical machine is closely related to its 2D radial cross section. When optimizing a 2D cross section, special attention must be paid to the geometry and to the definition of the parameters along with their boundaries. Even if properly bounded, complex geometries generated by optimization algorithms can lead to geometrically infeasible candidates. These cannot be manufactured because they contain generally undesirable geometric relationships between air, magnets, and steel. Different commercial and open-source finite element analysis (FEA) design tools treat the infeasible designs differently. The results vary from simulation stop to successful FEA calculation of the infeasible candidate, which wastes time by producing useless data. To prevent the infeasible designs from entering the optimization competition and possibly appearing incorrectly as optimal solutions, and to reduce optimization time, it is important to capture the infeasible designs during optimization. Moreover, the FEA tool requires a precisely determined interior point to assign the material to each closed region (air, steel, epoxy, magnet...). This can be very challenging for complex geometries. To avoid creating geometry or material regions that are not valid, this paper proposes a novel robust methods for checking feasibility and determining interior points on geometric shape objects. In this paper, the proposed method is applied to the optimization of electrical machines.

Keywords Electric machine · Design feasibility · Robust · Material · Region · Shape object

1 Motivation

Our research group is involved in the state-of-the-art design of electrical machines based on mathematical optimization. The presented methods have been proven in industrial applications and can be applied to any similar problem that can be defined with geometric shapes following the procedure described in the last sections of the paper. Considering the fact that this paper deals with a complex problem and proposes a solution that is relatively simple to implement, the reader is gradually introduced to several topics: electric

machine optimization workflow, geometric feasibility, standard feasibility detection, region inner-point detection issues, and finally, the proposed robust set of solutions.

2 Introduction

The electrification of the transportation sector will be one of the biggest disruptions to market dynamics over the next two decades. This will create significant winners and notable losers among vehicle original equipment manufacturers (OEMs) (International Energy Agency 2020).

All the major OEMs have launched their electric vehicles (EVs) to the market. Despite many advantages, EVs are not cost competitive as conventional vehicles, which is the main requirement for large-scale market penetration (Sarlioglu et al. 2017; De La Parra et al. 2009). For this to become a reality, continuous research is required to develop optimized and cost-effective technologies in three main areas: battery, inverter, and electric machine.

Responsible Editor: Tae Hee Lee

✉ Branko Ban
branko.ban@fer.hr; branko.ban@torquery.com

¹ Department of Electric Machines, Drives and Automation, University of Zagreb, Faculty of Electrical Engineering and Computing (FER), Zagreb, Croatia

² Torquery Consulting, Göteborg, Sweden

In the design of an electrical machine, the objective is to reduce component cost while maintaining sufficient efficiency and torque density. Since these requirements are in conflict, modern electrical machine design techniques require a kind of mathematical optimization procedure (Brâmă and Enblom 1996; Zhao and Schofield 2020; Lee et al. 2021). This is particularly evident in the problem of increasing efficiency through global legislative initiatives (EU 2009; European Environment Agency 2016).

In most cases, the search for the optimal design of an electrical machine is closely related to its 2D radial cross-section. The increase in parametric complexity correlates with an increase in the performance of the optimal design, but also with a longer optimization time (Pellegrino et al. 2015; Lu et al. 2017) and a higher probability of producing a geometrically infeasible design. In addition, some FEA tools require a precisely determined interior point to assign the material to each closed region (air, steel, magnet...), which can be difficult to determine for complex geometries.

The paper provides a novel solution to both problems through a novel robust feasibility verification procedure and inner-point detection using Matlab polyshape objects. The generality of approach is demonstrated through a set of simple, but extremely robust algorithms. The approach elevates geometric design analysis from geometric primitives (points, lines and arcs) to the level of objects (shapes), applicable to any type of machine geometry as an upgrade to existing code.

3 Optimization methodology

Most of the requirements for the design of electric machines are in conflict with each other (reduction of volume or mass, increase of efficiency, etc.). Therefore, a manual design that satisfies all constraints can be an overwhelming task due to a large number of coupled parameters that affect the performance and quality of the machine. The solution is in the use of mathematical optimization.

Optimization algorithms can be divided into gradient based methods and stochastic or metaheuristic methods. Gradient-based methods converge quickly but have difficulty with global optima.

Usually they require feasible starting point which can be a problematic task in complex problems (Quasi Newton method (Kamper et al. 1996). Stochastic methods are heavily used in electrical machine optimization (Powell’s method (Kamper et al. 1996). The disadvantage is that convergence can take days and the global optimum cannot be mathematically proven. On the other hand, from the engineer’s point of view, these methods can find a satisfactory global result. Popular metaheuristic methods are based on natural behaviour (Genetic algorithm, Differential evolution (Lampinen

2002; Zarko et al. 2017), Particle swarm (Bramerdorfer et al. 2016), but they can also be iterative (Lee et al. 2010), or based on approximation (Lee and Jang 2021).

All methods are generally set to solve a multi-objective problem, which is mathematically defined as follows: find the vector of parameters (1), subject to D parameter boundary constraints (2) and subject to m inequality constraint functions (3), that will minimize (or maximize) n objective functions (4). A vector \vec{x} of D variables specifies dimensions, dimensionless ratios, current densities, material types used, etc. The goal of design optimization is to have a chosen objective function $f(\vec{x})$ reach its minimum or maximum value while keeping other engineering indices within an acceptable range.

$$\vec{x} = [x_1, x_2, \dots, x_D], \quad \vec{x} \in R^D \tag{1}$$

$$x_i^{(L)} \leq x_i \leq x_i^{(U)}, \quad i = 1, \dots, D \tag{2}$$

$$g_j(\vec{x}) \leq 0, \quad j = 1, \dots, m \tag{3}$$

$$\min(f_k(\vec{x})), \quad k = 1, \dots, n \tag{4}$$

3.1 Cross section parametrization

Each machine geometry is described by a set of parameters. The most influential design parameters that make up the vector \vec{x} are usually identified using a sensitivity analysis tool. All parameters are bounded in predefined intervals, called boundary constraints, which define the search space or the design space.

Some authors use model parameters (stator bore diameter, stator slot depth, etc.) directly as optimization variables, while other authors use ratios of model parameters as optimization variables (Žarko et al. 2005; Zarko et al. 2017). A better approach (which can improve the efficiency of gradient-based algorithms) is to choose variables given as dimensionless ratios of related geometric parameters, e.g. ratio of stator inner diameter to stator outer diameter, ratio of tooth (or slot) width to slot pitch, magnet pole arc relative to pole pitch, etc.

Some parameters can just be considered as optimization variables directly within the given interval (stator outer diameter, stack length, slot current density). On the other hand, some parameters have practical limitations and should not be normalized. E.g. minimum permanent magnet width is tied to the magnet manufacturing process. Finally, a designer might choose a combination of normalized and model parameters which might create geometrical feasibility issues.

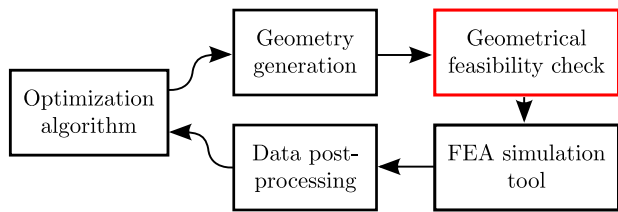


Fig. 1 FC as an optimization workflow add-on feature

3.2 Optimization workflow

A typical optimization workflow is a series of computations consisting of: optimization algorithm that generates optimization variables according to the given parameter boundaries, geometry generation block that passes the design to the selected FEA tool for performance calculations, and finally post-processing block that returns the computed data to the optimization algorithm for further evaluation (Fig. 1, black). Additionally, a geometric feasibility checking (FC) block can be part of the optimization workflow (Fig. 1, red).

3.3 Geometric feasibility

The term feasibility usually refers to the solution and means that the solution satisfies all given constraints. In other words, the region enclosed by $\forall g_j(\vec{x}) = 0$ is called a feasible region. This paper concentrates on another type of feasibility called *geometric or model feasibility*. Geometrically feasible model is valid for solving if there are no overlapping edges or non-conventional geometric relations. Infeasible candidate is the one that cannot be produced as a real machine because there are overlapping magnets, non-rectangular shaped magnets, air pockets overlapping magnets etc. Infeasible candidates should not be evaluated for performance because theoretically they can falsely appear as optimal solutions but can never be considered for manufacturing/production. It is important to note that geometric feasibility checking methods from the following sections are intended to be used only as an optimization procedure add-on (Fig. 1).

3.3.1 Optim. workflow without FC

If the optimization software does not include a feasibility check (FC), two different scenarios may occur during the FEA calculation (depending on the selected FEA tool).

In the first case, the FEA tool detects that the design is erroneous and throws an error. In this case, the designer must implement a try-catch procedure which will capture the event, otherwise the optimization procedure will fail (try-catch adds $t_{extra} \geq 4s$ per design evaluation). In the second case, the FEA tool does not detect the infeasibility and a full FEA calculation is performed. This is the worst case

scenario which will produce useless results and cause significant increase of optimization time (e.g., detailed transient electromagnetic simulations can take $t_{extra} \geq 15min$).

3.3.2 Optimization workflow with FC

However, if the optimization software includes a feasibility detection procedure, the designer can either attempt to correct the problematic instance or skip it. There are two typical ways to correct the optimization candidate prior to performance evaluation (passing it to the FEA calculation).

First, the entire set of optimization variables for that candidate is reinitialized randomly within the specified parameter bounds until geometric feasibility is achieved. This is a brute-force approach, but it is mandatory since evolutionary optimization algorithms (e.g. Genetic Algorithm, Differential Evolution) must have the same number of members in each population of optimization candidates. This is due to the fact that the each generation must be equal or better than the previous as the algorithm advances towards the optimum.

The alternative is forced feasibility, where each infeasible design is subjected to minimal parameter modification until feasibility is reached (e.g., the magnetic layer angle α_V is modified until w_{min} is reached, Fig. 2b). This approach can be complicated and requires an advanced parameterization with minimal feasibility constraints (Ban et al. , 2021).

Depending on the complexity of the design, both methods may increase execution time ($t_{extra} = 2 - 15s$). On the other hand, detecting and skipping the infeasible design actually does not impact execution time ($t_{extra} = 0$).

4 Standard approach for feasibility detection

The standard approach to feasibility detection is specific to each parameterized template, which typically requires immense programming/development resources for research groups engaged in electric machine design

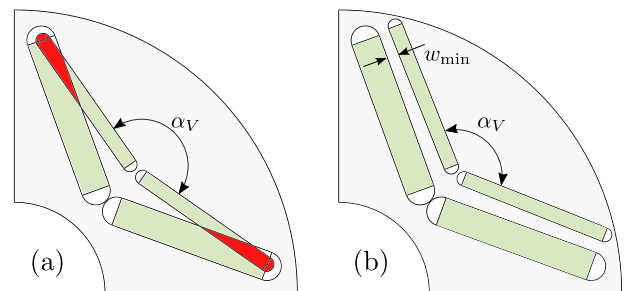


Fig. 2 Infeasible geometry (a) and forced feasibility (b)

optimization. Not only are top-level differences between templates relevant, e.g., a single-layer V-shape geometry compared to spoke interior permanent magnet machine (IPM), but also peculiarities such as air-pockets around magnets and curvature of posts and bridges have a significant impact on potential geometric feasibility. Modern high performance machines, especially in automotive traction, are all about these subtle design features. This means that an extensive study of the mathematical geometry dependencies has to be performed between arcs and lines that are either adjacent or have the possibility to touch or intersect during optimization process. All geometry primitives such as points, lines, arcs must be mathematically defined through coordinates or equations, ideally in both polar and Cartesian coordinate systems.

Depending on the definition of the optimization variables, this process can be fairly simple in some cases. For example, if the optimization variable for stator bore is defined as *ratio of stator bore diameter to stator outer diameter*

$$0.55 < D_{bore}/D_{outer} < 0.75 \tag{5}$$

then it is assured that the stator bore is always, as it should be, within the outer dimensions of the stator. A similar approach can be used for the height of the stator yoke - it must be shorter than the height of the stator annulus because both the slot and back iron must fit inside the stator. Therefore, this optimization variable is also defined as a ratio:

$$0.2 < 2h_{yoke}/(D_{outer} - D_{bore}) < 0.6 \tag{6}$$

Finally, the slot width or the tooth width, depending on the choice of stator slot type must be smaller than stator slot pitch in order to fit in the slot + the tooth inside one slot pitch.

However, when it comes to IPM rotors, especially multi-layered configurations as in Fig. 3, the mathematical description is much more complicated and, more importantly, it needs to be refined after each intervention in the template change. This is often the case in modern high performance automotive traction motors.

Typically, a single-layer, V-shape IPM rotor is described with a large number of rotor variables. The complexity can vary between different software packages or user defined templates in general-purpose FEA tools. In the case of commercial design tools, the minimum number of parameters to describe a layer is approximately 11. For multi-layer configurations, it increases linearly, so that a typical 2-layer V-shaped IPM traction motor (rotor shown in Fig. 3a) requires 22 variables just for magnets and barriers. If such a geometry is subjected to an optimization process to explore its full potential, or in

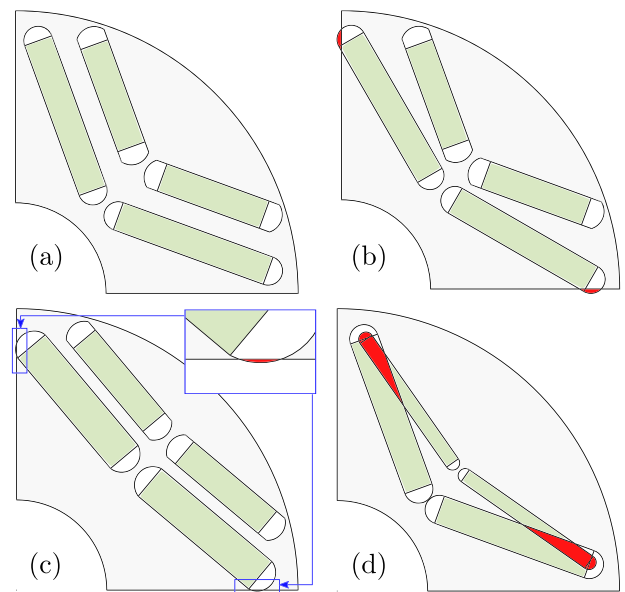


Fig. 3 Example of 2-layer V-shape IPM: **a** feasible case, **b** barrier definition point crossing polar lines, **c** barrier arc crossing polar lines, **d** barrier collision

other words, if the limits of the optimization parameters are set wide enough, there can be a large number of possible overlaps between air pockets, flux barriers, and magnets of a given layer or between different layers (Figs. 2, 3b–d).

The first step in the the standard approach would be to check whether any point (object vertex) is outside the rotor boundary: towards the stator and airgap, or inside the shaft. This is most easily achieved by checking the radial polar coordinates: any point with a radius greater than the outer radius of the rotor, or with a radius smaller than the inner radius of the rotor, means that the geometry is not feasible. A similar test exists to check if any point (object vertex) can be found outside the boundaries of each rotor pole (Fig. 3b). This is easily achieved by checking the angular polar coordinates: The angular coordinates should be within one pole. However, other tests, such as checking that barrier-limit arcs do not cross the interpolar line (Fig. 3c) and checking that there is no possible intersection between two layers (Fig. 3d), require hard-coding more complicated mathematical dependencies.

All of these calculations need to be changed, or at least reviewed, if the geometry slightly changes. The exact math can become considerably more complicated if barrier air pockets take stress relief shapes in the form of successive tangential arcs and ellipses, or if cooling channels and mass reduction holes are present in the geometry.

Algorithm 1 Feasibility verification example for 2-layer V-shape IPM geometry

```

1: function CHECK_FEASIBILITY
2:   for all points do
3:     verify whether radial coordinates are inside rotor
4:     verify whether angular coordinates are inside one
       pole
5:   for all layers do
6:     verify whether x-coordinates of all points are sorted
7:     verify that arcs do not cross interpolar line
8:   verify layer disposition
9:   verify possible intersection between two layers
    
```

The procedures for feasibility verification are specific and different for each different geometry. The pseudocode for a 2-layer V-shape IPM is shown in Algorithm 1. It is difficult to tackle all possible geometry failure cases so sometimes the algorithm can let the infeasible geometry further down the optimization pipeline. Then it is up to the wrapper of the FEA solver to try and catch the error and ignore the solution. This invalid geometry can be examined later and the feasibility checking function can be further improved.

It can be seen that this method is not robust and needs to be modified even for small changes in the geometry features of the topology under study. Therefore, a novel feasibility handling algorithm is presented in the next chapter.

5 Robust feasibility detection

For optimization purposes, the cross-sectional geometry of the stator and rotor of the machine can be reduced to 2D Euclidean space. Geometry parameterization is performed in either Cartesian or polar coordinates, specifying all geometric primitives: Points, Lines, Arcs, and Polylines, which are sets of multiple lines that model a complex curve (polyline can be approximated with series of arcs and lines before sending a drawing *.dxf* to FEA solver). A set of connected primitives forms an object as a shape, such as a rotor barrier, which has mathematical properties: Area, Perimeter, Centroid etc. If the entire machine geometry can be defined by shapes - software objects, it would be very convenient to have some sort of functional tool to determine the correlation between different shapes. Correlations include Boolean functions, intersections, areas etc. This novel approach is made possible by the Matlab Polyshape class (Mathworks 2020), which enables elevation of primitives to an object (shape) level. Once created, the shape objects can be organized in the form of a vector. The polyshape functionality allows a quick analysis of vectorized shape objects. One of the functions is *Intersection*, which returns information when there is an intersection between members of the shape vector. This provides a robust feasibility check regardless of

parameter boundaries and regardless of the complexity of the geometry shape. Considering that any electric machine topology can be reduced to geometric primitives, the proposed method can be implemented on all types of geometries as an upgrade of pre-existing code.

The main advantage of this approach is moving away from strict mathematical feasibility verification to shape object level which allows great design freedom, instead of relying on the rather complicated procedure described in the previous chapter (all functionality has been verified on Matlab releases after 2019b). Currently, there is no open-source code in Python or other interesting scripting languages that can provide the same functionality as Matlab polyshapes. However, this does not limit the presented novel approach. Considering the outlined benefits, open-source community will close this gap soon.

5.1 Polyshape function - details

Polyshape function creates a polygon defined by 2-D vertices and returns a polyshape object with properties describing its vertices, solid regions, and holes (Mathworks 2020). Essentially, polyshape is a structure that defines all vertices and holes within the 2-D shape. The syntax breakdown is given below (detailed variable description in Table 3).

$$P_{x,y} = Point(x_p, y_p) \tag{7}$$

$$L_{x,y} = Line(P_1, P_2) \tag{8}$$

$$A_{x,y} = Arc(P_{Or}, P_1, P_2) \tag{9}$$

$$M_{dxf} = \begin{pmatrix} L_1 & L_2 & \dots & L_n \\ A_1 & A_2 & \dots & A_m \end{pmatrix} \tag{10}$$

$$\vec{x}_s = [A_{3x}, L_{1x}, L_{3x}, A_{1x} \dots] \tag{11}$$

$$\vec{y}_s = [A_{3y}, L_{1y}, L_{3y}, A_{1y} \dots] \tag{12}$$

$$poly = polyshape(\vec{x}_s, \vec{y}_s) \tag{13}$$

$$polyvec = [poly_1, poly_2, \dots] \tag{14}$$

$$C_{x,y} = Centroid(poly) \tag{15}$$

Some of the predefined functions for manipulating polyshape structures are listed in Table 1. For better

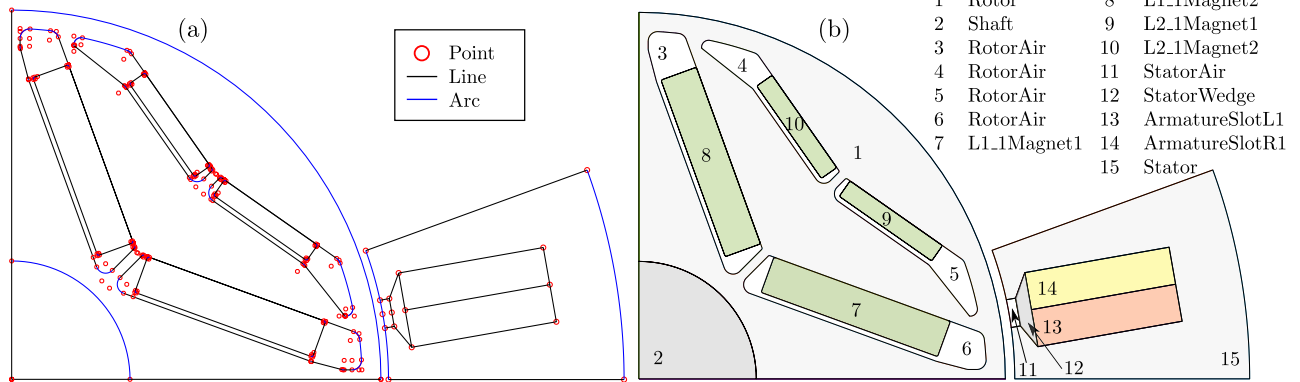


Fig. 4 All geometry points, lines and arcs (a); Machinecross section with all polyshapes (b)

Table 1 List of used primitives and polyshape functions

Function	Arguments	Return
Point	x_p, y_p	Point primitive
Line	Start point, end point	Line primitive
Arc	Origin, start, end points	Arc primitive
Polyshape	\vec{x}_s, \vec{y}_s	Shape object
Area	poly	Number
Centroid	poly	Centroid point ($C_{x,y}$)
Overlaps	polyvec	Intersection matrix
Polybuffer	poly, buffer	Polyshape ($poly_{buff}$)
Subtract	$poly_1,$	Polyshape ($poly_{sub}$)
Union	$poly_1, poly_2$	Polyshape ($poly_{union}$)
Intersect	$poly_1, poly_2$	Polyshape ($poly_{sect}$)
Xor	$poly_1, poly_2$	Polyshape ($poly_{xor}$)
Isinterior	poly, $P_{x,y}$	Boolean true or false

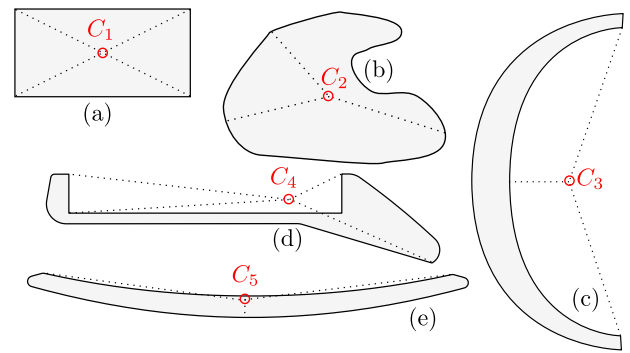


Fig. 5 Convex (a), general (b) and concave shapes (c, d, e)

understanding, a pseudocode formulation is used in this paper, the functional source code is available in the (Ban 2021).

5.2 Geometry polyshape definition

The automated geometry parameterization (Fig. 4a) defines all rotor and stator point objects (7). Line objects are defined by two points (8), while arc objects are defined by origin, start and end points (9). When generated, line and arc objects contain corresponding vertex data. Shape \vec{x}_s, \vec{y}_s vertex vectors are constructed by concatenating line and arc vertices in user-defined order (11), (12). Finally, \vec{x}_s, \vec{y}_s are the arguments to the *polyshape* construction function (13). If there are multiple shapes (e.g., rotor of an electric machine), they can be vectorized (14), Fig. 4b.

All adjacent shapes are built from the same set of polygons with a high number of vertices, which means that there

will be no resolution problems in detecting intersections. It is important to note that when exporting the validated design for FEA calculation, the arcs do not consist of many polylines, but of *.dxf* primitives, so that the selected FEA software can optimise the arc meshing and speed up the calculation process. On the other hand, when assigning values to polyshapes, the arc and line vertices are passed as discrete vectors (11), (12). This means that the matrix of line and arc primitives (10), and the polyshape vector (14) are stored and processed separately.

5.3 Convex and concave shapes

All electromagnetic FEA tools require that a certain material is assigned to every closed region, except when boundary conditions handle holes in the model. In automated optimization procedures it is therefore necessary to define the shape region precisely, which can be a problem. The problem is even greater when complex geometries are used in the optimization of high performance machines.

In general, a generated shape can be either convex or concave (by default, shapes with holes are not allowed). A shape is said to be convex if, for any two points in the shape, the straight line segment between them lies entirely within the shape. Convex polygon centroid is always within the vertex envelope (Fig. 5a), which need not be the case for concave shapes (Fig. 5c–e). A typical example of a strictly convex shape is the permanent magnet rectangle (Fig. 5a), while the general shape may have “dents” (Fig. 5b).

On the other hand, air barriers are inherently concave because permanent magnets (PM’s) are glued to the barrier surface and form separate shapes, thus creating a concave air pocket with an outer centroid (Fig. 5d). Furthermore, synchronous reluctance machine (SyRM) barriers are always concave, and depending on the curvature can have outer centroid. In the example of Fig. 5e, the centroid is within the shape limits, but very close to the edge, which can lead to problems in FEA calculations.

Overall, closed region inner-point detection by assigning the centroid point works well for convex shapes, but is unreliable for concave shapes.

5.4 Region inner-point detection

A robust region detection algorithm (Algorithm 2) was developed in combination with the existing *polyshape* functions and applied to all objects within the polyshape vector except magnets. Magnets are convex by default and require a specific magnetization direction determined by the *GetMagnetAngle* function (Algorithm 3).

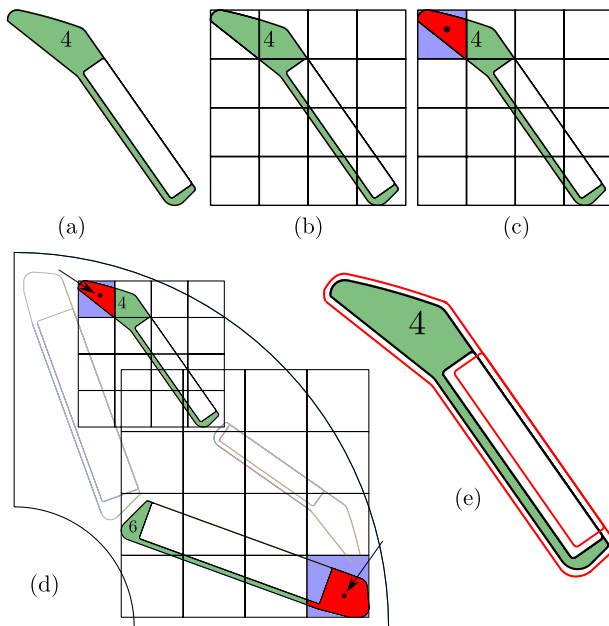


Fig. 6 Concave shapes robust region detection meshing example (a–d), functionality of *Polybuffer* function (e)

GetRegion function argument is polyshape structure $poly_{in}$ (Fig. 6a green). $poly_{in} \vec{x}_s, \vec{y}_s$ vertex limits are extracted resulting in a 4x4 vectorized polyshape rectangle mesh (Algorithm 2:ln:6–7, Fig. 6b). Each rectangle is intersected with $poly_{in}$ to form an output vector of intersection points (Algorithm 2:ln:9, Fig. 6b). The intersection element with the largest area is identified with the (Algorithm 2:ln:10, Fig. 6c).

Algorithm 2 Region inner-point detection

```

1: for i = 1 to numel(polyvec) do
2:   poly_in = polyvec(i)
3:   if poly_in != "Magnet" then
4:     function GETREGION(poly_in)
5:       function GENERATEMESH(poly_in)
6:         Calc. poly_rec 1-16 based on poly_in x,y limits
7:         polyvec_mesh = [poly_rec1, ..., poly_rec16]
8:         return polyvec_mesh
9:       polyvec_sect = Interscest (polyvec_mesh, poly_in)
10:      poly_big = find ( max ( Area (polyvec_sect) ) )
11:      C_x,y = Centroid(poly_big)
12:      if Isinterior(poly_in, C_x,y) then
13:        return C_x,y ▷ Centroid is the closed region
14:      inner point
15:    else
16:      function GETREGION(poly_big) ▷ Run again
17:    else
18:      function GETMAGNETANGLE(poly_in, τ, α_V)
19:        ...
20:      return C_x,y, α_M

```

The next step is to compute the temporary inner-point calculation (Algorithm 2:ln:11). The point $C_{x,y}$ is checked to be inside the original $poly_{in}$ with boolean function (Algorithm 2:ln:12). Finally, if $C_{x,y}$ is inside of the shape, it is returned as a region interior point, otherwise the procedure is repeated recursively on $poly_{big}$ (Alg. 2:ln:15).

The proposed algorithm basically searches for a convex sector of the initial polyshape. Brute-force tests of the presented method prove that the inner-point of the region is always found within the shape boundaries, regardless of the generated geometry.

Polyshape mesh can be set to any rectangular dimension. Considering that the function execution time is proportional to the number of used mesh shapes, it is important to set the optimal mesh size. Different combinations of mesh sizes were tested on randomly generated concave shapes. In case of 2×2 mesh, there is a 40% probability that the inner region of concave shape is found in the first function

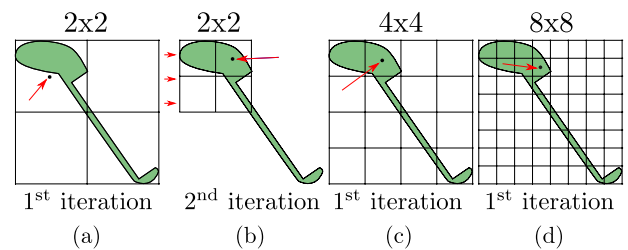


Fig. 7 Example of region detection mesh sizing

iteration (e.g. Fig 7a). The second iteration (e.g. Fig 7b) captures the inner region in 90% cases and sets the total number of mesh shapes to $2 \times 2 + 2 \times 2 = 8$ (1st plus 2nd iteration). On the other hand, when tested with 4×4 mesh, the inner region was in 90% cases found in the first iteration resulting in a total of $4 \times 4 = 16$ mesh shapes (e.g. Fig 7c).

Finally, 8×8 mesh finds the inner region in the first iteration in 98% cases, but with the expense of $8 \times 8 = 64$ shapes (e.g. Fig 7d). Compared with previous alternatives, the shape number is high and can potentially be doubled in nd iteration. Considering that 4×4 mesh has a rather high probability of finding the inner region in the first function iteration, 4×4 was selected as the optimal number of mesh shapes.

5.5 Magnetization direction

In addition to region inner-point, permanent magnets have magnetization direction (Fig. 8). The procedure for custom magnet shapes must be implemented individually. In this section, the procedure for V-shape rotor designs (Alg. 3) is explained. The magnet shape with the magnet angle parameter α_V and the pole step constant $\tau = \pi/p$ where p is the number of pole pairs, is passed to the function GetMagnetAngle. The function computes magnet centroid region point $C_{x,y}$ (Algorithm 3:ln:2) and the magnetization angle α_M . Algorithm 3:ln:6-12 and Fig.8 show the α_M calculation procedure which works when $\alpha_V \geq 180^\circ$, and even in the case of square-shaped magnets.

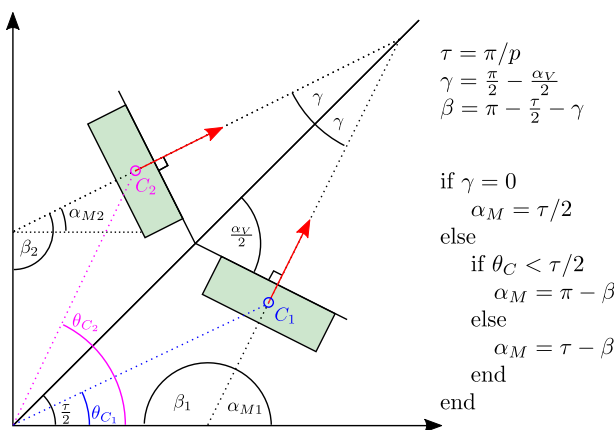


Fig. 8 Determining magnetization direction

Algorithm 3 Magnetization direction and region detection

```

1: function GETMAGNETANGLE(polyin, tau, alpha_V)
2:   Cx,y = Centroid(polyin)
3:   [theta_C, Rc] = cart2pol(Cx,y)
4:   gamma = (pi - alpha_V)/2
5:   beta = pi - tau/2 - gamma
6:   if gamma == 0 then
7:     alpha_M = tau/2
8:   else
9:     if theta_C < tau/2 then
10:      alpha_M = pi - beta
11:     else
12:      alpha_M = tau - beta
13:   return Cx,y, alpha_M
    
```

5.6 Feasibility check

The complete machine cross section with all polyshapes and assigned material regions including the rectangular mesh intersections is shown in Fig. 9a. In this example, a total of 15 polyshapes are stored in a vector form (14). The polyshape vector is passed to the overlaps function which returns overlaps matrix M_{ovl} (Alg. 4:ln:3). If M_{ovl} is a unitary matrix (Algorithm 4:ln:4), the design is feasible and there are no overlaps (Fig.9a, b), otherwise the generated design is infeasible (Fig. 9c, d). If the user wants to include a limit on the distance between certain shapes (useful for detecting material elements that are too thin to be manufactured), the Polybuffer function can temporarily increase the borders of the shape during feasibility check (Algorithm4:ln:2, Fig. 6e). Additionally, the same function is used to avoid geometrical conflicts (11), (12) in borderline cases (e.g. two shapes are touching).

Algorithm 4 Robust feasibility check

```

1: function CHECKFEASIBILITY(polyvec)
2:   polyvec = polybuffer (selected polyvec elements,
   buffer)
3:   Movl = overlaps (polyvec)
4:   flag = isequal (Movl, eye ( size (Movl, 1) ))
5:   if flag then
6:     disp ('Feasible geometry!')
7:   else
8:     disp ('Infeasible geometry!')
9:   return flag
    
```

5.7 Impact on total execution time

The feasibility and region detection procedure is performed only once during geometry generation, with a typical duration of 0.5–2 s. The transient calculation of a single operating point in ANSYS Motor-CAD for a two-layer IPM machine geometry typically takes between 30–60 s. If additional calculations are performed during the design

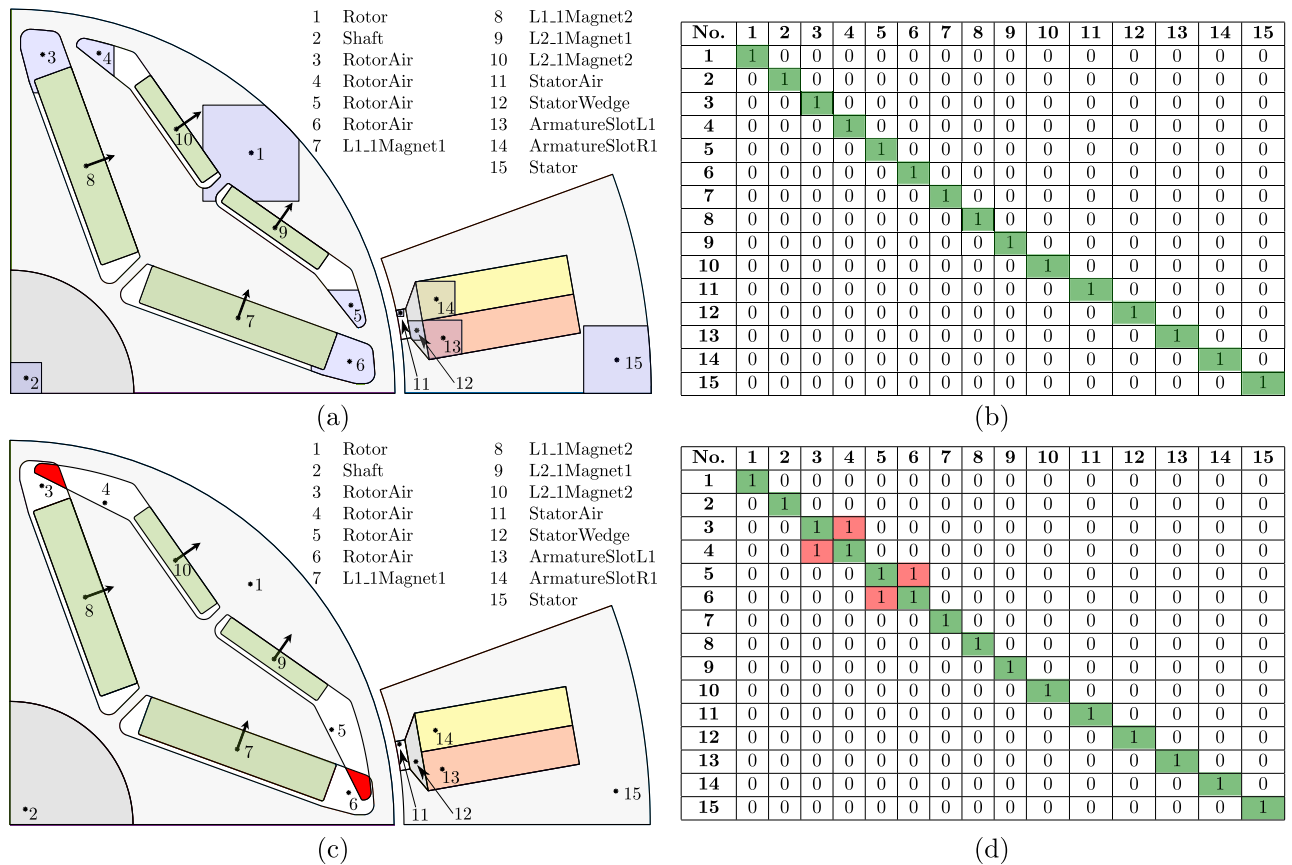


Fig. 9 Feasible (a, b) and infeasible geometry (c, d)

Table 2 FC impact on total optimization time

Run	1	2	3	4
Feasible designs	758	749	731	749
Infeasible designs	242	251	269	251
Total	1000	1000	1000	1000
Calc. time try-catch, no FC [h]	64.0	63.2	61.7	63.2
Calc. time with FC [h]	63.6	62.8	61.3	62.8
Calc. time worst case [h]	83.3	83.3	83.3	83.3
Time save, try-catch to worst case [%]	23.2	24.1	25.9	24.1
Time save, FC to worst case [%]	23.6	24.6	26.4	24.6

evaluation (thermal transients, drive cycle analysis, etc.), the cumulative time can increase to 10–15 min.

As an experiment, a sensitivity analysis with 4 consecutive runs of 1000 iterations was performed for a well-defined two-layer V-shape rotor geometry with 44 parameters (Table 2). The design space has been specified by

defining upper and lower bounds of all design parameters. A set of parameters for each design has been generated by scanning the multidimensional space via Space filling Latin Hypercube sampling method using Ansys OptiSLang surrogate modelling tool. The average design evaluation time is 300 s (5 min). Using try-catch adds 4 s (304 s per design evaluation), while using feasibility check adds 2 s (302 s per design evaluation).

Let us first consider the worst-case scenario without try-catch or FC (FEA tool runs the entire simulation). This approach leads to a maximum duration of 83.3 h per run. On the other hand, the try-catch procedure detects all possible errors, leading to an average execution time of 63.1 h (here we assume the scenario where the FEA tool outputs an error for each infeasible design). Finally, using FC results in an average execution time of 62.6 h.

As expected, the try-catch and FC procedures result in virtually the same execution time and a significant overall time savings (25% or 20 h shorter execution time). The

conclusion is that the use of FC has no impact on the total execution time. Unlike the try-catch procedure, FC can provide the information about the colliding regions and parameters that can be exploited in surrogate (metamodel) optimization, or tools such as Ansys OptiSLang (Riviere et al. 2019, 2020).

6 Conclusion

Optimization is an important and inevitable part of the modern electric machine design process. When properly applied, optimization leads to a design that satisfies all imposed requirements.

Even when properly constrained, complex geometries generated by optimization algorithm can lead to infeasible designs that in worst case increase optimization time or propagate non-manufacturable candidates. In addition, the accurate detection of interior points for each closed region in order to assign material can be a serious challenge.

The standard procedure for solving these issues is based on hard coding of simple or complex mathematical relationships between geometric elements. This method tends to be inflexible to any major changes and leads to a complex geometry code. The paper provides a solution to both problems through a novel robust feasibility verification procedure and inner-point detection using Matlab polyshape objects. The generality of the approach allows application in any other script language. The polyshape approach elevates geometric design analysis from geometric primitives (points, lines and arcs) to the level of objects (shapes), applicable to any type of machine geometry as an upgrade to existing code. In addition to geometrical properties (vertex coordinates), elevation to shapes allows severely simplified surface, mass and Boolean calculations. When implemented, the method represents a paradigm shift in electric machine design.

The main benefits of robust feasibility checking are: preventing infeasible (non-manufacturable) candidates to be propagated or to win in the optimization competition, gathering information about which shapes and parameters cause problems and finally, greater freedom in defining geometry parameter boundaries when describing complex geometries.

Appendix

See Tables 3 and 4.

Table 3 Complete list of variables and functions

Variable	Description
α_M	Magnetization direction according to Fig. 8
α_V	V angle of the the rotor magnets (Fig. 8)
β	Angle according to Fig. 8
γ	Angle according to Fig. 8
τ	Angle of one pole step according to Fig. 8
x_p	Individual point x coordinate
y_p	Individual point y coordinate
\vec{x}_s	Shape x vertex vector
\vec{y}_s	Shape y vertex vector
$P_{x,y}$	Point primitive defined by x_p, y_p
$L_{x,y}$	Line primitive defined by two point objects
$A_{x,y}$	Arc primitive defined by three point objects
$C_{x,y}$	Polyshape centroid point
θ_C	$C_{x,y}$ angular coordinate
R_C	$C_{x,y}$ radial coordinate
D_{bore}	Stator bore diameter
D_{outer}	Stator outer diameter
h_{yoke}	Stator yoke height
e_{in}	Inner barrier eccentricity
e_{out}	Outer barrier eccentricity
M_{ovl}	Matrix of shape overlaps
M_{dx}	Matrix of line and arc primitives
p	Number of pole pairs
$w_{c\ min}$	Minimum flux carrier width
$.dxf$	Drawing Interchange Format
GenerateMesh	Function that generates 4x4 polyshape mesh
GetMagnetAngle	Magnetization angle calculation function
GetRegion	Polyshape inner region point calc. function
<i>Polyshape</i>	Polyshape constructor function
poly	Polyshape structure defined by \vec{x}_s, \vec{x}_y
polyvec	Vector of polyshapes
poly _{big}	Polyshape with the biggest area in polyvec _{sect}
poly _{in}	Input polyshape vector
poly _{recl-16}	16 mesh polyshapes
polyvec _{mesh}	Vector containing all mesh polyshapes
polyvec _{sect}	Intersect. between the polyvec _{mesh} and polyvec _{in}

Table 4 List of abbreviations

Abbreviation	Description
EV	Electric vehicle
FC	Feasibility check
FEA	Finite element analysis
IPM	Interior permanent magnet
OEM	Original equipment manufacturer
PM	Permanent magnet
SyRM	Synchronous reluctance machine

Supplementary Information The online version contains supplementary material available at <https://doi.org/10.1007/s00158-022-03263-4>.

Acknowledgements This work was supported by Motor Design Limited.

Declarations

Conflict of interest The authors declare that they have no conflict of interest.

Replication of results Minimum example Matlab code has been published for open-access on GitLab site (Ban 2021).

Open Access This article is licensed under a Creative Commons Attribution 4.0 International License, which permits use, sharing, adaptation, distribution and reproduction in any medium or format, as long as you give appropriate credit to the original author(s) and the source, provide a link to the Creative Commons licence, and indicate if changes were made. The images or other third party material in this article are included in the article's Creative Commons licence, unless indicated otherwise in a credit line to the material. If material is not included in the article's Creative Commons licence and your intended use is not permitted by statutory regulation or exceeds the permitted use, you will need to obtain permission directly from the copyright holder. To view a copy of this licence, visit <http://creativecommons.org/licenses/by/4.0/>.

References

- Ban B, Stipetic S, Jercic T (2021) Minimum set of rotor parameters for synchronous reluctance machine and improved optimization convergence via forced rotor barrier feasibility. *Energies* 14(10):16. <https://doi.org/10.3390/en14102744> (ISSN 19961073)
- Branko B (2021) A minimum code example: robust feasibility verification and region inner-point detection algorithms for geometric shape objects in e-machine optimization, <https://bit.ly/3sPutFo>
- Lee C, Lee J, Jang In G (2021) Shape optimization-based design investigation of the switched reluctance motors regarding the target torque and current limitation. *Struct Multidisc Optim* 64(2):859–870. <https://doi.org/10.1007/s00158-021-02897-0>
- Lu C, Ferrari S, Pellegrino G (2017) Two design procedures for PM synchronous machines for electric powertrains. *IEEE Trans Transp Electr*. <https://doi.org/10.1109/TTE.2016.2646738>
- De La Parra HZ, Freddy M, Sjoerd B (2009) Challenges for electric machines and power electronics in automotive applications. International Conference on Ecological Vehicles and Renewable Energies,(EVER'09), pp 1–9
- EU (2009) Commission Regulation (EC) 640/2009 Implementing directive 2005/32/EC of the european parliament and of the council with regard to ecodesign requirements for electric motors. *Offic J Europ Union* (640): L 191/26
- European Environment Agency (2016) Electric Vvhicles in Europe. ISSN 1557-170X. <https://www.eea.europa.eu/publications/electric-vehicles-in-europe>
- Gerd B, Ciprian ZA, Siegfried S, Edwin L, Wolfgang A (2016) Possibilities for speeding up the FE-based optimization of electrical machines-a case study. *IEEE Transactions on Industry Applications*. ISSN 00939994. <https://doi.org/10.1109/TIA.2016.2587702>
- Pellegrino G, Cupertino F, Gerada C (2015) Automatic design of synchronous reluctance motors focusing on barrier shape optimization. *IEEE Trans Indus Appl*. <https://doi.org/10.1109/TIA.2014.2345953>
- International Energy Agency (2020) Global EV outlook 2020. URL <https://www.iea.org/reports/global-ev-outlook-2020>
- Lee J, Jeong HS, Kikuchi N (2010) Topology optimization of switched reluctance motors for the desired torque profile. *Struct Multidisc Optim* 42(5):783–796. <https://doi.org/10.1007/s00158-010-0547-1>
- Jouni L (2002) Multi-constrained nonlinear optimization by the differential evolution algorithm. In: *Soft Computing and Industry*. Springer-Verlag London. https://doi.org/10.1007/978-1-4471-0123-9_26
- Kamper MJ, Van Der Merwe FS, Williamson S (1996) Direct finite element design optimisation of the cageless reluctance synchronous machine. *IEEE Trans Energy Convers* 11(3):547–553. <https://doi.org/10.1109/60.537006> (ISSN 08858969)
- Lee C, Jang In G (2021) Topology optimization of multiple-barrier synchronous reluctance motors with initial random hollow circles. *Struct Multidisc Optim* 64(4):2213–2224. <https://doi.org/10.1007/s00158-021-02976-2> (ISSN 16151488)
- Mathworks (2020) Matlab polyshape function. <https://www.mathworks.com/help/matlab/ref/polyshape.html>
- Nicolas R, Giuseppe V, Marco V, Giuseppe F, Di Leonardo L, Mircea P (2019) Design analysis of a high speed copper rotor induction motor for a traction application. In: (2019) *IEEE International Electric Machines and Drives Conference, IEMDC 2019*. <https://doi.org/10.1109/IEMDC.2019.8785124>
- Nicolas R, Markus S, James G (2020) An innovative multi-objective optimization approach for the multiphysics design of electrical machines. In: *2020 IEEE Transportation Electrification Conference and Expo, ITEC 2020*, pp 691–696. <https://doi.org/10.1109/ITEC48692.2020.9161650>
- Bulent S, Casey TM, Di H, Li S (2017) Driving toward accessibility: a review of technological improvements for electric machines, power electronics, and batteries for electric and hybrid vehicles. *IEEE Ind Appl Mag* 23(1):14–25. <https://doi.org/10.1109/MIAS.2016.2600739> (ISSN 10772618)
- Torsten B, Roger E (1996) Extensions to structural optimization software to enable multidisciplinary applications. In: *6th Symposium on Multidisciplinary Analysis and Optimization, (X)*: 1202–1211, <https://doi.org/10.2514/6.1996-4168>
- Zarko D, Stipetic S, Martinovic M, Kovacic M, Jercic T, Hanic Z (2017) Reduction of computational efforts in finite element-based permanent magnet traction motor optimization. *IEEE Trans Industr Electron* 65(2):1799–1807. <https://doi.org/10.1109/TIE.2017.2736485> (ISSN 02780046)
- Zhao N, Schofield N (2020) An induction machine design with parameter optimization for a 120-kW electric vehicle. *IEEE Trans Transp Electr* 6(2):592–601. <https://doi.org/10.1109/TTE.2020.2993456> (ISSN 23327782)
- Žarko D, Drago B, Lipo TA (2005) Design optimization of Interior Permanent Magnet (IPM) motors with maximized torque output in the entire speed range. In: *2005 European Conference on Power Electronics and Applications*. <https://doi.org/10.1109/epe.2005.2192969>

Publisher's Note Springer Nature remains neutral with regard to jurisdictional claims in published maps and institutional affiliations.

Publication 7: Systematic Metamodel-based Optimization Study of Synchronous Reluctance Machine Rotor Barrier Topologies

Paper details:

B. Ban and S. Stipetić, "Systematic Metamodel-based Optimization Study of Synchronous Reluctance Machine Rotor Barrier Topologies", in Special Issue Synchronous Reluctance Motor-Drive Advancements, *Machines* 2022, 10(8), 712. August 2022.

Available at:<https://doi.org/10.3390/machines10080712>

Article

Systematic Metamodel-Based Optimization Study of Synchronous Reluctance Machine Rotor Barrier Topologies

 Branko Ban ^{1,2,*}  and Stjepan Stipetic ¹ 

¹ Department of Electric Machines, Drives and Automation, Faculty of Electrical Engineering and Computing (FER), University of Zagreb, Unska 3, 10000 Zagreb, Croatia

² Torquery Consulting, Blidvädersgatan 56, 41830 Göteborg, Sweden

* Correspondence: branko.ban@fer.hr

Abstract: Nowadays, due to the confidence in modeling tools and rapid product iteration, electric machine designers primarily rely on simulations. This approach reduces time and cost and is very useful when comparing different machine topologies. The prototype stage usually comes after the depletion of all simulation resources. When designing a synchronous reluctance machine, the first step is the selection of rotor barrier type. The literature provides several topologies but does not clearly state which one yields the best performance. The goal of this paper is to determine the best variant for a six-pole machine and the selected requirements using a metamodel-based optimization approach. Seven rotor topologies with different complexities were derived from circular, hyperbolic, and Zhukovsky barrier types (circular concentric, circular variable depth, hyperbolic with fixed eccentricity, hyperbolic with variable eccentricity, original Zhukovsky, modified Zhukovsky variable depth and modified Zhukovsky with equal barrier depth). The novelty of the proposed strategy is in the systematic and fair comparison of different rotor topologies. This approach significantly reduces the total optimization time from several weeks to a few days. Additionally, a novel modified Zhukovsky variable depth topology, which merges the best qualities of all considered variants, was developed. An identical optimization strategy was applied to all variants, and the final results prove that the barrier type substantially affects the final performance of the machine. The best results are achieved by the modified Zhukovsky variable depth topology. In relation to the worst (baseline) topology, the performance gain is 14.9% and the power factor is increased from 0.61 to 0.67. An additional study using different numbers of barrier layers (3, 4, and 5) was conducted to determine the best topology. The best results were achieved with the original four barrier layers.

Keywords: synchronous reluctance; barrier comparison; rotor topology; metamodeling; optimization



Citation: Ban, B.; Stipetic, S. Systematic Metamodel-Based Optimization Study of Synchronous Reluctance Machine Rotor Barrier Topologies. *Machines* **2022**, *10*, 712. <https://doi.org/10.3390/machines10080712>

Academic Editor:
Toomas Vaimann

Received: 1 July 2022
Accepted: 16 August 2022
Published: 19 August 2022

Publisher's Note: MDPI stays neutral with regard to jurisdictional claims in published maps and institutional affiliations.



Copyright: © 2022 by the authors. Licensee MDPI, Basel, Switzerland. This article is an open access article distributed under the terms and conditions of the Creative Commons Attribution (CC BY) license (<https://creativecommons.org/licenses/by/4.0/>).

1. Introduction

In recent years, global legislation is stimulating an increase in electric vehicle (EV) production. This has led to a paradigm shift in the automotive industry, forcing the rapid development of propulsion technology, especially in the area of electric traction machines. Due to them having the highest torque and power density compared to other machines, interior rare-earth permanent magnet synchronous machines (IPM) are preferred for automotive traction. Although the performance benefits are undisputed, the use of rare-earth permanent magnet (PM) materials, such as neodymium or dysprosium, has been a commercial risk. This risk can potentially increase as EVs start to penetrate the market on a large scale (Figure 1).

Historically, this has forced some vehicle producers to consider alternative machine designs, which either use no or a minimal amount of rare-earth material. There are notable first-generation passenger vehicles, such as Tesla Model S and Audi e-tron, which use induction machines (IM), and the second-generation Chevrolet Volt, which uses rare-earth-free Ferrite IPM. Currently, there is no commercial use of synchronous reluctance machines

(SyRM) for automotive traction, but due to the cost reduction benefits, they represent a valid alternative [1]. The research presented in [2] provides a theoretical review of major SyRM aspects and highlights potential use niches. The selected application is a commercial vehicle power take-off, an interface that actuates additional body systems, usually powered through variable-speed hydraulic pump (e.g., refuse compressors, hook-lifts, concrete mixers, etc.). In the case of electric vehicles, the interface is referred to as electric power take-off (e-PTO). Considering that the e-PTO needs to be reliable, robust, and cheap, SyRM is the preferred alternative [3,4].

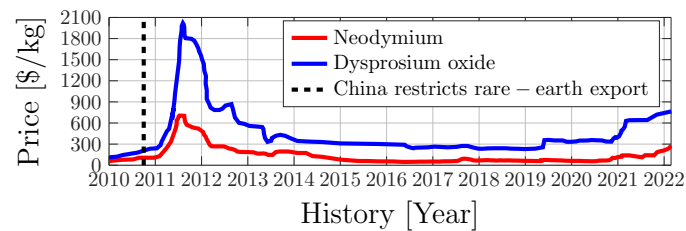


Figure 1. Historical rare-earth material prices.

This paper will concentrate on the e-PTO SyRM design and optimization with requirements carried over from [4]; all terminology is according to Figure 2a.

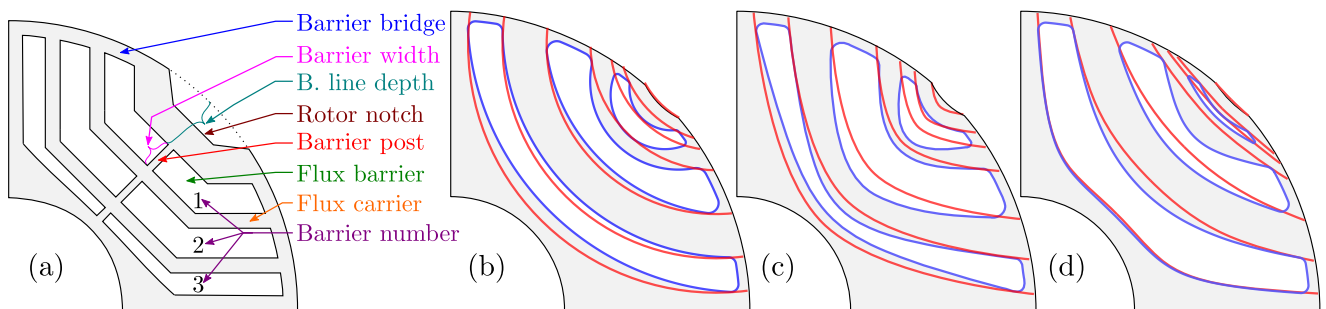


Figure 2. (a) SyRM terminology; SyRM rotor barrier types: (b) Circular variable depth (blue), concentric (red); (c) Hyperbolic variable eccentricity (blue), fixed eccentricity (red); (d) Modified Zhukovsky (blue), original Zhukovsky (red);

Most automotive manufacturers have a strategy of reusing components when possible to increase production volume, which leads to price reduction. The presumption is that the e-PTO inverter will have the same part number as a truck traction inverter (i.e., the max power rating for a traction inverter is 180 kW). The obvious conclusion is that the inverter will be oversized for e-PTO application, which effectively eliminates the low power factor issue [4]. Furthermore, the PTO shaft has historically been a part of the diesel engine and has a quite big torque ripple [3,4]. Instead of using torque ripple minimization as an optimization objective, max. ripple was limited to $\leq 15\%$ (a posteriori ripple reduction options were demonstrated through rotor skewing).

Modern electric machine design is strictly tied with some type of multi-objective mathematical optimization workflow. An important milestone in electric machine optimization was the introduction of Differential evolution (DE) algorithm coupled with finite element analysis (FEA) by Lampinen [5]. Further enhancements of the approach were carried out by Žarko et al. [6,7], leading to an overall reduction in optimization time. Current state-of-the-art research projects still heavily depend on similar approaches utilizing different types of optimization algorithms (OAs) such as particle swarm, ant colony, and genetic algorithms [1,8–10]. Although the optimization times are gradually reducing, it is important to note that FEA-based design by means of OA has the serious drawback of a considerable computational burden [9]. This is due to the long FEA simulation time needed to evaluate

a single rotor candidate and the high number of FEA evaluations required by the OA to converge (it can take up to a week until the optimization converges). More details about the typical optimization approach are available in the Section 3.1.

On the other hand, this paper presents a novel, meta-model-based optimization strategy that offers a systematic and fair comparison of different electric machine topologies (Section 3.2). Instead of constantly reiterating and modifying best design variants over generations, the proposed method utilizes meta-modeling (or surrogate modeling) to radically decrease optimization time. Although the method is applicable to any type of electric machine, this paper concentrates on the SyRM e-PTO application. Considering the high number of optimized designs, the approach significantly reduces evaluation time from several weeks to a few days (nine different designs were optimized). Additionally, this study introduces a novel modified Zhukovsky variable depth topology, which merges the best qualities of all considered SyRM rotor variants.

To the best of our knowledge, the currently available literature does not cover the proposed approach applied on SyRM design.

1.1. SyRM Advantages

One advantage of SyRM compared to IM and IPM is the lack of squirrel cage and magnets, which results in reduced material and manufacturing costs. This feature leads to SyRM having minimal rotor losses compared to both alternatives [11], and higher efficiency compared to IM [12]. Furthermore, the SyRM control algorithm is very similar to IPM, meaning that the same drive can be used in both cases. Obviously, there are no issues with demagnetization. Finally, SyRM does not produce back electromotive force, which secures fault tolerance and can simplify the electric vehicle drive train (mechanical disconnect is not required), resulting in a cheaper transmission system.

1.2. SyRM Disadvantages and Potential Solutions

The main disadvantage of SyRM compared to IPM is reduced power and torque density. The situation can be improved by using hairpin stator technology which increases the fill factor [13], or by improvements in rotor design. References [12,14] emphasize the benefits of SyRM design for high-speed operation, resulting in higher efficiency system compared with IPM alternative. Ideally, the rotor should be designed without barrier posts [15], with minimal barrier bridge thickness [9,16]. This will obviously compromise mechanical integrity. Nevertheless, this issue can be solved by the use of “smooth barrier” topologies (e.g., circular, hyperbolic...) with injected epoxy resin [15], and carefully applied barrier corner fillets [9,10,16].

The benefits of barrier corner filleting are illustrated in Figure 3, presenting the mechanical stress distribution maps of identical rotors without and with barrier fillets, calculated on the rotational speed of $n = 3000$ rpm. The mechanical factor of safety, FOS (the ratio between material yield stress and the maximum calculated stress) of Figure 3a rotor is 0.95 indicating likely failure. The addition of fillets to the rotor structure in Figure 3b increases FOS to 2, indicating normal operation without any mechanical issues.

The next SyRM disadvantage compared to IM and IPM is higher torque ripple. Depending on the application, ripple has to be reduced to an acceptable level which is usually 2–4% for vehicle traction or $\approx 10\%$ in industrial applications.

A typical a posteriori (post optimization) method for torque ripple reduction is rotor (or stator) skewing. The disadvantage of the approach is the reduction in average torque and increased production cost.

On the other hand, a priori (prior to optimization) ripple reduction methods are: increasing the number of poles, application of barrier corner fillets [10], use of barrier notch (Figure 2a), and use of asymmetric pole designs [17].

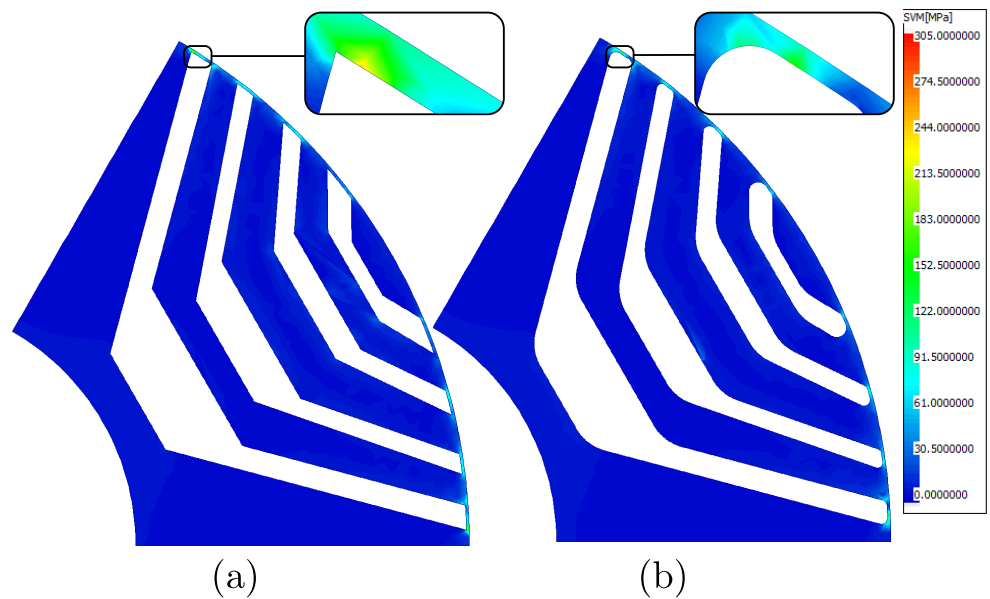


Figure 3. SyRM rotor mechanical stress distribution without (a) and with (b) barrier fillets.

The function of the barrier notch is to further increase rotor reluctance, otherwise, the flux lines would distribute between adjacent slots thus contributing to the loss of torque and consequently increasing the torque ripple. Detail instructions on slot construction methods are available in [18]. Considering that the high pole number has a strong negative impact on power factor, SyRM machines typically have 4 or 6 poles (more than 6 poles correspond to power factors ≤ 0.6). In case inverter size is not a design constraint, higher pole number combinations can be investigated. Nevertheless, implementation of other a priori methods will effectively reduce torque ripple without major design penalties. Asymmetric pole design is especially interesting because it can significantly reduce torque ripple [19] and potentially eliminate the need for a posterioriskewing, thus making SyRM the cheapest machine variant on the market.

The unavoidable disadvantage of SyRM is the lowest power factor compared to IM and IPM. The only solution to compensate for this drawback is in mass production of inverter switching modules which will enable cheaper technology, with higher current ratings. This will most likely happen when EVs penetrate the market on a large scale.

When it comes to SyRM performance improvements, Tawfiq et. al. [20] stipulate four main areas: rotor optimization, utilization of higher steel grade, winding configuration and inverter control strategies. A great example of SyRM optimization tool-set is provided in Syre platform [21] which additionally enables sensorless controller code generation and the simulation model itself. Winding configuration approaches vary from increasing the number of phases [22,23] to the implementation of delta-star [24], or even concentrated winding [8], all resulting in torque density improvement. Finally, according to [25], the selection of steel grade has a severe impact on SyRM efficiency where the selection of higher grade steel can increase the efficiency by 9%.

2. SyRM Rotor Barriers

The first step in the SyRM design is the selection of rotor barrier type. The literature provides references to several barrier topologies: circular, hyperbolic [26,27], Zhukovsky fluid type [28,29], segmented, etc. The open-source Syre project offers more details and instructions on geometry generation [30]. Currently, the literature does not clearly state which barrier topology yields the best performance. The goal of this paper is to calculate the best topology for the selected requirements within a defined optimization space.

Considering that sharp edges tend to cause mechanical issues, only barrier topologies based on smooth analytical functions have been analyzed (circular, hyperbolic, and

Zhukovsky). Depending on the parametrization, each design variant has a sub-variant. E.g., circular barriers can be concentric or have variable depth, while hyperbolic barriers can have equal or variable eccentricity. On the other hand, the Zhukovsky type cannot be analytically modified to secure variable barrier depth (by definition, Zhukovsky streamlines cannot mutually intersect), in this case, conformal mapping is used to create a modified Zhukovsky barrier type with variable depth lines (barrier construction details for all variants will be covered in the future publications).

Seven barrier topologies have been studied:

1. Circular concentric (CrC), Figure 2b (red);
2. Circular variable depth (CrVD), Figure 2b (blue);
3. Hyperbolic, fixed eccentricity (HyFE), Figure 2c (red);
4. Hyperbolic, variable eccentricity (HyVE), Figure 2c (blue);
5. Original Zhukovsky (Zh), Figure 2d (red);
6. Modified Zhukovsky variable depth (MZhVD), Figure 2d (blue);
7. Modified Zhukovsky with equal depth (MZhED, a special case of previous topology).

2.1. Automated Barrier Design

To simplify, the following figures are drawn for a two and three barrier rotor, the description of all parameters is explained in Tables 3 and 4.

Detailed construction instruction including the pseudo-code is available in [18].

The initial step in rotor construction (Figure 4a) is to specify number of pole pairs (p), rotor barriers (k) and barrier bridge thickness (w_{bb}). The user then specifies dimensionless $\vartheta_{min}, \vartheta_{max} \in [0, 1]$ (Table 4, 37–38). Temporary construction points vector E_{ABC} is then created with equidistant angular spacing ($\Delta\vartheta_r$). Barrier notch point (E_n) is specified with additional parameter ϑ_{notch} (Table 4, 39) relative to ϑ_{min} with radial component equal to rotor radius.

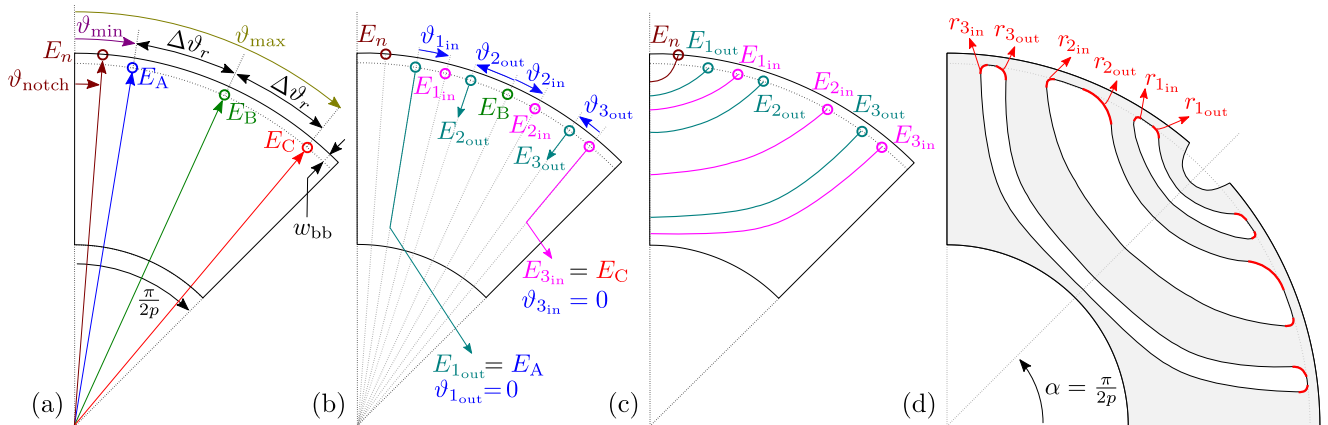


Figure 4. Rotor barrier construction procedure for a three barrier rotor, $k=3$

The second step (Figure 4b) is the construction of inner and outer barrier line starting points ($E_{1..k in}, E_{1..k out}$). The points are calculated relative to E_{ABC} , based on additional set of dimensionless parameters $\vartheta_{1..k in}, \vartheta_{1..k out} \in [0, 1]$ (Table 4, 15–22).

The last element in barrier line definition is the depth of each line defined by depth parameters $D_{1..k in}, D_{1..k out}, D_n \in [0, 1]$, depending of the barrier type (Figure 4c, Table 4, 41–48).

The final step is the rotation around the center point by the angle $\alpha = \pi/(2p)$ and mirroring the geometry around the half pole axis (Figure 4d). Barrier fillets ($r_{1..k in}, r_{1..k out} \in [0, 1]$, Table 4, 23–30) responsible for securing mechanical integrity of the rotor are added to the geometry (adding precise fillets to the discrete lines is a complex problem which is planned to be explained in the future publications). The final rotor geometry is exported as *.dxf* to the FEA tool.

2.2. Barrier Depth Variation

The width of the each barrier depends on initial inner and outer line starting points $E_{1..k\ in}$, $E_{1..k\ out}$, and depth coefficients $D_{1..k\ in}$, $D_{1..k\ out}$. Depending on the selected topology, barrier width can be uniform (CrC), approximately uniform (HyFE) or variable (CrVD, HyVE, Zh, MZhED, MZhVD). Considering that the barrier width has a substantial impact on the machine performance, this section will explain how inner and outer barrier depth coefficients affect each of the studied topologies, with a simplified presumption of equal line starting points [18].

In the case of HyFE and CrC, all barrier depths are equal ($D_{1..k\ in}$, $D_{1..k\ out}$). With this simplification, depth variation results in a symmetrical offset that keeps the uniform barrier width (Figure 5a,b). On the other hand, CrVD and HyVE have a higher degree of freedom with unconstrained depth variation resulting in variable barrier width (Figure 5c,d).

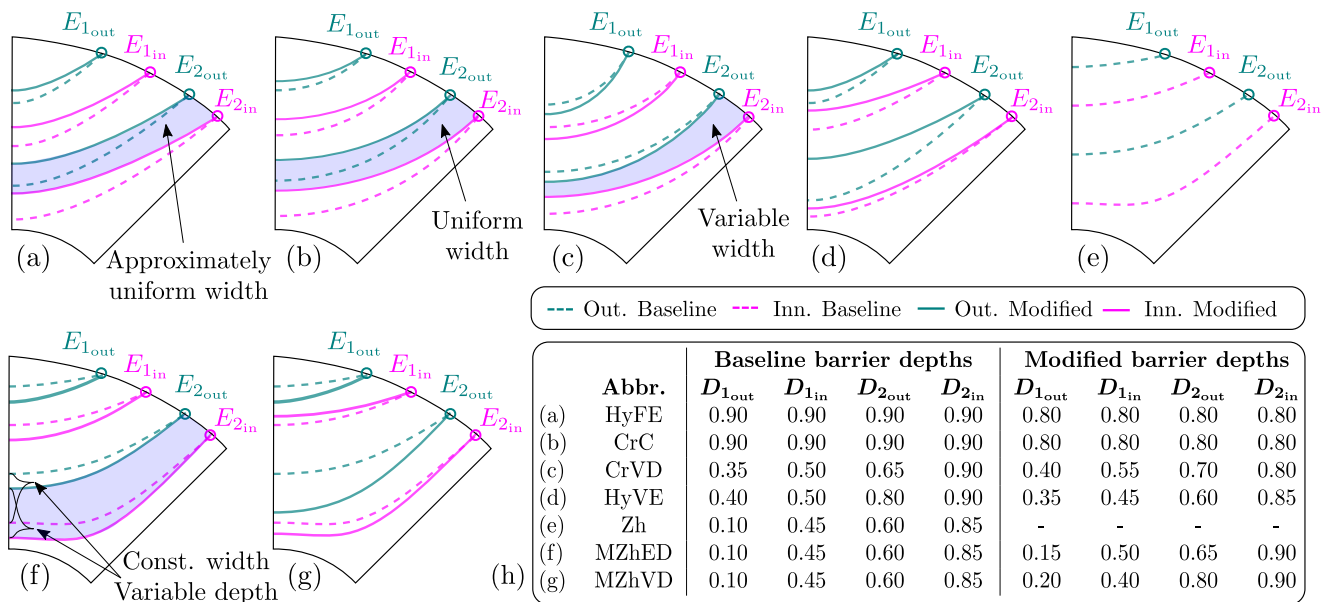


Figure 5. Barrier depth variation influence on different 2-barrier ($k = 2$) SyRM topologies (depth coefficient table is illustrative).

Zh barrier type (Figure 5e) is a special case because it does not support any depth variation. Barrier line depths are defined directly from starting points and cannot be modified. In order to explore the possible benefits of depth variation, Zh type was modified to the following variants. MZhED, where all depths are equal variation, thus achieving symmetrical positive or negative offset (Figure 5f), and MZhVD where barrier depths have full freedom (Figure 5g).

A table of different barrier line depth parameter combinations is provided in Figure 5h. It is important to note that barriers are constructed in such a way that the design is geometrically feasible (there are no barrier intersections of any kind).

2.3. Zhukovskiy Barrier Modification

As previously mentioned, Zh lines cannot mutually intersect. To secure barrier depth variability and improve machine performance, we introduce barrier depth modification in complex plain via dimensionless depth parameters D_{in} , D_{out} , D_n .

Generated rotor barrier lines are defined by sorted vertices containing corresponding x, y coordinates which can be drawn on a 2D real Euclidean plane (Figure 6a). For easier manipulation, real plain coordinates are redefined in complex z -plane ($z = x + jy$), Figure 6b. Considering that the vertices are the same in the real and complex plane, this is a trivial transformation [18].

Electric machine rotors have a circular layout which can be exploited by selecting the convenient complex function $f(z)$ and applying forward conformal mapping to a complex w -plane ($w = u + jv$), Figure 6c. Geometrical modifications of the barrier geometry are then performed in the w -plane and, upon completion, returned back to the z (and real) plane via inverse conformal mapping.

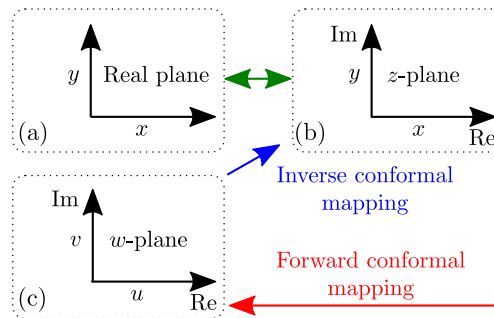


Figure 6. Mapping workflow. Euclidean plane (a); Complex z plane (b); Complex w plane;

Original Zh barrier lines with corresponding x, y vertices are written as $z = x + jy$ (Figure 7a, red) and conformally transformed to w -plane via $w = \ln z$ complex function as $w = u + jv$ (Figure 7b, red).

Upon modification (Figure 7b, blue), barrier lines are mapped back to z -plane via inverse complex function $z = e^w$ (Figure 7a, blue). The main benefit of the approach is easier barrier modification in the w -plane which leads to simplified software coding.

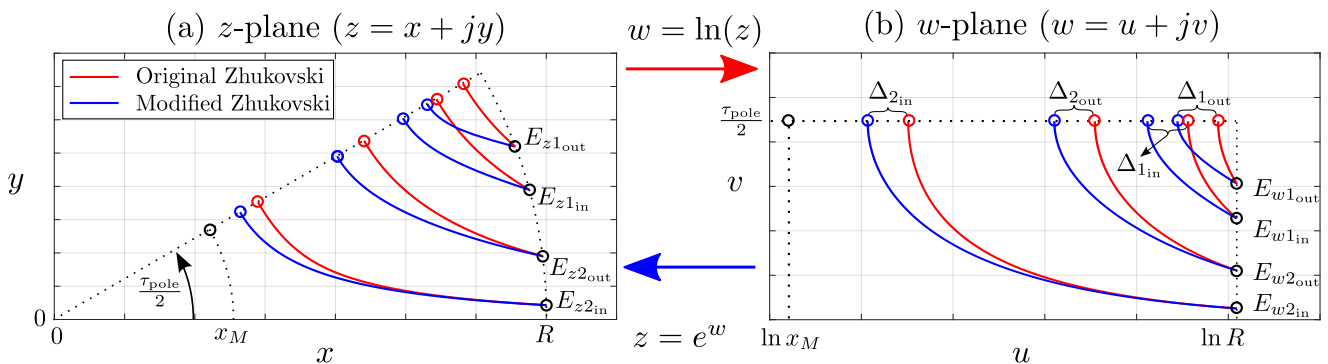


Figure 7. Modification of Zhukovsky lines via conformal mapping.

3. Optimization

3.1. Typical Optimization pProcedure

Most of the electric machine design goals are in conflict with each other and thus form a multi-objective problem (e.g., reduction in volume and mass while increasing the efficiency). When used in EVs, an increased machine weight contributes to the driving range reduction, while a larger volume creates issues with mechanical integration within the drivetrain. Obviously, an optimal trade-off between conflicting requirements is a design imperative. Considering a large number of coupled parameters that affect the final design, manual design is usually not an option. Nowadays, mathematical optimization is used for obtaining better designs.

Optimization algorithms (OAs) can be divided into gradient-based methods and stochastic (metaheuristic) methods. Gradient methods converge fast but have difficulties with global optima because they require a feasible starting point, which can be a problematic task in complex problems [31]. Stochastic methods are heavily used in electrical machine optimization [31]. The drawback is that the convergence can last for days, and the global optimum cannot be mathematically proven. Additionally, some popular metaheuristic

methods are based on natural behavior (Genetic algorithm (GA) [32], Differential evolution (DE) [5], Particle swarm, but they can also be iterative [33], or based on approximation [34]. From an engineering standpoint, both approaches can find a satisfying result.

IPM and SyRM design is highly affected by the saturation within the rotor structure which implies the use of computationally intensive FEA. A typical optimization system consists of the FEA tool (e.g., Ansys Motor-CAD), OA (e.g., DE), and external software, which handles model building and FEA tool communication (e.g., Matlab). When using this (or similar) system, the user has to initially specify all design boundaries and parameters (including upper and lower bounds). OA then generates a set of optimization parameters that define an optimization candidate (a complete machine model). After calculation, FEA results are returned to the OA for evaluation. OA then generates a new population of optimization parameters, repeats the procedure, and propagates through generations until reaching the optimal machine model (Figure 8, color coding according to the used system elements).

According to [32], the GA and the DE are the most preferred OAs, because both algorithms provide fast and accurate solutions for multi-objective problems and they can be run without any need for experimental data. The obvious drawback is that OA requires thousands of design evaluations for proper parameter propagation, which can substantially increase optimization time e.g., DE algorithm took 27500 FEA evaluations and lasted 7 days [4].

The alternative is topology optimization, which can potentially generate novel structures unrelated to traditional, smooth-shape SyRM barriers. The method applies the on/off method based on the normalized Gaussian network (NGnet) [35]; e.g., the algorithm sets the rotor quadrants to consist of either steel or air. However, when using this method, it is difficult to obtain thin-layered flux barriers that are easy to manufacture and can withstand mechanical stresses.

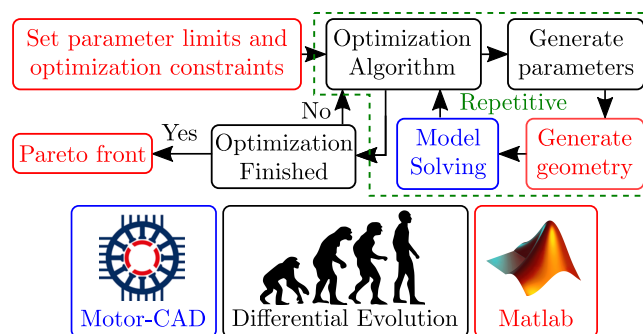


Figure 8. Typical optimization workflow.

The final approach is to use a metamodel (also referred as surrogate modeling by [36]) based optimization strategy, e.g., Adaptive-Sampling Kriging Algorithm (ASKA), [37]. The ASKA applies kriging interpolation of sampled objective function model which has lower computation time compared with a standard approach. Nevertheless, the accuracy is determined by the sampling quality and objective function complexity. This paper uses a dedicated optimization tool Ansys Optislang (OSL) which combines the standard procedure (OA + FEA tool + external software) with advanced sensitivity analysis and metamodeling, Figure 9.

The additional functionality enables motor designers to leverage the design space and most importantly reduce optimization time [38] (typical optimization time is 2–3 days).

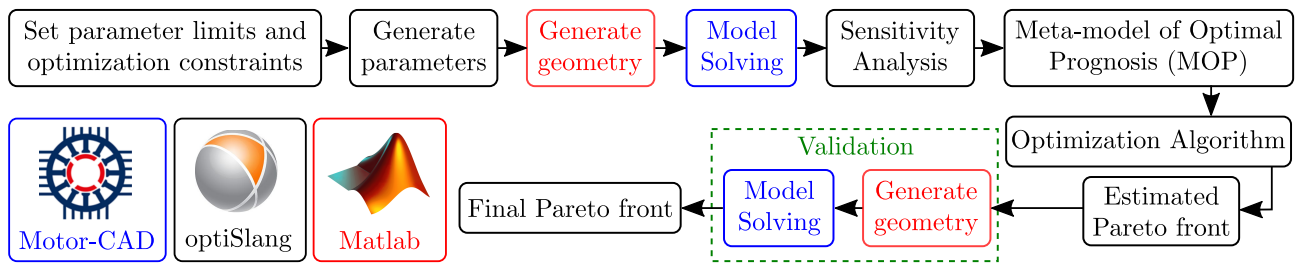


Figure 9. Optimization workflow with Matlab scripting and Motor-CAD FEA tool within Optislang environment.

3.2. OptiSlang Optimization Details

The logic of the OSL tool process is outlined in Figure 9. First, the user has to initially specify all design parameters (including upper and lower bounds) and a number of designs ($N_{Dsg} = 300$) for initial evaluation. OSL then generates parameters (scans the multidimensional space with a specified sampling method), calls Matlab script which generates electric machine model, and runs FEA calculation for each of the N_{Dsg} designs. Once the variation study has been completed, OSL runs the sensitivity analysis of output parameters in relation to input parameters. Next, OSL creates the so-called metamodels of Optimal Prognosis (MOPs), showing the relationships between performance outputs and design input variables.

The following example highlights the connection between sensitivity analysis and a single MOP (in reality, a model has multiple MOPs created for crucial optimization responses).

In Figure 10, the importance of all input variables is quantified using a variance-based measure called single Coefficient of Prognosis (CoP). The full model CoP (or total CoP) value written at the top of the figure is a crucial measure that is used to assess the forecast quality of the meta-model. This value is always lower than or equal to 100%. The higher this value, the more accurate the MOP prediction. In Figure 11, the torque output MOP is plotted against the two most important parameters, namely the split ratio and stack length. The CoP and MOP approach is used for modeling each critical design response listed in Section 3.4.

The user then selects the preferred optimization algorithm which is applied directly to the MOP with user-specified optimization goals and inequality constraints. The key point here is that the metamodel evaluates almost instantly since it is a mathematical function, instead of a computationally intensive FEA calculation. For multi-objective problems, the best designs from the solution space can be interpreted with the use of a Pareto front. Finally, the number of the MOP-based estimated optimization results (N_{Par}) are validated and verified by running FEA software. Differences may emerge depending on the quality of the calculated MOPs. In that case, the user can either add design samples to the sensitivity analysis or tweak the optimization constraints to increase MOP quality.

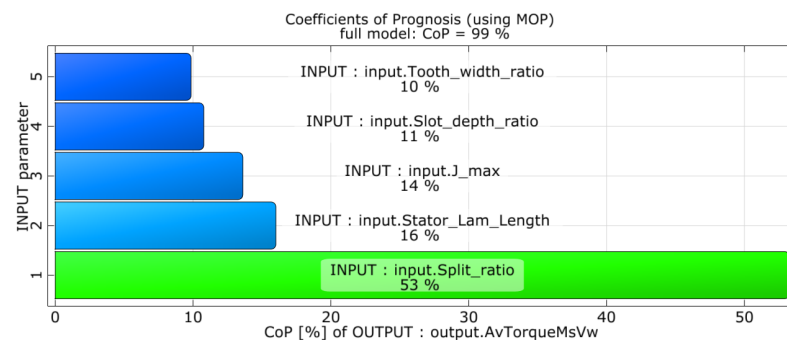


Figure 10. Example of torque response coefficient of prognosis.

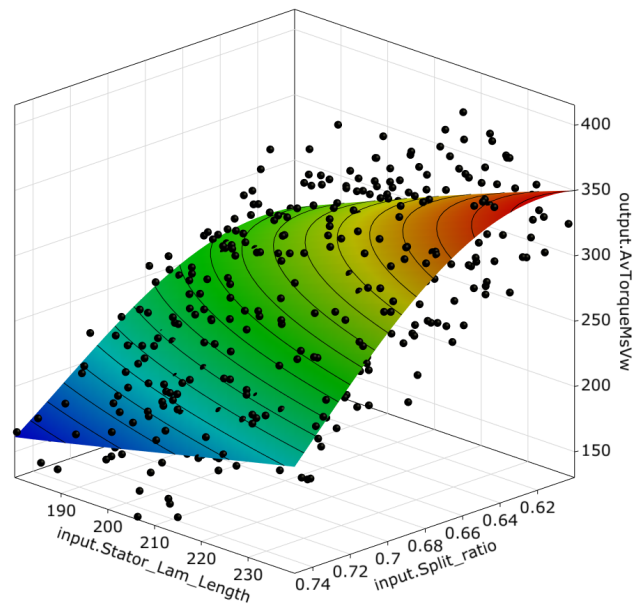


Figure 11. Example of torque response MOP (black dots are the sampling data calculated during the sensitivity analysis).

The strong points of this strategy are:

1. Instead of several thousands, OSL runs only $N_{Dsg} + N_{Par}$ FEA calls;
2. Once sensitivity analysis is completed on N_{Dsg} , the user sets objectives, constraints and runs a fast GA optimization procedure (N_{Par} FEA calls). In case some of the goals and constraints have to be modified, sensitivity analysis does not have to be repeated. The user only re-runs optimization and validates it on N_{Par} FEA calls. This is very handy for projects with fluid requirements (e.g., change of rated battery voltage, driving cycle, peak power requirement etc.);
3. Thousands of designs can be evaluated through MOPs within minutes by the selected optimization algorithm;
4. Sensitivity analysis gives a valuable insight into where to concentrate the efforts for specified motor requirements [38].

3.3. Performance Requirements

The requirements for e-PTO machine are derived from [4] and listed in Table 1.

Table 1. Peak operation requirements at base speed.

Description	Symbol	Value	Unit
Base speed	n_b	1700	rpm
Max. operating speed	n_{max}	2500	rpm
Max. torque	T_{max}	≥ 200	Nm
Battery voltage	U_{DC}	610	V
Max. phase current	$I_{s max}$	300	A_{rms}

3.4. Optimization Objectives and Inequality Constraints

The optimization of the 2D cross-section is set up as a multi-objective problem which is mathematically defined as: find the vector of Parameters (1), subject to D parameter boundary Constraints (2) and subject to m inequality constraints Function (3), which will minimize (or maximize) n objective Function (4).

$$\vec{x} = [x_1, x_2, \dots, x_D], \quad \vec{x} \in R^D \quad (1)$$

$$x_i^{(L)} \leq x_i \leq x_i^{(U)}, \quad i = 1, \dots, D \quad (2)$$

$$g_j(\vec{x}) \leq 0, \quad j = 1, \dots, m \quad (3)$$

$$f_k(\vec{x}) \leq 0, \quad k = 1, \dots, n \quad (4)$$

Inequality constraints usually arise from various electromagnetic, thermal, mechanical, manufacturing, economic or normative limits such as maximum winding temperature, maximum rotor stress, minimum magnet dimensions, maximum active material cost, maximum noise, etc.

Inequality constraints (Table 2) are taken into consideration in the optimization algorithm box in Figure 9. The constraint function g_1 checks rotor structural factor of safety at maximum over-speed ($1.2 \cdot n_{\max}$). Next, the procedure contains several subfunctions designed according to ultra-fast scaling laws [39]. Multiple magnetostatic FEA calculations are performed to find the optimal maximum torque-per-ampere (MTPA) control angle. The number of turns per coil and the number of parallel paths of the machine is then matched to the required base speed. Constraint g_2 checks the losses are within limits. g_3 and g_4 check that maximum stator yoke and tooth flux density are below limits (the purpose is to penalize the designs with increased iron losses). Constraint g_5 is related to thermal loading coefficient (THL) which is equal to current density multiplied by electrical loading ($\text{THL} = J \cdot A$). THL indicates if the machine can be cooled down at specified peak performance. The empirical values indicate that water cooling is possible if $\text{THL} \leq 1.9 \text{ MA}^2/\text{m}^3$.

Finally, a transient FEA calculation is performed at base speed. The transient is performed for the machine without skewing. To fulfill g_6 , the calculated TPV must be higher than the limit. If the torque ripple (T_{ripp}) is higher than the limit, the machine does not satisfy the constraint g_7 .

The optimization algorithm generates the designs, and the variants which fulfill all inequality constraints populate the estimated Pareto front (optimization goals according to Table 2). The final step is the validation of the estimated Pareto front which completes the optimization process.

Table 2. Inequality constraints and optimization goals.

No:	Constraint Description	Symbol	Limit
g_1	Stress yield factor at $1.2 \cdot n_{\max}$	FOS	≥ 2
g_2	Total loss	P_{loss}	$\leq 6000 \text{ W}$
g_3	Flux density in stator yoke	$B_{\text{sy,max}}$	$\leq 1.6 \text{ T}$
g_4	Flux density in stator tooth	$B_{\text{st,max}}$	$\leq 1.9 \text{ T}$
g_5	Thermal loading $J \cdot A$	THL	$\leq 1.9 \text{ MA}^2/\text{m}^3$
g_6	Torque per volume	TPV	$\geq 25 \text{ Nm}/\text{dm}^3$
g_7	Torque ripple without skewing	T_{ripp}	$\leq 15\%$
No:	Optimization Goals	Symbol	Unit
f_1	Minimize total loss	P_{loss}	W
f_2	Maximize torque per rotor volume	TPV	Nm/dm^3

3.5. Preset Model

Although four poles are a usual choice due to the higher power factor, we selected a six-pole machine. The reason is the higher theoretical torque density and lower torque ripple. In e-PTO application, the lower power factor is not an issue due to the use of an oversized inverter [4]. The number of slots is 54 with 4 rotor flux barriers, resulting in a two-layer integer slot distributed winding. This combination provides a good compromise between the inherent ability to mitigate torque pulsations, susceptibility to noise, and the ability to

use multiple parallel paths. The ideal number of turns per coil (N_c) and parallel paths (a_p) for matching the base speed is automatically calculated based on winding feasibility and ultra-fast scaling laws [39].

All seven topology variants have been optimized in Ansys Optislang. The initial sensitivity study used for MOP building was performed on $N_{Dsg} = 300$ models per topology. Optimization was conducted using the inbuilt OSL Evolutionary algorithm.

Table 3 lists constant parameters which are equal for all topologies (No. 1–14). The optimization variable range (design space) was initially determined based on the empirical data from the previous projects. A dummy sensitivity analysis was then conducted for fine-tuning any problematic parameter(s). The final optimization variables and respective optimization ranges for each topology (No. 15–49, color coding according to Figure 4) are listed in Table 4.

Table 3. List of constant design parameters.

No:	Description	Symbol	Value/Range	Unit
1	Stator diameter	D_s	214	mm
2	Shaft diameter	D_{sh}	54	mm
3	Phase number	N_{ph}	3	-
4	No. of turns	N_c	Automatic	-
5	Parallel paths	a_p	Automatic	-
6	Coil throw	y_c	9	-
7	Barrier number	k	4	-
8	Pole pairs	p	3	-
9	Slot number	N_s	54	-
10	Barrier bridge	w_{bb}	0.3	mm
11	Airgap	δ	0.7	mm
12	Slot opening	w_{op}	2	mm
13	Fill factor	-	0.43	-
14	Tooth tip depth	d_t	0.5	mm

Table 4. List of optimization variables.

No:	Description	Symbol	Value/Range	Unit
15Point	1 inner angle	θ_{1in}	[0.22, 0.47]	-
16Point	1 outer angle	θ_{1out}	0-	-
17Point	2 inner angle	θ_{2in}	[-0.08, 0.46]	-
18Point	2 outer angle	θ_{2out}	[-0.06, 0.16]	-
19Point	3 inner angle	θ_{3in}	[0.06, 0.25]	-
20Point	3 outer angle	θ_{3out}	[0.09, 0.11]	-
21Point	4 inner angle	θ_{4in}	0-	-
22Point	4 outer angle	θ_{4out}	[0.32, 0.35]	-
23–26	Corner radius in	$r_{1..k_{in}}$	[0, 1]	-
27–30	Corner radius out	$r_{1..k_{out}}$	[0, 1]	-
31	Slot corner radius	r_{sc}	[0, 1]	-
32	Slot depth ratio	$\frac{D_s - D_b}{2}$	[0.45, 0.6]	-
33	Split ratio	D_s / D_b	[0.6, 0.75]	-
34	Active length	l_s	[180, 240]	mm
35	Tooth tip angle	α_t	[5, 40]	°
36	Tooth width ratio	$\frac{D_b \pi}{N_s} - w_{op}$	[0.7, 0.9]	-
37	Min. angle	θ_{min}	[0.15, 0.3]	-
38	Max. angle	θ_{max}	[0.9, 0.95]	-
39	Notch angle	θ_n	[0.1, 1]	-
40	Current density	J	[17, 22]	A/mm ²
41–44	Barrier depths	$D_{1..k_{in}}$	[0.2, 1]	-
45–48	Barrier depths	$D_{1..k_{out}}$	[0.2, 1]	-
49	Notch depth	D_n	[0, 1]	-

4. Optimization Results

4.1. Rotor Topology Selection

Figure 12 contains the validated Pareto fronts which fulfil all inequality constraints. For easier comparison, seven designs (one per topology) with approximately the same losses (5200 W) have been selected. Table 5 summarizes the performance of each design at base speed and MTPA conditions from the worst (left) to the best topology (right). All optimized cross-sections are shown in Figure 14, while Table 6 list optimized variables for each design.

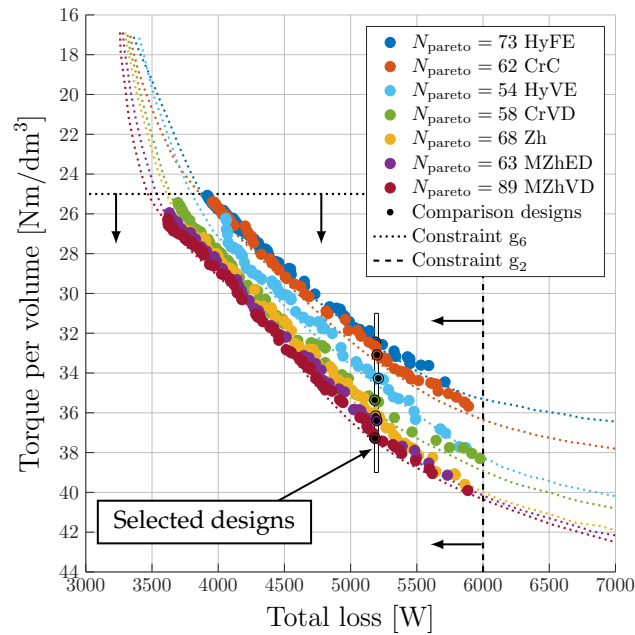


Figure 12. Validated Pareto front within constraints g_2 and g_6 . Dotted colored lines represent estimated Pareto fronts. N_{pareto} is the number of designs placed on each front.

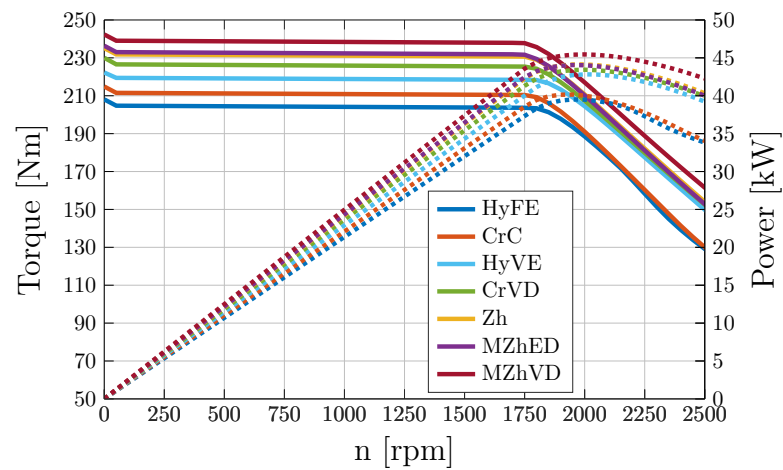


Figure 13. Performance curves of selected designs (Table 5).

Table 5. Final result comparison table.

Name	Unit	HyFE	CrC	HyVE	CrVD	Zh	MZhED	MZhVD
TPV	Nm/dm ³	32.5	33.1	34.3	35.4	36.2	36.4	37.3
V_{active}	dm ³	6.47	6.47	6.47	6.47	6.47	6.47	6.47
P_{loss}	kW	5188	5199	5209	5182	5188	5197	5184
P_{mech}	kW	37.4	38.1	39.5	40.8	41.7	41.9	43.0
T_{avg}	Nm	210.1	214.2	221.9	229.0	234.1	235.6	241.3
$T_{\text{ripp.}}$	%	12.1	14.1	11.7	12.7	9.7	9.3	13.7
n	rpm	1700	1700	1700	1700	1700	1700	1700
$B_{\text{sy,max}}$	T	1.53	1.53	1.39	1.60	1.52	1.54	1.56
$B_{\text{st,max}}$	T	1.86	1.87	1.87	1.82	1.87	1.86	1.84
FOS	-	8.8	9.4	7.3	6.3	3.6	5.2	6.3
m	kg	45.6	46.0	44.2	44.3	45.0	44.8	44.1
THL	MA ² /m ³	1.52	1.53	1.57	1.47	1.53	1.52	1.52
l_s	mm	180	180	180	180	180	180	180
γ	°	57.9	60.3	61.4	62.5	61.8	61.8	62.9
I_{max}	A _{rms}	95.6	95.6	94.3	94.1	95.9	95.7	95.7
$\cos \varphi$	-	0.61	0.62	0.66	0.67	0.67	0.67	0.69
η	%	87.8	88.0	88.3	88.7	88.9	89.0	89.2
Gain	%	0.0	1.9	5.6	9.0	11.4	12.1	14.9

Performance wise, HyFE topology yields the worst results (TPV = 32.5 Nm/dm³, $\cos \varphi = 0.61$) and will be considered the baseline design (Gain = 0%). Performance gain is calculated via: $\text{Gain} = (T_{\text{avg}}/T_{\text{HyFE avg}} - 1) \cdot 100\%$.

CrC topology is slightly better (2% gain) but still has rather low power factor (TPV = 33.1 Nm/dm³, $\cos \varphi = 0.62$). Next, HyVE yields better results (TPV = 34.3 Nm/dm³, $\cos \varphi = 0.66$, 5.6% gain) but is superseded by CrVD topology (TPV = 35.4 Nm/dm³, $\cos \varphi = 0.67$, 9% gain).

Even better performance results are achieved by standard Zh (TPV = 36.2 Nm/dm³, 11.4% gain) and MZhED topology (TPV = 36.4 Nm/dm³, 12.1% gain) but without any power factor increase ($\cos \varphi = 0.67$). Finally, the best result is obtained by MZhVD topology with full barrier depth variance (TPV = 37.3 Nm/dm³, $\cos \varphi = 0.69$, 14.9% gain). All designs fulfill the structural integrity constraint ($\text{FOS} \geq 2$). Corresponding torque-speed curves for the studied topologies are shown on Figure 13.

The maximization of torque per volume ($\text{TPV} = T_{\text{avg}}/V_{\text{active}}$) leads to maximization of average torque and minimization of active volume. In this case, stator diameter is fixed meaning that stack length will be minimal ($l_s = 180$ mm, Table 5). Average torque maximization should always be considered together with torque ripple. Both are obtained by running a transient calculation which is a standard time-stepping simulation where the position of the rotor changes place synchronously in time with stator magnetomotive force. Transient simulation is a computationally expensive part of the design evaluation and depending on required details can take several minutes.

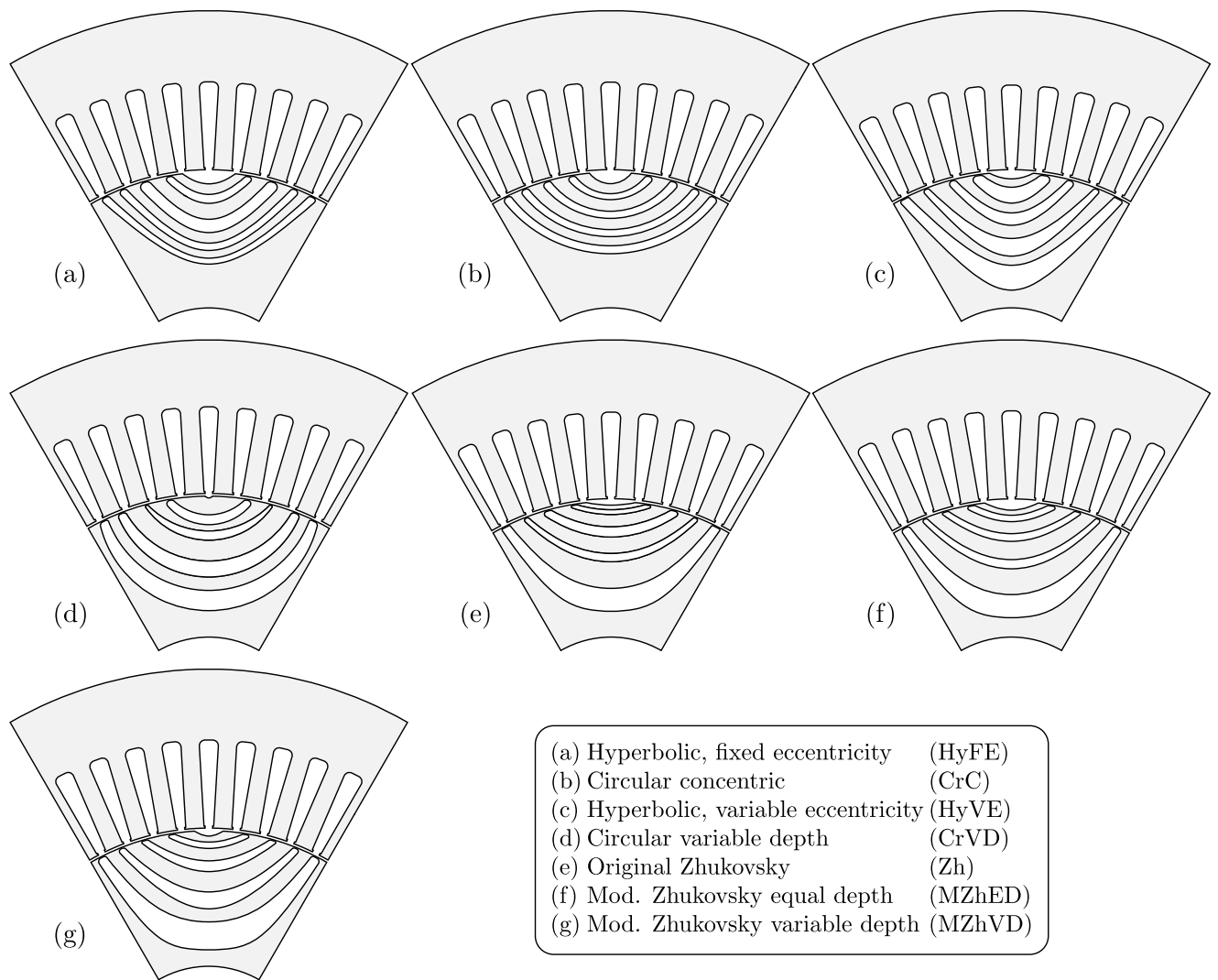


Figure 14. Optimized cross sections per topology.

Table 6. List of all optimized parameters for design variants with $k = 4$.

No:	Description	Symbol	Zh	MZhED	HyFE	CrC	MZhVD	HyVE	CrVD	Unit
1	Stator diameter	D_s	214	214	214	214	214	214	214	mm
2	Shaft diameter	D_{sh}	54	54	54	54	54	54	54	mm
3	Phase number	N_{ph}	3	3	3	3	3	3	3	-
4	No. of turns	N_c	21	21	21	21	22	21	21	-
5	Parallel paths	a_p	6	6	6	6	6	6	6	-
6	Coil throw	y_c	9	9	9	9	9	9	9	-
7	Barrier number	k	4	4	4	4	4	4	4	-
8	Pole pairs	p	3	3	3	3	3	3	3	-
9	Slot number	N_s	54	54	54	54	54	54	54	-
10	Barrier bridge	w_{bb}	0.3	0.3	0.3	0.3	0.3	0.3	0.3	mm
11	Airgap	δ	0.7	0.7	0.7	0.7	0.7	0.7	0.7	mm
12	Slot opening	w_{op}	2	2	2	2	2	2	2	mm
13	Fill factor	-	0.43	0.43	0.43	0.43	0.43	0.43	0.43	-
14	Tooth tip depth	d_t	0.5	0.5	0.5	0.5	0.5	0.5	0.5	mm
15	Point 1 inner angle	$\vartheta_{1_{in}}$	0.350	0.420	0.350	0.350	0.350	0.46-		
16	Point 1 outer angle	$\vartheta_{1_{out}}$	0.000	0.000	0.000	0.000	0.000	0.00-		
17	Point 2 inner angle	$\vartheta_{2_{in}}$	0.400	0.330	0.460	0.360	0.290	0.120	0.25-	
18	Point 2 outer angle	$\vartheta_{2_{out}}$	0.00	-0.040	0.060	0.010	0.000	0.000	0.06-	
19	Point 3 inner angle	$\vartheta_{3_{in}}$	0.120	0.130	0.250	0.240	0.180	0.240	0.14-	
20	Point 3 outer angle	$\vartheta_{3_{out}}$	0.090	0.090	0.090	0.090	0.090	0.09-		
21	Point 4 inner angle	$\vartheta_{4_{in}}$	0.000	0.000	0.000	0.000	0.000	0.00-		
22	Point 4 outer angle	$\vartheta_{4_{out}}$	0.350	0.350	0.350	0.350	0.350	0.35-		
23	Corner radius 1 inner	$r_{1_{in}}$	0.890	0.900	0.940	0.900	0.910	0.900	0.89-	
24	Corner radius 1 outer	$r_{1_{out}}$	0.900	0.900	0.890	0.880	0.890	0.900	0.91-	
25	Corner radius 2 inner	$r_{2_{in}}$	0.880	0.160	0.900	0.900	0.500	0.900	0.90-	
26	Corner radius 2 outer	$r_{2_{out}}$	0.870	0.900	0.900	0.550	0.900	0.990	0.90-	
27	Corner radius 3 inner	$r_{3_{in}}$	0.880	0.890	0.900	0.890	0.900	0.880	0.89-	
28	Corner radius 3 outer	$r_{3_{out}}$	0.900	0.900	0.900	0.900	0.900	0.900	0.90-	
29	Corner radius 4 inner	$r_{4_{in}}$	0.020	0.850	0.730	0.990	0.950	0.890	0.49-	
30	Corner radius 4 outer	$r_{4_{out}}$	0.200	0.770	0.740	0.850	0.630	0.540	0.20-	
31	Slot corner radius	r_{sc}	0.62	0.61	0.63	0.62	0.59	0.61	0.63	-
32	Slot depth ratio	$\frac{D_s - D_b}{2}$	0.48	0.45	0.46	0.50	0.46	0.46	0.46	-
33	Split ratio	D_s / D_b	0.67	0.72	0.61	0.72	0.67	0.66	0.61	-
34	Active length	l_s	180	180	180	180	180	180	180	mm
35	Tooth tip angle	α_t	9.45	9.48	9.49	9.50	9.48	9.47	9.49	°
36	Tooth width ratio	$\frac{D_b \pi}{N_s} - w_{op}$	0.88	0.82	0.78	0.87	0.71	0.84	0.78	-
37	Min. angle	ϑ_{min}	0.140	0.160	0.160	0.150	0.150	0.150	0.12-	
38	Max. angle	ϑ_{max}	0.480	0.490	0.480	0.480	0.500	0.470	0.50-	
39	Notch angle	ϑ_n	0.720	0.730	0.710	0.590	0.420	0.100	0.75-	
40	Current density	J	17	17	17	17	17	17	17	A/mm ²
41	Barrier depth 1	$D_{1_{in}}$	-0.900	0.670	0.800	0.700	0.400	0.40-		
42	Barrier depth 2	$D_{2_{in}}$	-0.900	0.670	0.800	0.480	0.590	0.39-		
43	Barrier depth 3	$D_{3_{in}}$	-0.900	0.670	0.800	0.480	0.430	0.42-		
44	Barrier depth 4	$D_{4_{in}}$	-0.900	0.670	0.800	0.710	0.600	0.63-		
45	Barrier depth 1	$D_{1_{out}}$	-0.900	0.670	0.800	0.800	0.400	0.64-		
46	Barrier depth 2	$D_{2_{out}}$	-0.900	0.670	0.800	0.810	0.530	0.79-		
47	Barrier depth 3	$D_{3_{out}}$	-0.900	0.670	0.800	0.790	0.680	0.79-		
48	Barrier depth 4	$D_{4_{out}}$	-0.900	0.670	0.800	0.920	0.800	0.42-		
49	Notch depth	D_n	-0.900	0.670	0.800	0.600	0.500	0.50-		

4.2. Torque Ripple Mitigation

One of the inherent disadvantages of the SyRM is the increased torque ripple. The issue can be mitigated with the use of asymmetric rotor poles [17,19] or with rotor or stator skewing [40,41]. The drawback of using skewing in optimization is a prolonged transient calculation (it has to be done for each of the rotor slices, e.g., 5 segment rotor skew will have 5 times longer transient simulation). Additionally, the PTO shaft has historically been a part of the Diesel engine which has a quite big ripple [3,4], so the decision was made to optimize the e-PTO machine without skewing.

Typically, SyRM torque ripple is minimized by continuous rotor skewing [40]. The alternatives are segmented rotor skewing or continuous stator skewing. Stator skewing is usually out of scope due to higher production complexity. To illustrate the benefits and drawbacks of the skewing, we have performed post-optimization transient simulation of 5 segment rotor skew (Figure 15b), and continuous rotor skew (Figure 15c). Both approaches yield similar results with a slight advantage to segmented rotor skewing. Since continuous skewing leads to increased manufacturing costs, a segmented skewing of the rotor might also be a good choice [41]. Note that torque ripple for all topologies is less than 15% which is a good feature for a non-skewed SyRM (Figure 15a). The total skew is $360/54 = 6.66^\circ$ mech. (angle of one stator slot).

Note that skewing reduces both the average torque by approx. 3–4%, and torque ripple to approx. 2–5% depending on the topology.

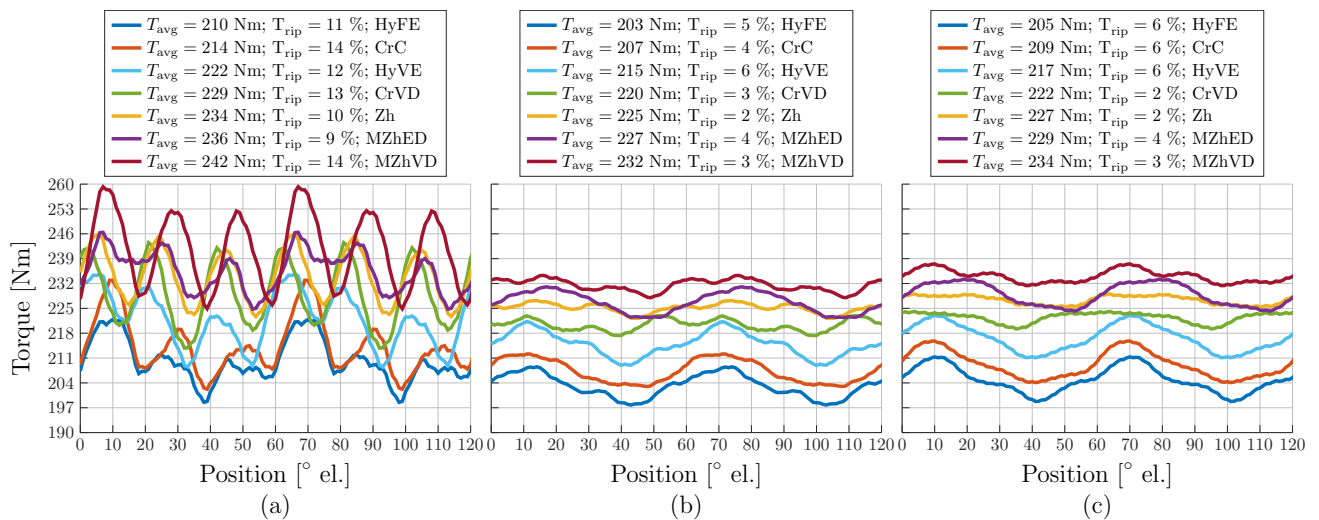


Figure 15. (a) Transient torque without skewing; (b) Transient torque with 5 segment rotor skewing; (c) Continuous skewing.

4.3. Barrier Number Considerations

The purpose of rotor barriers is to create magnetic anisotropy and achieve a high inductance saliency ratio (5), thus producing a high reluctance torque component (6). Simplified, more rotor barriers with an appropriate combination of poles and stator slots should correspond to higher electromagnetic torque.

According to [42,43], the golden rule of barrier number selection is given in the (7). The same approach was used in this paper leading to $k \leq 54/4/3 \leq 4.5 \rightarrow k = 4$. Other combinations of barrier numbers and stator slots might lead to increased torque ripple and decreased performance.

$$\xi = L_d/L_q \quad (5)$$

$$T_{em} = \frac{3}{2}p(L_d - L_q)i_q i_d \quad (6)$$

$$k \leq N_s/(4p) \quad (7)$$

To confirm that $k = 4$ is the proper number of barrier layers, a separate optimization for $k = 3-5$ was performed on the best barrier type (MZhVD), with equal performance requirements and design selection method as in the previous sections.

Figure 16 shows the Pareto fronts of the optimized designs (results listed in Table 7). It is apparent that three-layer topology is sub-optimal compared with $k = 4, 5$. In this case, three-layer topology is considered the baseline design. Performance gain is calculated via: $\text{Gain} = (T_{\text{avg}}/T_{\text{MZhVD } k=3 \text{ avg}} - 1) \cdot 100\%$.

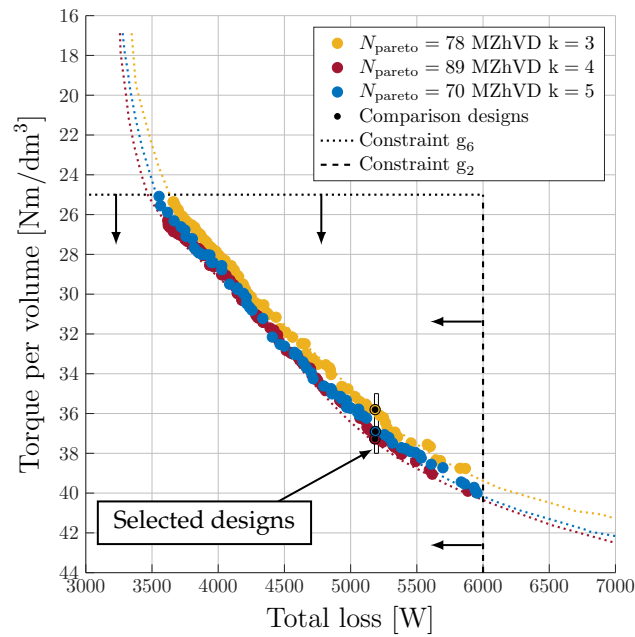


Figure 16. Validated MZhVD Pareto front for $k = 3-5$ within constraints g_2 and g_6 . Dotted colored lines represent estimated Pareto fronts. N_{pareto} is the number of designs placed on each front.

Table 7. Comparison table of MZhVD topology performance for $k = 3-5$.

Name	Unit	$k = 3$	$k = 4$	$k = 5$
TPV	Nm/dm ³	35.8	37.3	36.9
V_{active}	dm ³	6.47	6.47	6.47
P_{loss}	kW	5184.84	5184	5187
P_{mech}	kW	41.3	43.0	42.5
T_{avg}	Nm	231.8	241.3	238.9
$T_{\text{ripp.}}$	%	15.3	13.7	13.2
n	rpm	1700	1700	1700
$B_{\text{sy,max}}$	T	1.59	1.56	1.56
$B_{\text{st,max}}$	T	1.87	1.84	1.83
FOS	-	2.6	6.3	2.0
m	kg	43.2	44.1	44.0
THL	MA ² /m ³	1.43	1.52	1.45
l_s	mm	180	180	180
γ	°	62.2	62.9	63.2
I_{max}	A_{rms}	89.7	95.7	91.5
$\cos \varphi$	-	0.70	0.69	0.70
η	%	88.8	89.2	89.1
Gain	%	0.0	4.1	3.1

Compared with the three-layer variant, $k = 4$ yields the highest performance gain (4.1%) while $k = 5$ results in 3.1% gain. Furthermore, the three-layer variant results in a

higher torque ripple (15.3%) while $k = 4, 5$ has approximately the same ripple (13.7% and 13.2% respectively).

An additional parameter in favor of $k = 4$ is a mechanical factor of safety (FOS = 6.3). Three barrier layers reduce FOS to 2.6 (the reduction accrues due to more steel in the rotor structure), while $k = 5$ has borderline FOS = 2 due to the more air barriers at a reduced amount of steel in the rotor structure.

Considering that $k = 4$ is performance wise better than $k = 3, 5$, the comparison confirms that the original barrier number selection was the appropriate choice (all optimized cross sections are listed in Figure 17).

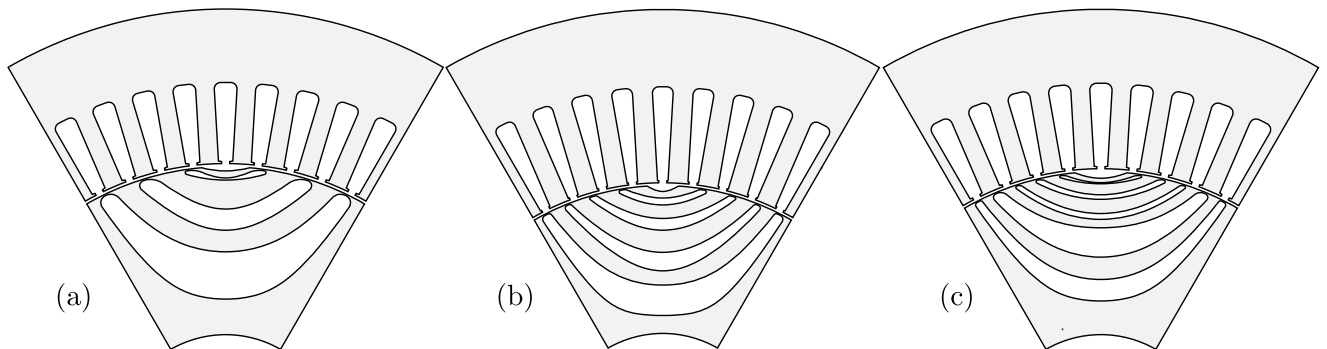


Figure 17. Optimized cross sections of MZhVD topology; (a) $k = 3$; (b) $k = 4$; (c) $k = 5$.

4.4. Execution Time and Computational Cost

The entire optimization process was conducted on a computing workstation with 4 core Intel Core i7 central processing unit (CPU). Execution time of the entire study is summarized in Table 8. The number of CPU cores is important because it enables parallel computing during sensitivity analysis and Pareto front validation (more cores results in shorter overall execution time). The selected number of designs for sensitivity analysis (variation study) of each design variant is $N_{Dsg} = 300$.

Table 8. Execution time comparison for the entire study.

Stage		Avg. Design Eval. Time	Sensitivity Analysis	MOP Building	OSL Optimization	Pareto Validation	Total Execution Time	Total Execution Time
Type	k	[s]	[min]	[min]	[min]	[min]	[min]	[h]
Zh	4	55.02	114.6	211.0	11.7	45.9	383.2	6.39
MZhED	4	55.60	115.8	218.9	12.2	46.3	393.2	6.55
MZhVD	3	55.89	116.4	232.0	12.9	46.6	407.9	6.80
HyFE	4	56.30	117.3	249.8	13.9	46.9	427.9	7.13
CrC	4	57.20	119.2	248.5	13.8	47.7	429.1	7.15
MZhVD	4	58.30	121.5	246.6	13.7	48.6	430.3	7.17
HyVE	4	58.20	121.3	248.6	13.8	48.5	432.2	7.20
CrVD	4	58.40	121.7	249.4	13.9	48.7	433.6	7.23
MZhVD	5	60.50	126.0	261.2	14.5	50.4	452.2	7.54

Total sensitivity analysis time mainly depends on the average design evaluation time of a particular topology, which is a function of parametric topology complexity and FEA tool procedures (e.g., adaptive meshing density). It is important to note that the average design execution time for all variants is in the range of 55–61 s, which results in a total sensitivity analysis time of 114–126 min. The building of surrogate models (MOP) is purely a function of the parametric complexity of each topology which varies in a range of 211 min (Zh, $k = 4$) for the simplest, to 261 min for the most complex topology (MZhVD, $k = 5$). OSL optimization is the shortest component which takes approximately 12 min. Next, Pareto

front validation is conducted on $N_{\text{par}} = 200$ designs. This step is effectively the same as in the sensitivity analysis, and the execution time solely depends on the average design evaluation time and N_{par} .

Finally, the total execution time is summarized based on all previous steps. It varies from 6.39 h (Zh, $k = 4$) to 7.54 h (MZhVD, $k = 4$).

Without the use of the proposed meta-modeling procedure, the total execution time with the same level of details would take several weeks. On the other hand, the total execution time for the entire study (9 investigated topologies) is 63.2 h.

4.5. Efficiency Consideration

Automotive applications are characterized by variable load. Considering that e-PTO load is quite intermittent ([3], e.g., refuse compression, hook-lift loading...), in correspondence with the automotive company which partially sponsored the presented research, it was decided to design the SyRM for peak load operation (maximum current at base speed).

By analyzing the efficiency of the best topology (MZhVD) at the base speed (Table 5), one might conclude that the efficiency is quite low (89.2%). On the other hand, considering that the machine is optimized for peak operation (temporary overload condition), seemingly low efficiency is expected behavior. A more detailed analysis of the entire efficiency map reveals higher efficiency values (Figure 18). Typically water cooled e-PTO machine has a continuous torque envelope of approx. 50% of the max torque (dashed line on Figure 18) yielding 92% efficiency at base speed. Furthermore, if e-PTO hydraulic pump is selected for the max. efficiency area (2400 rpm), efficiency increases to 94%. In case efficiency is still unsatisfactory, changing lamination to higher grade magnetic steel can easily push the efficiency to the premium range [25].

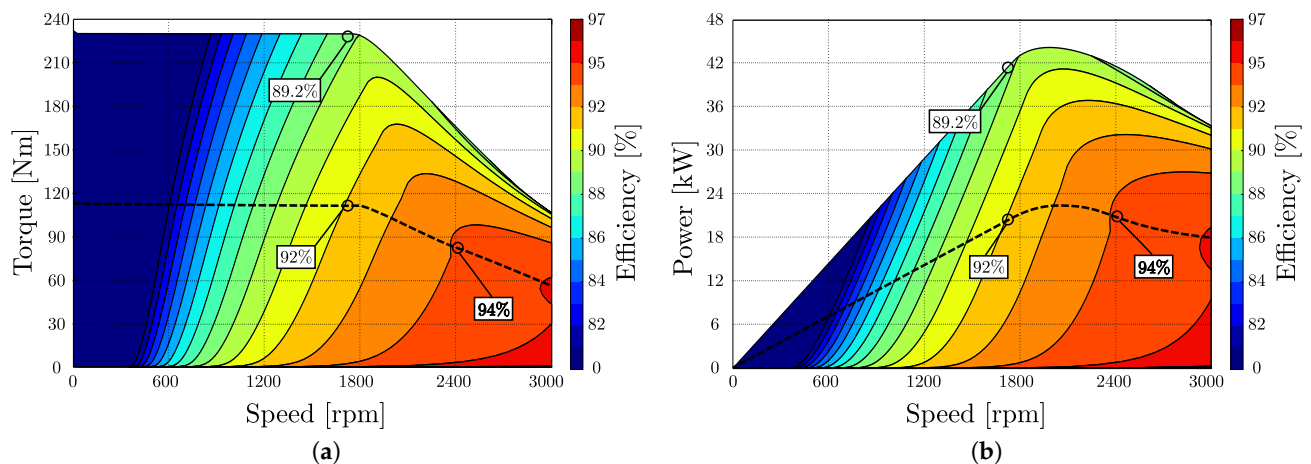


Figure 18. MZhVD efficiency relative to the (a) torque-speed and (b) power-speed characteristic.

5. Conclusions

Nowadays, due to the confidence in FEA modeling, and rapid product iteration (especially in the automotive sector), electric machine designers primarily rely on simulations. This approach reduces time and cost and is very useful when comparing different machine topologies. Considering that prototyping comes in later project stages, no machines have been produced and tested. Nevertheless, considering that the presented tool chain (Matlab, Motor-CAD, and OptiSlang) is widely used in the automotive industry, we are confident that the results are highly relevant.

As expected, the SyRM rotor barrier topology substantially affects the final machine performance. The consequence of barrier depth variation is variable flux carrier thickness, which has a positive impact on performance and mechanical integrity.

Seven six-pole rotor topologies have been derived from standard barrier types. Simple variants (HyFE, CrC) have the worst performance; more complex designs with limited flux

carrier variation (HyVE, CrVD) yield slight improvement. Better results (but without any power factor increase) are achieved by Zh and MZhED. The best performance and a power factor increase are achieved by a novel MZhVD topology.

The novelty of the proposed approach reflects in the systematic comparison of different “smooth barrier” SyRM topologies via metamodel-based optimization. This offers a fair topology comparison and finally proves that modified Zhukowsky-based topologies yield the best results in terms of TPV and higher power factor.

We want to emphasize that the goal of the paper is to present the novel metamodel based optimization method, and the comparison of SyRM rotor barrier types. This was successfully shown in the case of the e-PTO motor. All design variants are optimized on equal terms, which gives us confidence in the results. Since the conflicting optimization objectives were maximizing TPV and minimization of losses, we are strongly convinced that equal results in barrier performance differences would appear if a different application example was selected. Therefore, the specifics of the e-PTO application and the selected Pareto front combinations of TPV vs. total loss do not limit the performance of the method and do not limit the generality of the method.

Furthermore, the presented machines are optimized for short-term maximum load, which was determined as a critical e-PTO function. The main motivation for the project was to minimize the cost of the machine. Reduced SyRM mass will increase the vehicle range, while the shorter axial length and cheaper stator/rotor steel contribute to the production cost savings. Machine efficiency has not been considered an optimization objective due to the specific use scenario. If higher grade magnetic steel is selected, the efficiency would increase.

Several follow-up projects are planned to be derived from the presented work:

1. Asymmetric rotor topologies with the purpose of torque ripple reduction without skewing.
2. Torque ripple mitigation methods based on non-uniform rotor skew angles and variable segment lengths.
3. Algorithm for the addition of precise corner fillets to arbitrary poly-line curves.

Author Contributions: Conceptualization, B.B.; methodology, B.B. and S.S.; validation, B.B. and S.S.; original draft preparation, B.B.; review and editing, S.S.; visualization, B.B.; supervision, S.S.; funding acquisition, S.S. All authors have read and agreed to the published version of the manuscript.

Funding: This work was partially supported by the Croatian Science Foundation under the project IP-2018-01-5822-HYDREL.

Institutional Review Board Statement: Not applicable.

Informed Consent Statement: Not applicable.

Data Availability Statement: Not applicable.

Acknowledgments: This paper is an extension of Branko Ban’s Ph.D. research work on Synchronous Reluctance machines mentored by Stjepan Stipetic.

Conflicts of Interest: The authors declare no conflict of interest.

Abbreviations

The following abbreviations are used in this manuscript:

Abbreviation	Description
ASKA	Adaptive-Sampling Kriging Algorithm
CoP	Coefficient of prognosis
CPU	Central processing unit
CrC	Circular concentric barrier
CrVD	Circular variable depth barrier
DE	Differential evolution
e-PTO	Electric power take off
EV	Electric vehicle
FEA	Finite element analysis
GA	Genetic algorithm
HyFE	Hyperbolic fixed eccentricity barrier
HyVE	Hyperbolic variable eccentricity barrier
IM	Induction machine
IPM	Interior permanent magnet
MOP	Model of prognosis
MTPA	Maximum torque per Ampere
MZhED	Modified Zhukovsky equal depth barrier
MZhVD	Modified Zhukovsky variable depth barrier
NGnet	Normalized Gaussian network
OA	Optimization algorithm
OSL	OptiSlang
PM	Permanent magnet
PTO	Power take off
SyRM	Synchronous reluctance machine
TPV	Torque per volume
THL	Thermal loading coefficient
Zh	Original Zhukovsky barrier

References

1. Murataliyev, M.; Degano, M.; Nardo, M.D.; Bianchi, N.; Gerada, C. Synchronous Reluctance Machines: A Comprehensive Review and Technology Comparison. *Proc. IEEE* **2022**, *110*, 382–399.
2. Ban, B.; Stipetic, S.; Klanac, M. Synchronous reluctance machines: Theory, design and the potential Use in traction applications. In Proceedings of the International Conference on Electrical Drives and Power Electronics, High Tatras, Slovakia, 24–26 September 2019; pp. 177–188.
3. Ban, B.; Stipetić, S. Electric Multipurpose Vehicle Power Take-Off: Overview, Load Cycles and Actuation via Synchronous Reluctance Machine. In Proceedings of the International Aegean Conference on Electrical Machines and Power Electronics (ACEMP-OPTIM), Istanbul, Turkey, 27–29 August 2019.
4. Ban, B.; Stipetic, S. Design and optimization of synchronous reluctance machine for actuation of electric multi-purpose vehicle power take-off. In Proceedings of the 2020 International Conference on Electrical Machines, (ICEM 2020), Online, 23–26 March 2020; pp. 1750–1757.
5. Lampinen, J. Multi-Constrained Nonlinear Optimization by the Differential Evolution Algorithm. In *Soft Computing and Industry*; Springer: London, UK, 2002.
6. Zarko, D. A Systematic Approach to Optimized Design of Permanent Magnet Motors with Reduced Torque Pulsations. Ph.D. Thesis, University of Wisconsin, Madison, WI, USA, 2004.
7. Stipetic, S.; Miebach, W.; Zarko, D. Optimization in design of electric machines: Methodology and workflow. In Proceedings of the Joint International Conference-ACEMP 2015: Aegean Conference on Electrical Machines and Power Electronics, OPTIM 2015: Optimization of Electrical and Electronic Equipment and ELECTROMOTION 2015: International Symposium on Advanced Electromechanical Moti, Side, Turkey, 2–4 September 2016; pp. 441–448.
8. Gamba, M.; Pellegrino, G.; Armando, E.; Ferrari, S. Synchronous Reluctance Motor with Concentrated Windings for IE4 Efficiency. In Proceedings of the IEEE Energy Conversion Congress and Exposition (ECCE), Cincinnati, OH, USA, 1–5 October 2017.
9. Calzo, G.L.; Galea, M. Design Optimization of a High-Speed Synchronous Reluctance Machine. *IEEE Trans. Ind. Appl.* **2018**, *54*, 233–243.
10. Babetto, C.; Bacco, G.; Bianchi, N. Synchronous Reluctance Machine Optimization for High-Speed Applications. *IEEE Trans. Energy Convers.* **2018**, *33*, 1266–1273.
11. De Pancorbo, S.M.; Ugalde, G.; Poza, J.; Egea, A. Comparative study between induction motor and Synchronous Reluctance Motor for electrical railway traction applications. In Proceedings of the 5th International Conference on Electric Drives Production, (EDPC 2015), Nuremberg, Germany, 15–16 September 2015; pp. 2–6.

12. Villan, M.; Tursini, M.; Popescu, M.; Fabri, G.; Credo, A.; Di Leonardo, L. Experimental comparison between induction and synchronous reluctance motor-drives. In Proceedings of the 2018 23rd International Conference on Electrical Machines, ICEM 2018, Alexandroupoli, Greece, 3–6 September 2018; pp. 1188–1194.
13. Villani, M. High Performance Electrical Motors for Automotive Applications—Status and Future of Motors with Low Cost Permanent Magnets. Ph.D. Thesis, University of l’Aquila, Aquila, Italy, 2020.
14. Castagnaro, E.; Bianchi, N. *High-Speed Synchronous Reluctance Motor for Electric-Spindle Application*; Institute of Electrical and Electronics Engineers Inc.: Piscataway, NJ, USA, 2020; pp. 2419–2425.
15. Bao, Y.; Degano, M.; Wang, S.; Chuan, L.; Zhang, H.; Xu, Z.; Gerada, C. A Novel Concept of Ribless Synchronous Reluctance Motor for Enhanced Torque Capability. *IEEE Trans. Ind. Electron.* **2020**, *67*, 2553–2563.
16. Credo, A.; Fabri, G.; Villani, M.; Popescu, M. High speed synchronous reluctance motors for electric vehicles: A focus on rotor mechanical design. In Proceedings of the 2019 IEEE International Electric Machines and Drives Conference, (IEMDC 2019), San Diego, CA, USA, 12–15 May 2019; pp. 165–171.
17. Kafadar, A.S.; Tap, A.; Ergene, L.T. Torque ripple reduction of SynRM using machaon type lamination. In Proceedings of the 2018 6th International Conference on Control Engineering and Information Technology, (CEIT 2018), Istanbul, Turkey, 25–27 October 2018; pp. 25–27.
18. Ban, B.; Stipetic, S. Absolutely Feasible Synchronous Reluctance Machine Rotor Barrier Topologies with Minimal Parametric Complexity. *Machines* **2022**, *10*, 206.
19. Ferrari, M.; Bianchi, N.; Doria, A.; Fornasiero, E. Design of Synchronous Reluctance Motor for Hybrid Electric Vehicles. *IEEE Trans. Ind. Appl.* **2015**, *51*, 21–36.
20. Tawfiq, K.B.; Ibrahim, M.N.; El-Kholy, E.E.; Sergeant, P. Performance Improvement of Synchronous Reluctance Machines—A Review Research. *IEEE Trans. Magn.* **2021**, *57*, 99.
21. Varatharajan, A.; Brunelli, D.; Ferrari, S.; Pescetto, P.; Pellegrino, G. *SyreDrive: Automated Sensorless Control Code Generation for Synchronous Reluctance Motor Drives*; Institute of Electrical and Electronics Engineers Inc.: Piscataway, NJ, USA, 2021; pp. 192–197.
22. Tawfiq, K.B.; Ibrahim, M.N.; El-Kholy, E.E.; Sergeant, P. Performance Analysis of a Rewound Multiphase Synchronous Reluctance Machine. *IEEE J. Emerg. Sel. Top. Power Electron.* **2022**, *10*, 297–309.
23. Tawfiq, K.B.; Ibrahim, M.N.; El-Kholy, E.E.; Sergeant, P. Construction of Synchronous Reluctance Machines with Combined Star-Pentagon Configuration Using Standard Three-Phase Stator Frames. *IEEE Trans. Ind. Electron.* **2022**, *69*, 7582–7595.
24. Ibrahim, M.N.F.; Abdel-Khalik, A.S.; Rashad, E.M.; Sergeant, P. An Improved Torque Density Synchronous Reluctance Machine with a Combined Star-Delta Winding Layout. *IEEE Trans. Energy Convers.* **2018**, *33*, 1015–1024.
25. Ibrahim, M.N.; Sergeant, P.; Rashad, E.M. Synchronous Reluctance Motor Performance Based on Different Electrical Steel Grades. *IEEE Trans. Magn.* **2015**, *51*, 7403304.
26. Mirazimi, M.S.; Kiyoumars, A. Magnetic Field Analysis of Multi-Flux-Barrier Interior Permanent-Magnet Motors Through Conformal Mapping. *IEEE Trans. Magn.* **2017**, *53*, 7002512.
27. Mirazimi, M.S.; Kiyoumars, A. Magnetic Field Analysis of SynRel and PMASynRel Machines with Hyperbolic Flux Barriers Using Conformal Mapping. *IEEE Trans. Transp. Electrification* **2020**, *6*, 52–61.
28. Taghavi, S.; Pillay, P. Design aspects of a 50hp 6-pole synchronous reluctance motor for electrified powertrain applications. In Proceedings of the IECON 2017—43rd Annual Conference of the IEEE Industrial Electronics Society, Beijing, China, 29 October–1 November 2017; pp. 2252–2257.
29. Gamba, M.; Pellegrino, G.; Cupertino, F. Optimal number of rotor parameters for the automatic design of Synchronous Reluctance machines. In Proceedings of the 2014 International Conference on Electrical Machines, ICEM 2014, Berlin, Germany, 9 February 2014; pp. 1334–1340.
30. Cupertino, F.; Pellegrino, G.; Cagnetta, P.; Ferrari, S.; Perta, M. SyRE: Synchronous Reluctance (Machines)-Evolution, 2021.
31. Kamper, M.J.; Van Der Merwe, F.S.; Williamson, S. Direct Finite Element Design Optimisation of the Cageless Reluctance Synchronous Machine. *IEEE Trans. Energy Convers.* **1996**, *11*, 547–553.
32. Gundogdu, T.; Komurgoz, G. A systematic design optimization approach for interior permanent magnet machines equipped with novel semi-overlapping windings. *Struct. Multidiscip. Optim.* **2021**, *63*, 1491–1512.
33. Lee, J.; Seo, J.H.; Kikuchi, N. Topology optimization of switched reluctance motors for the desired torque profile. *Struct. Multidiscip. Optim.* **2010**, *42*, 783–796.
34. Lee, C.; Jang, I.G. Topology optimization of multiple-barrier synchronous reluctance motors with initial random hollow circles. *Struct. Multidiscip. Optim.* **2021**, *64*, 2213–2224.
35. Otomo, Y.; Igarashi, H. Topology Optimization Using Gabor Filter: Application to Synchronous Reluctance Motor. *IEEE Trans. Magn.* **2021**, *9464*, 18–21.
36. Bramerdorfer, G.; Zăvoianu, A.C. Surrogate-Based Multi-Objective Optimization of Electrical Machine Designs Facilitating Tolerance Analysis. *IEEE Trans. Magn.* **2017**, *53*, 1–11.
37. Son, J.c.; Ahn, J.m.; Lim, J. Optimal Design of PMA-SynRM for Electric Vehicles Exploiting Adaptive-Sampling Kriging Algorithm. *IEEE Access* **2021**, *9*, 41174–41183.
38. Riviere, N.; Volpe, G.; Villani, M.; Fabri, G.; Di Leonardo, L.; Popescu, M. Design analysis of a high speed copper rotor induction motor for a traction application. In Proceedings of the 2019 IEEE International Electric Machines and Drives Conference, (IEMDC 2019), San Diego, CA, USA, 12–15 May 2019.

39. Stipetic, S.; Zarko, D.; Popescu, M. Ultra-fast axial and radial scaling of synchronous permanent magnet machines. *IET Electr. Power Appl.* **2016**, *10*, 658–666.
40. Bomela, X.B.; Kamper, M.J. Effect of stator chording and rotor skewing on performance of reluctance synchronous machine. *IEEE Trans. Ind. Appl.* **2002**, *38*, 91–100.
41. Hubert, T.; Reinlein, M.; Kremser, A.; Herzog, H.G. Torque ripple minimization of reluctance synchronous machines by continuous and discrete rotor skewing. In Proceedings of the 2015 5th International Conference on Electric Drives Production, (EDPC 2015), Nuremberg, Germany, 15–16 September 2015.
42. Pellegrino, G. Permanent Magnet Machine Design and Analysis with a Focus to Flux-switching PM and PM-assisted Synchronous Reluctance Machines Part II: PM-assisted Synch Rel Machines Tutorials. In Proceedings of the 2016 International Conference on Electrical Machines, (ICEM 2016), Lausanne, Switzerland, 4–7 September 2016.
43. Vagati, A.; Pastorelli, M.; Franceschini, G.; Petrache, S.C. Design of low-torque-ripple synchronous reluctance motors. *IEEE Trans. Ind. Appl.* **1998**, *34*, 758–765.

Bibliography

- [1]European Environment Agency, “Electric vehicles in europe”, page 60, accessed at: <https://www.eea.europa.eu/publications/electric-vehicles-in-europe>26.08.2022.
- [2]Eshani, M., Gao, Y., Gay, S., Emadi, A., Modern electric, hybrid electric and fuel cell vehicles 2nd. Edition. CRC Press, 2010.
- [3]Parra, H. Z. D. L., Magnussen, F., Bosga, S., “Challenges for electric machines and power electronics in automotive applications”, International Conference on Ecological Vehicles and Renewable Energies,(EVER’09), 2009, pages 1-9.
- [4]Bourzac, K., “The rare-earth crisis”, accessed at:<https://www.technologyreview.com/s/423730/the-rare-earth-crisis/>26.08.2022.
- [5]Justin, R., “Rare earths: Neither rare, nor earths - bbc news”, accessed at: <https://www.bbc.com/news/magazine-26687605>21.03.2017.
- [6]U.S. Department of Energy, “Fy 2016 annual progress report for electric drive technologies program”, pages 65-76, 2017.
- [7]Riba, J. R., López-Torres, C., Romeral, L., Garcia, A., “Rare-earth-free propulsion motors for electric vehicles: A technology review”, Renewable and Sustainable Energy Reviews, Vol. 57, 2016, pages 367-379.
- [8]Estenlund, S., Alaküla, M., Reinap, A., “Pm-less machine topologies for ev traction: A literature review”, 2016 International Conference on Electrical Systems for Aircraft, Railway, Ship Propulsion and Road Vehicles and International Transportation Electrification Conference, ESARS-ITEC 2016, 2016.
- [9]Pellegrino, G., Jahns, T. M., Bianchi, N., Soong, W. L., Cupertino, F., The Rediscovery of Synchronous Reluctance and Ferrite Permanent Magnet Motors Tutorial Course Notes. Springer, 2016.

- [10] Duck, P., Jurgens, J., Ponick, B., “Calculation of synchronous reluctance machines used as traction drives”, 2015 IEEE Vehicle Power and Propulsion Conference, VPPC 2015 - Proceedings, 2015, pages 0-4.
- [11] Parasiliti, F., Villani, M., Lucidi, S., Rinaldi, F., “Finite-element-based multiobjective design optimization procedure of interior permanent magnet synchronous motors for wide constant-power region operation”, IEEE Transactions on Industrial Electronics, 2012.
- [12] Barcaro, M., Bianchi, N., Magnussen, F., “Permanent-magnet optimization in permanent-magnet-assisted synchronous reluctance motor for a wide constant-power speed range”, IEEE Transactions on Industrial Electronics, 2012.
- [13] Lee, H. I., Noh, M. D., “Optimal design of radial-flux toroidally wound brushless dc machines”, IEEE Transactions on Industrial Electronics, 2011.
- [14] Lei, G., Zhu, J. G., Guo, Y. G., Hu, J. F., Xu, W., Shao, K. R., “Robust design optimization of pm-smc motors for six sigma quality manufacturing”, IEEE Transactions on Magnetics, 2013.
- [15] Chu, W. Q., Zhu, Z. Q., Chen, J. T., “Simplified analytical optimization and comparison of torque densities between electrically excited and permanent-magnet machines”, IEEE Transactions on Industrial Electronics, Vol. 61, 2014, pages 5000-5011.
- [16] Hasanien, H. M., “Particle swarm design optimization of transverse flux linear motor for weight reduction and improvement of thrust force”, IEEE Transactions on Industrial Electronics, Vol. 58, 2011, pages 4048-4056.
- [17] Tapia, J. A., Pyrhönen, J., Puranen, J., Lindh, P., Nyman, S., “Optimal design of large permanent magnet synchronous generators”, IEEE Transactions on Magnetics, 2013.
- [18] Tapia, J. A., Parviainen, A., Pyrhonen, J., Lindh, P., Wallace, R. R., “Optimal design procedure for an external rotor permanent-magnet machine”, 2012, pages 2695-2701.
- [19] Alberti, L., Bianchi, N., Boglietti, A., Cavagnino, A., “Core axial lengthening as effective solution to improve the induction motor efficiency classes”, 2011, pages 3391-3398.
- [20] Boglietti, A., Cavagnino, A., Ferraris, L., Lazzari, M., Luparia, G., “No tooling cost process for induction motors energy efficiency improvements”, IEEE Transactions on Industry Applications, 2005.
- [21] Bramerdorfer, G., Cavagnino, A., Vaschetto, S., “Impact of im pole count on material cost increase for achieving mandatory efficiency requirements”, 2016.

- [22]El-Refaie, A. M., “Motors/generators for traction /propulsion applications: A review”, 2011 IEEE International Electric Machines and Drives Conference, IEMDC 2011, 2011, pages 490-497.
- [23]Pellegrino, G., Cupertino, F., Gerada, C., “Automatic design of synchronous reluctance motors focusing on barrier shape optimization”, IEEE Transactions on Industry Applications, Vol. 51, 2015, pages 1465-1474.
- [24]Lu, C., Ferrari, S., Pellegrino, G., “Two design procedures for pm synchronous machines for electric powertrains”, IEEE Transactions on Transportation Electrification, Vol. 3, 2017, pages 98-107.
- [25]Mirazimi, M. S., Kiyomarsi, A., “Magnetic field analysis of synrel and pmasynrel machines with hyperbolic flux barriers using conformal mapping”, IEEE Transactions on Transportation Electrification, Vol. 6, 2020, pages 52-61.
- [26]Gamba, M., Pellegrino, G., Cupertino, F., “Optimal number of rotor parameters for the automatic design of synchronous reluctance machines”, Proceedings - 2014 International Conference on Electrical Machines, ICEM 2014, 2014, pages 1334-1340.
- [27]Hsu, J. S., Ayers, C., Coomer, C., “Report on toyota/prius motor design and manufacturing assessment”, page 14, accessed at:<https://goo.gl/fuEtvS26>.08.2022.
- [28]Kabasawa, A., Takahashi, K., “Development of the ima motor for the v6 hybrid midsize sedan”, SAE transactions, Vol. 2005, 2005, page 8.
- [29]Pancorbo, S. M. D., Ugalde, G., Poza, J., Egea, A., “Comparative study between induction motor and synchronous reluctance motor for electrical railway traction applications”, 2015 5th International Conference on Electric Drives Production, EDPC 2015 - Proceedings, 2015, pages 2-6.
- [30]Villan, M., Tursini, M., Popescu, M., Fabri, G., Credo, A., Leonardo, L. D., “Experimental comparison between induction and synchronous reluctance motor-drives”, Proceedings - 2018 23rd International Conference on Electrical Machines, ICEM 2018, 2018, pages 1188-1194.
- [31]Villani, M., “High performance electrical motors for automotive applications – status and future of motors with low cost permanent magnets”, page 15, accessed at:http://www.refreedrive.eu/wp-content/downloads/2018_WMM_Paper_UNIVAQ.pdf 26.08.2022.

- [32] Bao, Y., Degano, M., Wang, S., Chuan, L., Zhang, H., Xu, Z., Gerada, C., “A novel concept of ribless synchronous reluctance motor for enhanced torque capability”, *IEEE Transactions on Industrial Electronics*, Vol. 67, 2020, pages 2553-2563.
- [33] Calzo, G. L., Galea, M., “Design optimization of a high-speed synchronous reluctance machine”, *IEEE Transactions on Industry Applications*, Vol. 54, 2018, pages 233-243.
- [34] Credo, A., Fabri, G., Villani, M., Popescu, M., “High speed synchronous reluctance motors for electric vehicles: A focus on rotor mechanical design”, 2019 IEEE International Electric Machines and Drives Conference, IEMDC 2019, 2019, pages 165-171.
- [35] Babetto, C., Bacco, G., Bianchi, N., “Synchronous reluctance machine optimization for high-speed applications”, *IEEE Transactions on Energy Conversion*, Vol. 33, 2018, pages 1266-1273.
- [36] Kafadar, A. S., Tap, A., Ergene, L. T., “Torque ripple reduction of synrm using machaon type lamination”, 2018 6th International Conference on Control Engineering and Information Technology, CEIT 2018, 2018, pages 25-27.
- [37] Ferrari, M., Bianchi, N., Doria, A., Fornasiero, E., “Design of synchronous reluctance motor for hybrid electric vehicles”, *IEEE Transactions on Industry Applications*, Vol. 51, 2015, pages 21-36.
- [38] Ban, B., Stipeti ć, S., “Design and Torque Ripple Reduction Methods for Synchronous Reluctance Machine applied in Electric Power Take-off actuation”, *Proceedings - 2022 25th International Conference on Electrical Machines, ICEM 2022*, 2022.
- [39] Jahns, T., “Getting rare-earth magnets out of ev traction machines: A review of the many approaches being pursued to minimize or eliminate rare-earth magnets from future ev drivetrains”, *IEEE Electrification Magazine*, Vol. 5, 2017, pages 6-18.
- [40] Liu, C. T., Chung, H. Y., Lin, S. Y., “On the electromagnetic steel selections and performance impact assessments of synchronous reluctance motors”, *IEEE Transactions on Industry Applications*, Vol. 53, 2017, pages 2569-2577.
- [41] Barta, J., Ondrusek, C., “Rotor design and optimization of synchronous reluctance machine”, *MM Science Journal*, Vol. 9, 2015, pages 555-559.
- [42] Reddy, P. B., El-Refaiie, A. M., Galioto, S., Alexander, J. P., “Design of synchronous reluctance motor utilizing dual-phase material for traction applications”, *IEEE Transactions on Industry Applications*, Vol. 53, 2017, pages 1948-1957.

- [43]El-Refaie, A., Raminosoa, T., Reddy, P., Galioto, S., Pan, D., Grace, K., Alexander, J., Huh, K. K., “Comparison of traction motors that reduce or eliminate rare-earth materials”, IET Electrical Systems in Transportation Research, Vol. 7, 2016, pages 207-214.
- [44]Ibrahim, M. N., Sergeant, P., Rashad, E. M., “Synchronous reluctance motor performance based on different electrical steel grades”, IEEE Transactions on Magnetics, Vol. 51, 2015, pages 1-4.
- [45]Soong, W. L., Miller, T. J., “Field-weakening performance of brushless synchronous ac motor drives”, IEE Proceedings: Electric Power Applications, Vol. 141, 1994, pages 331-340.
- [46]Fratta, A., Vagati, A., “A reluctance motor drive for high dynamic performance applications”, IEEE Transactions on Industry Applications, Vol. 28, 1992, pages 873-879, accessed at:<http://ieeexplore.ieee.org/lpdocs/epic03/wrapper.htm?arnumber=148454>
- [47]Marongiu, I., Vagati, A., “Improved modelling of a distributed anisotropy synchronous reluctance machine”, IEEE Industry Applications Society Annual Meeting, 1992, pages 238-243.
- [48]Vagati, A., “The synchronous reluctance solution: a new alternative in ac drives”, Proceedings of IECON'94 - 20th Annual Conference of IEEE Industrial Electronics, Vol. 1, 1994, pages 1-13.
- [49]Soong, W. L., Staton, D. A., Miller, T. J. E., “Design of a new axially-laminated interior permanent magnet motor”, IEEE Transactions on Industry Applications, Vol. 31, 1995, pages 358-367.
- [50]Fukami, T., Momiyama, M., Shima, K., Hanaoka, R., Takata, S., “Steady-state analysis of a dual-winding reluctance generator with a multiple-barrier rotor”, IEEE Transactions on Energy Conversion, Vol. 23, 2008, pages 492-498.
- [51]Moghaddam, R. R., Magnussen, F., Sadarangani, C., “Synchronous reluctance machine (synrm) design”, pages 1-103, accessed at:<http://www.diva-portal.org/smash/get/diva2:753114/FULLTEXT01.pdf2007>.
- [52]Bianchi, N., Chalmers, B. J., “Axially laminated reluctance motor: Analytical and finite-element methods for magnetic analysis”, IEEE Transactions on Magnetics, Vol. 38, 2002, pages 239-245.
- [53]Kazmierkowski, M. P., Reluctance Electric Machines: Design and Control [Book News]. CRC Press, 2019, Vol. 13.

- [54]Vagati, A., “Synchronous reluctance electrical motor having a low torque-ripple design”, Patent, 1998, accessed at:<http://www.google.com/patents/US5818140>
- [55]ABB, “Dolsynrm concept introduction up to ie5 efficiency”, page 5, accessed at: <https://bit.ly/2PwSuym26.08.2022>.
- [56]REEL, “Reel supreme® – the ie5* magnet-free synchronous reluctance motor datasheet”, page 36, accessed at:<https://bit.ly/3KnMMsI26.08.2022>.
- [57]ABB, “Iec 60034-30-1 standard on efficiency classes for low voltage ac motors”, accessed at:<https://goo.gl/qvLUzr24.04.2029>.
- [58]Ricardo, “Ricardo develops next-generation electric vehicle motor”, accessed at: <https://goo.gl/CGH8tH26.08.2022>.
- [59]John, R., “Motorbrain summary report: Nanoelectronics for electric vehicle intelligent failsafe powertrain”, pages 1-127, accessed at:<http://www.motorbrain.eu/2015>.
- [60]Kimiabeigi, M., Widmer, J. D., Long, R., Gao, Y., Goss, J., Martin, R., Lisle, T., Vizan, J. M. S., Michaelides, A., Mecrow, B., “High-performance low-cost electric motor for electric vehicles using ferrite magnets”, *IEEE Transactions on Industrial Electronics*, Vol. 63, 2016, pages 113-122.
- [61]Merwerth, J., Halbedel, J., Schlangen, G., “Electrical drive motor for a vehicle”, Patent, 2012, accessed at:<https://goo.gl/WiLsMq>
- [62]Boldea, I., Tutelea, L. N., Parsa, L., Dorrell, D., “Automotive electric propulsion systems with reduced or no permanent magnets: An overview”, *IEEE Transactions on Industrial Electronics*, Vol. 61, 2014, pages 5696-5711.
- [63]Germishuizen, J. J., der Merwe, F. S. V., der Westhuizen, K. V., Kamper, M. J., “Performance comparison of reluctance synchronous and induction traction drives for electrical multiple units”, *Conference Record - IAS Annual Meeting (IEEE Industry Applications Society)*, 2000.
- [64]Bianchi, N., Bolognani, S., Carraro, E., Castiello, M., Fornasiero, E., “Electric vehicle traction based on synchronous reluctance motors”, *IEEE Transactions on Industry Applications*, Vol. 52, 2016, pages 4762-4769.
- [65]VOLVO, “Power take-offs: Fields of application and calculation guide”, accessed at:[http://productinfo.vtc.volvo.se/files/pdf/lo/PowerTake-off\(PTO\)_Eng_08_580114.pdf](http://productinfo.vtc.volvo.se/files/pdf/lo/PowerTake-off(PTO)_Eng_08_580114.pdf) 22.03.2018.

- [66]CleanTechnica, “Volvo blasts into electric trucks with new garbage & delivery trucks”, accessed at:<https://cleantechnica.com/2018/05/16/volvo-blasts-into-electric-trucks-with-new-garbage-delivery-trucks/>26.08.2022.
- [67]AB-Volvo, “Premiere for volvo first all-electric truck”, page 4, accessed at: <https://www.volvogroup.com/en-en/news/2018/apr/news-2879838.html>26.08.2022.
- [68]Ban, B., Stipeti ć, S., “Electric multipurpose vehicle power take-off: Overview, load cycles and actuation via synchronous reluctance machine”, ACEMP-OPTIM, 2019.
- [69]Ban, B., Stipetic, S., Klanac, M., “Synchronous reluctance machines: Theory, design and the potential use in traction applications”, International Conference on Electrical Drives and Power Electronics, Vol. 2019-Septe, 2019, pages 177-188.
- [70]VOLVO, “Body builder instructions: Pto and pumps”, accessed at:<https://bit.ly/3AosaMf> 26.08.2022.
- [71]Hubert, T., Reinlein, M., Kremser, A., Herzog, H.-G., “Torque ripple minimization of reluctance synchronous machines by continuous and discrete rotor skewing”, 2015.
- [72]Ferrari, S., “Design , analysis and testing procedures for synchronous reluctance and permanent magnet machines”, 2020.
- [73]Stipetic, S., Zarko, D., Cavar, N., “Design methodology for series of ie4/ie5 synchronous reluctance motors based on radial scaling”, Proceedings - 2018 23rd International Conference on Electrical Machines, ICEM 2018, 2018, pages 146-151.
- [74]Mirazimi, M. S., Kiyoumars, A., “Magnetic field analysis of multi-flux-barrier interior permanent-magnet motors through conformal mapping”, IEEE Transactions on Magnetics, Vol. 53, 2017.
- [75]Taghavi, S., Pillay, P., “Design aspects of a 50hp 6-pole synchronous reluctance motor for electrified powertrain applications”, Proceedings IECON 2017 - 43rd Annual Conference of the IEEE Industrial Electronics Society, Vol. 2017-Janua, 2017, pages 2252-2257.
- [76]Cupertino, F., Pellegrino, G., Cagnetta, P., Ferrari, S., Perta, M., “Syre: Synchronous reluctance (machines) - evolution”, accessed at:<https://sourceforge.net/projects/syr-e/> 26.08.2022.
- [77]Pellegrino, G., Cupertino, F., Gerada, C., “Automatic design of synchronous reluctance motors focusing on barrier shape optimization”, IEEE Transactions on Industry Applications, 2015.

- [78]Lu, C., Ferrari, S., Pellegrino, G., “Two design procedures for pm synchronous machines for electric powertrains”, *IEEE Transactions on Transportation Electrification*, 2017.
- [79]Ban, B., Stipetic, S., Jercic, T., “Minimum set of rotor parameters for synchronous reluctance machine and improved optimization convergence via forced rotor barrier feasibility”, *Energies*, Vol. 14, 2021, page 16, accessed at:<https://www.mdpi.com/1996-1073/14/10/2744>
- [80]Kamper, M. J., Merwe, F. S. V. D., Williamson, S., “Direct finite element design optimisation of the cageless reluctance synchronous machine”, *IEEE Transactions on Energy Conversion*, Vol. 11, 1996, pages 547-553.
- [81]Lampinen, J., “Multi-constrained nonlinear optimization by the differential evolution algorithm”, 2002.
- [82]Zarko, D., Stipetic, S., Martinovic, M., Kovacic, M., Jercic, T., Hanic, Z., “Reduction of computational efforts in finite element-based permanent magnet traction motor optimization”, *IEEE Transactions on Industrial Electronics*, Vol. 65, 2017, pages 1799-1807.
- [83]Bramerdorfer, G., Zavoianu, A. C., Silber, S., Lughofer, E., Amrhein, W., “Possibilities for speeding up the fe-based optimization of electrical machines-a case study”, *IEEE Transactions on Industry Applications*, 2016.
- [84]Lee, J., Seo, J. H., Kikuchi, N., “Topology optimization of switched reluctance motors for the desired torque profile”, *Structural and Multidisciplinary Optimization*, Vol. 42, 2010, pages 783-796.
- [85]Lee, C., Jang, I. G., “Topology optimization of multiple-barrier synchronous reluctance motors with initial random hollow circles”, *Structural and Multidisciplinary Optimization*, Vol. 64, 2021, pages 2213-2224.
- [86]Riviere, N., Volpe, G., Villani, M., Fabri, G., Leonardo, L. D., Popescu, M., “Design analysis of a high speed copper rotor induction motor for a traction application”, 2019.
- [87]Riviere, N., Stokmaier, M., Goss, J., “An innovative multi-objective optimization approach for the multiphysics design of electrical machines”, 2020, pages 691-696.
- [88]Mathworks, “Matlab polyshape function”, accessed at:<https://www.mathworks.com/help/matlab/ref/polyshape.html>26.08.2020.
- [89]Stipetic, S., Miebach, W., Zarko, D., “Optimization in design of electric machines: Methodology and workflow”, *Joint International Conference - ACEMP 2015: Aegean Conference on Electrical Machines and Power Electronics, OPTIM 2015: Optimization of*

Electrical and Electronic Equipment and ELECTROMOTION 2015: International Symposium on Advanced Electromechanical Moti, 2016, pages 441-448.

- [90]Ban, B., Stipetic, S., “Design and optimization of synchronous reluctance machine for actuation of electric multi-purpose vehicle power take-off”, Proceedings - 2020 International Conference on Electrical Machines, ICEM 2020, 2020, pages 1750-1757.
- [91]Ban, B., Stipetic, S., “Systematic metamodel-based optimisation study of synchronous reluctance machine rotor barrier topologies”, *Machines*, Vol. 10, 2022, pages 1-23, accessed at:<https://www.mdpi.com/2075-1702/10/8/712>
- [92]Ban, B., Stipetic, S., “Absolutely feasible synchronous reluctance machine rotor barrier topologies with minimal parametric complexity”, *Machines*, Vol. 10, 2022, pages 1-22, accessed at:<https://www.mdpi.com/2075-1702/10/3/206>
- [93]Ban, B., Stipetic, S., “Robust feasibility verification and region inner-point detection algorithms for geometric shape objects applied to electric machine optimization workflow”, *Structural and Multidisciplinary Optimization*, Vol. 175, 2022, pages 1-11, accessed at:<https://link.springer.com/article/10.1007/s00158-022-03263-4>

List of abbreviations

AxLam	Axially laminated SyRM
CrCC	Circular concentric SyRM rotor topology
CrVDC	Circular variable depth SyRM rotor topology
dx	Autocad drawing exchange format
ePTO	Electric power take-off
EV	Electric vehicle
FC	Feasibility check
FEA	Finite element method
FW	Field weakening
HyFE	Hyperbolic fixed eccentricity SyRM rotor topology
HyVE	Hyperbolic variable eccentricity SyRM rotor topology
IM	Induction machine
IPM	Interior permanent magnet
MZhED	Modified Zhukovsky equal depth SyRM rotor topology
MzhVD	Modified Zhukovsky variable depth SyRM rotor topology
PM	Permanent magnet
PMASR	Permanent magnet assisted SyRM
PTO	Power take-off
SPM	Surface permanent magnet
SyRM	Synchronous reluctance machine
TrLam	Transversely laminated SyRM
Zh	Zhukovsky SyRM rotor topology

List of Figures

1.1.	Historical rare-earth material prices.	2
2.1.	Example of four pole machine families with corresponding dq axes: IPM with a) distributed and b) concentrated winding stator; SPM with c) distributed and d) concentrated winding stator; e) SyRM; f) Axially laminated SyRM (AxLam); g) "weak" PM material PMASR; and h) "strong" PM material PMASR. Green arrows indicate PM magnetization direction, Pub.1.	6
2.2.	SyRM rotor nomenclature.	7
2.3.	Theoretical performance comparison of SyRM, ferrite and NdFeB PMASR at fixed saliency ratio, Pub.1.	8
2.4.	Voltage phasor diagram of SyRM (green) and PMASR (blue) for a given stator current (stator resistance is neglected $R_s = 0$) [9].. . . .	9
2.5.	Voltage and current constrains, voltage vector diagrams and equations for dominant reluctance torque component family (left) and dominant alignment torque component family (right)..	10
2.6.	IPM design plane [9].. . . .	11
2.7.	a) Transversally laminated rotor (TrLam) and b) Axially laminated rotor (AxLam) [50].. . . .	12
2.8.	Sketch of rotor with uniform, and non-uniform distribution of the AxLam laminations.. . . .	12
2.9.	a) Diesel engine rear PTO mount; b) diesel engine with mounted hydraulic pump; c) Transmission with direct PTO mount; d) transmission with geared PTO [70]; geared PTO propelling hydraulic pump e) and universal joint shaft f); direct PTO propelling hydraulic pump g) and universal joint shaft h).. . . .	15
3.1.	(a) SyRM terminology; SyRM rotor barrier types: (b) Circular variable depth; (c) Hyperbolic variable eccentricity; (d) Modified Zhukovsky (blue), original Zhukovsky (red).. . . .	16

3.2.	Rotor barrier construction procedure. Initial rotor construction step (a) ; Construction of inner and outer barrier line starting points (b) ; calculation of barrier intersection points (c) ; calculation of barrier vertices (d) ; vertex mirroring (e) ; rotation around center and addition of barrier fillets (f) ;	.17
3.3.	Barrier depth variation influence on different 2-barrier ($k = 2$) SyRM topologies. Circular (a) ; Hyperbolic (b) , Zhukovsky (c) and Modified Zhukovsky barrier types (d) ..	.18
3.4.	Validated Pareto fronts for each design variant, Pub.7.	.21
3.5.	Optimized cross sections per topology, Pub.7..	.22
4.1.	Feasibility detection as an optimization workflow add-on feature.	.25
4.2.	Infeasible geometry (a) and forced feasibility (b).	.25
4.3.	Illustration of feasible (a,c) and infeasible geometry (b,d).	.27
4.4.	Example of 2-layer V-shape IPM: (a) feasible case, (b) barrier definition point crossing polar lines, (c) barrier arc crossing polar lines, (d) barrier collision.	.29
4.5.	Shape robust region detection meshing example (a-d).	.30
4.6.	Feasible (a,b) and infeasible geometry (c,d).	.31
5.1.	Infeasible geometry (a) and forced feasibility (b) ..	.35

List of Tables

3.1. Illustrative depth coefficient table for Figure3.3..18
3.2. Calculation of total parameter number. Color coding is according to Fig.3.2 variables..19
3.3. Summary of parametric complexity presented in Pub.5..20
3.4. Optimization result comparison table, Pub.7..21
4.1. Analysis of infeasibility detection in different FEA tools.28
4.2. FC impact on total optimization time.32

Biography

Branko Ban was born in Šibenik (Croatia) on 8th March 1991. He finished Faust Vrančić elementary school and afterwards graduated the Antun Vrančić Gymnasium (Mathematical division), both in Šibenik. He completed Bachelor (2012.) and Master (2015.) studies in Electrical Engineering at the University of Zagreb (Faculty of electrical engineering and computing). In 2014. he spent one semester at Chalmers University of Technology, Göteborg, Sweden through Erasmus student exchange program. He started the doctoral studies at University of Zagreb in 2017., under the mentorship of Associate Professor Stjepan Stipetić.

Since 2015., he is working in the automotive sector in areas related to electric machine R&D and quality assurance. He is involved in educational activities in the fields of hybrid and electric vehicle traction and electrical safety. His areas of interest are geometrical parametrization and optimization of synchronous reluctance, and interior permanent magnet machines.

In addition to Bachelor and Master thesis, Branko Ban is an author and a coauthor of 4 journal and 9 conference publications.

Publication list

- 1.B. Ban, "Selection of Electric Motor Drives for Electric Vehicles", Bachelor thesis, University of Zagreb, Faculty of electrical engineering and computing (FER), Zagreb, 29th June 2012.
Available at: FER library (Croatian only)
- 2.B. Ban, "Computer Application for Electric Automobile Power Systems Dimensioning", Master thesis, University of Zagreb, Faculty of electrical engineering and computing (FER), Zagreb, 10th February 2015.
Available at:<https://urn.nsk.hr/urn:nbn:hr:168:448612>(Croatian only)
- 3.B. Ban, M. Vražić and I. Bahun "Electric Vehicle Model with Driving Cycle based Algorithm for Battery and Motor Minimization", in International Conference on Electrical Drives and Power Electronics (EDPE), The High Tatras, 21-23 Sept. 2015.
Available at:<https://doi.org/10.1109/EDPE.2015.7325297>

- 4.D. Vuljaj, B. Ban, L. Grković and M. Vražić "Hybrid drive dimensioning using Matlab", in 35th Conference on Transportation Systems with International Participation (Automation in transportation), Zagreb, 3-8 Nov. 2015.
Available at:urn.nsk.hr/urn:nbn:hr:168:401985(Croatian only), as L. Grković Master thesis
- 5.D. Vuljaj, B. Ban and M. Vražić, "Hibrid Drive Dimensioning using MATLAB Software Package", in 13th International Conference on Development and Application Systems, Suceava, 19-21 May 2016.
Available at:<https://doi.org/10.1109/DAAS.2016.7492568>
- 6.B. Ban, S. Stipetić and M. Klanac "Synchronous Reluctance Machines: Theory, Design and the Potential Use in Traction Applications", in International Conference on Electrical Drives & Power Electronics (EDPE), The High Tatras, 24-26 September 2019.
Available at:<https://doi.org/10.1109/EDPE.2019.8883905>
- 7.B. Ban and S. Stipetić, "Electric Multipurpose Vehicle Power Take-Off: Overview, Load Cycles and Actuation via Synchronous Reluctance Machine", in International Aegean Conference on Electrical Machines and Power Electronics (ACEMP) & International Conference on Optimization of Electrical and Electronic Equipment (OPTIM), Istanbul, 27-29 August 2019.
Available at:<https://doi.org/10.1109/ACEMP-OPTIM44294.2019.9007187>
- 8.B. Ban and S. Stipetić, "Design and optimization of Synchronous Reluctance Machine for actuation of Electric Multi-purpose Vehicle Power Take-Off", in International Conference on Electrical Machines (ICEM), Gothenburg, 23-26 Aug. 2020.
Available at:<https://doi.org/10.1109/ICEM49940.2020.9270784>
- 9.B. Ban, S. Stipetić and T. Jerčić "Minimum Set of Rotor Parameters for Synch. Reluctance Machine and Improved Optimization Convergence via Forced Rotor Barrier Feasibility", in Special Issue Optimization and Simulation of Permanent Magnet Motors, *Energies*, 2021, 14(10), 2744. April 2021.
Available at:<https://doi.org/10.3390/en14102744>
- 10.B. Ban and S. Stipetić "Absolutely Feasible Synchronous Reluctance Machine Rotor Barrier Topologies with Minimal Parametric Complexity", in Special Issue Synchronous Reluctance Motor-Drive Advancements, *Machines* 2022, 10(3), 206. January 2022.
Available at:<https://doi.org/10.3390/machines10030206>
- 11.B. Ban and S. Stipetić, "Robust Feasibility Verification and Region Inner-Point Detection Algorithms for Geometric Shape Objects applied to Electric Machine Optimization Workflow", in *Journal of Structural and Multidisciplinary Optimization*. June 2022.
Available at:<https://doi.org/10.1007/s00158-022-03263-4>
- 12.B. Ban and S. Stipetić, "Systematic Metamodel-based Optimization Study of Synchronous Reluctance Machine Rotor Barrier Topologies", in Special Issue Synchronous Reluctance Motor-Drive Advancements, *Machines* 2022, 10(8), 712. August 2022.
Available at:<https://doi.org/10.3390/machines10080712>

- 13.B. Ban, A. Andersson and S. Stipeti ć, "Design and Torque Ripple Reduction Methods for Synchronous Reluctance Machine applied in Electric Power Take-off actuation", in 2022 International Conference on Electrical Machines (ICEM), Valencia, 5-8 Sep. 2022.
Available at:<https://doi.org/10.1109/ICEM51905.2022.9910674>.
- 14.A. Kersten, A. Andersson, B. Ban, M. Rodén, A. Norouzzadeh, and S. Rydén, "Electric Vehicle Heating Management Techniques utilizing Drivetrain-Loss-Heating of Refrigerant", in 48th Annual Conference of the Industrial Electronics Society, IECON 2022. Brussels, 17-20 Oct. 2022.
Available at:<https://doi.org/10.1109/IECON49645.2022.9968738>
- 15.B. Ban, A. Kersten, A. Andersson, S. Stipeti ć, "Metamodel-based Design and Optimization of a Spoke-Type Interior Permanent Magnet Machine for a Vehicle Traction Application", in 14th International Symposium on Industrial Electronics (INDEL), Banja Luka, 9-11 Nov. 2022.
Available at:<https://doi.org/10.1109/INDEL55690.2022.9965493>

Životopis

Branko Ban je rođen 8. ožujka 1991. u Šibeniku. Završio je osnovnu školu Faust Vrančić te matematičku gimnaziju Antuna Vrančića u Šibeniku. 2012. je stekao diplomu prvostupnika Elektrotehnike i informacijske tehnologije, smjer Energetika na Fakultetu elektrotehnike i računarstva Sveučilišta u Zagrebu. Na istoj ustanovi je i diplomirao na profilu Elektrotehnički sustavi i tehnologije 2015. godine. 2014. godine je studirao jedan semestar na Sveučilištu Chalmers, Göteborg, Švedska u sklopu Erasmus studentske razmjene. 2017. godine započinje doktorski studij na Fakultetu elektrotehnike i računarstva Sveučilišta u Zagrebu pod mentorstvom izv. prof. dr. sc. Stjepana Stipetića. Od 2015. radi kao konzultant u automobilskom sektoru u područjima vezanim za istraživanje i razvoj te kontrolu kvalitete električnih motora. Sudjeluje u izvođenju predavanja iz području vučnih sustava hibridnih i električnih vozila te sigurnosti na radu. Bavi se znanstvenim radom u područjima parametrizacije i optimizacije sinkronih reluktantnih te motora s permanentnim magnetima.

Branko Ban je do sada (nakon objave završnog i diplomskog rada), kao autor i koautor objavio 4 rada u znanstvenim časopisima te 9 radova u zbornicima međunarodnih skupova.